School of Civil and Mechanical Engineering
Department of Mechanical Engineering

Development and Validation of Computational Fluid Dynamics Models for the Coupled Simulation of Heat Transfer and Fluid Flow in the Coral Microenvironments

Robert Harsono Ong

This thesis is presented for the degree of
Doctor of Philosophy - Mechanical Engineering
of
Curtin University

December 2014

Declaration

To the best of my knowledge and belief this thesis contains no material previously published by any other person except where due acknowledgement has been made.

This thesis contains no material which has been accepted for the award of any other degree or diploma in any university.

All investigations presented in this thesis are my own except where specific reference has been made to the work of others.

Signature:

Date:

Abstract

Coral bleaching and mortality have typically been characterised by the anomaly of sea surface temperature (SST). However, many studies have established that corals in some areas emerged relatively unscathed from anomalously high SST maxima that equal or exceed those associated with extensive bleaching. This thesis qualitatively and quantitatively explored the temperature deviations between coral surface temperature and ambient seawater temperature that likely determines the microscale physical processes involved in coral bleaching. It was deemed to be imperative to be able to gain a clear understanding of how the key physiological and environmental stressors – irradiance, water flow, and coral morphological features (colony shape, size, tissue thickness, and pigmentation) – drive the temperature microenvironment of corals, which may subsequently improve the bleaching or recovery predictions, thereby leading to more effective reef management.

The work presented in this thesis applied Computational Fluid Dynamics (CFD) technique coupled with hydrodynamic modelling and ray-tracing technique to predict coral surface warming due to the effects of various primary and secondary stressors under both controlled laboratory-scale conditions and shallow reef-flat environments. A detailed overview of the mechanistic basis for understanding the role of radiative heat flux, water flow and circulation pattern, and coral morphological features in affecting the microscale temperature was described. Secondary stressors – such as cloud cover, water clarity, flow regimes, waves and wind-driven currents, permeability and porosity of both tissue layer and skeletal matrix, colony pigmentation, tissue thickness – were covered in the "ecosystem" models developed as part of this work. The model results were validated thoroughly against published laboratory and field observations.

This thesis demonstrates that modelling microscale temperature could yield important insights into thermoregulation in corals. In combination with more detailed studies of added temporal and spatial data, this approach may hopefully allow the construction of physical systems which closely predict reality.

Acknowledgements

"The road to a PhD is like the mountain road at an observatory: bumpy and sometimes muddy, with a giddy feeling at the end." - unknown

I would like to acknowledge the following people, without whom this task would have been much more difficult.

First and foremost, to my supervisors, Dr. Andrew King and A/Prof. Benjamin Mullins for providing supports and for being gentlemen through and through. To my associate co-supervisors: Dr. Julian Caley and Dr. Timothy Cooper for their help and to Dr. Daijiro Kobashi and Dr. Jaap Kaandorp for their collaboration contributions.

I also would like to thank all the people in the OpenFOAM, Radiance, Curtin Fluid Dynamics Research Group (FDRG), and ROMS-SWAN forums for their numerous discussion over the course of the model development. A big thank you to especially Martin Becker for his help in providing valuable insight to OpenFOAM and PyFOAM.

A heartfelt gratitude to my parents and my sister for their support and everything they have done during these years.

Additional financial supports for this research provided by iVEC and SUT are gratefully acknowledged.

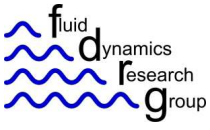

Contents

List of Figures

List of Tables

Nomenclature

Symbols

C_p	specific heat capacity	$\frac{J}{kg \cdot K}$
k	thermal conductivity	$\frac{W}{m \cdot K}$
S_i	flow sink term	$\frac{m}{s}$
S_h	heat source term	$\frac{W}{m^2}$
D	Darcy's coefficient (viscous loss term)	$\frac{m}{s}$
F	Forchheimer's coefficient (inertia loss term)	$\frac{m}{s}$
Q	intensity of solar radiation	$\frac{W}{m^2}$
$\dot{q}$	heat irradiance for each cell	$\frac{W}{m^2}$
θ	the angle of incidence	$\circ$
d	diameter	m
p	pressure	$\frac{kg}{m \cdot s^2}$
$\partial p / \partial x$	pressure gradient in x-cartesian coordinate	$\frac{Pa}{m}$
A	surface area	m^2
I	irradiance	$\frac{W}{m^2}$
A/V	surface area-to-volume ratio	m^{-1}
V	coral volume	m^3
n	number of cell	–
i, j, k	generic counters	–

x, y, z	cartesian coordinates	$-$
T	temperature	K
t	time	s
y^+	non-dimensional wall distance	m
y	wall distance	m
$\mathbf{U}$	velocity vector	$\frac{m}{s}$
Re	Reynolds number	$-$
Pr	Prandtl number	$-$
Nu	Nusselt number	$-$
Sh	Sherwood number	$-$
u, v, w	velocity components in x,y,z direction	$\frac{m}{s}$
k	turbulent kinetic energy	$\frac{m^2}{s^2}$
I	turbulent intensity	$\%$
l	turbulent length scale	m
C_μ	coefficient for eddy viscosity	$-$
C_ω	coefficient in specific turbulent dissipation equation	$-$
C_ϵ	coefficient in specific turbulent dissipation equation	$-$
f_μ	damping function for eddy viscosity	$-$
$f_{1,2}$	damping functions for ϵ equation	$-$

Greek Symbols

$\Delta_{x,y}$	dimensions of bidimensional control volume	$-$
ϵ	turbulent kinetic energy dissipation	$\frac{m^2}{s^3}$
Γ_T	thermal diffusivity	$\frac{m^2}{s}$
α	tissue absorptivity	$-$

τ	Reynolds-stress tensor	$\frac{m^2}{s^2}$
φ	porosity	%
μ	dynamic viscosity	$\frac{kg}{m \cdot s}$
μ_t	eddy viscosity	$\frac{m^2}{s}$
ν	kinematic viscosity	$\frac{m^2}{s}$
ρ	density	$\frac{kg}{m^3}$
ω	specific turbulent kinetic energy dissipation	$\frac{m^2}{s^3}$

Subscripts

$_c$	coral
$_m$	medium
$_t$	tissue
$_f$	fluid
$_{rad}$	incident radiation

Superscripts

$'$	correction
$''$	fluctuation
$\sim$	Favre averaged
$^-$	Reynolds averaged

Chapter 1

Introduction

1.1 General introduction

Coral reefs are highly diversified and productive ecosystems described by many as "rainforests of the sea". They present a range of benefits, not only to the surrounding ecosystem (by providing habitat and food to many diverse aquatic flora & fauna), but also represent a significant economic benefit to local communities (for example, tourism and fisheries) which also provide protection to shorelines from the impact of waves and storms. However, a large number of studies have raised concerns about the long-term degradation of the world's coral reefs, with some estimates suggesting that approximately 30% of the world's reef area destroyed so far, and this number is expected to double in the next few decades (Hoegh-Guldberg, 1999a; Hoegh-Guldberg et al., 2007; Hughes et al., 2003). The major risks to coral reefs can be divided into two categories: (1) anthropogenic drivers, which include climate change, ocean acidification, water pollution, destructive fishing and overfishing, and contact uses (i.e. tourism); (2) environmental drivers, which include extreme weather conditions (tropical storms or hurricanes, ENSO - El Niño Southern Oscillation), local variability (i.e. sedimentation, water quality, solar radiation, sea temperature), outbreaks of crown of thorns starfish (*Acanthaster planci*), and diseases. Historically, reefs have evolved to cope with a variety of natural disturbances, however there is a growing body of evidence to indicate that the recovery rate of corals is often depressed due to the increase in frequency and severity of various human-induced impacts, possibly exceeding the rate at which coral communities can recruit and reproduce (Brown, 1997; Glynn, 1993; Hoegh-Guldberg, 1999a; Muscatine and Porter, 1977).

Increases in the global mean temperature and increases in sea surface temperature (SST) are now widely accepted as real. In combination with a variety of other emergent threats (i.e. ocean acidification, ozone depletion, sedimentation, etc.), coral bleaching may well be the biggest threat to coral reefs now and in

the future (Hoegh-Guldberg, 1999a; Hoegh-Guldberg et al., 2007; Hughes et al., 2003). The increasing magnitude and frequency of coral reef bleaching events has had devastating and widespread effects worldwide. The occurrence of large scale bleaching events often correlate with increased SST anomalies (Baker et al., 2008; Hoegh-Guldberg, 1999a; Hughes et al., 2003; McWilliams et al., 2005). This direct link between anomalously high SST and coral bleaching raises further concerns that rising SST, driven by global warming, could cause an increase in the frequency and severity of mass bleaching events, However, a recent number of contradictory findings of coral cover on the Great Barrier Reef (GBR) based on the collection of annual long-term data suggest that the impact of SST-induced coral bleaching on the GBR over the last few decades was found to be minimal (Death et al., 2012; Osborne et al., 2011; Sweatman et al., 2011). While the SST approach may be useful for predicting the localised onset of bleaching temperature thresholds, there may be several drawbacks to its use (McWilliams et al., 2005). For example, the bleaching thresholds are highly variable and may not be comparable between methods using different data sets (Mumby et al., 2001) or with different coral species compositions (Baird and Marshall, 2002; Hoegh-Guldberg and Salvat, 1995). Thermal thresholds also do not take into account other climatic variables that may influence bleaching, for instance, cloud cover on radiative stress (Mumby et al., 2001). The extent of variability in bleaching threshold varies among species owing to their morphological characteristics, hence, severity and recovery may vary between bleaching events. Therefore, this bleaching variability is not consistent with the idea of a step function of SST and bleaching event characteristics.

This thesis presents a new prediction technique that couples heat and mass transfer with fluid dynamics to study the coral thermal microenvironment at various spatial scales with a view to better understanding the sources of such variability in bleaching thresholds. This is achieved through the development of Computational Fluid Dynamics (CFD) models of different coral species, morphologies and pigmentations and examining their responses to varying thermal consistency and flow conditions. For the purposes of this thesis, the thermal microenvironment can be defined as the temperature of the colony surface and of the boundary layer directly above it, which can deviate substantially from the mean temperature of the surrounding seawater. This temperature deviation is a function of several factors, though it is predominantly due to radiative heat flux and water flow on the coral surface. A heat balance is maintained between losses from convection into the surrounding water (dependent on water flow and other surface characteristics involved in the boundary layer formation), heat conduction into deeper layers of the coral, and emission of short and long-wave radiation incident on the coral surface (Fabricius, 2006). Furthermore, this thesis provides a conceptual study of the capabilities of CFD to be coupled with atmosphere-

ocean general circulation models (GCM) , which serves as an initial motivation to explore the full range of parameters that could trigger coral bleaching events. While climate change is difficult to combat, exploring spatial and temporal trends of bleaching frequency or intensity is the first step in its mitigation. Accurate predictions of bleaching stress would also allow governments and institutions to prioritise reef conservation by designing more effective Marine Protected Areas (MPA) in geographic regions that are projected to suffer the least from fluctuations in environmental extremes.

1.2 Literature review of the nature of thermally induced bleaching

In most of the literature on coral bleaching, the relationship between bleaching and temperature has been assessed on the basis of data obtained on sea surface temperatures (SST). However, it is the temperature of the colony surface and of the boundary layer directly above it that determines physiological processes, and these temperatures can deviate substantially from the surrounding seawater. This deviation of surface temperatures from ambient seawater temperatures is a function of several factors. Three main factors include the short-wave solar radiation incident on the surface of the coral and the proportion of the incident radiation absorbed by its surface (short-wave absorptivity), the coral's morphology (size, shape, and composition – i.e. tissue thickness, pigmentation and permeability), and water flow and circulation patterns around it (physical oceanography within and surrounding the coral reef) which can materially affect heat and mass transfer of corals under various flow rates and regimes. There is also an existing body of literature that explores the molecular and cellular responses of coral symbionts and physiological basis of bleaching.

Many studies have linked elevated SST with coral bleaching, which is generally considered to be the primary stress impacting corals and associated with global warming (Brown, 1987; Fitt et al., 2001; Glynn, 1993; Glynn and D'croz, 1990; Glynn, 1991; Goreau, 1992; Jokiel and Coles, 1990; Pittock, 1999; Wilkinson, 2000; Williams and Willaims, 1990). However, a variety of other stressors can cause bleaching (Brown, 1997; Coles and Brown, 2003; Glynn, 1993; Lesser, 2004), but the physiological and cellular mechanisms by which these stressors cause bleaching are not well understood (Douglas, 2003). Several studies have also discussed the coral bleaching mitigation effects of upwelling-induced decreases in water temperature during times of highest heat stress (Chollett et al., 2010; Glynn, 1996; Riegl and Piller, 2003). However, in other studies, e.g. (Bayraktarov et al., 2013), differences in absolute water temperatures between exposed and sheltered sites were insignificant and calculated temperature anomalies be-

tween sites were comparable. Consequently, their data indicated that the decrease in water temperature was not responsible for the observed coral bleaching and recovery dynamics between the investigated sites (Bayraktarov et al., 2013).

The concept of thermal thresholds comes from the notion that knowing the thermal limits of a species of coral will assist in predicting the frequency and intensity of bleaching events. While information detailing temperature anomalies, predominantly expressed as "HotSpots" and "Degree Heating Weeks (DHW)" (Liu et al., 2003; Van Oppen and Lough, 2008), are now routinely being used to forecast bleaching risks; such products however cannot accurately predict bleaching below the landscape scale and may lead to potentially erroneous statements concerning the health of coral reefs globally. Improving current metrics requires multi disciplinary knowledge, spanning biology, physics, and ecology, but also due to the complexity and heterogeneity of reef environment, extensive spatial and temporal information is also needed. This thesis re-evaluates the thermal physiology of reef corals by indicating how sub-lethal responses to coral surface warming are related to other variables in setting the physiological limits of corals.

Elevated sea temperature: The primary cause of mass bleaching is increased sea temperatures. Mass bleaching, however, affects reefs at regional to global scales and cannot be explained solely by localised stressors operating at smaller local spatial scales. Corals live at the upper-limits of their thermal environment such that water temperatures elevated by only 1-2 °C above the maximum monthly average in summer can result in bleaching. Prolonged exposure to "bleaching" temperatures will eventually kill the coral; however, if temperatures quickly return to normal levels, the corals may recover. However, it is interesting to note that a few studies that have observed no bleaching despite high SST anomalies in various spatial and temporal scales.

Solar radiation: There are examples from both the field and the laboratory where solar radiation alone has been implicated in the bleaching of reef corals. In some instances, particular loss of chlorophyll because of bleaching were demonstrated under specific wavelengths: Photosynthetically active radiation (PAR), 400-700 nm and Ultraviolet radiation (UVR), 280-400 nm. There have been also a number of reports in which corals have bleached when changes in solar radiation combined to produce particularly stressful conditions, such as during periods of low wind velocity and calm seas, which favour the intense heating of shallow waters and subsequent strong penetration of solar radiation. Many studies also suggests that the spatial extent and patterns of bleaching response may be influenced by factors that determine the amount of solar radiation to which corals are exposed. These factors might include cloud cover attenuation in the water column, the rise and fall of turbidity from runoff, and tidal flushing.

Elevated sea temperature and solar radiation: The most widely acknowledged cause of bleaching is elevated seawater temperatures and high solar radiation, ex-

acerbated by other stressors (i.e. low salinity, low cloud cover). Their synergistic and additive effects on coral bleaching are well established.

The following section reviews and summarise literature studies relevant to the relationship between a range of stressors and thermal stress in corals that often lead to bleaching.

1.2.1 Basic coral anatomy and symbiosis

Corals are colonies of polyps connected by a common gastrovascular system. Polyps are small fleshy extensions of the coral (typically millimeters in diameter) compared to the often massive structure of the colony (Muller-Parker and D'Elia, 1997). Corals are composed of two cell layers: the epidermis and the gastrodermis (Figure 1.1). These cell layers are separated by a thin tissue layer (mesoglea) that is made up of collagen, mucopolysaccharides, and cells, and has a relatively high refractive index (Barnes, 1980; Dubinsky and Jokiel, 1994; Johnsen and Widder, 1999; Muller-Parker and D'Elia, 1997).

Corals lives in a mutual symbiotic relationship with dinoflagellate algae (zooxanthellae) that live within their tissue. This relationship provides the corals with nutrients necessary for calcium metabolic processes required for coral skeletal growth (Figure 1.2). Areal densities of zooxanthellae normally exceed one million per square centimeter of coral surface, although algal density in corals can be highly variable both temporally and spatially (Muller-Parker and D'Elia, 1997). The zooxanthellae can produce excess photosynthetic product, these products are rich in carbon but are believed to lack sufficient nitrogen and phosphorous to solely support algal reproduction (Jones and Yellowlees, 1997; Szmant et al., 1990). The same applies for the coral host, which often receives adequate sustenance from zooxanthellae for daily respiration, but only provides minor contributions towards tissue growth and reproduction (Dubinsky and Jokiel, 1994).

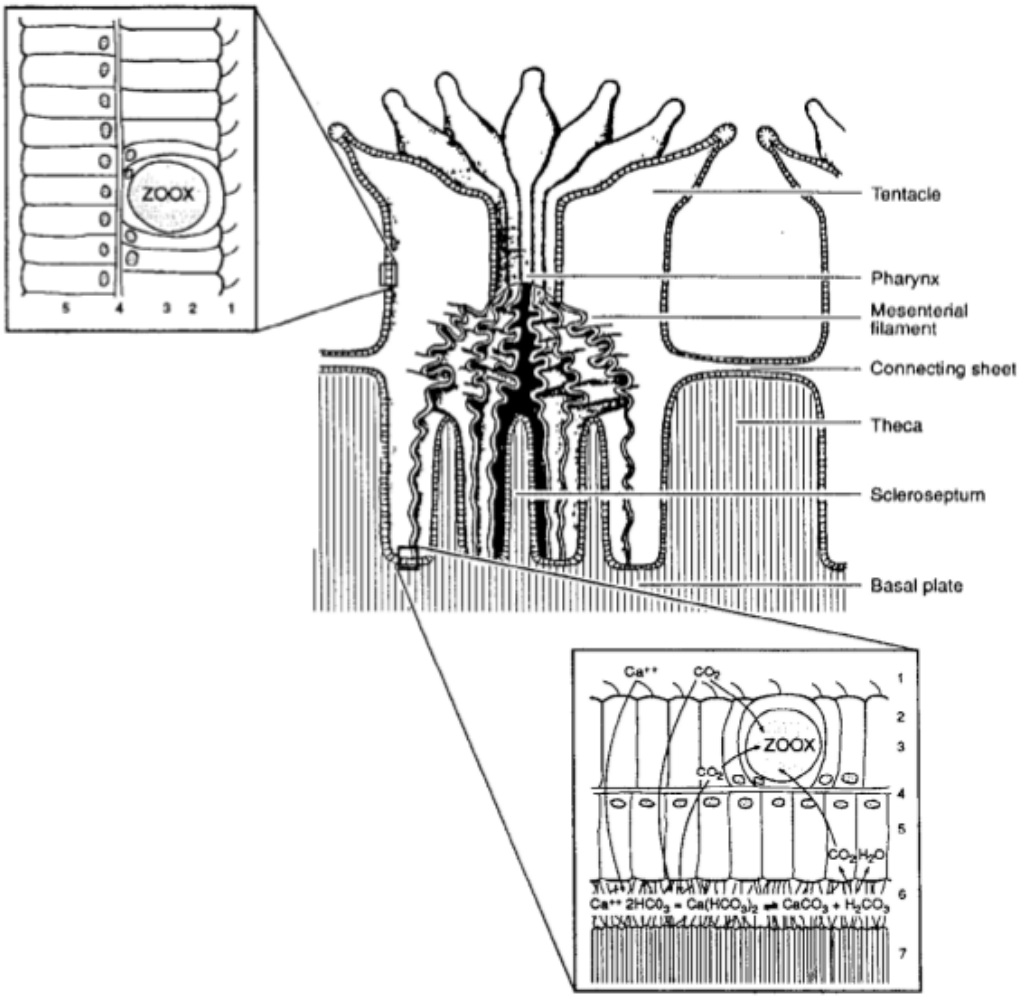

Figure 1.1. Schematic diagram of coral cross-section, with boxed insets showing coral tissues layers in contact with the seawater and the skeleton. From Barnes (1980) (Barnes, 1980), Muller-Parker and D'Elia (1997) (Muller-Parker and D'Elia, 1997), and Kuhlmann (1988) (Kühlmann, 1988).

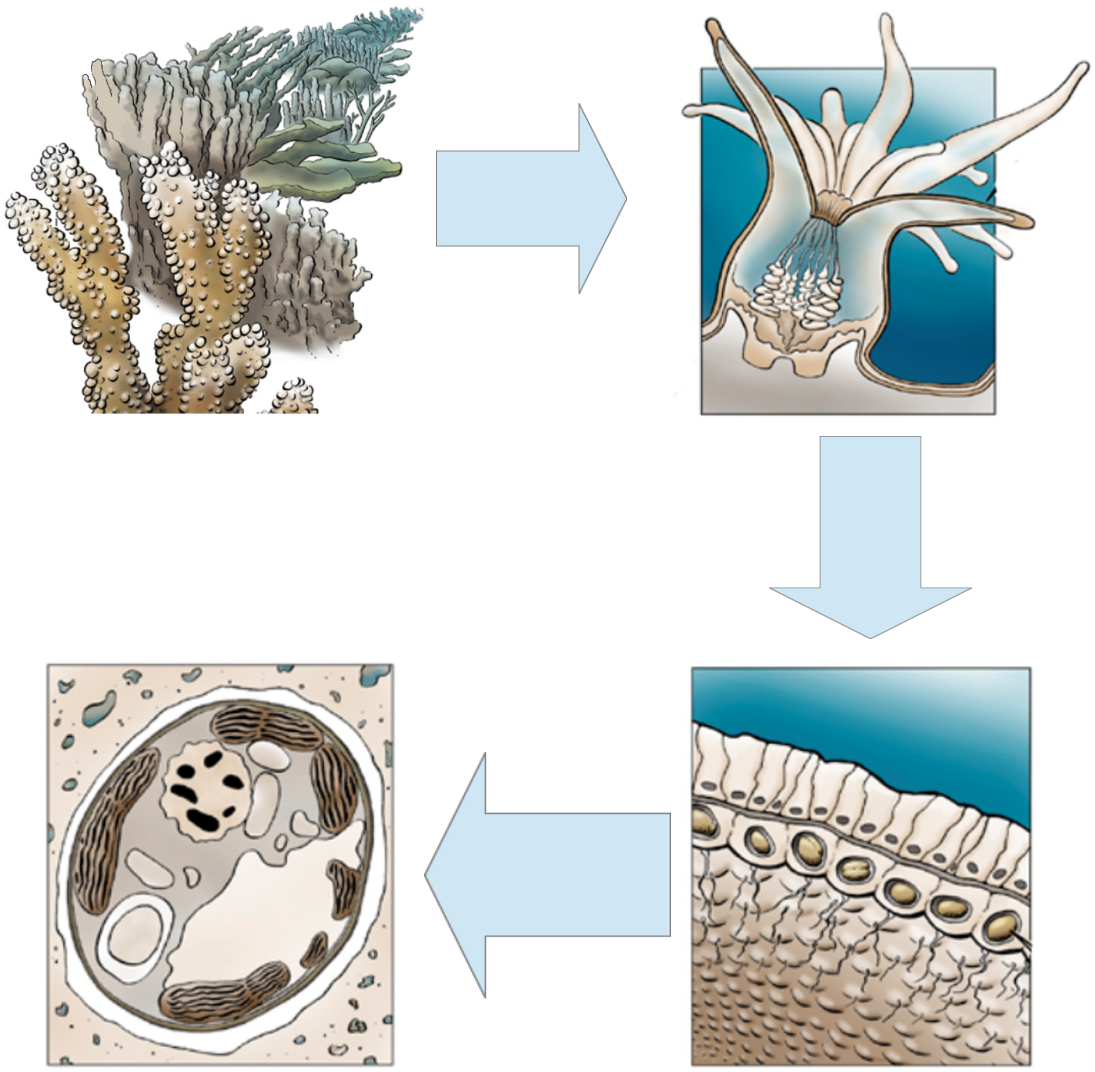

Figure 1.2. Diagram of the coral symbiosis. A cross-section of a single coral polyp from a coral colony is shown in the upper left-hand boxed inset. The arrow leading from the coral polyp points to a section through the two tissue layers of the oral surface of the polyp. Adapted from Muller-Parker and D'Elia (1997) (Muller-Parker and D'Elia, 1997).

1.2.2 Coral bleaching

1.2.2.1 A definition

Corals, as well as numerous species of cnidarians, mollusks, polychaetes, protists and other taxa, are hosts to dinoflagellate symbionts, *Symbiodinium*. Bleaching is a stress response that results when the coral-algae relationship breaks down that leads to the visible paling of the host organism, either due to the loss of pigments when zooxanthellae are degraded from the coral hosts or when pigments within the algae are expelled along with the algae (Figure 1.3) (Brown, 1997; Hoegh-Guldberg, 1999a; Marshall and Schuttenberg, 2006). In severe cases where zooxanthellae loss is prolonged (i.e. the stress-induced bleaching is severe and depleted zooxanthellae populations do not recover), the coral host usually dies within days or weeks. The cellular damage to the symbionts and/or their hosts is a response to thermal stress. Natural and anthropogenic variations in the reef environment including high or low SSTs, increased solar irradiance, suspended sedimentation, turbid inorganic nutrients, and decreased salinity can disrupt the enzyme systems in zooxanthellae that offer protection against oxygen toxicity, resulting in the overproduction of oxygen radicals that often leads to bleaching (Baker et al., 2008; Hoegh-Guldberg, 1999a; Lesser, 2006; Muscatine and Porter, 1977).

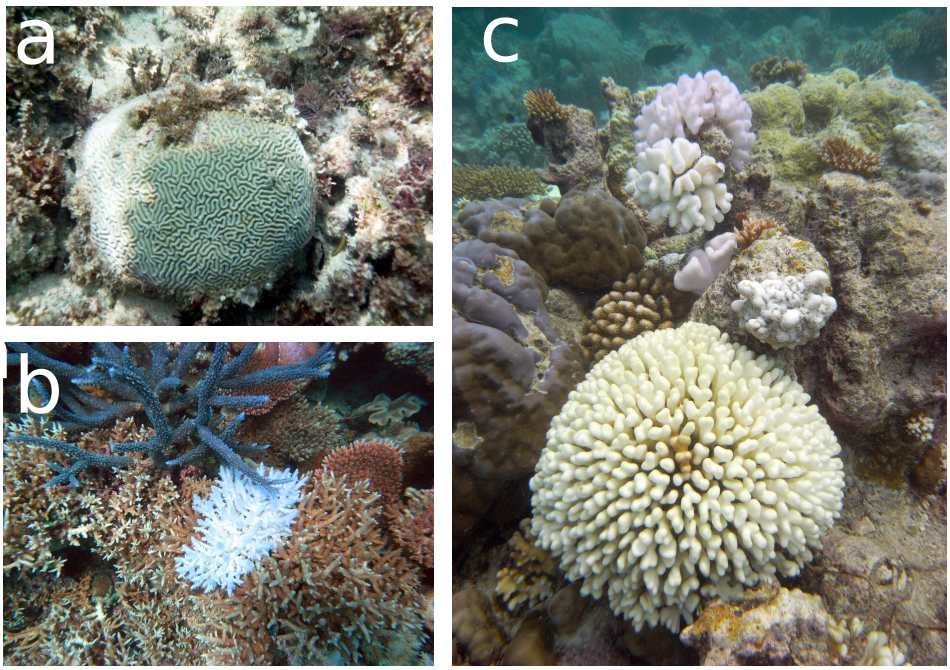

Figure 1.3. (a) Partially bleached *Porites* spp. (b) Partially bleached*Acropora* spp. (c) Totally bleached *Pocilliopora* spp.

1.2.2.2 Past events

Coral reef bleaching events principally driven by increased SST, have been reported in all major reef regions since the 1970s and have increased dramatically in number since the early 1980s (Figure 1.4) (Baker et al., 2008; Glynn, 1993; Hoegh-Guldberg, 1999a; Hoegh-Guldberg et al., 2007; Hughes et al., 2003). Many of these events have seen a decline in reef health, indicated by increases in coral diseases, presence of bioeroders, or the loss of marine habitat including reef fishes and other biotas (Baker et al., 2008). The magnitude and frequency of coral bleaching events during the past few decades has increased rapidly, with numerous mass bleaching events reported, involving hundreds of reefs, and on occasion, whole ocean basins. As a result, many of these events and the associated colony recovery rates have been studied over decadal scales, and some compilations are available in the published studies (Brown, 1997; Coles and Brown, 2003; Glynn, 1996; Wilkinson, 2000; Wilkinson et al., 2008; Williams and Willaims, 1990), as well as online databases provided by agencies such as WorldFish Center, National Oceanic and Atmospheric Administration (NOAA), and Great Barrier Reef Marine Park Authority (GBRMPA).

Typically bleaching events within affected regions are not uniform, exhibiting patchiness over micro (mm to cm) to meso (km) scales (Baker et al., 2008; Brown, 1997; Brown et al., 2002; Glynn, 1993). Variability in bleaching is believed to result predominantly from morphology and genetic compositions as well as spatial and temporal fluctuations in environmental conditions. Evidently, the occurrence of mass bleaching events have been reported from virtually every region that supports coral reefs, and no region of the world's tropical and subtropical seas appears safe from bleaching (Figure 1.4).

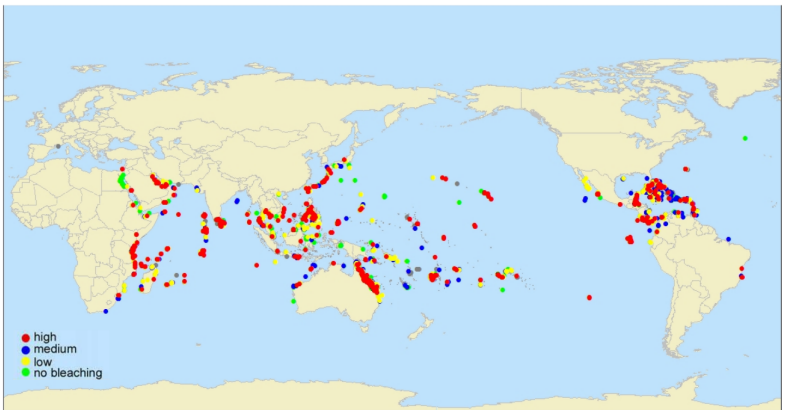

Figure 1.4. Reef database of worldwide bleaching records (from January 1963 to November 2014). The global map is obtained from ReefGIS, http://reefgis.reefbase.org/

1.2.2.3 Loss and recovery trends and future outlook

Recovery of reefs from severe bleaching impacts have been variable across all spatial scales with some reefs have experiencing more rapid recovery compared to others (Baker et al., 2008; Brown, 1997; Brown et al., 2002; Glynn, 1993; Hoegh-Guldberg, 1999a; Hughes et al., 2003). Some studies have recorded a significant overall recovery of coral cover in the Indian Ocean following widespread bleaching in 1998 (Baker et al., 2008; Lambo and Ormond, 2006; Ledlie et al., 2007; McClanahan et al., 2005; Riegl, 1999; Smith et al., 2006; Wilkinson, 2004). On the contrary, coral cover in the Western Atlantic Ocean has continued to decline due to multiple smaller bleaching events and a diverse set of chronic secondary stressors (Baker et al., 2008; Rogers et al., 2008; Wilkinson et al., 2008). No clear trends are apparent in the eastern Pacific where some reefs are recovering and others are not (Baker et al., 2008; Birkeland et al., 2008; Craig et al., 2005; Wakeford et al., 2008; Wilkinson, 2004).

Major anthropogenic risk factors that ultimately leads to coral bleaching and mortality were recently found to account for only 10% of coral cover losses in the GBR during the period of 1985-2012, whereas large-scale acute disturbances such as tropical cyclones and coral predation by crown-of-thorns starfish accounted for 48% and 42%, respectively (Death et al., 2012). On the contrary, a few studies suggested that coral cover was higher and found no evidence of consistent decline in coral cover since 1995 in the GBR (Osborne et al., 2011; Sweatman et al., 2011), and estimated optimistic future survival rates even under higher SST scenarios (Kleypas et al., 2008; McClanahan et al., 2007).

There is a general agreement in the literature that coral bleaching will be a severe threat to continued coral survival for the next 30-50 years even under the most optimistic climate scenarios (Baker et al., 2008). Mitigation of anthropogenic as well as large-scale acute disturbances are essential to prevent further loss in coral cover. Nevertheless, future predictions also need to include intrinsic and extrinsic stressors, such as the coral symbiotic and morphological properties, and the temporal and spatial environmental condition, in order to estimate the potential response of bleaching and survival rates.

1.2.3 The cellular and physiological basis of bleaching

Bleaching was first described as an injury to corals as a result of high temperatures following several days of hot and calm weather in the Dry Tortugas, Florida (Baker et al., 2008; Mayor, 1914). Following that observation, a study described bleaching as loss of coral pigmentation as a result of reduced salinity and light exclusion (Coles and Brown, 2003; Vaughan, 1914). Furthermore, during the Low Islands (GBR) expedition in 1928-1929, bleaching was described as a decline

in cellular concentrations of symbionts in coral host that had been exposed to elevated temperature and secondary stresses (Baker et al., 2008; Coles and Brown, 2003; Yonge et al., 1931). Following a series of mass bleaching events in the Pacific and Caribbean during the late 1980s, marine scientists and biologists made rapid progress in understanding the molecular underpinnings of bleaching, in particular how interactions between temperature and light result disrupt photosynthesis (i.e. Photosystem II, PSII) (Brown et al., 2000; Fitt and Warner, 1995; Fitt et al., 2001; Iglesias-Prieto et al., 1992; Jones et al., 1998; Lesser, 1996; Warner et al., 1996, 1999); how enzymatic antioxidants degrade oxygen free radicals (Lesser et al., 1990), and how the xanthophyll cycle dissipates excess absorbed energy (Brown et al., 1999).

In general, bleaching often results from accumulated oxidative stress occuring on the thylakoid membrane of the chloroplast of zooxanthellae (Downs et al., 2002; Lesser, 1997, 1996). This phenomenon leads to photoinhibition, which is the photodamage of PSII due to the dysfunction and subsequent degradation of D_1 protein cells within the PSII reaction center, as shown in Figure 1.5 (Aro et al., 1993; Hoegh-Guldberg, 1999a; Jones and Hoegh-Guldberg, 2001; Jones et al., 1998). Essentially, bleaching occurs when the PSII system lowers the sensitivity of zooxanthellae to photoinhibition, in which light becomes a liability under conditions of higher than normal temperatures (Jones and Hoegh-Guldberg, 2001; Jones et al., 1998).

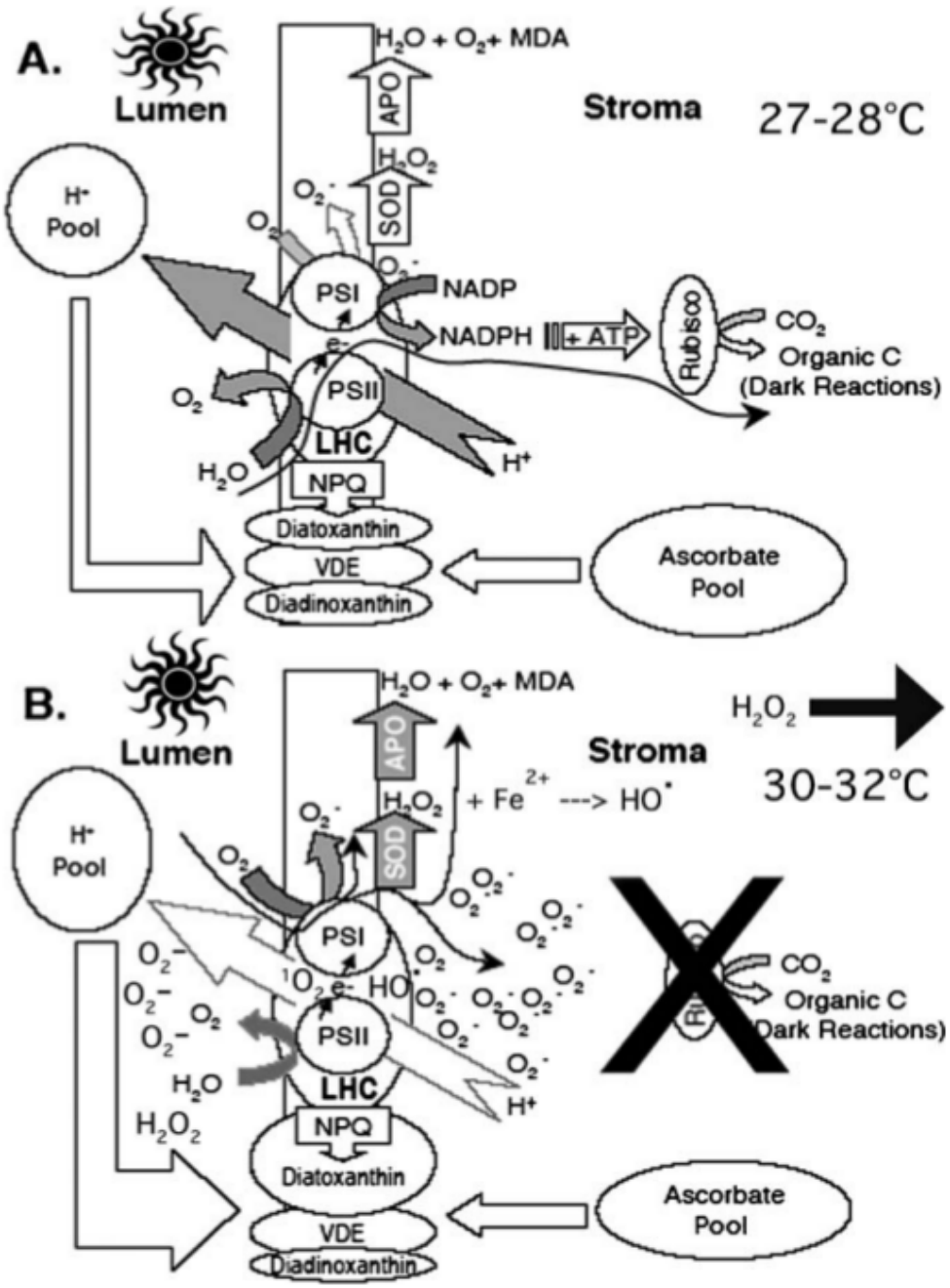

Figure 1.5. Photoinhibition model of coral bleaching. Adapted from Lesser 1997, Jones *et al.* 1998, Hoegh-Guldberg 1999 (Hoegh-Guldberg, 1999a; Jones et al., 1998; Lesser, 1997). (A) The two photosystems (PSI and PSII) pass light energy to the dark reactions where CO_2 is fixed and regulated by the interconversion of the enzyme systems. (B) Heat stress interrupts the flow of energy to the dark reactions which is then converted to active oxygen that makes up the photosynthetic components of the zooxanthellae. Abbreviation; SOD: superoxide dismutase; APO: ascorbate peroxidase; VDE: violaxanthin de-epoxidase.

1.2.4 The environmental factors that drive and mitigate bleaching

A variety of other stressors have been identified that can cause and mitigate the frequency and intensity of bleaching.

1.2.4.1 The role of temperature

The single most important factor driving coral bleaching events is the increasing frequency of high temperature anomalies. Most of regional bleaching episodes of coral reef bleaching documented to date have been attributed to high temperatures (Brown, 1987; Fitt et al., 2001; Glynn, 1993; Glynn and D'croz, 1990; Glynn, 1991; Goreau, 1992; Jokiel and Coles, 1990; Pittock, 1999; Wilkinson, 2000; Williams and Willaims, 1990). Bleaching and mortality due to low temperatures has also been well documented (Coles and Jokiel, 1977; Coles and Fadlallah, 1991; Glynn and D'croz, 1990), however the cold stress mechanism (like heat stress) can also lead to bleaching by impairing the function of PSII (Hoegh-Guldberg et al., 2005; LaJeunesse et al., 2007; Saxby et al., 2003).

The historical correlation between climate change and coral extinction is frequently discussed in the literature due to the belief that elevated SST is the primary driver in bleaching. However, questions still exist as to the combination of heat and exposure time needed for bleaching to occur. To answer this, the heat-threshold (many refer to bleaching-threshold) provides indication of the likeliness of bleaching (Berkelmans, 2002; Glynn, 1993, 1996; Goreau et al., 1997; Goreau and Hayes, 1994; Hoegh-Guldberg, 1999a), however this idea was highly contested and is still debated until today (Fitt et al., 2001; Manzello et al., 2007; McClanahan et al., 2007). The idea was based on the existence of upper and lower temperature thresholds based on SST data which, when exceeded, will result in physiological stress resulting in the breakdown of symbiosis (Baker et al., 2008; Glynn, 1993).

As a measure to backcast and forecast bleaching episodes based on SST data, several indicators have been established. The most-used and earliest developed indicators are the monthly mean SST above a local threshold (Brown et al., 1996; Goreau, 1991) and cumulative heat-stress (Gleeson and Strong, 1995; Glynn, 1990b; Podestá and Glynn, 1997). The NOAA has taken advantage of this long data series by establishing SST climatology upon which it has based a number of satellite global 50-km resolution experimental products, namely Hotspot and Degree Heating Week (DHW) (Liu et al., 2003). The Hotspot approach uses a Degree Heating Month (DHM) index which is defined as the cumulative sum of anomalies that has surpassed 1°C above the maximum mean-monthly summer temperature in that particular region (Goreau and Hayes, 1994). Shortly after

DHM, a degree days (DD) index was developed (Podestá and Glynn, 1997), which is a summation of differences between daily SST values and mean SSTs over the warm phase of the year. Time-integrated bleaching thresholds were proposed to estimate bleaching intensity by examining the records (Figure 1.6), which used a 3-day maximum temperature to estimate bleaching intensity on the GBR (Berkelmans, 2002; Berkelmans et al., 2004; Manzello et al., 2007).

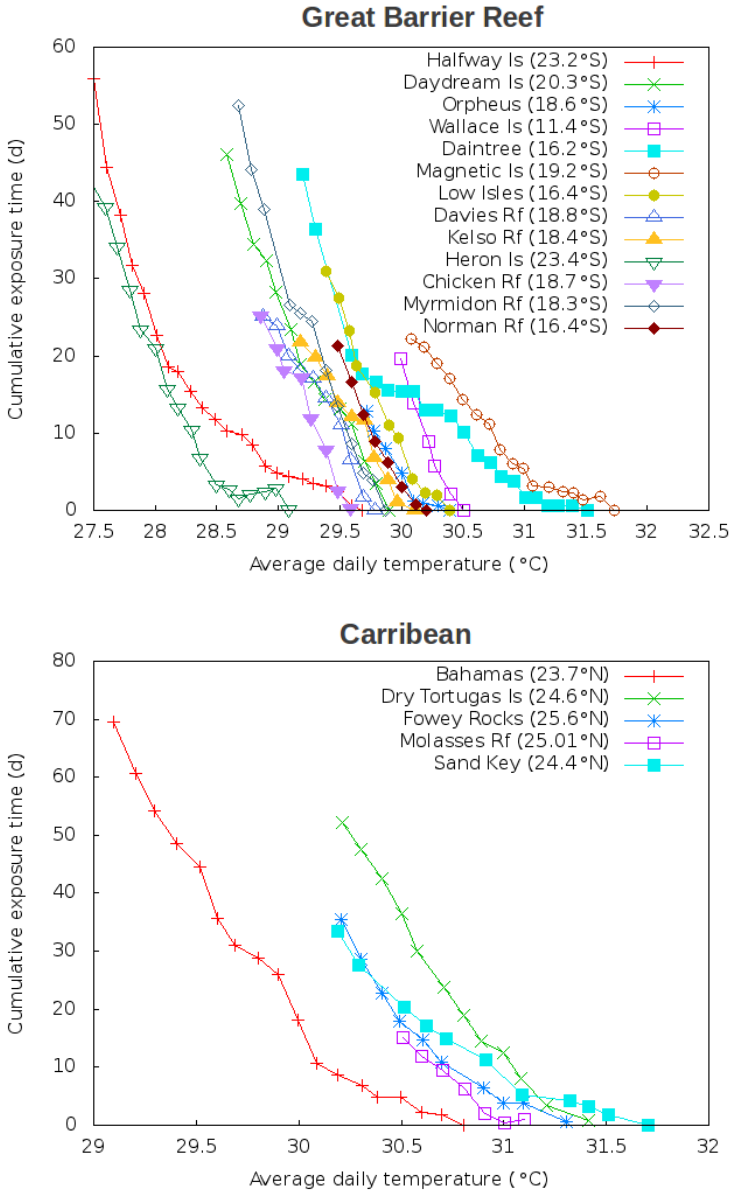

Figure 1.6. The time-integrated bleaching threshold for reef sites on the GBR (Berkelmans, 2002) and the Caribbean (Manzello et al., 2007).

The Degree Heating Week (DHW) measures accumulated thermal stress over a 12-week period by calculating the number of degree-weeks by which temperatures exceed the mean annual maximum temperature (Liu et al., 2003). DHWs have been relatively successful in predicting coral bleaching events, and have been incorporated into NOAAs Coral Reef Watch program. However, a particular study found that DHWs, combined with information on past temperature anomalies and coral community sensitivity, only predicted about one-half of Indian Ocean bleaching in 2005, suggesting that these metrics might not be good predictors of milder bleaching events (McClanahan et al., 2007).

1.2.4.2 The role of regional weather conditions

Large-sale ocean-atmosphere phenomena, in particular El Nino-Southern Oscillation (ENSO), have been implicated as a probably driver of the temperature anomolies that likely cause bleaching (Glynn, 1993, 1984, 1990a,b; Prahl, 1983, 1985; Wilkinson, 1999). Many studies have associated ENSO with extensive bleaching in the eastern Pacific (Hueerkamp et al., 2001; Podestá and Glynn, 1997) and Palau (Bruno et al., 2001). Other large-scale ocean-atmosphere phenomena such as the Pacific Decadal Oscillation (PDO) and the Indian Ocean Dipole (IOD) have appeared to be the drivers of thermal anomolies associated with bleaching events in Hawaii and the western Indian Ocean, respectively (Jokiel and Brown, 2004; McClanahan et al., 2007).

Short and long-term effects of large-scale weather patterns are important in modulating the bleaching response (Skirving et al., 2006). A particular study has attributed absence of bleaching in the Tuamotu Islands in 1998 to high cloud cover since heat-flux into the ocean was dramatically reduced compared with clear and calm days (Mumby et al., 2001). In addition to clouds, the presence of aerosols may affect the scattering of radiation and thus decrease heat-flux to the ocean. A study showed that high levels of aerosols effectively mitigated bleaching conditions, even during ENSO phenomenon (Gill et al., 2006). Furthermore, storm conditions (and even hurricanes) can mitigate bleaching due to strong wave action that lead to vertical mixing, therefore removing excess heat from shallow water (Heron et al., 2004; Manzello et al., 2007; Skirving et al., 2006).

1.2.4.3 The role of water flow and circulation patterns

Physical oceanography can help explain the spatial variability of coral bleaching. Unlike the biological approach which focuses on the coral's reaction to stress, the physical approach investigates where the stress is located. If the water in certain areas of a reef becomes hotter than other areas during a bleaching period, spatial variability in bleaching would be expected. Spatial patterns of coral bleaching

may be attributed to the spatial variability of water flow and circulation patterns.

Water-mass of the ocean is constantly moving in various temporal and spatial scales. The scales and causes of these water motions are many, beginning with the great ocean currents, tidal currents and local waves (Kraines et al., 1998; Vogel, 1981). Hydrodynamic force is a direct environmental factor, but water motion also affects other factors, including nutrient availability, light penetration (turbidity), temperature, and salinity changes (Baird and Atkinson, 1997; Lobban et al., 1985). Because of the high density of water, a wave or current exerts greater force than do winds. Therefore, too much water motion can impose drag and dislodge corals (Denny, 1985, 1988). However, too little water motion can impose diffusion stresses due to impairment of molecular uptake and release (Wheeler, 1988).

Some studies have also stressed the importance of water flow in modulating physiological processes in corals by enhancing photosynthesis and increasing respiration rates of coral tissues (Atkinson et al., 1994; Bruno and Edmunds, 1998; Dennison and Barnes, 1988; Lesser et al., 1994; Patterson et al., 1991; Sebens et al., 2003). Water flow affects the rate of nutrient uptake and ingestion rates of particulate material, hence, some corals will grow more rapidly when flow increases (Jokiel, 1978; Kuffner, 2001; Sebens et al., 2003).

Differential rates of water-flow are largely a consequence of the effect of frictional drag force across the coral's boundary layers thereby changing mass-transfer rates of gases and metabolites (Atkinson and Bilger, 1992; Nakamura et al., 2001; Patterson and Sebens, 1989). When water-flow rates are low, thick diffusive boundary layers prevent efficient passive diffusion processes. Several studies have shown positive correlations between water-flow conditions and the rates of (1) photosynthesis (Dennison and Barnes, 1988; Lesser et al., 1994), (2) growth (Jokiel, 1978; Sebens et al., 2003), (3) phosphate uptake (Atkinson and Bilger, 1992), (4) micosporine-like amino acid accumulation under ultraviolet light exposure (Kuffner, 2001) and (5) survival under high irradiance and SSTs (Nakamura et al., 2001). Water flow increases mass transfer of inorganic nutrients (Nakamura et al., 2001) and dissolved gases across the diffuse boundary layer between the water column and the coral tissue (Lesser et al., 1994), thereby reducing oxidative stress and limiting photoinhibition, which in turn may prevent or minimize coral bleaching (Finelli et al., 2006; Nakamura et al., 2005).

1.2.4.4 The role of irradiance

Solar radiation underpins primary production on coral reefs and contributes to coral bleaching (Hoegh-Guldberg, 1999a). High irradiances usually occur together, and their synergistic effects on coral bleaching are well established (Jones and Hoegh-Guldberg, 2001). But since seawater temperatures change more slowly

than irradiance levels, warming events followed by cloudy weather or sudden increases in turbidity may result in simultaneous elevations in seawater temperatures and reduced irradiances. Solar irradiance has many potential targets and mechanisms (e.g. radiant energy heating, desiccation, wavelength-related photosystem damage, and other wavelength-related cell/molecular damage). Field observations of minimal bleaching despite warming events have been attributed to reduced irradiances from cloud cover (Mumby et al., 2001) or turbidity (Phongsuwan, 1998), and laboratory experiments have shown greater photoinhibition and bleaching of corals kept at elevated temperatures when exposed to high irradiances than low irradiances (Lesser and Farrell, 2004). However, elevated seawater temperatures reduce photosystem function in isolated reef coral zooxanthellae kept in the dark (Warner et al., 1996) or at low irradiance (Warner et al., 1999). Effects of elevated seawater temperatures at different irradiance levels are particularly relevant to corals in shallow back reef systems, where seawater temperatures are often elevated and irradiance levels can rapidly fluctuate with changing weather conditions as well as the rise and fall of turbidity from runoff and tidal flushing (Dahlgren and Marr, 2004).

Atmospheric conditions affect the amount of heat transferred through the air-sea interface. Heat passes through the air-sea interface through radiation, conduction, convection, and water-phase transformation. A latent heat flux is used to denote the heat transfer from a water-phase transformation, such as evaporation. Finally, solar radiation is separated into shortwave (Ultraviolet radiation [UVR], 280-400 nm) and longwave (Photosynthetically active radiation [PAR], 400-700 nm) components. In most bleaching cases due to solar damage, UVR has been documented to have more damaging effects in cell/molecular levels because it enhances photoinhibition at high irradiance and accumulates mycosporine-like amino acids (MAA) (Brown et al., 1994; Gleason and Wellington, 1993; Jokiel et al., 1982; Lesser and Shick, 1989). Symbiotic algae, zooxanthellae, are also routinely exposed to UVR in shallow coral reef system (Jokiel, 1980), with UV-A (320-400 nm) and UV-B (280-30 nm) penetrating to considerable depths (20 m or greater) in clear seawater (Calkins and Thordardottir, 1980; Jerlov, 1950; Lesser and Shick, 1989; Smith and Baker, 1979). There are predominantly two major factors that determine the amount of UVR received by submerged corals; the first factor is related to the stratospheric ozone depletion (partly caused by climate change amongst other stressors) which may affect weather patterns and consequently allowing more UVR into the ocean, and the second factor is the attenuation of UVR in the water column (Brown, 1997).

Attenuation of solar irradiance in the visible and near-UV wavelengths can be attributed to five atmospheric processes: Rayleigh scattering, absorption by oxygen, absorption by ozone, scattering and absorption by aerosols, and absorption by water vapour (Gregg and Carder, 1990). Irradiance that is not scattered

by the atmosphere proceeds directly to the Earth's surface as direct irradiance, and that which is scattered out of the direct beam but still proceeds toward the Earth's surface as diffuse irradiance. The sum of the direct and diffuse components defines the global irradiance.

$$I_{gh} = I_{dh} + I_{dn}\sin\theta \tag{1.1}$$

where I_{gh} is the global horizontal irradiance, I_{dh} is the diffuse horizontal irradiance, I_{dn} is the direct normal irradiance, and θ is the sun altitude.

Variations in direct irradiance below the water surface are mainly caused by three oceanographic factors: the transmittance of irradiance through the water column (turbidity) (Van Duin et al., 2001), water depth (tides) (Kleypas, 1996; Pond and Pickard, 1983), and the sea-state (rough or smooth water surface) (Weinberg, 1976); while the attenuation of diffuse irradiance is mainly affected by the variations in clouds (Mumby et al., 2001; Wright, 1995). If light availability for benthic communities shows multiple periodicities, it will have consequences for temporal patterns of primary productivity, light stress, or both (Anthony et al., 2004). Furthermore, in particular habitats in which light periodically becomes limiting for growth (e.g., in deep and turbid waters), the effect of external sources of light reduction on the health or stress status of benthic primary producers might depend critically on their timing relative to the natural irradiance pattern (Anthony et al., 2004). For instance, tidal immersions - low-tide occurrences that leave corals exposed - are damaging to shallow-water reefs, especially on the reef flat and the reef crest. The amount of damage incurred depends on the time of day and the weather conditions that coincide with low tide. During the day, corals are exposed to UVR, which may stress them and cause them to expel their symbiotic zooxanthellae. In this thesis I examine the contributions of clouds, turbidity, tides, and sea-state to the variation of irradiance.

1.2.4.5 The role of morphology and size

Coral populations clearly differ in their susceptibility to thermal stress, some are simply more physiologically tolerant, yet other differences are influenced by colony morphology, colony size and depth distribution. Although, physiological responses are measured in hours and days, population changes take weeks, months or years, yet ultimately the latter is a time-integrated response of the former. For example, experimental work shows that massive colonies are less sensitive to an increase in water flow and thermal stress compared with more complex morphologies (Finelli et al., 2006), which may be related to the general tolerance of massive colonies to thermal stress reported from all oceans.

Coral morphology (size, shape, and composition (i.e. tissue thickness and permeability)) is one of the dominant drivers to determine the variation in bleach-

ing susceptibility (Loya et al., 2001; Marshall and Baird, 2000; Shenkar et al., 2005). The taxonomy of the scleractinian coral is typically confounded by the existence of morphological variations, ranging from highly complex branching structures to simple hemispherical and encrusting forms (Veron, 1995, 2000). The within species variation in morphology and skeletal characters and growth forms are highly influenced by irradiance and water flow rates (Anthony et al., 2004; Berkelmans et al., 2004), which highlights the importance of temperature microenvironments not only in the context of thermal stress but also in relation to temperature-controlled growth rates (Fabricius, 2006).

Surveys conducted over a broad range of habitats and biogeographic regions have shown that scleractinian corals with branching morphologies generally suffer higher rates of mortality than species with massive and encrusting morphologies; while coral species with massive and encrusting morphologies frequently bleach during periods of elevated temperature, but they also often demonstrate a high rate of survival (Brown and Suharsono, 1990; Fujioka, 1999; Glynn, 1983, 1990a; Hoegh-Guldberg and Salvat, 1995; Jokiel and Coles, 1990; Loch et al., 2004; Loya et al., 2001; Marshall and Baird, 2000; McClanahan, 2000; McClanahan and Maina, 2003; Wilkinson, 2000). For examples, fast growing and finely branched species, such as *Acropora* and *Pocillopora*, are considered to be highly susceptible to thermal stress and experience high rates of whole colony mortality (Baird and Marshall, 2002; Guest et al., 2012; Loya et al., 2001). In contrast, massive corals such as *Porites* and *Faviids* are viewed to be more resistant to thermal stress and more frequently experience partial, rather than whole colony mortality (Baird and Marshall, 2002; Guest et al., 2012; Loya et al., 2001; Woesik et al., 2001). Therefore, the accumulating evidence that some types of corals tend to bleach more readily than others may be defined by a possible relationship between colony morphology and bleaching.

Corals are distributed across a wide range of light habitats from high-light environments on shallow-water reef flats (Hoegh-Guldberg and Jones, 1999; Jones and Hoegh-Guldberg, 2001) to low-light environments in deep water (Fricke et al., 1987; Kaiser et al., 1993; Mass et al., 2007), shaded caves (Anthony and Hoegh-Guldberg, 2003; Kaniewska et al., 2008), and turbid water (Anthony and Fabricius, 2000). A few studies were conducted to investigate the ambient light levels across coral habitats (Anthony and Hoegh-Guldberg, 2003; Falkowski et al., 1990). Furthermore, a few laboratory studies have examined irradiance levels within coral tissue (Kühl, 2005; Magnusson et al., 2007) or in the skeleton underneath (Fine et al., 2005; Magnusson et al., 2007; Shibata and Haxo, 1969), and differences in light attenuation between coral species (Magnusson et al., 2007).

Colony size also plays an important role in determining patterns of mortality on bleached reefs. Small juvenile colonies of some species can survive better than large, mature colonies (Loya et al., 2001; Mumby, 1999; Riegl, 2002; Van Woesik

et al., 2004). Consequently, repetitive bleaching events might shift the age distribution of coral colonies toward smaller colonies with lower fecundities (Done, 1999), in turn hindering the recovery of these reefs. However, this may not be true of all sites and species, and may vary according to how other environmental stressors interact with bleaching. This suggests that large colonies might be more resistant than small colonies to environmental disturbances, such as nutrients and sedimentation (Bak and Meesters, 1999). These studies provide evidence that colony-level differences can affect bleaching susceptibility and suggest that the impact of future thermal stress events may be biased toward larger colonies of dominant reef-building species (Brandt, 2009).

Presently, the two most common size-normalising parameters for Scleractinian corals are the surface area of the skeleton covered by living tissue, and tissue biomass. The surface area of the skeleton has been used to standardise physiological data for >60 years (Kanwisher and Wainwright, 1967; Motoda, 1940), however it has gained widespread acceptance with the publication of the simple method using aluminium foil (Marsh, 1970). Although alternative techniques such as dye-dipping (Hoegh-Guldberg, 1988) provide greater resolution for morphologically complex skeletons, none of the available methods quantifies the actual area of coral tissue, which arguably is more biologically relevant than skeletal area (Edmunds and Gates, 2002; Patterson, 1992a); hence, there is no clear relationship between skeletal area and actual surface area (Edmunds and Gates, 2002).

Determining surface area and volume of coral is essential to understanding their interaction with external and internal physical and biological processes. The suite of analytical techniques employed by coral biologists have advanced significantly in the last decades to estimate three-dimensional morphological coral properties (mainly surface area, Table 1.1) with various accuracy and environmental scale measurements. While these methods have been shown to be reliable for simple coral growth forms, large degrees of error were introduced when applying them to more complex growth forms (Edmunds and Gates, 2002; Holmes, 2008; Jones et al., 2008). Wax dipping provided the best estimate of the surface area of coral skeletons which had external corallites, regardless of morphological complexty; whereas X-ray computed tomography (CT) scanning provided the highest resolution surface area estimates by detecting surface features smaller than 1000 μm^2 (Veal et al., 2010).

Moreover, one of the main challenges for biological assessment of coral reefs over large temporal and spatial scales is the ability to extrapolate data obtained at the laboratory scale to spatially extensive physiological data sets such as tissue biomass, coral surface area, colony weight and volume (Holmes, 2008). This thesis utilises the cell looping technique to calculate incremented cell area and volume over a mesh-based representation of coral morphology.

Table 1.1. List of published methods for estimating the surface area of corals

Method	Reference
Geometric shape fitting	(Jones et al., 2008; Kanwisher and Wainwright, 1967; Odum and Odum, 1955)
Aluminium foil	(Marsh, 1970)
Paraffin wax	(Stimson and Kinzie, 1991)
Latex	(Meyer and Schultz, 1985)
Dye uptake	(Hoegh-Guldberg, 1988)
Calculation of surface index	(Chancerelle, 2000; Dahl, 1973; Holmes et al., 2008)
Photogrammetry	(Bythell et al., 2001; Done et al., 1982)
3D reconstruction using video	(Cocito et al., 2003)
Laser scanning	(Holmes, 2008; Raz-Bahat et al., 2009)
Structured light	(Veal et al., 2010)
X-Ray CT scan	(Kaandorp and Kübler, 2001; Laforsch et al., 2008; Naumann et al., 2009)

1.2.5 Variations in bleaching susceptibility

The implications of short-term temperature stress, cumulative temperature stress, or temperature variability for predicting the onset of bleaching and severity are still largely unstudied in the literature. The temperature variability is predominantly determined by fluctuations in environmental conditions, spatial heterogeneity of reef surfaces, genetic differences in hosts or symbionts, and differences in environmental history (Baker et al., 2008). Corals are also able to acclimate to their environment. For instance, corals living in warmer and tropical waters are likely to have a greater tolerance to high SST than the same species living in cooler and subtropical regions (Berkelmans, 2002). Furthermore, past experience of environmental stress of bleaching may also indicate whether coral communities tend to be more resilient when faced with a subsequent thermal stress (Brown et al., 2002; Coles and Brown, 2003). Theory also indicates at there should be no barrier to genetic adaptation of greater bleaching resistance in response to natural selection imposed by bleaching (Day et al., 2008). The rates of such adaptation remain largely unexplored. Understanding how each of these characteristics interact remains one of the greatest challenges in predicting bleaching responses. Hence, predicting whether a particular reef will bleach is complex and requires

a large amount of information regarding its location, species composition, and more importantly the intensity of the bleaching stress itself (Bird, 2005; Skirving et al., 2006).

Many studies have now reported variation in bleaching susceptibility between reefs, within reefs, and even within single coral colonies. The bleaching response is complex due to the highly diversified adaptive capabilities and tolerances of various symbiotic algae (*Symbiodinium* spp.) to environmental stress. There is ample evidence that certain *Symbiodinium* are more stress tolerant than others and subsequently some corals can thrive under warmer than normal conditions (Coles and Brown, 2003; Rowan, 2004), which in part indicates that symbiosis alteration may be one mechanisms by which corals may adapt to global warming. Differences in bleaching susceptibility have also been variously ascribed to differences in physiology or morphology, in particular the overall growth form (Marshall and Baird, 2000).

1.2.5.1 Spatial and temporal scales

Coral bleaching events are predominantly related to high SST anomalies with high irradiance acting as a secondary effect, however, many bleaching-related observations found enormous heterogeneity both in temporal and spatial scales. What has become evident is that the thermal tolerances of coral populations appear to vary on small spatial scales (Berkelmans et al., 2004; Berkelmans and Oliver, 1999). Most studies agree that the ocean-atmosphere interactions play an important role in supplying energy to sustain the water circulation and convection during the course of heat and mass transfers. For instances, the effects of bleaching when there was a high degree of water mixing (Heron et al., 2008), poor water quality (Wooldridge, 2009), cold water upwellings (Glynn, 1993), and high cloud cover (Mumby et al., 2001).

1.2.5.2 Acclimatisation of corals to warmer conditions

The ability of corals to adapt and tolerate changes in global warming has been a key topic of debate for over a decade (Coles and Brown, 2003; Gates and Edmunds, 1999; Hoegh-Guldberg, 1999a; Hoegh-Guldberg et al., 2007; Smith and Buddemeier, 1992). Acclimatisation refers to compensatory changes in the metabolism of an organism exposed to multiple natural variations in the environment (Gates and Edmunds, 1999; Prosser, 1991). Bleaching temperature thresholds of reef corals vary locally, and conditions that often leads to coral mortality in some regions may have no effect on corals in others (Baker et al., 2008). To gain insight into the responses of coral communities to shifting environmental conditions, it is necessary to assess the magnitude of change and

the rate at which such changes might have some impacts on the physiology and consequently the thermal stress of corals.

The SST anomalies that typically become an indicator of coral bleaching, are often short-term and unpredictable in the long term. Their magnitude and duration is determined by seasonal patterns as well as ocean-atmosphere interaction, such as the El Nino-Southern Oscillation. Consequently, adaptation or acclimatisation must respond to unpredictable and dramatic spikes in temperature that may challenge adaptive mechanisms suited to gradual and continuous increases in baseline or average SST (Baker et al., 2008; Hoegh-Guldberg, 1999a).

In general, corals can acclimatise by modifying their cellular metabolism as well as by selecting individuals within populations that are better equipped to cope with warmer conditions (Day et al., 2008; Hoegh-Guldberg, 1999a; Smith and Buddemeier, 1992). However, an answer to the key question – whether corals can respond to warmer conditions quickly enough to keep up with global climate change remains elusive.

1.2.6 Current coral bleaching predictions

Detecting bleaching remains difficult due in part to the complex physiological and physical factors that confound observations (Baker et al., 2008). Current predictive modelling techniques are based, at least in part, on remote mapping of SST via satellite and aircraft sensors with sufficiently high spectral and spatial resolutions. Other statistically based predictions such as meta-analysis and Bayesian belief network (BBN) have recently become the methods of choice to describe the trends in reefs worldwide (Baker et al., 2008). Other analytical and numerical investigations were also implemented to study the climate, environment, and morphology of a coral colony and reefs.

1.2.6.1 Remote sensing approaches

Remote sensing is often implemented to estimate the extent of coral bleaching and mortality through satellite or aircraft based images of SST anomalies and hot spots in near real-time. Hot spots are defined as patches of hot water that have surpassed the maximum mean-monthly summer temperature in that particular region (Goreau and Hayes, 1994). Coral Reef Watch (CRW) - which was established in 2000 by the National Oceanic and Atmospheric Administration (NOAA) - has been providing twice-weekly charts of hot spots around the world. Hot spots are, however, limited to describing the location and degree of stress without providing an insight into the length of time scale that the coral is exposed to the water anomaly. Building on this framework, CRW has introduced a DHW map which measures the time-integrated cumulative impact of thermal

stress on coral, and is calculated as the product of the exposure-time and degrees of thermal stress over a rolling 12-week time period (Bird, 2005; Liu et al., 2003; Skirving et al., 2006).

Satellite remote sensing to detect physical parameters that may drive coral bleaching should be encouraged, however, the development of advanced satellite sensors with high spatial and spectral resolutions is still yet to materialise. Some environmental properties of reefs that can be measured using remote sensing are listed in Table 1.2 (Mumby et al., 2004).

1.2.6.2 Meta-analysis

Meta-analysis is a statistical method that provides an estimation of the overall magnitude of large-scale and long-term trends in coral reefs and other ecosystems (Baker et al., 2008; Côté et al., 2005; Hedges et al., 1985; Parmesan and Yohe, 2003). Several studies have used this approach to describe the causes and rate of coral reef decline in the Caribbean (Gardner et al., 2003), the Pacific (Bruno and Selig, 2007) and even worldwide (Jackson et al., 2001; Pandolfi et al., 2003, 2005). For detailed discussion of the statistics of meta-analysis, readers may refer to these studies (Hedges et al., 1985; Parmesan and Yohe, 2003).

1.2.6.3 Bayesian belief network

Bayesian belief networks (BBN) are a causal reasoning tool that offers a holistic approach to coral bleaching predictions. The method provides a mathematical framework based on past events and allowing information content of the data to predict the future possibility of large-scale coral bleaching events occurring. The difficulty in setting up a BBN is that it requires a large amount of inter-disciplinary input data based on probabilistic understanding and past experience provided by ecologists, oceanographers, climatologists, bio-statisticians and spatial analysts. The accuracy of the model will depend on what the nodes measure and is summarised through a conditional probability distribution in the form of conditional probability table (CPT).

Table 1.2. Physical parameters that may be measured using remote sensing. Adapted from (Mumby et al., 2004).

Platform	**Aircraft**		**Satellite**								
Sensor type	Hyper-spectral	Micro-wave	Hyper-spectral	Multi-spectral (high res.)	Multi-spectral (medium res.)	Multi-spectral (low res.)	Meteoro-logical	Radar-scattero-meter	Radar	Radar-Altimeter	Radio-meter
Examples of sensor	AVIRIS, CASI, ATM	SLFMR	Hyperion	IKONOS, Quick-bird	Landsat TM, SPOT, IRS	SeaWiFS, MODIS	GOES, GMS, METE-ORSAT	SAR, Quick-SCAT	TRMM	TOPEX, JASON-1	AVHRR, ATSR
SST						√	√				√
UVR						√					√
PAR			√	√		√	√				√
Attenuation coeff.	√		√	√	√		√				√
Cloud cover			√	√	√	√	√				√
Sea level										√	
Salinity		√									
Chl-a	√		√	√	√		√				
Algal conc.	√		√		√		√				
Sedimentation	√		√	√	√		√				√
Wind speed								√		√	
Ocean circ.						√	√			√	√
Coastal circ.						√	√				?√
Precipitation									√		

√ indicates routinely possible; ?√ indicates demonstrated in limited cases only

1.2.6.4 Forecasting from climate models

Hoegh-Guldberg (1999) (Hoegh-Guldberg, 1999a) explicitly forecast the frequency and severity of bleaching events, which eventually became the basis of climate models. This work was a semi-quantitative prediction such that the model assumed a single bleaching threshold at any given site and no capacity for acclimatisation or adaptation of corals over time (Baker et al., 2008). By synthesising field data on bleaching temerature thresholds with coupled atmosphere-ocean general circulation models (GCM) from the 2nd assessment (1996) of the Intergovernmental Panel on Climate Change (Houghton, 1996), Hoegh-Guldberg concluded that severe bleaching events were likely to become "commonplace" worldwide by 2020 (Baker et al., 2008; Hoegh-Guldberg, 1999a). Furthermore, a more comprehensive study (Donner et al., 2005) predicted the likelihood of future bleaching under climate change by incorporating models from the 3rd IPCC (2001) and a bleaching prediction algorithm developed by NOAAs Coral Reef Watch (Baker et al., 2008).

1.2.6.5 Hydrodynamic modelling of reef systems

Efforts to identify local physical or environmental conditions that characterise reef areas using hydrodynamic modelling tools are relatively common in literature. Hydrodynamic models can be used to describe oceanographic currents and from these predict SST patterns for future, severe, mass coral bleaching events. Hydrodynamic modelling can also assist in the investigation of other issues that relate to the coral reef ecosystem; connectivity with biological events (e.g., coral/fish spawning) and anthropogenic interactions (e.g., sewage outfall, pollution spills) can be monitored and/or predicted.

Reef morphology and hydrodynamics: Reef morphology is highly variable. Initial reef hydrodynamic studies largely focused on those coral reefs classified as barrier reefs or atolls, systems where the shallow-reef lies adjacent to a deep and expansive lagoon that connects freely to the open ocean (Atkinson et al., 1981; Munk and Sargent, 1948; Taebi et al., 2012). The presence of an unbounded lagoon adjacent to these reefs can establish distinct momentum balances in different regions of the reeflagoon system. In particular, the presence of a lagoon can allow strong wave-driven currents to be established across reefs. Even in the vicinity of wave breaking, the radiation stress gradients may be balanced by not only wave set-up gradients, but also by shear stresses associated with a cross-reef flow (Symonds et al., 1995; Taebi et al., 2012).

Bathymetry: One of the most important inputs to a high resolution hydrodynamic model is the bathymetry. The effect of incorrect bathymetry on the models can be significant and, as such, the accuracy of bathymetry can be cru-

cial to the success of the numerical model (Heron and Skirving, 2004) (a detailed discussion is given in (Gille et al., 2004)). For remote geographic locations, where in-situ data are limited, remote sensing techniques can provide such bathymetry. A numerical study that developed a theoretical basis for describing water depth by passive remote sensing (Lyzenga, 1978). Another study then applied this knowledge to investigate shallow regions with low bottom-albedo and variable bottom-types (e.g., sand, coral, algae, seagrass) using satellite data and developed a new algorithm for estimating water depths to 25 m and beyond (Stumpf et al., 2003).

The General Ocean Turbulence Model (GOTM): It simulates small- scale turbulence and vertical mixing in the ocean water column. It is a one dimensional, hydrostatic water column model which uses the Boussinesq approximation when calculating the turbulent eddy viscosity (Burchard, 2002). GOTM allows the selection of a range of state-of-the-art turbulence closure schemes. A dimensionless stability function, a turbulent velocity scale, and turbulent macro length scale are all needed to calculate the Kolmogorov-Prandtl relations. Several zero-, one-, and two-equation models used to calculate the turbulent velocity and macro length scales, as well as various stability functions, are available in GOTM (Burchard, 2002). Further detail on the particular turbulence schemes available in GOTM can be found in (Burchard, 2002).

1.2.6.6 Modelling vertical temperature profile

Following the work of Simpson and Hunter (1974) (Simpson and Hunter, 1974), water currents and bathymetric data may be used to provide the parameterization that was used to determine the vertical temperature profile of spatial distribution from SST to the local depth of water (Bird, 2005; Heron and Skirving, 2004). Processes that contribute to vertical mixing are wind stress, tidal currents/bottom friction, and internal mixing. These processes form a pattern of SST for each time step in the model. Temperature changes due to advection were then added (Bird, 2005). At each time step, water from each grid point was advected according to the prescribed direction and current speed at that point. If the source water was warmer than the destination water then the destination must have been well-mixed. As such, any advected hot water to this region would then also be mixed (Bird, 2005; Heron and Skirving, 2004).

1.2.6.7 Modelling growth form

The coral growth process generates a wide range of colony morphologies, such as spherical, plate-like and branching forms. These morphologies are species specific, but also show high intraspecific variability. This intraspecific variability

is probably caused by environmental parameters, such as light availability and the amount of water flow (Kaandorp, 1999; Kaandorp and Kübler, 2001; Kaandorp and Sloot, 2001; Merks et al., 2003a). The effect of light availability was studied in two pioneering coral modelling studies (Graus and MacIntyre, 1976; Graus and Macintyre, 1982), and the effect of fluid flow on coral growth was studied in previous works (Kaandorp, 1999; Kaandorp et al., 1996; Kaandorp and Sloot, 2001). Using lattice Boltzmann methods to solve the complicated interior flow problem, and assuming that local growth is limited by diffusion to the structure (diffusion limited accretion) (Monismith, 2007), they produce structures that are quite similar in appearance to branching corals (Kaandorp et al., 2003, 2005). Applying a similar technique may also lead to branch orientation that optimises nutrient uptake or pray capture (Helmuth and Sebens, 1993; Monismith, 2007).

1.2.7 Limitations to existing prediction approaches

Studies associated to coral bleaching has been dominated by small-scale laboratory, continuous field and in-situ observations, and predictive modelling studies based on remotely sensed sea conditions, particularly SST. The Hotspot and DHW predictive modelling have proved quite successful in predicting past bleaching events (Baker et al., 2008; Moore et al., 2012; Spillman et al., 2011). There is also a general appreciation of the importance of statistical methods such as meta-analysis and BBN in predicting trends of reefs worldwide. Nevertheless, limitations exist which should be addressed for each of the techniques.

The most challenging limitations in using satellite or aircraft-based imaging sensors to obtain SST data is the lack of both spectral and spatial resolutions and the difficulties of ground calibration to achieve measures of absolute accuracy. In addition, predictive modelling, in turn, is limited by the assumption that SST, or other such parameters, adequately represents key physiological features of the ecology that are related to bleaching. The hot spot information is limited to just identifying the possible location and degree of thermal stress rather than the corals reaction to the stress. Meanwhile, DHW is an oversimplification which calculates the accumulated heat stress based on the product of the degree heating and exposure time. The hot spots and DHW prediction techniques do not give indication of the thermal stress and coral response at varying depths.

The meta-analysis prediction method has been repeatedly criticised in favour of expert consensus views which seem to be less contentious and quantitative (Aronson et al., 2003; Aronson and Precht, 2006; Hoegh-Guldberg et al., 2007; Hughes et al., 2003). Furthermore, for complex and heterogeneous coral ecosystems, setting up a BBN requires a large amount of input data. So far (to the knowledge of the author), no models have appropriately include the presence of irradiance or water flow in their networks.

Current hydrodynamic models are used to specifically quantify the role of momentum forcing on reef systems without any assessment on the effects and interactions with the heat budget in controlling the thermal stress in coral microenvironment. Moreover, the growth modelling technique using lattice Boltzmann methods, which predicts a specific preferential growth orientation based on the mass transfer uptake of nutrients, excludes the effect of flow variations and heat budgets within the interior and exterior of coral morphology. These parameters (i.e., flow, pressure, temperature, etc), related to coral morphology, are likely to be important determinants of mass and heat transfer in corals, and ultimately may be important determinants of their sensitivity to bleaching.

Despite significant advances in climate modelling and given the potentially critical importance in predicting reef futures, surprisingly few models have updated the simplistic early predictions of bleaching frequency or intensity, or attempted to explore spatial trends that might predict the potential response of reef globally (Baker et al., 2008). In addition, these models provide little quantitative data on which a model of heat and momentum budgets could be computationally established, and, in particular, between different coral morphologies.

As a result, current bleaching predictions have highlighted the need for a comprehensive update on bleaching mechanisms, which encompasses the fields of biology (cellular physiology, organismal biology), ecology (ecology and ecosystem biology), and physics (environmental conditions within specified regions). However, to find the common link between these interdisciplinary fields is a complex task and may only be achieved by better integrating experimental data and computational analysis.

1.3 Numerical modelling of the coral thermal microenvironment

In most existing literature, the temperature of the ambient water represented by SST is always assumed to be the same as the coral temperature. However, it is the temperature of the colony surface and of the boundary layer directly above it that determines physiological processes and this can deviate substantially from the temperature of the larger body of surrounding seawater. This is termed the coral thermal microenvironment. This temperature deviation is a function of several factors, though it is predominantly due to radiative heat flux and water flow on the coral surface. A heat balance is maintained between losses from convection into the surrounding water (dependent on water flow and other surface characteristics involved in the boundary layer formation), heat conduction into deeper layers of the coral, and emission of short and long-wave radiation incident on the coral surface (Fabricius, 2006). Therefore, it is imperative to distinguish

between the temperature of (1) the thin layer of living tissue embedded in the surface of a coral that is exposed to direct solar radiation, (2) the ambient water, and (3) the coral skeleton.

Few experimental studies have considered the temperature of corals and the heat fluxes at their surface. Brown *et al.* (2002) investigated the temperature of different surfaces of corals but found no differences. Fabricius (2006) measured the surface temperature of a number of shallow-water corals and showed that more densely pigmented corals were heated more than less densely pigmented corals, an effect that was enhanced under low water flow (Fabricius, 2006). Jimenez *et al.* (2008) also detailed the heat budget of a coral exposed to solar radiation and water flow in controlled laboratory experiments and on the reef flat under naturally fluctuating conditions of flow and irradiance (Jimenez et al., 2008). These studies provide qualitative evidence that the thermal microenvironment can play an important role in the microscale processes involved in coral bleaching. Furthermore, while useful, these experiments are inevitably restricted to few species and locations due to the relatively high cost and difficulty in obtaining accurate measurements. In contrast to experimental techniques, numerical modelling methods allow for detailed interrogation of these parameters without difficulty.

This thesis presents a new prediction technique which aims to assess the effects and interactions of the key stressors – namely the coral morphological features (shape, size, tissue thickness, skeletal matrix and tissue permeability values), and the meteorological and atmospherical attributes – in driving the variability of the coral thermal microenvironment. This is achieved through the development of Computational Fluid Dynamics (CFD) models, which can be readily coupled with other hydrodynamic and ray-tracing techniques in order to explore the full range of temporal and spatial environmental stressors that could ultimately be used to predict the frequency and intensity of coral bleaching scenarios – even for individual species, colonies or parts of colonies. Although full scale modelling of coral reef systems is unlikely to be able to replicate the full complexity observed in nature, it is often possible to construct progressively more complex models (termed multiscale models) of physical systems which closely reproduce reality.

1.4 Research objectives

Three primary objectives of this thesis are:

1. To develop a CFD modelling framework to predict heat transfer and thermal microenvironment of corals at laboratory- and meso-scale conditions.

2. To model the effect of metocean raw data on the overall prediction of thermal microenvironment of corals in a shallow reef-flats (<5 m depth).

3. To determine the effect of morphological features (size, shape, tissue thickness, and regulation of the permeability in tissular and skeletal layers) on the thermal behaviour of its microenvironment.

1.5 Thesis outline

The outline of the thesis is as follows: **Chapter 2** discusses the importance of heat and momentum budgets on the coral thermal microenvironments and discusses the integration of a coupled-ocean-atmosphere system complemented with CFD analysis at a controlled laboratory-scale and a shallow-reef flat environment.

The following chapters investigate the degree of robustness of the numerical model using representative cases of heat budgets and thermal stress in the coral microenvironments under controlled laboratory and shallow-reef scale conditions. Simulations have been conducted against various experimental studies, available from literature as reference cases. **Chapter 3** presents validation of the effects of laminar and turbulent flow with fixed irradiance and various coral pigmentations at a laboratory-scale environment. It also explores the effect of smooth and polyped surfaces in coral architectures on the overall surface warming. **Chapter 4** validates results of the daylight illuminance under multiple sky conditions and the underwater attenuation coeficients due to turbidity, tide, and cloud cover. It also validates irradiance levels at the microscale of branching and massive coral surfaces. **Chapter 5** presents a coupled CFD and hydrodynamic model (coupled ROMS-SWAN) as well as a ray-tracing model (Radiance) to study the differential bleaching pattern case study observed in a shallow-reef flat environment. **Chapter 6** addresses objective 3 presenting parametric studies on a range of species, with varying sizes and shapes. Finally, **Chapter 7** provides discussion on how the coral thermal microenvironment is a key factor in observing and predicting coral bleaching as well as highlighting the investigations arising from this research and future recommended studies. Some further materials and backgrounds of CFD and Radiance are available on the **Appendix 1** and **Appendix 2**, respectively.

Chapter 2

Hydro and thermal physics in coral microenvironments

In this chapter I establish the framework for examining the hydrodynamic and thermal processes of corals at the individual-, colony-, and reef-scales. This chapter analyses the importance of computational fluid dynamics and heat transfer theory for predicting temperature rises at the coral surfaces under a broad suite of environmental conditions in order to better understanding the role of the range of physical environment in influencing the physiology and community dynamics of reef-building corals.

The hydrodynamics of coral reefs, coral colonies, and even individual coral reefs entails a wide range of scales of fluid motions, starting with the largest scales that characterise eddies produced by island wakes, smaller depth-scale turbulent features determined by reef topography, and to the smallest scales of flow in a single individual coral colony. In this chapter, I only investigate relatively small spatial scales and the smaller turbulent feature scales. It is hoped that this chapter will serve as a prerequisite before embarking on a quest to model a large-scale whereby the hydrodynamic modelling combined with an improved knowledge of coral physiology or morphology, can go a long way to understanding the nature of coral bleaching and allowing for improved monitoring and predictions.

Although the mass transfer theory is not specifically discussed in this chapter, the analogy – based on the notion that just as temperature gradients drive potential for heat transfer in a water flow provides the driving potential for mass transfer – may principally be applied in a similar manner.

Readers are encouraged to refer to Appendix 1 and Appendix 2 for a more detailed analysis of CFD equations and the concept of ray-tracing mechanisms (Radiance) used in this chapter.

2.1 Flow at the scale of an individual coral colony

Temporal and spatial variation in water-flow across the topography of coral reefs are major determinants of bleaching severity, however have often been overlooked. Water motion, both from colony-scale to reef-scale, is important for the well-being and functioning of coral reefs (Hearn, 2011; Monismith, 2007). The mass of the ocean moves constantly at various scales from large-scale ocean currents to small-scale circulation pattern i.e. tidal and wave currents. The movements and patterns of flow in ocean currents are influenced mainly by wind direction and strength as well as density differences in water masses due to temperature and salinity variations. At the reef-scale, water circulation can affect larval retention, export and connectivity between reefs (Cowen and Sponaugle, 2009). At the colony scale, flow affects the transport, dispersal, and retention of fluxes of nutrients and carbon uptakes (Falter et al., 2004; Thomas and Atkinson, 1997), gas exchange (Mass et al., 2010; Patterson et al., 1991; Sebens et al., 2003), the ability of polyps to capture particles (Sebens et al., 1998), coral growth morphology (Kaandorp et al., 2003), and reef metabolism and calcification rates (Baird and Atkinson, 1997; Wyatt et al., 2010).

Water flow at the reef-scale is highly variable due to local topographical variation, hence, flow may differ substantially from one colony to an other. Although such colony scale effects on flow can be important, most previous field studies of water circulation over reefs have focused on regional and lagoon-scale processes (Gourlay and Colleter, 2005; Hench et al., 2008; Lowe et al., 2009a,b). Previous laboratory and computational studies suggest that flow patterns around isolated coral colonies are qualitatively similar to wakes behind idealised geometries like cylinders and hemispheres. In branching corals, some water passes between branches; however, most water deviates around and even finely branching colonies generate significant wakes (Chang et al., 2009; Kaandorp et al., 2003). If corals are sparsely spaced, each colony interacts individually with the free stream flow, but if colonies are more densely spaced, their wakes interact and flow speeds are reduced in a canopy layer that contains solid obstacles. In unsteady flows generated by waves, time-varying pressure gradients force fluid between branches and colonies (Lowe et al., 2007, 2005).

Thermal stress at the scale of the coral microenvironment water flow has not been investigated in details. However, such dynamics may be of importance for understanding and monitoring heat-induced stress at reef-scale and colony-scale. To date, most studies of flow at the colony-scale have used laboratory and computational approaches with idealised geometries and/or flow conditions (Chang et al., 2009; Fabricius, 2006; Jimenez et al., 2008, 2011; Kaandorp et al., 2003; Lowe et al., 2007, 2005).

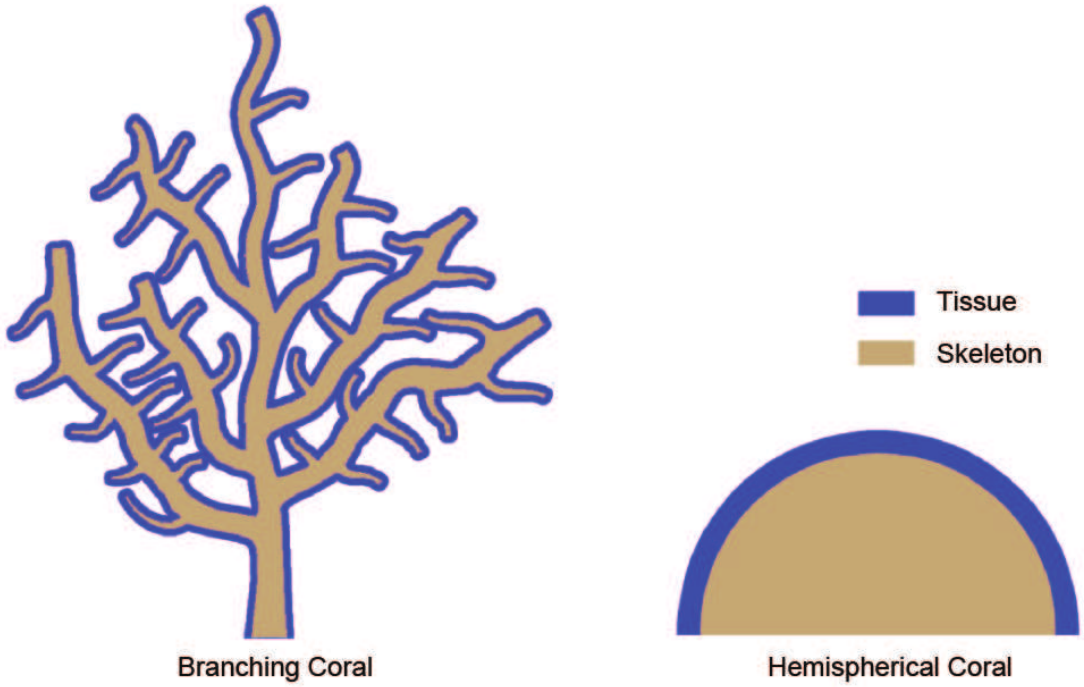

Figure 2.1. The distribution of living tissue and skeletal matrix in branching and massive corals (two dimensional cross section).

2.2 Flow and thermal regions in corals

The living tissue of corals that connect adjacent polyps forms a thin layer over the outermost few millimeters of its calcareous skeleton (Anthony et al., 2002; Barnes and Lough, 1992) (Figure 2.1). The flow of water through the coral tissue and skeleton (if it occurs), should significantly influence the thermal microenvironment of the coral. To my knowledge, there are no published reports of flow through living coral tissue or their skeleton. Therefore, in constructing these models, I have developed models that allowed us to evaluate a diverse range of scenarios. To do so, however, necessitated assumptions that will need to be tested in future work. In particular, I assumed that there is unlikely to be any significant permeability through intact living tissue, however, in many cases, the activity of borers and coral grazers will result in openings allowing percolation and increased skeletal porosity. Coral species with denser skeletons experience less percolation type flow.

Assuming a starting condition whereby the temperature of the coral and the surrounding water are the same, heat transfer within and around corals will be affected by three main mechanisms: (1) the rate of incident radiation absorbed

by the exposed tissue surface, (2) the rate of heat loss due to convection from the tissue and skeleton into the surrounding water, and (3) the rate of heat conduction from the tissue into the skeleton. The models I present here consider all of these mechanisms. It is, therefore, necessary to specify two thermal and porous regions, the tissue and skeleton, in the models. This models also assume thermal effects of mass and nutrient transfer during photosynthesis to be negligible (Cooper, 2008).

2.2.1 Thermal physics in hemispherical and branching corals

To aid understanding of heat transfer processes in corals, a simple heat balance between heating and cooling in a coral can be written as

$$Q_{\text{eff. heating}} = Q_{\text{absorb}} - Q_{\text{cool}} \tag{2.1}$$

where Q_{absorb} is the heat absorbed by a coral due to solar irradiance and Q_{cool} is the energy that is transferred from the coral surface to the surrounding environment. Applying Newton's law of cooling and rearranging the above equation, Q_{cool} and Q_{absorb} can be expressed as

$$Q_{\text{cool}} = hA(T_{\text{tissue}} - T_{\text{water}}) \tag{2.2}$$

$$Q_{\text{absorb}} = \alpha IA \tag{2.3}$$

where h is the heat transfer coefficient between the coral surface and the surrounding environment, I is the total irradiation, α is the tissue absorptivity, and A is the surface area of the coral. Heat transfer is directly proportional to surface area, whereas heat capacity is proportional to volume. Hence the A/V ratio influences heat accumulation and dissipation. Branching corals have larger surface area to volume ratio, $S = A/V$, than massive corals and therefore can be expected to acquire and dissipate more heat.

The rate of temperature rise in the coral can be written as

$$Q_{\text{eff. heating}} = \rho V C_p \frac{dT}{dt} = \alpha IA - hA(T_{coral} - T_{fluid}) \tag{2.4}$$

where ρ is the coral density, C_p is the coral specific heat capacity, and dT/dt is the rate of temperature rise in the coral. Thus, from equations 2.2, 2.3, and 2.4 the temperature rise in a coral should be highly dependent on its ratio of A and V. Defining a surface area to volume ratio, $S = A/V$, the above equations can be solved and a time constant, τ, can be identified for the coral, such that

$$\tau = \frac{\rho C_p}{hS} \tag{2.5}$$

This equation illustrates the strong dependence of the time constant (or heating rate) on S (as S varies considerably between hemispherical and branching corals). The time constant, τ, therefore increases with increasing volume and decreases with increasing surface area, and the A/V ratio will be an important determinant of the speed with which an equilibrium temperature is reached, as well as the final temperature achieved. This expression also includes a dependence on the boundary layer thickness due to the convective heat transfer coefficient 'h'.

While coral shapes are not always characterised by ideal geometrical shapes, here I define the shapes of massive and branching corals to be either hemispherical and cylindrical, respectively. While, a caricature of nature, this conceptualisation represents the ends of the shape spectrum of corals. The surface areas of hemispherical and branching corals are given by $3\pi r^2$ and $2\pi r^2 + 4\pi rz$, respectively, where r is the radius and z is height of a cylindrical (or branch) section. The corresponding volumes for the hemispherical and branching corals are $\frac{2}{3}\pi r^3$ and $\pi r^2 z$, respectively. Under the steady-state lighting conditions, Q_{cool} must be equal to Q_{absorb} and the A/V ratio will affect the final temperature of the coral. Under transient lighting conditions, the A/V ratio will be important in determining the speed, with which an equilibrium temperature is reached, as well as the final temperature. Recent experimental work (Jimenez et al., 2011) has measured thermal heterogeneity on a micro-scale in individual polyps. Here, the current geometry assumes homogeneity, however, a more spatially resolved geometry could readily be substituted.

2.2.1.1 Conduction

Conduction from the tissue to the skeleton: The heat conduction is proportional to the temperature difference between the tissue T_{tissue} and the skeleton $T_{skeleton}$, the coral surface area A and the thermal conductivity of aragonite k:

$$Q_{cond} = kA_{tissue}\frac{(T_{tissue} - T_{skeleton})}{\chi_{tissue}} \tag{2.6}$$

where χ_{tissue} is the tissue thickness. Contrary to this equation, the conduction heat budget in Jimenez *et al.* (2008) neglected the tissue thickness.

2.2.1.2 Convection

Convection flux from the sun-exposed tissue to ambient water: The convective heat transport can be assumed to obey Newton's law of cooling and is proportional to the difference in temperature between the water T_{water} and the coral T_{tissue} temperatures, the coral surface area A, and the heat transfer coefficient of water h:

$$Q_{conv} = hA(T_{tissue} - T_{water}) \tag{2.7}$$

The heat transfer coefficient for convection depends on the nature of the motion of the fluid, velocity, and temperature differences. Theoretically, convective heat transfer is modelled using the Nusselt number, the Prandtl number, the Grashof number and the Rayleigh number. These depend on the Reynolds number which defines the flow regime and the effects of coral morphology on shear stress (Patterson, 1992a,b).

2.2.1.3 Radiation

Absorbed radiative heat flux: For single radiation wavelength and homogeneous water the amount of radiant energy absorbed, ΔI, in an interval of depth, Δz, is dependent on the amount of irradiance on that interval, which can be written as

$$\Delta I = -\alpha I \Delta z \tag{2.8}$$

where α is coral tissue absorptivity coeffiecient equal to the inverse of the optical depth, I is the incident of solar irradiance, and z is the water depth.

The equation. 2.8 leads directly to the expression of the radiant energy, $I(z)$, at depth z in the water column in terms of the energy I_0 incident at the surface.

$$I(z) = I_0 \exp(-\alpha z) \tag{2.9}$$

The heat flux due to absorption of radiation, ΔQ, is proportional to ΔI, α, and the coral surface area (A). Defined as the fraction of incident radiation absorbed by the surface, α, accounts for a range of factors affecting the amount of absorbed light, such as the optical properties of both the host tissue (host pigments, tissue thickness) and the zooxanthellae (symbiont density, photosynthetic pigments).

$$\Delta Q = \alpha \Delta I A \tag{2.10}$$

Equations 2.8 and 2.9 work for a single absorbing constituent in the water, and for absorption coefficients which have no variation in depth. However, often the optical depth $(1/\alpha)$ varies with wavelength for different types of Jerlov water (see below). The incident radiation varies with wavelength as

$$I_0 = \sum_{\lambda} E(\lambda) \Delta \lambda \tag{2.11}$$

where $E(\lambda)$ is the energy density at the sea surface. Because each wavelength has its own value of optical depth $(1/\alpha)$, the attenuation through the water column to depth for each wavelength must be added to find the total remaining energy at that depth

$$I(z) = \sum_{z} \sum_{\lambda} E(\lambda) \exp(-\alpha z) \Delta \lambda \Delta z \tag{2.12}$$

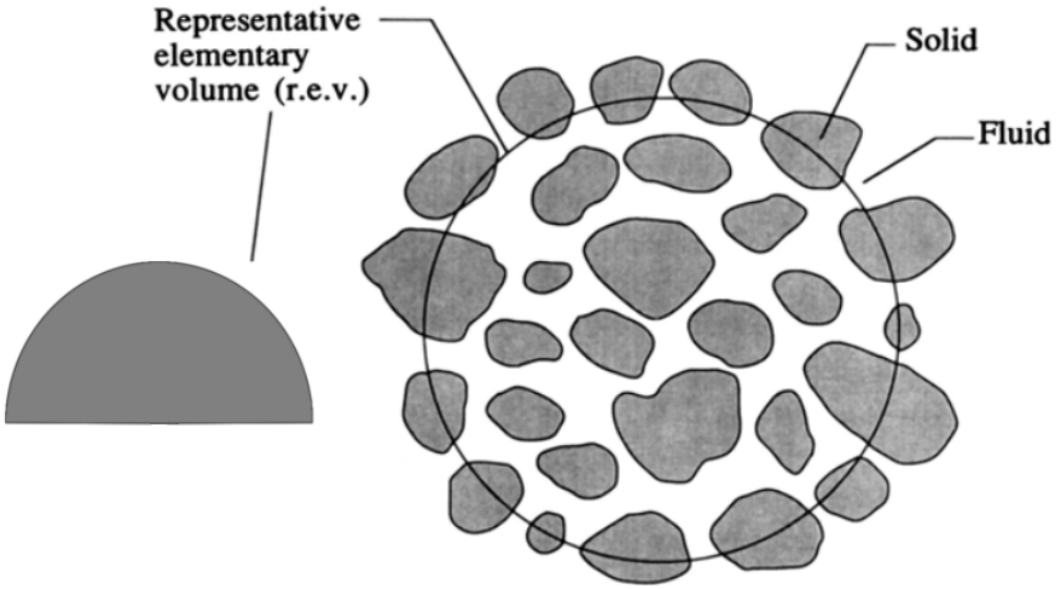

Figure 2.2. The representative elementary volume (R.E.V.) of porous coral. Adapted from Nield and Bejan (2006) (Nield and Bejan, 2006).

A more detailed analysis of temporal variation in irradiance due to water clarity, cloud cover, and tides is presented below. Note that due to the low temperature difference between the water and the coral, radiative heat transfer from the coral were neglected.

2.2.2 Fluid flow and heat transfer through a porous coral

The porosity φ of a coral is defined as the fraction of the total volume of the coral that is occupied by void space. Thus 1-φ is the fraction that is occupied by aragonitic skeleton.

2.2.2.1 Fluid flow through a porous coral

In deriving the laws governing the macroscopic variables is to begin averaging over volumes containing pores. A macroscopic variable is defined as an appropriate mean over a sufficiently large representative elementary volume (R.E.V.), as shown in Figure 2.2:

Applying Darcy's equation over a r.e.v.:

$$\mathbf{v}_f = -\frac{K}{\mu}\nabla p \tag{2.13}$$

where $\mathbf{v}_f$ is the Darcy velocity vector, $\partial P/\partial x$ is the pressure gradient in the flow direction and μ is the dynamic viscosity of the fluid. The coefficient K is the intrinsic permeability and is dependent on the geometry of the medium. Using Carman-Kozeny, K can be written as

$$K = \frac{D^2\varphi^3}{180(1-\varphi)^2} \tag{2.14}$$

where D_p is the diameter of the medium (coral).

Since Darcy's empirical flow neglects inertial or time dependent effects, the law is only valid for creeping flows ($Re << 1$). To account for an increased pressure drop at higher flow rate, the Forchheimer empirical model flow is used:

$$\nabla p = -\frac{\mu}{K}\mathbf{v_f} + \beta\rho{\mathbf{v_f}}^2 \tag{2.15}$$

where β is the Forchheimer coefficient which is given by:

$$\beta = \frac{C_E}{\sqrt{K}} \tag{2.16}$$

where C_E is the Ergun constant which is strongly dependent on the flow regime.

2.2.2.2 Heat transfer through a porous coral

Assuming that there is local thermal equilibrium so that $T_s = T_f = T$, where T_s and T_f are the temperatures of the solid and fluid phases, respectively. Taking averages over r.e.v, for the solid and fluid phases yield:

$$(1-\varphi)(\rho c)_s\frac{\partial T_s}{\partial t} = (1-\varphi)\nabla\cdot(k_s\nabla T_s) + (1-\varphi)q_s \tag{2.17}$$

$$\varphi(\rho c_p)_f\frac{\partial T_f}{\partial t} + (\rho c_p)_f U\cdot\nabla T_f = \varphi\nabla\cdot(k_f\nabla T_f) + \varphi q_f \tag{2.18}$$

where the subscripts s and f refer to the solid and fluid phases, respectively, U is the velocity vector, c is the specific heat of the solid, c_p is the specific heat at constant pressure of the fluid, k is the thermal conductivity, and $\dot{q}$ is the heat production per unit of volume [W/m^3].

2.3 CFD governing equations

The physical laws governing porous media, fluid flow, and heat transfer processes must firstly be defined as differential equations. The mass continuity governing

equation was developed from the mass balance over a control volume (cell), fixed in space, through which the fluid flows and can be written as

$$\frac{\partial \rho}{\partial t} + \nabla \cdot (\rho \mathbf{U}) = 0 \tag{2.19}$$

where $\mathbf{U}$ is the superficial velocity vector. Because the present model is at the laboratory scale, any differences in seawater density will be very small, and are therefore ignored, and fluid flow is treated as being incompressible. However, the application of this modelling framework at larger scales, will require these assumptions to be re-visited because changes in density are likely with changes in salinity and temperature.

The momentum governing equation for laminar, viscous, incompressible, single-phase water flow through a porous medium is given by

$$\frac{\partial}{\partial t}(\varphi \mathbf{U}) + \nabla \cdot (\mathbf{U} \cdot \mathbf{U}) = \nu \nabla^2 \mathbf{U} - \frac{\nabla p}{\rho} + S_i \tag{2.20}$$

where φ is porosity, ν is kinematic viscosity, p is pressure, and k is thermal conductivity. The flow sink term, S_i is composed of two parts, a viscous loss term and inertial loss term, creating a pressure drop that is proportional to the velocity and square of the velocity, respectively.

$$S_i = -(\nu D_{ij} + \frac{1}{2}|\mathbf{U}|F_{ij})\mathbf{U} \tag{2.21}$$

where D_{ij} and F_{ij} are represented as the scalars D and F. This is the classical Darcy-Forchheimer equation. In this study, corals were assumed to possess homogeneous permeability and were treated as having isotropic permeability. The Blake-Kozeny equation specifies viscous energy loss primarily in laminar flow as,

$$D = \frac{150(1-\varphi)^2}{d^2 \varphi^3} \tag{2.22}$$

where, d is the diameter of the coral sample under investigation. The Burke-Plummer equation denotes the kinetic energy loss primarily in turbulent flow as,

$$F = \frac{1.75(1-\varphi)}{d\varphi^3} \tag{2.23}$$

Because the pressure drop for low velocity flow, as modelled here, is predominantly determined by viscous forces, the inertial or kinetic energy term can be omitted. However, for high velocity flow, kinetic forces dominate the pressure drop and must be retained.

The averaged momentum equation for steady, turbulent incompressible flow can be written as:

$$\frac{\partial}{\partial x_j}\left(\overline{u_j u_i}\right) = -\frac{\partial}{\partial x_i}\left(\frac{\bar{p}}{\rho}\right) + \frac{1}{\rho}\frac{\partial}{\partial x_j}\left(\tau_{ij} + \tau_{t_{ij}}\right) - \overline{S_i} \tag{2.24}$$

The above equation is known as the Reynolds-Average Navier Stokes equations (RANS), where $\tau_{t_{ij}}$ is the Reynolds-stress tensor and τ_{ij} is the mean laminar viscous stress and is given by (see Appendix 1):

$$\tau_{ij} = \mu\left[\left(\frac{\partial \overline{u_i}}{\partial x_j} + \frac{\partial \overline{u_j}}{\partial x_i}\right) - \frac{2}{3}\left(\frac{\partial \overline{u_k}}{\partial x_k}\right)\delta_{ij}\right] \tag{2.25}$$

The Reynolds-stress tensor represents the transfer of momentum due to turbulent fluctuations which is given by

$$\tau_{t_{ij}} = 2\mu_T S_{ij} - \frac{2}{3}\rho k \delta_{ij} \tag{2.26}$$

where S_{ij} is the mean strain-rate tensor and k is turbulent kinetic energy which is given as

$$k = \frac{1}{2}\overline{u_i}'\overline{u_i'} = \frac{1}{2}\left(\overline{u'^2} + \overline{v'^2} + \overline{w'^2}\right) \tag{2.27}$$

The degree of turbulence can be adequately described using the intensity of turbulence, I, and the scale of turbulence, l.

The final transport equation is the energy governing equation, which accounts for heat flow within the models, including the effects of incident solar radiation. In the porous zone models, I have treated all the corals as isotropic media with uniform porosity and permeability. Although this may not be realistic in some cases, I consider this to be a reasonable starting approximation. To describe the temperature distribution in the porous coral tissue and skeleton, I assumed an instantaneous local thermal equilibrium whereby $T_c = T_f = T$ (where T_c and T_f are the temperatures of the coral and the fluid, respectively). It can be expressed as

$$(\rho C_p)_m \frac{\partial}{\partial t} T + (\rho C_p)_m \nabla \cdot \mathbf{U} T = \nabla \cdot (k_m \nabla T) + S_h \tag{2.28}$$

where S_h accounts for heat source (such as the incident radiation on the tissue, Q_{rad}). Averaged material properties for the porous media were calculated using

$$\rho_{eff} = (1-\varphi)\rho_c + \varphi\rho_f \tag{2.29}$$

$$C_{p_{eff}} = (1-\varphi)C_{p_c} + \varphi C_{p_f} \tag{2.30}$$

$$k_{eff} = (1-\varphi)k_c + \varphi k_f \tag{2.31}$$

where Equations 2.29, 2.30, and 2.31 represent effective density, effective heat capacity, and effective thermal conductivity of the medium, respectively. These values were then used to calculate the thermal diffusivity of the medium, Γ_{T_m}, which is given by

$$\Gamma_{T_m} = \frac{k_m}{(\rho C_p)_m} \tag{2.32}$$

The source term added to the energy equation needs to be modified to have the same dimensions as the other terms. The absorbed heat irradiance to each cell in coral tissue in contact is $\dot{q} \cdot A$ [J s^{-1}]. The other terms in the energy equation has the dimensions of [J s^{-1} m^{-3}] before dividing by $(C_p \cdot \rho)$. Therefore the source term needs to be divided with the cell volume of the corresponding cell in order to obtain the correct dimension (see Appendix 1).

The overall heat transfer parameters are highly dependent on the geometry and density of the corals. Dividing equation 2.28 by the $(\rho C_p)_m$ term yields a more standardised transport energy equation for porous media given as

$$\frac{\partial}{\partial t}T + \nabla \cdot \mathbf{U}T = \Gamma_T \nabla^2 T + \frac{\Gamma_T}{k} S_h \tag{2.33}$$

The angle of incidence (θ) and intensity (Q_{rad}) of solar radiation that strikes the coral's surface (tissue) is also accounted for in the model. However, for the purpose of validating the models against experimental measurements, the Q_{rad} term was calculated using an overhead (90°) incident angle for solar radiation delivered to the tissue surface. Hence, Equation 2.33 can be written as:

$$\frac{\partial}{\partial t}T + \nabla \cdot \mathbf{U}T = \Gamma_T \nabla^2 T + \frac{\alpha Q_{rad}}{\rho C_p} \tag{2.34}$$

The heat transfer energy equation in the incompressible turbulent flow remains unchanged as the above with the additional viscous dissipation term added on the right hand side of the equation. This term is important only in flows with big velocity gradients, which is not the case here and thus, it is expected to be negligible when determining the temperature. The turbulent heat dissipation can be written as

$$\left(\overline{\mathbf{U}} \cdot \nabla T\right) = \frac{k \nabla^2 T}{\rho C_p} + \left(\tau : \nabla \overline{\mathbf{U}}\right) \tag{2.35}$$

When a fluid flows over a surface, its first layer normally sticks to the boundary (no slip boundary condition). This phenomenon causes the flow to decrease, in this case, in the vicinity of the bounding coral surface, creating the hydrodynamic boundary layer. A similar principle applies when the temperature between the fluid and surface differ. The first layer of the fluid obtains its heat from the coral surface through pure conduction. It then gives its newly acquired energy to all

of the other fluid molecules through convection with which it comes in contact. This layer between the fluid and the bounding coral surface is called the thermal boundary layer. In this work, Equations 2.20 and 2.34 directly account for these boundary layers based on the ascribed boundary conditions. The ratio of the thermal vs hydrodynamic thicknesses is given by the Prandtl number

$$Pr = \frac{\text{Viscous Diffusion Rate}}{\text{Thermal Diffusivity}} = \frac{\nu}{\Gamma_T} \tag{2.36}$$

Hence, a Prandtl number greater than 1 indicates that momentum diffusion is the more dominant process resulting in a slightly thinner thermal boundary layer (TBL) compared to the momentum boundary layer (MBL).

The mass, momentum, and energy conservation equations are solved over all the fluid control volumes in the computational domain using the Finite Volume Method (FVM). This solution provides results at each finite volume "cell" in the model, at discrete time intervals (refer to Appendix 1 for further detail).

2.3.1 Numerical simulations and schemes

The SIMPLE (semi implicit method for pressure-linked equations) and PIMPLE (merged PISO-SIMPLE) algorithms were used for both the steady-state and transient simulations, respectively (OpenCFD Ltd., 2010). The SIMPLE algorithm determines pressure on a staggered grid from velocity components by applying an iterative procedure coupled with the Navier-Stokes equations, whereas the PIMPLE combines SIMPLE which solves the pressure-velocity coupling implicitly while the PISO (pressure implicit with splitting of operators) algorithm rectifies the second pressure correction and corrects both velocities and pressures explicitly (Ferziger and Perić, 1999; OpenCFD Ltd., 2010; Versteeg and Malalasekera, 1995).

The schemes implemented for both convection divergence and Laplacian terms were the Gauss linear upwind cell limited least squares and the Gauss linear limited 0.5, respectively. The generalised geometric-algebraic multi-grid (GAMG), smoother Gauss-Seidel, and preconditioned bi-conjugate gradient (PBiCG) were used to discretised pressure, velocity, and temperature governing equations, respectively. The time discretisation schemes for laminar and turbulent simulations were set to be steady-state and Euler, respectively.

This thesis mainly used two types of grids, predefined block structured hexahedral and polyhedral, to represent both computational and coral domains with approximately 900,000 cells for laminar flow simulations. In turbulent simulations, it was necessary to place the grid line closest to the wall at an appropriate distance in order to resolve the boundary layers within the first layer of cells and the second layer consists only of flow with turbulent characteristics. For

most low-Reynolds turbulence cases, the y^+ was set approximately less than 1.0 ranging from 1 to 2.5 million computational cells.

Overall, the simulation in this thesis required ∼170 simulation runs on a 12-cores workstation, ∼1000 CPU hours, and ∼200 hours of both pre- and post-processing data to obtain the model results.

2.4 Flow at the scale of fringing reef

Water circulation is a major factor in controlling a variety of key processes in coral reef systems, including community structure, the exchange or dispersal of nutrients and sediment transport within reef organisms (Hearn, 2011; Monismith, 2007). Circulation on reefs is predominantly driven by tide, wind, and wave over-topping on the reef crest (Andrews and Pickard, 1990). The relative importance of each mechanism varies between reefs and is a function of both a reef's morphology and the meteorological and oceanic forcing conditions at the site (Lowe et al., 2009a). For fringing reefs, wave-over topping on the reef crest and the induced inflow is considered to be the main driving force of circulation in Caribbean reefs (Roberts et al., 1975, 1992), while tide is thought to be the main driving force in fringing reefs at the GBR (Parnell, 1988). However, there has been little consideration of the effect of wind direction on circulation. The reason is perhaps that most of the studies of water circulation on coral reefs have been in trade wind areas where wind conditions and induced swells are generally constant. However, the effect of wind is crucial for coral reefs that are located in the monsoon areas to determine the circulation pattern. Furthermore, the effect of wind on circulation on fringing reefs on Davies Reef was found to significant and contributed 60% of the total driving force (Pickard, 1986).

A typical fringing reef morphological system is often defined as having the following distinctive features (Figure 2.3): an intertidal zone, a shallow reef flat, a sloping forereef, and a back reef. Biological and morphological zonation of corals on fringing reefs is often weakly developed due to their generally shallow foundations (Hopley and Barnes, 1985).

The interaction between ocean and atmosphere has received increasing attention because it plays an important role in maintaining the existing climate and in causing the long-range evolution of weather and climate. However, because of the complexity of the phenomenon, it is very difficult to determine by simple physical reasoning, or by simple analytic solution, how the atmospheric circulation affects the ocean.

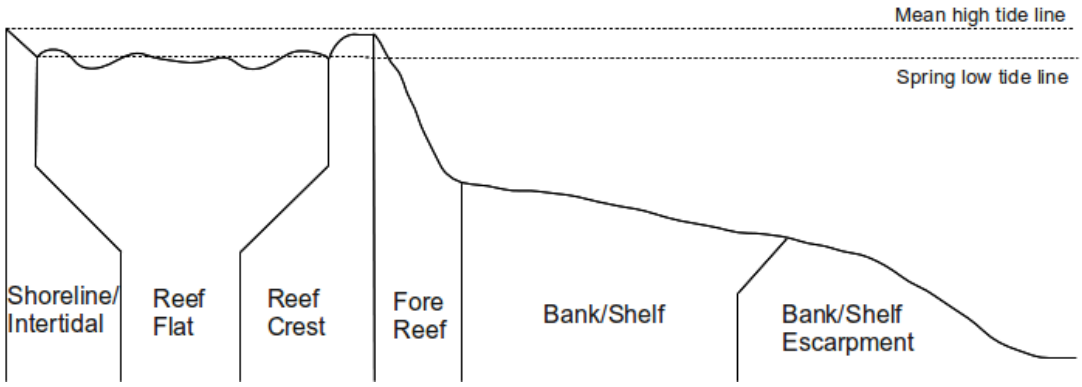

Figure 2.3. Fringing reef cross-section. Adapted from the Center for Coastal Monitoring and Assessment, http://ccma.nos.noaa.gov

2.5 Heat transfer process on a shallow reef flat

The previous section examined heat transfer processes at laboratory-scale conditions. This section briefly investigates the impact of atmospheric conditions on the amount of heat transferred through the air-sea interface. Heat passes through the air-sea interface through radiation, conduction, convection, and water-phase transformation. In oceanography, conduction and convection are grouped together to form a sensible heat flux. A latent heat flux is used to denote the heat transfer from a water-phase transformation, such as evaporation. Finally, radiation is separated into short-wave and long-wave components. Thus, some of the major solar heat flux determinants include short-wave radiation, long-wave radiation, latent heat flux, and sensible heat flux.

Net heat flux Q_a (Figure 2.4) is typically approximated as a residual of the measurable components of the surface heat budget (Weller and Anderson, 1996)

$$Q_n = Q_l + Q_s + Q_{LW} \uparrow + Q_{LW} \downarrow + (1 - \alpha_s)\, Q_{SW} \tag{2.37}$$

where Q_l and Q_s are latent and sensible heat fluxes that depend on wind speed, air temperature, atmospheric pressure, humidity, and sea surface temperature. $Q_{LW} \uparrow$ is emission of infrared (long-wave) radiation from the ocean surface, $Q_{LW} \downarrow$ is downward emission of infrared radiation from the atmosphere, and Q_{SW} is the incoming solar (short-wave) radiation, and α_s is the surface albedo.

The heat flux acts to change near surface buoyancy, whereby the net input of heat increases the stratification by warming the upper ocean, while heat loss generates convection by cooling the surface and increasing density. The convection driven by the latent heat loss of the ocean is further enhanced by the increased salinity due to evaporation (Edson et al., 1999).

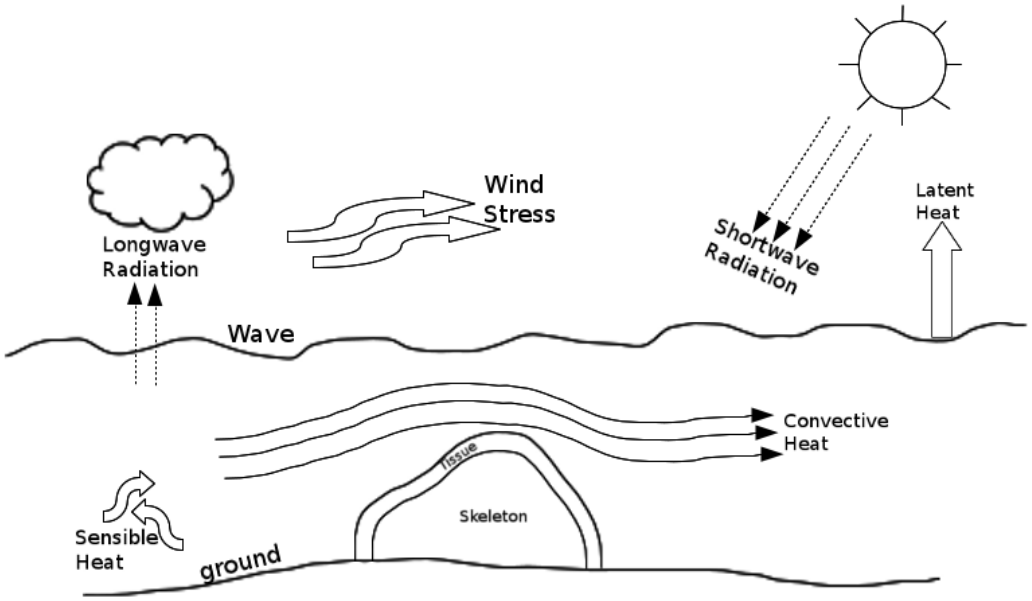

Figure 2.4. The heat balance of the system is maintained primarily by 4 fluxes: the sensible heat flux, the short-wave radiation flux, the long-wave radiation flux, and the latent heat flux.

Steady-state heat balance model - Under natural field conditions each of the above environmental parameters can fluctuate over relatively short time scales. However, a simpler but more tractable version of the unsteady model is useful for examining the steady-state (equilibrium) coral surface temperature exposed over long periods of time to constant environmental conditions. Model predictions are generated using ray-tracing models and environmental heat flux parameters collected using satellite-altimetry data.

2.6 A coupled CFD-ocean-atmosphere system

Few computational works have quantified water circulation in fringing reefs located in a monsoon area with a horizontal spatial resolution less than 200 m. Therefore, there exists a gap between physical oceanographic and atmospheric studies which typically focus on flow at the reef scale, and biological questions that often require knowledge of flow conditions at particular points on the reef or the spatial distribution of these smaller-scale flow fields (Hench and Rosman, 2013).

The framework of the models developed in this work aim to quantity the radiative transfer of natural daylight conjointly incorporating the dynamical processes

of spatial flow in coral microenvironment. The roughness conditions of the ocean surface can affect the elevation angle of the Sun that subsequently alter both the quality and quantity of light that enters the ocean. Hence, the models also considered the sea-state conditions such as calm to lightly rippled ocean surfaces. In my model of the physical system, the data values representing a single physical parameter - i.e. cloud cover, atmospheric pressure, sea turbidity, SST, tidal elevation, or wind velocity or stress direction - are grouped together to form a qualitative field that determines the mean variation of the downwelling irradiance and the vertical attenuation coefficients. Using simulation of a variety of cases with different flow velocities, downwelling irradiance, and salinity conditions, the thermal stress in corals can be quantified and analysed (Figure 2.5).

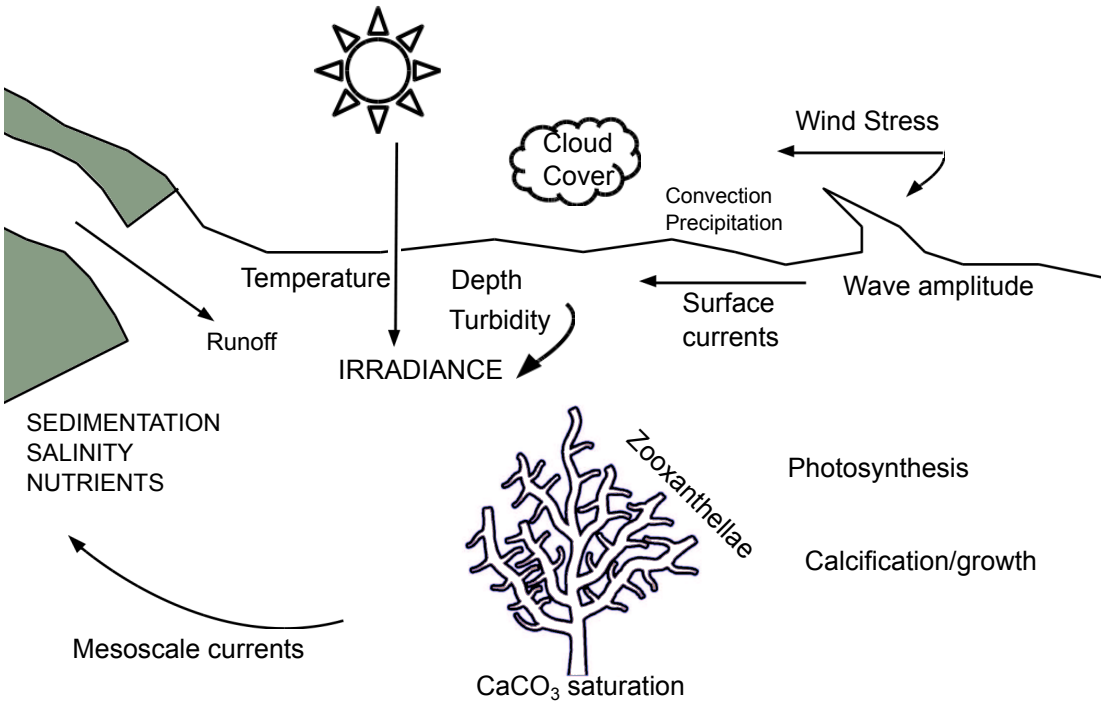

Figure 2.5. Schematic diagram summarising key meteorological and atmospherical processes of the system.

2.6.1 Nearshore ocean models

Here, I implemented a coupled model consists of Regional Ocean Modelling System (ROMS) for a hydrodynamic model and Simulated Waves Nearshore (AN) for a wave model. ROMS used for the study is a version with model coupling and nesting. The model is coupled with a tool called Model Coupling Toolkit

(MCT), which allows two-way coupling among multiple sub-models. With its two-way coupling, ROMS, in turn, provides SWAN with water elevations and current fields (Warner et al., 2008). The model implemented for this study is a 3-D barotropic model, which means that temperature and salinity values are constant and do not vary with time and depth.

Regional ocean modelling systems (ROMS): ROMS is a member of a general class of three-dimensional, free surface, terrain following numerical models that solve three dimensional Reynolds-averaged NavierStokes equations (RANS) using the hydrostatic and Boussinesq assumptions (Haidvogel et al., 2008; Shchepetkin and McWilliams, 2005).

Simulating waves nearshore (SWAN): The model SWAN is is a phase-averaged wave model that solves transport equations for wave action density N (energy density divided by relative frequency) in either stationary or non-stationary mode (Booij et al., 1999). SWAN can be run separately and the output used to force the hydrodynamic routines (one-way coupling) or, alternatively, SWAN can be run concurrently with the circulation model with two-way coupling whereby currents influence the wave field and waves affect the circulation (Booij et al., 2004).

Model Coupling Toolkit (MCT): The MCT allows the transmission and transformation of various distributed data between component models that constitute a parallel coupled system (Larson et al., 2005). The modules are used during the compilation and the libraries are linked to build the executable files. Each model calls the MCT during execution to send and receive data.

Surface to subsurface velocity projection: The approximation of the velocity variation with depth is consequently derivable in terms of orthogonal basis functions from the sea surface kinematic and dynamic boundary conditions; specifically, the viscous momentum and shear equations evaluated at the sea surface. For detailed model description, constraint, and governing equations, refer to (Shen and Evans, 2001).

2.6.2 Ray-tracing methods

The previous section described the overall treatment of the problem, without detailed discussion of the calculation of the solar irradiance source term S_h. While it is possible to calculate the radiative heat gain using one of many complete radiation models, these approaches are typically computationally expensive and give little benefit for the investigation of coral bleaching. The radiative transport process was implemented using a hybrid approach of Monte Carlo ray tracing suite of codes based on known light behaviour, Radiance (Ward, 1994c), with spatially spectral dependent absorption and scattering coefficients of seawater and coral colonies which in turn computes radiant energy falling on a coral surface

according to the Sun's location and atmospheric condition by interpolating the RGBE component values. RGBE is an image format that stores pixels as one byte each for RGB (red, green, and blue) values with a one byte shared exponent, thus it stores four bytes per pixel. For more on the use of Monte Carlo techniques, see Tregenze (1983) (Tregenza, 1983).

The rate at which solar energy falls on a unit horizontal surface per second are characterised into two basic components: direct normal and diffuse horizontal irradiances. Direct normal irradiance is the flux of beam radiation through a plane perpendicular to the direction of the sun at its current position in the sky, while diffuse horizontal irradiance is a solar radiation that has been scattered by molecules and aerosols in the atmosphere. The total solar radiation on a horizontal surface which is the sum of the diffuse radiation incident on a horizontal surface and the direct normal irradiance projected onto the horizontal surface is called global horizontal irradiance (Equation 2.38 and Figure 2.6).

$$I_{gh} = I_{dh} + I_{dn} \sin\theta \tag{2.38}$$

where I_{gh} is the global horizontal irradiance, I_{dh} is the diffuse horizontal irradiance, I_{dn} is the direct normal irradiance, and θ is the sun altitude.

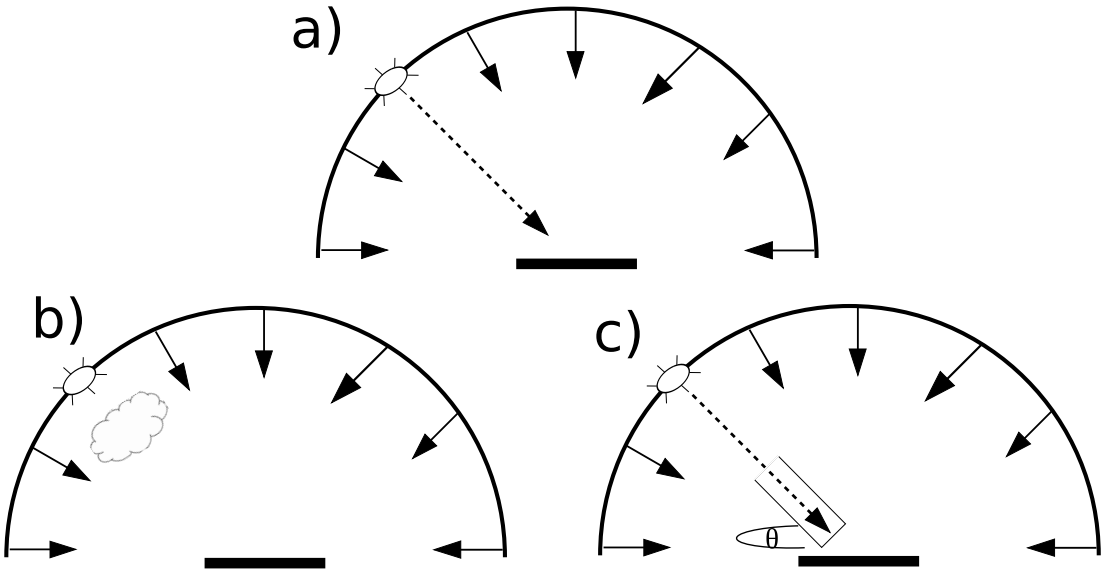

Figure 2.6. Irradiance on a flat-plate collector: (a) global horizontal (sky and sun), (b) diffuse horizontal (sky only), and (c) direct normal (sun only).

2.6.2.1 Radiance

The algorithm of Radiance is based on a backward ray-tracing program from Lawrence Berkeley Laboratory (Ward, 1990, 1992, 1994a,b,c; Ward and Heck-

bert, 1992; Ward and Rubinstein, 1988; Ward et al., 1988; Ward and Shakespeare, 1998). Radiance was used here to account for the contribution from unobstructed and interreflected solar radiation on the solar heat gain through coral surfaces. The algorithm employs recursive techniques in a lighting simulation program for daylighting and artificial lighting calculations and graphical rendering of a space. The program accounts for all surroundings, regardless of geometry, and calculates the luminance at positions throughout the scene. It can accommodate surfaces with arbitrary bi-directional reflectance and transmittance distribution functions (BRTDF), meaning surfaces with non-ideal specular or diffuse properties; surface roughness (texture); planar and non-planar surfaces; surfaces with varying geometries; and tilted surfaces.

The light behaviour of Radiance utilises the Monte Carlo technique to compute radiant energy falling on a point or surface by interpolating the three component values RGBE which follow the standard XYZ tristimulus colour space (International Commission on Illumination, CIE) (Ward, 1994c). These RGB channels are wavelength independent and can be used to produce a complete solar radiation spectrum, namely infrared, visible (photosynthetically active radiation, PAR), and ultraviolet radiation. I focus here mainly on the latter two spectrum. Radiance can also generate an accurate description of the distribution of cloud cover across the sky, which can be varied between sunny, cloudy, and overcast conditions. I denoted the state of the sky by using the fraction of the sky obscured by clouds, for example cloudy sky has more than 70% cloud cover. Secondary atmospheric variables such as sky turbidity, water vapour content, and cloud type can be readily implemented in the model.

2.6.2.2 Solar irradiance load model

My solar irradiance load model was used to calculate the heat source due to the radiation effects from the sun's rays that enter a computational domain by implementing the Radiance ray-tracing approach. The solar model is a highly efficient and practical means of applying solar loads as heat sources in the CFD energy equations. The solar model includes a solar calculator utility that can be used to construct the sun's location in the sky for a given time-of-day, date, and position.

The algorithm for determining the heat loads in the solarCalc was as follows:

1. Convert coral geometry information into the radiance scene description format

2. Provide solar position information as azimuth and elevation; or as latitude, longitude and time

3. Add additional objects to radiance scene description as required
4. For each triangular facet of the original geometry:
   Determine its centre and normal direction
   Execute Radiance to determine the facet irradiance
   Store the values for later search
5. For each computational cell on the coral surface:
   Determine the nearest intersecting facet
   Calculate the area of the facet intersecting the cell
   Search the computed irradiance on the facet
   Convert to volumetric heat source term for the cell
6. Store the resulting volumetric heat-source for use in the CFD simulation.

In step 1 the coral geometry is typically available as a stereo-lithography surface (STL) file, which is also used as the basis of the computational mesh. Additional objects that may be included in the scene are items such as a reflective ground, light scattering due to the ocean surface or other reef structures that may be present.

The resulting heat flux that is computed by the solar ray-tracing algorithm is coupled to the CFD calculation via a heat source term in the energy equation. The heat sources are added directly to computational cells bordering each face and are assigned to adjacent cells. Other inputs that affect the spectral models, such as material properties, absorptivity and transmissivity, angle of solar incidence can be readily included in the solar load model.

2.6.3 Variation of attenuation coefficients (K_d)

Solar radiation received at the ocean surface is constantly changing both temporally and spatially. Variations in the irradiance field above and below the water surface have implications for the energy balance of coral habitats in aquatic environments. Cloud cover, water clarity, sea-state, and tides combine to reduce the intensity of both the quality and quantity of light that enters the ocean.

There are many ways of measuring light attenuation in the oceans. A common method involves the use of a Secchi disk which measures the reflectance values of the intensity of light backscattered per meter of water depths (Preisendorfer, 1986). The light extinction coefficient, K_d, can be estimated using Beer-Lambert's law:

$$\bar{I}(\bar{k_d}, \bar{z}) = \bar{I}_0 \exp(-\bar{k_d}\bar{z}) \tag{2.39}$$

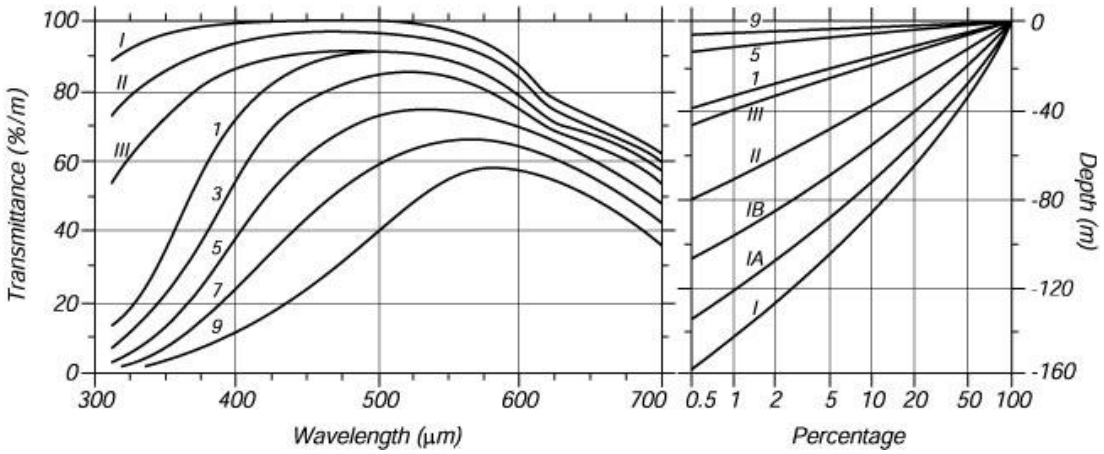

Figure 2.7. *Left:* Attenuation of daylight in the ocean in % per meter as a function of wavelength. *Right:* Percentage of 465 nm light reaching indicated depths for the same types of water. Adapted from Jerlov (1976) (Jerlov, 1976).

where, I_z is the intensity of light at depth z from I_0, the intensity of light at the ocean surface. However, this technique provides no insight to the attenuation of specific wavelengths within light spectrum.

2.6.3.1 Effects of water turbidity

Turbidity refers to the amount of light that is scattered or absorbed by a fluid. Some studies have associated the importance of turbidity with bleaching mitigation (Bayraktarov et al., 2013; Fabricius, 2005).

The water clarity can have a profound effect on the radiant heat entering the water column. Ocean water turbidity (inverse of clarity) has been classified into fourteen categories often referred to as Jerlov Water Types (Figure 2.7) (Jerlov, 1976). Five of these categories model deep ocean turbidity while the other nine model coastal turbidity. The study originally classified deep ocean water into three categories, I: extremely pure ocean water; II: turbid tropical-subtropical water; III: mid-latitude water; 1-9: coastal waters of increasing turbidity. Incidence angle is 90° for the first three cases, 45° for the other cases.

The waters with different optical properties can be characterised biologically as oligotrophic, mesotrophic, and eutrophic, ranging from the least to the most absorbent. Oligotrophic water has low biological production low nutrients. Eutrophic water has high biological production and high nutrients and mesotrophic water is moderate in both respects. The amount of irradiance varied and attenuated due to turbidity is shown in Figure 2.8 (Jerlov, 1976); the tabulations of vertical attenuation coefficients at any sea surface height can be readily estimated

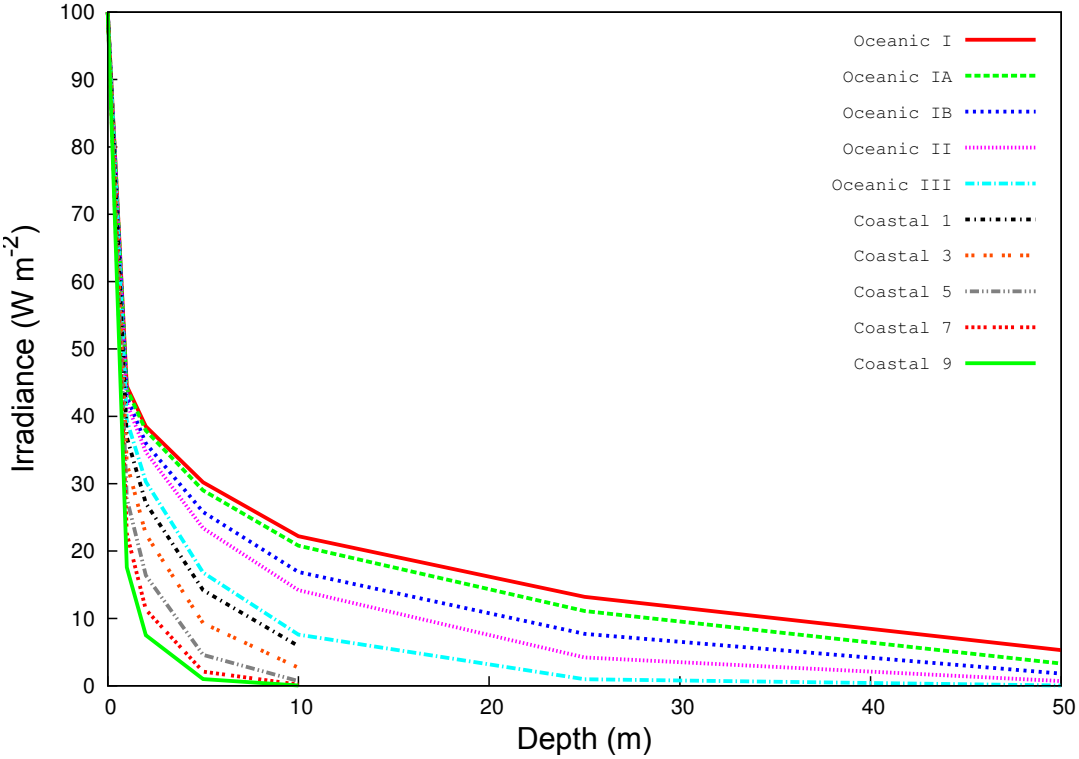

Figure 2.8. The amount of irradiance varied and attenuated due to turbidity. Adapted from Jerlov 1976 (Jerlov, 1976).

using Table 2.1.

Table 2.1. Loss of light in one metre of seawater (%). From Jerlov 1976 (Jerlov, 1976).

	violet		blue-green			yellow	orange	red
Wavelength (nm)	300	400	460	500	540	580	640	700
Oceanic, most clear	16%	4%	2%	3%	5%	9%	29%	42%
Oceanic, least clear	57%	16%	11%	10%	13%	19%	36%	55%
Coastal, average	-	63%	37%	29%	28%	30%	45%	74%

2.6.3.2 Effects of clouds

Local patterns of cloud cover may influence the susceptibility of reefs to mass bleaching and subsequent coral mortality during periods of anomalously high

SST (Mumby et al., 2001). Their findings explained that patterns of cloud cover may partly account for spatial patchiness in bleaching intensity and/or bleaching-induced mortality in other areas. They suggested that coral reef monitoring programmes consider the incorporation of cloud cover so that the synergies of SST and irradiance in determining mass coral bleaching might become clearer.

Sky models in Radiance may be useful in this context and can be divided into:

- the uniform luminance model
- the CIE overcast sky model
- the CIE clear sky model
- the Matsuura intermediate sky model

For details of each these sky models, refer to Appendix 2. In this thesis, I denote the state of the sky by using the fraction of the sky obscured by clouds, for example cloudy sky has more than 70% cloud cover.

2.6.3.3 Effects of tides

Spring low tides coinciding with high noon irradiance have the potential to cause widespread bleaching or mortality. However, tides can vary in range up to several meters and reduce the amount of irradiance on reef corals.

The model for the downward flux of solar radiation due to water depth is given by:

$$\frac{I_z}{I_0} = R^{(z/\zeta_1)} \tag{2.40}$$

where I is the irradiance at depth, z is the vertical coordinate positive upward with origin at mean sea level, I_0 is the incident less reflected and emergent irradiance at the surface, and ζ_1 is the attenuation length. The parameter values for R and ζ_1 are given in Table 2.2 (Paulson and Simpson, 1977), the values were then fitted to the data of Jerlov's (1976) (Jerlov, 1976, 1968) classification of water types of I, IA, IB, II, and III.

Table 2.2. Values of parameters based on Equation 2.40

Parameters	I	IA	IB	II	III
ζ_1 (m)	0.35	0.60	1.00	1.50	1.40
R (m)	0.58	0.62	0.67	0.77	0.78

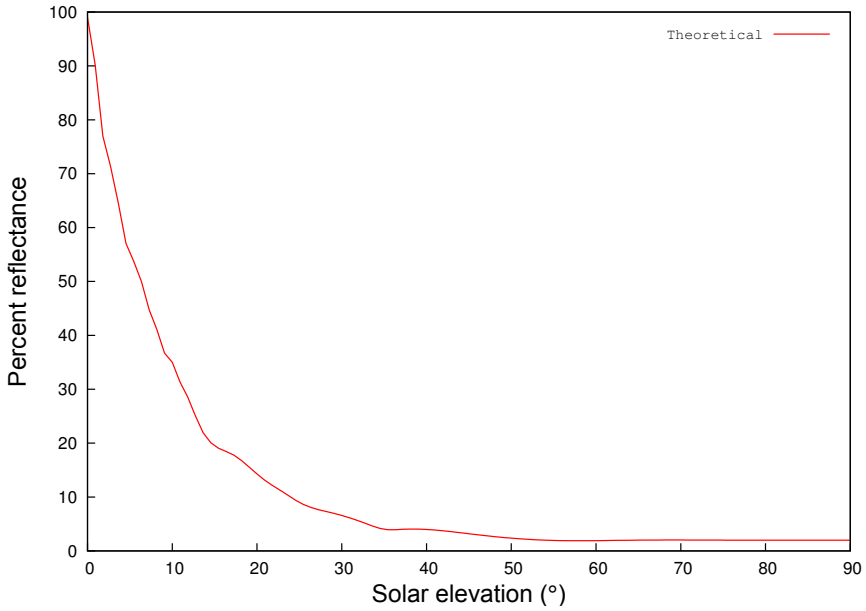

Figure 2.9. Theoretical percentage of sunlight reflected off different water surfaces.

2.6.3.4 Effects of sea-state

When light hits the water surface, some light penetrates and the rest is reflected. The amount of light that is reflected is determined by the angle between the light rays and the water surface. When the Sun's rays are perpendicular to a smooth ocean surface, reflectance is low. When the solar rays are oblique to the ocean surface, reflectance is increased. If the ocean is rough with waves, reflectance is increased when the Sun is at high elevation and decreased when it is at low elevation. Values associated with the change in sunlight reflectance with the Sun's elevation angle are listed in Table 2.3.

Table 2.3. Sunlight reflectance

Sun's elevation angle (°)	90	50	40	30	20	10	5
Reflectance (%)	3	3	4	6	12	27	42

The calculated values of percentage of reflectance from water surfaces based on Fresnel's law (Weinberg, 1976) is shown in Figure 2.9.

Since latitude is related to the elevation of the Sun above the horizon, light penetration is always less at the higher latitudes all else being equal. When the atmospheric effects (i.e. cloud cover, density layering, fog, and dust) are

considered with reflectance, solar elevation has a significant effect on the amount of light penetrating the ocean surface.

2.7 Summary

Corals and coral reefs are shaped by hydrodynamic and thermodynamic processes. This chapter detailed the development of a novel, open source, coupled CFD with ray-tracing and hydrodynamics models to explore the physiological and and environmental stressors – irradiance, water flow, and coral morphological features (colony shape, size, tissue thickness, and pigmentation) – that could ultimately be used to assess the variability of thermal stress in the coral microenvironments. These techniques will be validated and further developed in the following chapters.

Chapter 3

Flow and heat budgets at a controlled lab-scale environment

In this chapter, validation simulations against case studies of thermal stress in coral microenvironments under various scenarios at a laboratory scale condition are presented. Simulations have been validated against various experimental studies, available from the peer-reviewed literature as reference cases.

The works presented in this chapter are published as follows:

- Ong, R., A. King, B. Mullins, T. Cooper, and M. J. Caley (2012). Development and validation of computational fluid dynamics models for prediction of heat transfer and thermal microenvironments of corals. *PLoS ONE 7(6), e37842.*
- *Ong, R., A. King, B. Mullins, T. Cooper, and M. J. Caley (2011). Computational fluid dynamics model of thermal microenvironments of corals.* Modelling and Simulation (MODSIM).
- Ong, R., A. King, B. Mullins, M. J. Caley, and T. Cooper (2012). CFD simulation of low-Reynolds number turbulence models in coral thermal microenvironment. *Australian Fluid Mechanics Society.*

3.1 Validation case of laminar flow

The experimental study of Jimenez *et al.* (2008) (Jimenez et al., 2008) was used to validate the CFD modelling approach developed in this work. Jimenez *et al.* (2008) conducted their experiments in a flow chamber (10 cm height × 5 cm width × 25 cm length) with a sand covered floor. A steady inlet flow was maintained in the horizontal (length) direction. Measurements of coral surface temperatures of cylindrical branches cut from corals were made in their flow chamber (Jimenez et al., 2008). They explored coral surface temperatures under two environmental temperature scenarios: steady-state and transient.

In their steady-state experiment, flow was maintained at 0.002 m s^{-1}, and temperature at 26°C. Heat was provided by a fiber-optic light source with a collimating lens to focus light on the coral surface. The same experimental setup was also used outdoors, where corals (*Porites lobata* and *Stylophora pistillata*) were exposed to direct sunlight ranging from approximately 500 to 950 W m^{-2}. Coral surface warming was estimated as the difference between coral surface temperature and ambient water temperature after 30 min of exposure to direct solar irradiance. Downwelling irradiance was measured with a submersible light logger, while temperature measurements of both water and coral surface were made using thermocouples connected to a data logger.

The transient experiments, in contrast, were done to monitor the effects of temperature changes at the surface of corals under changing light regimes. The corals (*Cyphastrea serailia* and *Seriatopora hystrix*) were heated by direct illumination using a fiber optic light source (spectral range from 400-730 nm) fitted with an adjustable lens. Corals were held in darkness for approximately 5 min before a dark-light shift was imposed, employing an irradiance of 600 W m^{-2}. Temperatures were estimated by inserting microsensors into the coral tissue or into the mouth of a polyp. The point source temperatures were then averaged for each coral, in order to obtain an average tissue (surface) temperature.

Another set of steady-state experiments were carried out using two hemispherical colonies (*P. lobata* and *Favia* sp.) and one branch of *S. pistillata* to investigate thermal boundary layer properties. Here temperature profiles were measured at two irradiances (1,080 and 2,080 μmol photons m^{-2} s^{-1}; approximately 310 and 600 W m^{-2}) using two flow rates (0.002 m s^{-1} and 0.013 m s^{-1}). The thermal conductivity of tissue (silicone) is approximately set to 0.22 W$m^{-1}K^{-1}$, and the skeleton (aragonite) is set to 2.1 W$m^{-1}K^{-1}$ (Joshi, 2013). Based on their empirical models, Jimenez *et al.* (2008) suggested the light absorptivity of the tissue of the three coral species used in their steady-state experiment ranged from 0.13 to 0.28, depending upon species and pigmentation levels of individual colonies.

3.1.1 Grid independence analysis

Grid convergence was investigated to test whether the modelled solutions were independent of grid resolution. The purpose here was to reduce truncation error and establish the minimum degree of grid resolution required. Simulations were initially performed on coarse grids then followed by successively finer grids to observe the effects of grid resolutions on coral surface temperatures. I varied the number of grid cells from 150,000 to 1,000,000 cells with a constant time step of 1.0 s. As the grid becomes finer, the solution should become less sensitive to grid spacing and approach an asymptotic convergence value. I tested a range of coral species with massive and branching growth morphologies for grid convergence.

3.1.2 Model configurations

To simulate the conditions used by Jimenez *et al.* (2008), three-dimensional geometries for massive and branching corals were generated (Figure 3.1). The low Reynolds numbers estimated for their experimental setup indicated laminar flow conditions (Table 3.1). The characteristic length scale was defined as coral diameter. Coral geometries were modelled for both thermal regions, tissue and skeleton, each with its own thermal performance functions. The diameters and lengths of branching corals modelled here are the same as those used by Jimenez *et al.* (2008) (Jimenez et al., 2008).

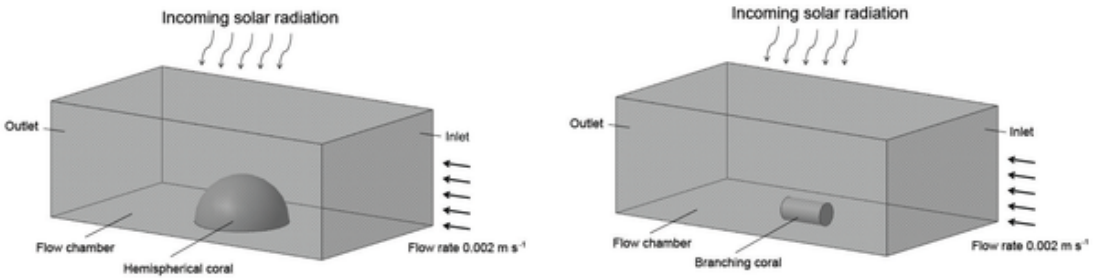

Figure 3.1. Conceptual representation for both models and the experiment apparatus used by Jimenez *et al.* (2008) *Left:* massive/hemispherical coral. *Right:* branching coral

The mesh near the coral was finer than anywhere else in the domain in order to adequately capture the momentum and thermal boundary layers. I used two types of grids, predefined block structured hexahedral and polyhedral, to represent both computational and coral domains with approximately 900,000 cells each depending on the shapes and sizes of the corals being considered. To decrease simulation time, computations were run in parallel using 4 CPU's using decomposition methods in OpenFOAM.

Table 3.1. Dimensions of corals used by Jimenez *et al.* (2008)

Species Name	Experiment	Diameter (mm)	*Re*
Porites lobata	Steady	35 (hemisphere)	72^a & 468^b
Stylophora pistillata	Steady	6 (cylindrical, 6 mm long)	12^a & 80^b
Favia sp.	Steady	35 (hemisphere)	72^a & 468^b
Cyphastrea serailia	Transient	50 (hemisphere)	100^a
Seriatopora hystrix	Transient	3 (cylindrical, 6 mm long)	6^a

^{a} indicates flow of 0.002 m s^{-1}, ^{b} indicates flow of 0.013 m s^{-1}

3.1.3 Skeletal density and permeability measurements

The mean bulk and true densities and porosities were estimated for cores of coral skeletons to provide data for modelling flow permeability through them. Here, I assessed the flow permeability and porosity of representative samples for each species used by Jimenez *et al.* (2008) (except for the hemispherical coral *C. serailia*, which was unavailable). Skeletal samples were sectioned into defined volumes, dried in an oven at 105° C, then weighed to estimate the skeletal bulk density ($\rho_b = \frac{m}{V}$). Porosity values were then calculated using equation 3.1. Porosity ϕ is defined as the fraction of the total volume of a medium, which is occupied by void space. Thus 1 - ϕ is the fraction that is occupied by solid material.

$$\phi = 1 - \frac{\rho_b}{\rho_t} \tag{3.1}$$

where ρ_b is the bulk density, and ρ_t is the true density.

To investigate the permeability of a coral to transmit fluids, samples of random coral specimens were placed in a test chamber half filled with water and then subjected to a given flow rate of air. The pressure gradient is determined by measuring the pressure differential across the upstream and downstream from the specimens, from which the coefficient permeability of each specimens was determined.

3.1.4 Sensitivity analysis

My estimates of skeletal bulk density of each coral species may have been prone to experimental error. If so, such error could have implications for predicting coral skeleton temperatures. To examine the potential accuracy of our skeletal

bulk-density predictions to the rate of temperature rise for hemispherical and branching coral skeletons, the volumes of each coral sample were varied ± 10% at a constant heat flux of 750 W/m^2 and steady inlet flow of 0.002 m s^{-1}. Table 4 summarises the parameters used for sensitivity analysis on hemispherical and branching coral skeletons.

Table 3.2. Parameters used in the sensitivity analysis

Inlet reference pressure	0 Pa
Inlet temperature	26 °C
Inlet velocity	0.002 m/s
Skeletal bulk volume	± 10%
Heat flux	750 W/m^2

3.1.5 Model boundary conditions

In order to adequately simulate the flow conditions corresponding to the experimental work of Jimenez *et al.* (2008), it was necessary to assign initial and boundary conditions to the flow domain. Fixed-value boundary conditions for superficial velocities of 0.002 m s^{-1} and 0.001 m s^{-1} were applied at the inlet and bottom domains, respectively. A zero-gradient boundary condition constrains the normal gradient of the boundary patch to zero, while the slip boundary condition sets the normal velocity component to zero. The pressure at the inlet was fixed at the zero gradient condition. The pressure at the outlet were fixed at the reference pressure, while the outlet velocity was fixed at the zero gradient. The velocity and pressure at the domain sides was fixed at the slip boundary condition. The initial and boundary conditions for velocity, pressure, and temperature are shown in Table 3.3.

Table 3.3. Initial and boundary conditions of Jimenez *et al.* (2008)

Variables	Initial Value	Walls	Top	Bottom	Inlet	Outlet
p_{ref}	0 Pa	S	S	ZG	ZG	FV
u	0.002 m s^{-1}	S	S	FV 0.001 m s^{-1}	FV	ZNG
T	26°C	S	S	FV	FV	ZG

S: Slip, ZG: Zero Gradient, ZNG: Zero Normal Gradient, FV: Fixed Value

3.1.6 Results

3.1.6.1 Skeletal density and coral permeability

The estimated (and assumed) porosity values for each of the species examined by Jimenez *et al.* (2008) are presented in Table 3.4.

Table 3.4. Estimated skeletal porosities

Species Name	Skeletal Porosity
Porites lobata	0.475± 0.003
Stylophora pistillata	0.431± 0.003
Cyphastrea serailia	0.500*
Seriatopora hystrix	0.405± 0.003

* Species not available. Realistic value for massive coral assumed

The experiment indicates that there was no significant permeability through intact living tissue, however, in many cases, the activity of borers and coral grazers will result in openings allowing percolation and increased skeletal porosity. The slight variations in both total porosity and porosity-permeability trend (Figure 3.2) can be explained to a large degree by the various range of coral sizes and depositional fabrics of calcite grainstones.

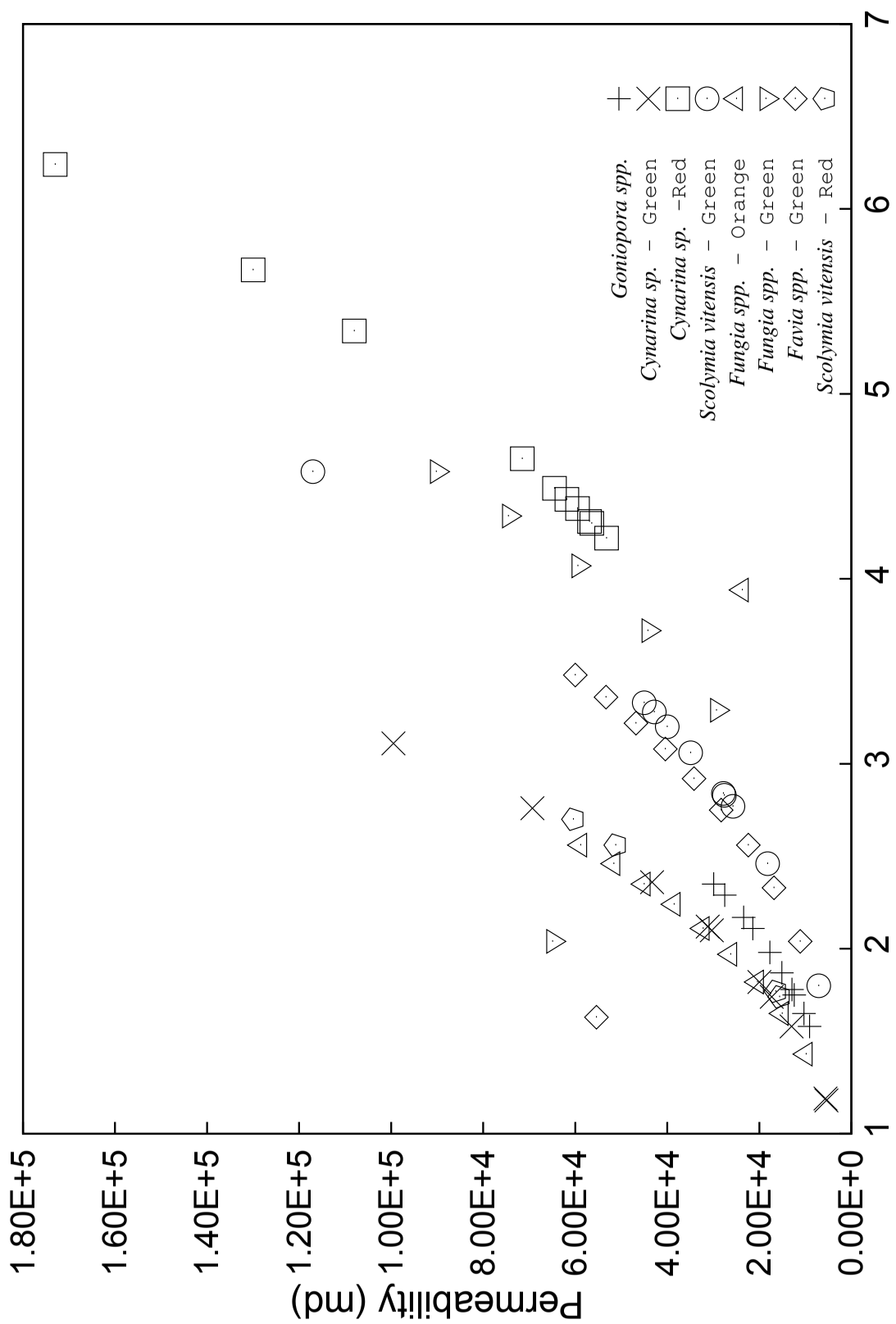

Figure 3.2. Permeability vs porosity of various coral specimens

3.1.6.2 Grid independence analysis

Except for *P. lobata*, the number of cells needed to reach steady-state coral tissue warming was approximately 600,000. For *P. lobata*, the surface warming oscillated strongly and only converged on a solution at approximately 800,000 cells (Figure 3.3). These results suggest that the grids used in the models (900,000 cells) were sufficiently fine to capture these heating dynamics, and therefore, the solutions were derived within this asymptotic range. Further refinement of the grid would be unlikely to yield significant variations to the results.

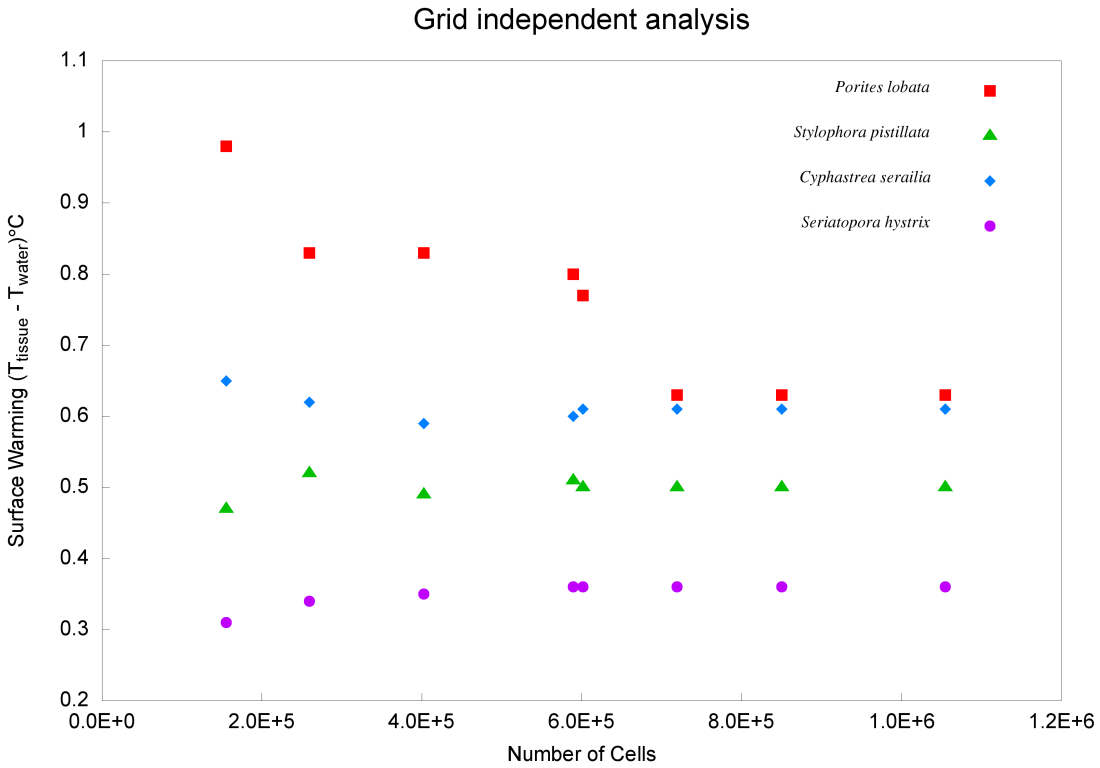

Figure 3.3. Grid independence analysis based on varying the number of grid cells at constant flow (0.002 m s^{-1}) and two irradiances (600 W m^{-2} for *C. serailia* and *S. hystrix* and 750 W m^{-2} for *P. lobata* and *S. pistillata*)

3.1.6.3 Steady-state simulation

Coral surface warming is given as a deviation from the ambient water temperature (26° C) under a constant inflow condition (0.002 m s^{-1}) and direct solar irradiances. For the hemispherical coral, *P. lobata*, the temperature differential increased with increasing irradiance at a flow rate of 0.002 m s^{-1} (Figure 3.4).

However, for the branching coral, *S. pistillata*, the surface warming showed no significant increase with increased irradiance at the same flow rate (Figure 3.5). For *S. pistillata*, the branching coral, the A/V ratio was 1,666, and for *P. lobata*, the hemispherical coral, the A/V ratio was 257.

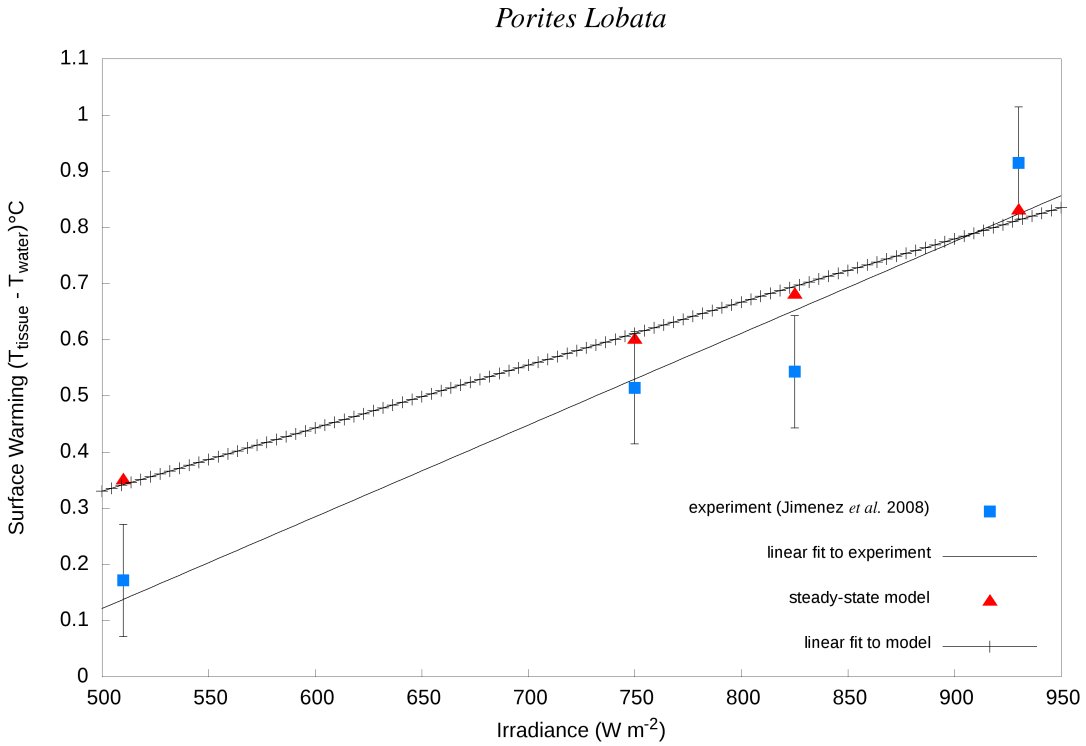

Figure 3.4. Comparisons of simulated and experimental surface warming of hemispherical coral *P. lobata*

Both the experimental data of Jimenez *et al.* (2008) and the CFD models agreed well with a linear relationship between coral surface warming and irradiance; consistent with heat transfer theory. The greatest temperature difference between the experimental and simulated data was 0.15°C (22%) for the hemispherical coral at 825 W m^{-2}. The average temperature difference between the models and experimental results for branching coral and hemispherical coral were 0.03°C and 0.13°C, respectively. An increase in flow velocity from 0.002 m s^{-1} to 0.013 m s^{-1} under constant irradiance of 600 W m^{-2} resulted in a slight decrease of surface warming for all coral species (Table 3.5).

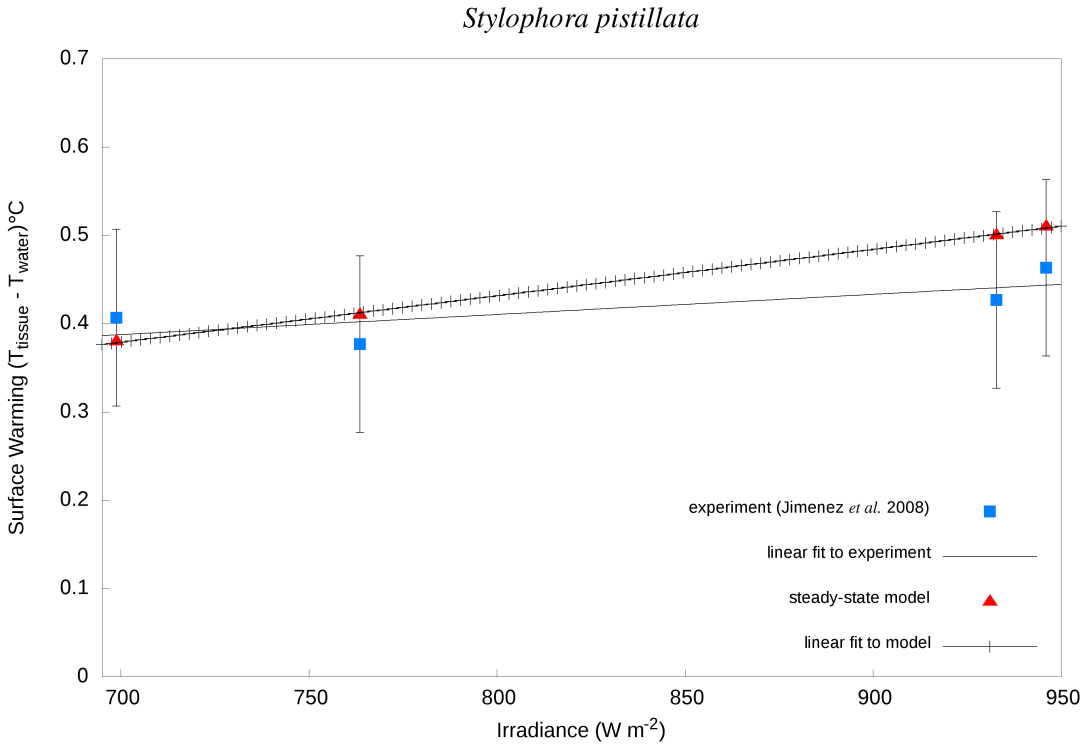

Figure 3.5. Comparisons of simulated and experimental surface warming of a branch of *S. pistillata*

Table 3.5. Effect of low flow (U=0.002 m s^{-1}) and high flow (U=0.013 m s^{-1}) on coral surface warming under constant irradiance of 600 W m^{-2}

	Favia sp.		*S. pistillata*		*P. lobata*	
Parameters	Low U	High U	Low U	High U	Low U	High U
$\triangle T$ (exp.)	0.56	0.35	0.38	0.16	0.60	0.57
$\triangle T$ (model)	0.50	0.35	0.35	0.21	0.58	0.52

3.1.6.4 Transient-state simulation

Dark-light shift simulations (described in the model validation section) were performed for the massive coral *C. serailia* and the branching coral *S. hystrix*. Illumination in the experimental data commenced at 143 s and 235 s for hemispherical and branching corals, respectively (Figure 3.6 and Figure 3.7). The time constants from both the modelled and experimental data after the onset

of illumination were nearly twice as long for the hemispherical coral (340±10s and 310±10s, respectively) than for the branching coral (180±10s and 220±10s, respectively). The calculated A/V ratios of the hemispherical coral (*C. serailia*) and the branching coral (*S. hystrix*) were 180 and 3,000, respectively. These differences in A/V ratios were consistent with the differences in time constants.

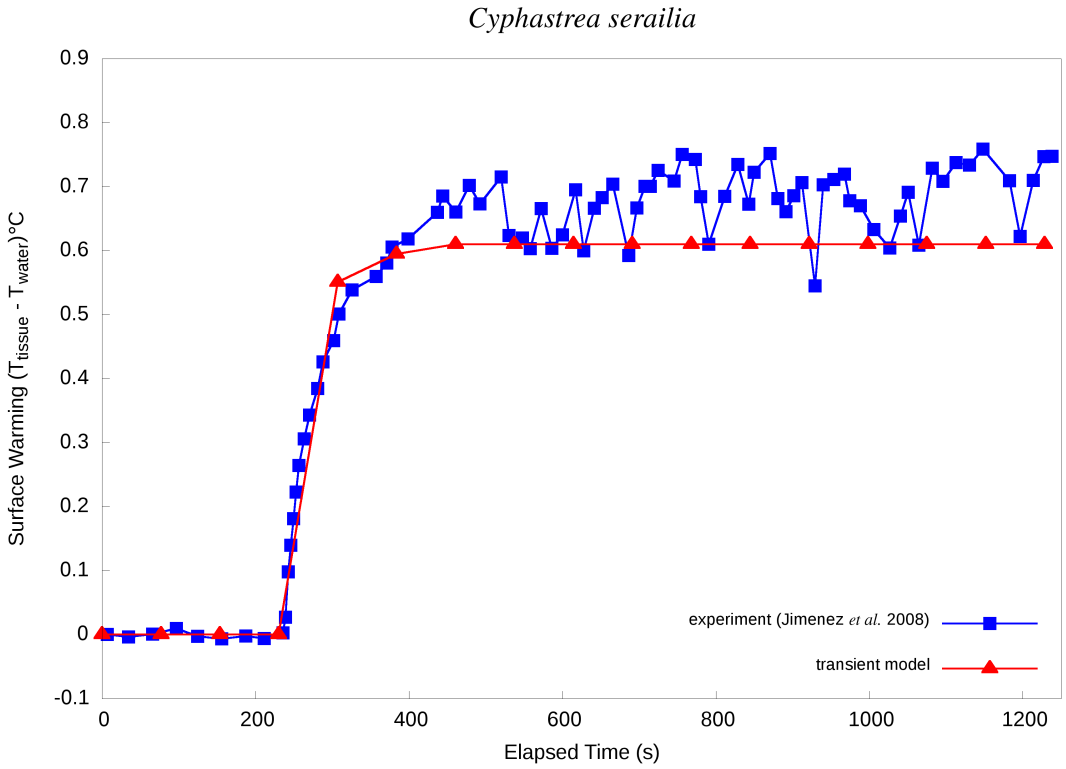

Figure 3.6. Surface warming of corals in response to a dark-light shift of hemispherical *C. serailia*

The results of the transient-state simulations agreed well with the experimental results of Jimenez *et al.* (2008), as well. The smaller temperature increase experienced by the branching coral compared to the hemispherical coral was also consistent with theoretical expectations and their experimental results. Mean temperature differences between their experiments and the simulations in hemispherical and branching corals were 0.08°C and 0.03°C, respectively.

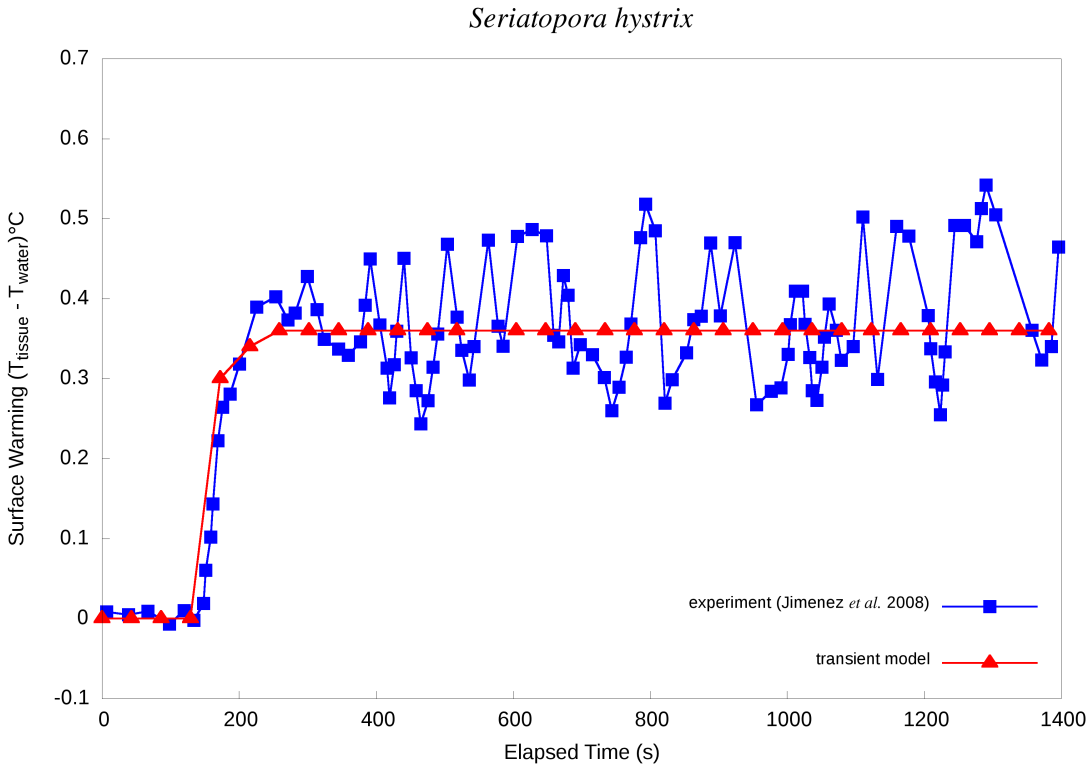

Figure 3.7. Surface warming of corals in response to a dark-light shift of branch of *S. hystrix*

3.1.6.5 Flow patterns inside corals

The two-dimensional velocity magnitude and coral surface warming at different cross-sectional planes are shown in Figure 3.8 and Figure 3.9 for both hemispherical and branching corals. Note that only one slice has coral within its bounds, the coral cross section is shown as a thick black line in the $Z_4 = [0]m$ plane. Due to the absence of turbulence, the flow fields show homogenous distributions throughout the domain and isotropic behaviour of coral tissue and skeleton.

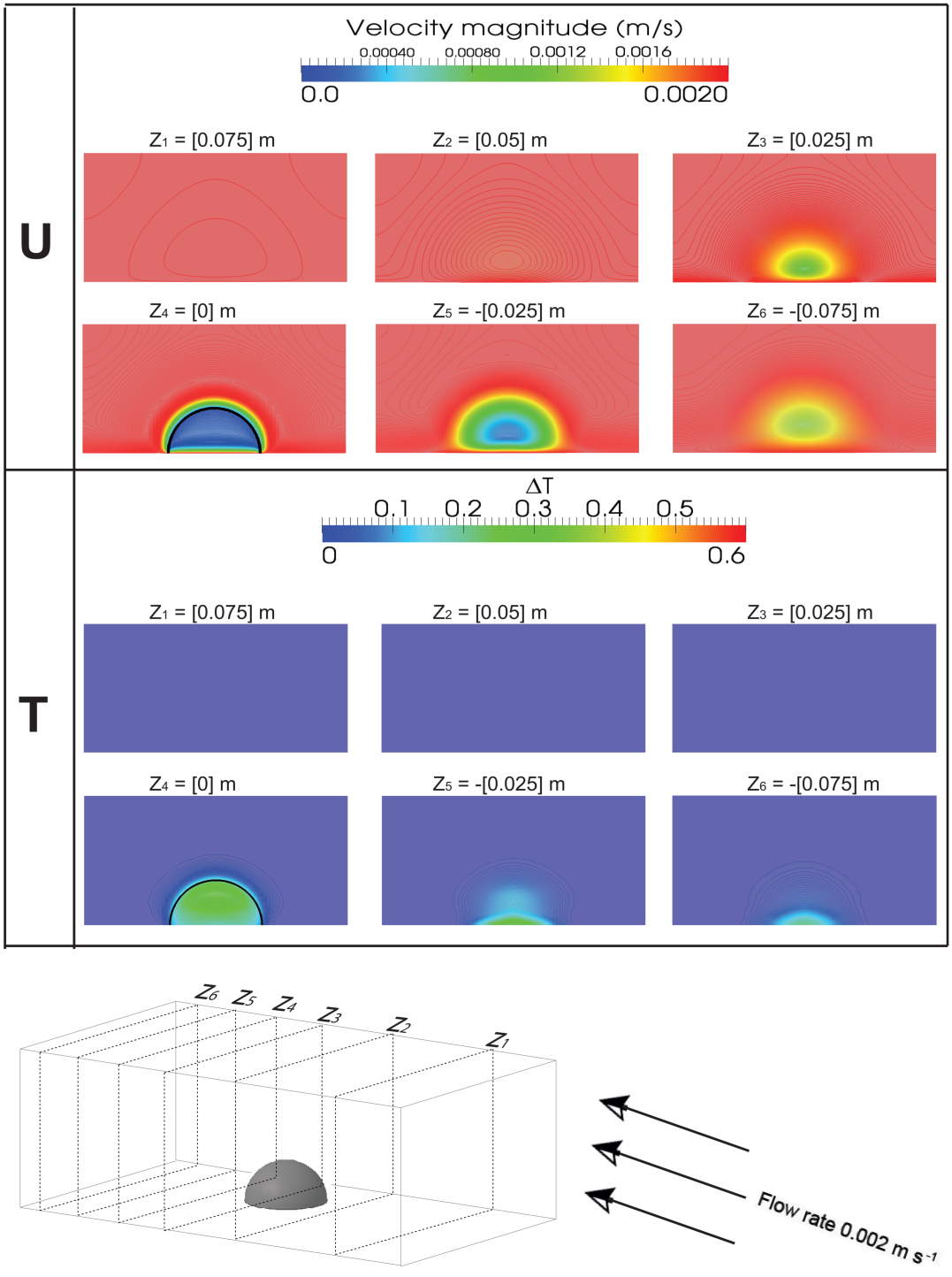

Figure 3.8. Slices of axial velocity, temperature magnitude, and contour for six different cross sectional planes of hemispherical *P. lobata*

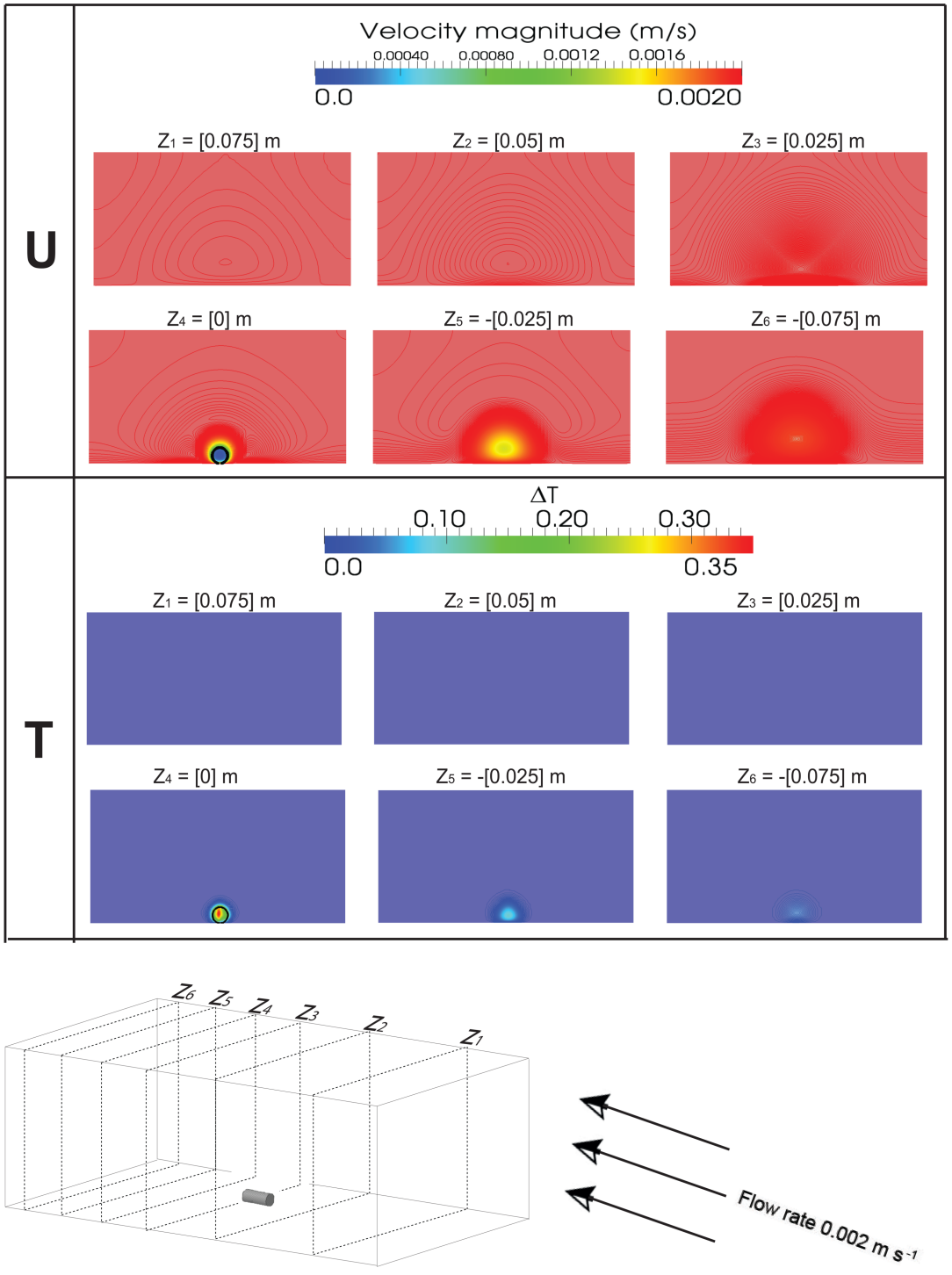

Figure 3.9. Slices of axial velocity, temperature magnitude, and contour for six different cross sectional planes of a branch of *S. pistillata*

3.1.6.6 Sensitivity analysis

An increase in bulk density at a constant heat flux decreased the overall surface temperature for hemispherical coral in a similar but inverse manner to porosity changes (Figure 3.10). However, the bulk density variation for branching coral had little or no effect on overall temperature rise.

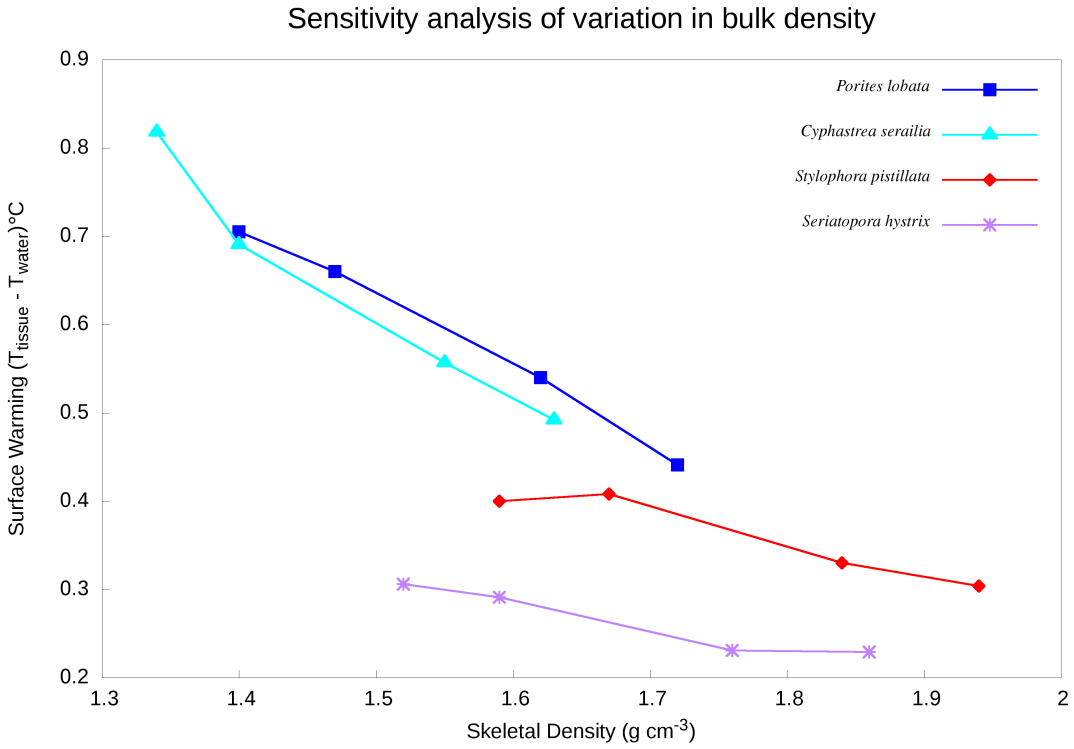

Figure 3.10. Sensitivity analysis of skeletal temperature rise to variations in bulk density under constant irradiance of 750 W m^{-2}

3.1.7 Discussion

The simulation results were broadly consistent with the experimental results of Jimenez *et al.* (2008) with respect to thermal and temporal responses of corals under irradiation, and the effects of coral shape and size. In steady-state light conditions, the effects of A/V ratios was as expected given heat loss should increase with increasing surface area and decrease with decreasing volume. The higher A/V ratio of the branching coral *S. pistillata* compared to the hemispherical coral *P. lobata* was consistent with the expectation from theory that heat

loss should be greater with a branching morphology. Under transient light conditions, the higher A/V ratio of the branching coral *S. hystrix* means that heat would be dissipated to the environment faster than it would be from the hemispherical/massive coral, *C. serailia*. Therefore, under equivalent illumination a longer time would be required for branching corals of an equivalent volume/-mass to reach equilibrium with their immediate thermal environment. Typically, however, massive corals have a considerably greater volume/mass ratio, and as I observed here, hemispherical corals heated at a slower rate, taking nearly twice as long to equilibrate. In this case, the effect of faster cooling resulting from different A/V ratios was over taken by thermal mass effects. Temperature values were obtained for each finite volume over the entire coral surface area in the CFD simulations, which contrasted with the microsensor approach of the experimental study (Jimenez et al., 2008). In this way, the highest temperature reached on a coral's surface (for the idealised geometry) was easily obtained.

An increase in skeletal bulk density (inversely proportional to porosity) may result in an increase in the viscous and inertial resistance where forced convection becomes ineffective. The penetration of flow through the coral skeleton will reduce the heat transfer coefficient and lead to decreased fluid residence time and contact surface area between coral skeleton and fluid. As a result, the intensity of energy transfer between phases will reduce the temperature gradient of the coral skeleton. Given substantial inter-colony variation in skeletal bulk density and porosity (Roche et al., 2010), such physical features of coral may be useful for predicting coral bleaching responses. It should, however, be noted that flow through corals would normally only be expected in injured (damaged/predated) corals, which would therefore already be stressed.

3.2 Validation case of turbulent flow

In the previous section, I established the potential of CFD in predicting the thermal stress imposed on corals by their thermal microenvironments under laminar flow conditions. However, in the overwhelming majority of cases, the external flow stream carries with it a certain degree of turbulence.

Here, the experimental study of Fabricius (2006) (Fabricius, 2006) was used to validate the low-Re turbulent CFD model. She conducted an experiment which exposed a range of different coral species and pigmentations (hemispherical coral (*Favia matthaii*), ≃90 mm) to direct sunlight ranging from high irradiance (1,500-1,600 μmol m^{-2} s^{-1} or ∼800 W m^{-2}) to low irradiance (120-350 μmol m^{-2} s^{-1} or ∼150 W m^{-2}) (Figure 3.11). Pigmentation was measured as background fluorescence, F_0, which here is defined as a proxy of a light-absorptivity coefficient where F_0=100 as near white and F_0=600 as dark brown. Measurements were taken outdoors in flow chambers with a steady inlet flow maintained at 0.01, 0.02, and 0.05 m s^{-1} (only the latter flow speed was investigated since I am interested in validating the turbulence models, $Re \simeq 4600$), and a temperature of 29.3°C. Coral surface warming was given as the difference between coral surface temperature and ambient water temperature after a period of exposure to solar irradiance.

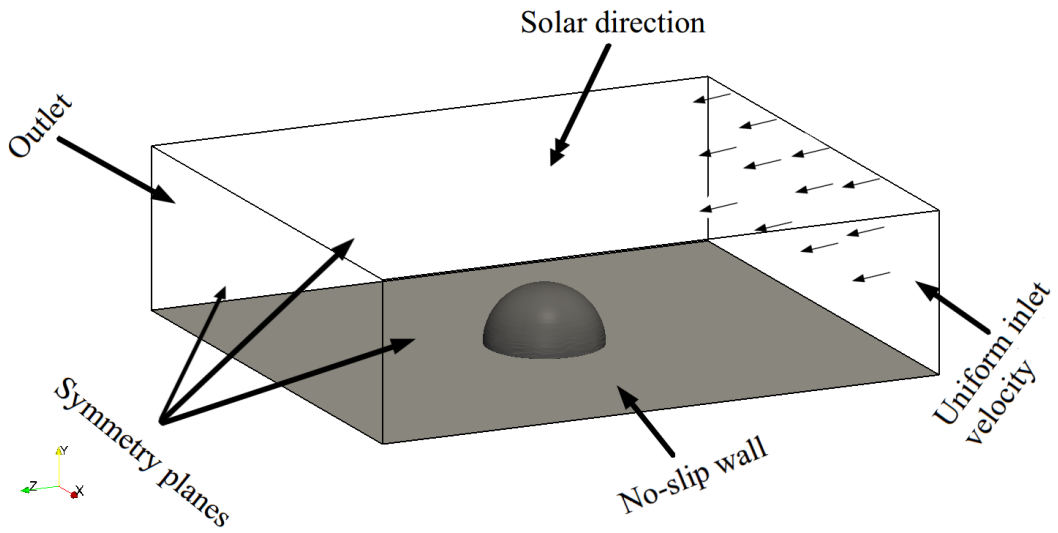

Figure 3.11. Model set-up and boundary conditions for the simulation

Although, the large eddy simulation (LES) and direct numerical simulation (DNS) may yield exact turbulence structure solved on the grid given the exact initial and boundary conditions. However, for the majority of experimental cases,

the turbulence structures are a mean representative of space and time scales of the ones occurring from the corresponding set of experiments. Furthermore, the focus of this work will shift from a smaller to larger scale, hence, RANS was selected because in practice LES and DNS are not effective choice of turbulent models. Moreover, the RANS was selected due to the widely used and trusted models for handling the low Reynolds number such as the Spalart-Allmaras (SA) and the Menter $k-\omega$ shear stress transport (SST) turbulence models.

3.2.1 Setting grid

The low Re turbulence model was employed in the region of the viscous sublayer, which lies approximately in $y^+ \leq 1$. The dimensionless quantity of normalised distance from the wall, y^+, is defined as

$$y^+ = \frac{y \cdot u_*}{\nu} \tag{3.2}$$

$$u_* = \sqrt{\frac{\tau_w}{\rho}} \tag{3.3}$$

$$\tau_w = \frac{C_f \, \rho \, {U_0}^2}{2} \tag{3.4}$$

$$C_f = \frac{0.0791}{Re^{-0.3}} \tag{3.5}$$

where y is the actual distance from the wall, u_* is the friction velocity, and τ_w is the wall shear stress (WSS).

In this particular case study, the $y^+ \simeq 0.5$ with $\simeq$1,500,000 cells.

3.2.2 Boundary conditions

To adequately accommodate the flow conditions corresponding to the experiment, it was necessary to specify free stream boundary conditions. I estimated the turbulence intensity, I, and length scale, l to be $\sim$0.05-0.1% and $\sim$30% of the coral diameter, respectively. The primitive turbulence model variables can then be computed from the following Table 3.6 and 3.7.

where C_μ represents a constant of 0.09. For a Cartesian coordinate system, k is given by:

$$k = \frac{1}{2}\left(U_x'^2 + U_y'^2 + U_z'^2\right) \tag{3.6}$$

where $U_x'^2$, $U_y'^2$, and $U_z'^2$ are the fluctuating components of the velocity in the three dimensional directions.

Table 3.6. Free-stream model variables

Parameter	formula
k	$\frac{3}{2}(I\bar{U})$
ϵ	$\frac{{C_\mu}^{0.75}k^{1.5}}{l}$
ω	${C_\mu}^{-0.25}\frac{\sqrt{k}}{l}$

To impose boundary layers in the viscous sublayer region and to accommodate convergence, the initial conditions of k and ω at the wall are specified differently from the free-stream conditions. The rest of the bounding boundaries were set as a symmetry plane which applies zero gradient condition for scalars and vector fields.

Table 3.7. Initial and boundary conditions of Fabricius (2006) validation study

Parameter	floor	inlet	outlet
k (m^2s^{-2})	10^{-10}	TIKEI	IO
ϵ (m^2s^{-3})	FV	TMLDRI	IO
ω (s^{-1})	$\frac{60\,\nu}{\beta_1\,y^2}$	TMLFI	IO
ν_t (m^2s^{-1})	C	C	C
u (m s^{-1})	(0 0 0)	FV	IO
T (K)	FV	FV	ZG

*SP: symmetry plane, ZG: zero gradient, ZNG: zero normal gradient, FV: fixed value, C: calculated, TIKEI: turbulent intensity kinetic energy inlet, TMLDRI: turbulent mixing length dissipation rate inlet, TMLFI: turbulent mixing length frequency inlet

3.2.3 Results and discussion

Due to the absence of empirical measurements of axial velocity and wall shear stress at the upstream of the outlet, here I only validate the turbulence models based on the heat transfer performance of measured coral surface warmings. In this study, four of the most popular Low-Reynolds-number models were selected in the benchmark comparisons - the two equations $k-\omega$ SST, the two equation $k-\epsilon$ model Launder-Sharma, the two equations $k-\omega$, and the one-equation model Spalart-Allmaras (Figure 3.12, 3.13, and 3.14). The $k-\omega$ SST and $k-\epsilon$ Launder-Sharma models both agree well with the experimental data and are much less dissipative which results in higher values of calculated velocity. These two models

tended to establish downstream laminar flow when the free-stream turbulence level was low $\left(\frac{\mu_t}{\mu} \leq 0.1\right)$ (Roy and Blottner, 2001). I also compared the sensitivity of the four models to free stream turbulent parameters and wall spacings. The results of the Spalart-Allmaras model show a reasonable agreement with the experimental data and insensitive to the free stream intensity values ranging from 1-15%. The two-equation models showed stronger sensitivity towards the turbulence levels in that the solutions tended to be laminar when the free stream levels were low, and vice versa (Roy and Blottner, 2001).

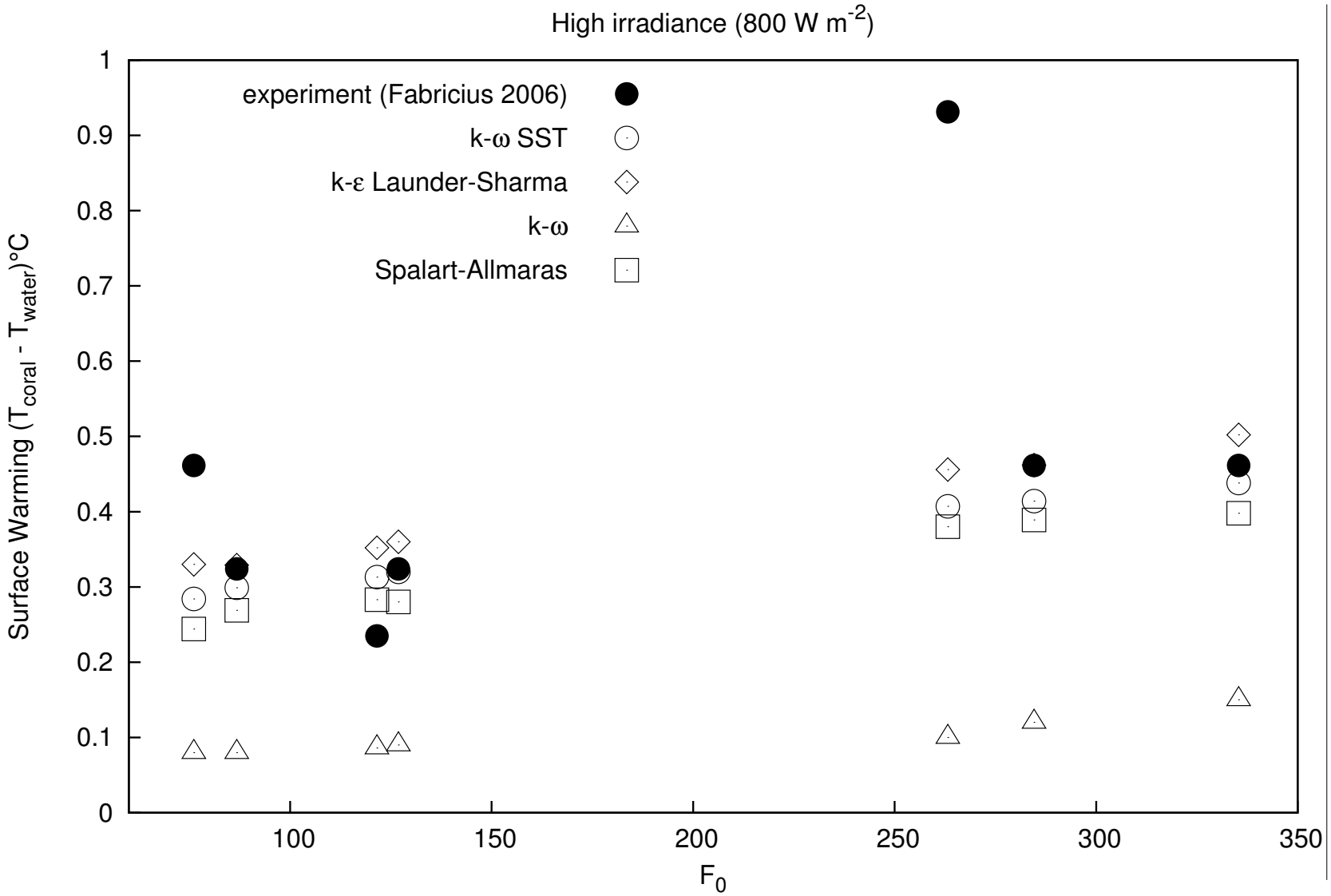

Figure 3.12. Effects of flow, irradiance, and pigmentation on *F. matthaii* surface warming at high irradiance

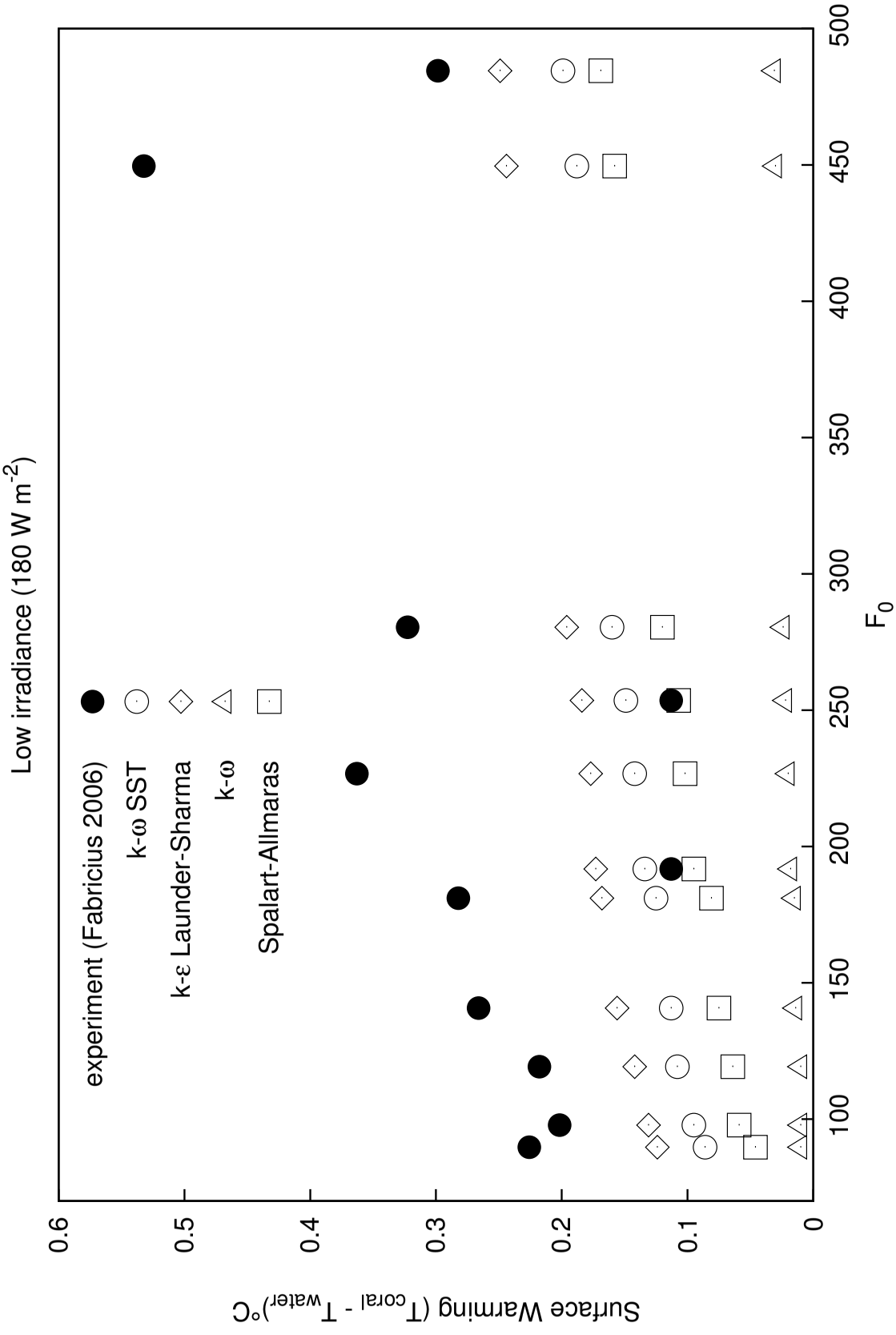

Figure 3.13. Effects of flow, irradiance, and pigmentation on *F. matthaii* surface warming at low irradiance

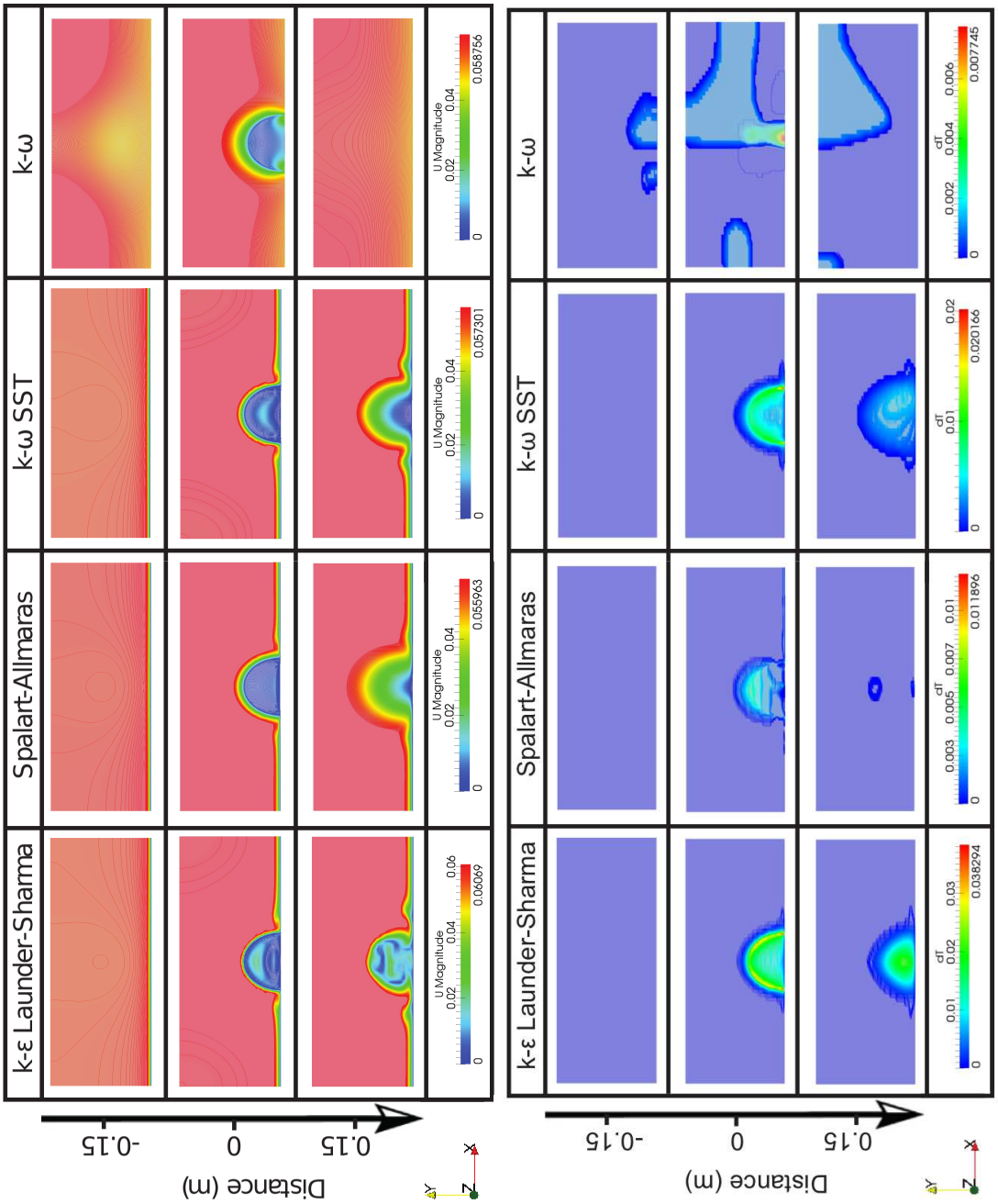

Figure 3.14. Simulation results of slices of axial velocity and temperature profiles of *F. matthaii* at low irradiance at F_0=100

The results demonstrated that the magnitude of the temperature rise in coral tended to increase linearly with increasing pigmentation/absorptivity (Figure 3.12 and 3.13). The mean and standard deviation of the low irradiance and high irradiance experimental results were 0.267±0.094 (99.7% confidence intervals: -0.015 to 0.549) 0.457±0.232 (99.7% confidence intervals: -0.239 to 1.153), respectively. The root mean squared error (RMSE) for each of the models associated with the experimental results is reported in Table 3.8.

Table 3.8. RMSE among the turbulence models and experimental results

RMSE (°C)	$k-\omega$ **SST**	$k-\omega$	$k-\epsilon$ **L-S**	**S-A**
Low irradiance	0.433	0.823	0.152	0.561
High irradiance	0.273	1.033	0.154	0.361

3.3 The effects of polyp-scale morphology in thermal microenvironments

Coral morphology, i.e. size, shape, and composition (e.g. tissue thickness and permeability) of coral colonies explains best observed variation in bleaching susceptibility (Guest et al., 2012; Ong et al., 2012; Shenkar et al., 2005). Variation in coral morphology, however, is confounded by coral systematics as morphology is strongly conserved among large groups of coral species and ranges from highly complex branching structures to simple hemispherical and encrusting forms (Veron, 1995, 2000). In coral species where colony architecture is influenced by light, differences in colony form may directly result in variation of thermal stress and subsequently alter the host's photoautotrophic activity (Hoogenboom et al., 2006; Porter, 1976).

Despite the potential importance of temperature of coral microenvironment into the regulation of coral energy budget and physiological processes, only a few of experimental studies have considered the temperature of corals and the heat fluxes at their surface. Fabricius (2006) measured the surface temperature of a number of shallow-water corals and showed that more densely pigmented corals heated more than less densely pigmented ones, an effect that was enhanced under low water flow conditions (Fabricius, 2006). Jimenez *et al.* (2008) also detailed the heat budget of a coral exposed to solar radiation and water flow under controlled experimental conditions and on a reef flat under naturally fluctuating conditions of flow and irradiance (Jimenez et al., 2008). These experimental studies provided the first evidence that the thermal microenvironment can play an important role in the microscale processes involved in coral bleaching. In order to better understand such relationships between water temperature and coral morphology, I previously developed a heat transfer model that was coupled with fluid dynamics to study coral thermal microenvironments under controlled laboratory conditions. Our approach using computational fluid dynamics (CFD) models allowed us to study different coral species, morphologies and pigmentations and model the response of these corals to various conditions of thermal consistency and flux and different flow conditions.

Corals are modular organisms in which each coral colony consists of numerous, interconnected, genetically identical modules, the polyps. Given the intricacy of modelling this micro-polyp scale architecture, it is impractical to achieve the level of texture detail using computer-aided-design (CAD) software. Previously, I investigated coral surface warming for smooth surface topographies with a uniform tissue layer covering the skeleton, thereby viewing colonial organisms as integrated wholes rather than structured collections of small polyps. Here I extend the work of the previous section 3.1 by analysing the effects of coral surface topog-

raphy and outlining the potential contributions of surface area-to-volume (A/V) ratios at different polyp depths (PD) to micro-polyp scale processes in influencing the thermal dynamics of coral microenvironments. A previously published study that explored the effects of convection and boundary layer thickness on colony morphology (Jimenez et al., 2011) was used for validation.

I used experimental boundary layer measurements collected in a flow chamber by Jimenez *et al.* (2011) (Jimenez et al., 2011) for coral colonies of two species to validate our CFD models. The two coral species used in their experiment, both with massive morphologies, were *Leptastrea purpurea*, (colony dimensions: diameter ∼35 mm, depth: ∼1 mm, and ∼1.3 mm spacing) and *Platygyra sinensis*, (colony dimensions: diameter ∼45 mm, depth: ∼2 mm). As discussed above, corals consist of two distinctive regions: an almost impermeable layer of tissue covering the surface of the colony and a highly porous calcareous skeleton and each region possesses slightly different thermal properties. Because the validation case study (i.e. Jimenez *et al.* (2011)) used corals that would likely have had significant permeability on their cut faces (see above), I structured our models to account for this combination of porous and non-porous surfaces. Furthermore, our model assumed the effect of metabolic mass transfer, the heat generated due to photochemical conversions, on the overall coral surface warming to be negligible (Cooper, 2008).

3.3.1 Model validation

Jimenez *et al.* (2011) used a flow chamber, 10 cm high, 5 cm wide, and 25 cm long with a sand covered floor maintained at a steady flow of 0.01 m s^{-1} at 25°C ambient temperature. Irradiance was provided by a fixed heat source set to 1500 μmol photons $m^{-2}s^{-1}$ (∼430 W m^{-2}). They constructed temperature contour maps using microsensors from multiple temperature micro-profiles measured along a transect across a single polyp and perpendicular to the direction of water flow (Jimenez et al., 2011). To simulate the conditions used by Jimenez *et al.* (2011), 3-D geometries for massive corals were modelled using computer-aided design open-source software, Blender, to resemble as closely as possible the shapes and dimensions of the coral colonies they used (Fig. 3.15). The low Reynolds numbers estimated for their experimental setup indicated laminar flow conditions (∼350-450).

I configured the polyped architecture as hemispherical dimples employed in each of the streamwise and spanwise directions with dimple spacing of approximately 1.2 mm. While I primarily consider effect of dimple depth by changing depth dimple spacing also changes. This is an unavoidable physical constraint, but it is also physiologically realistic. The aspect ratios of dimple depth to dimple diameter implemented here for *L. purpurea* and *P. sinensis* are approximately

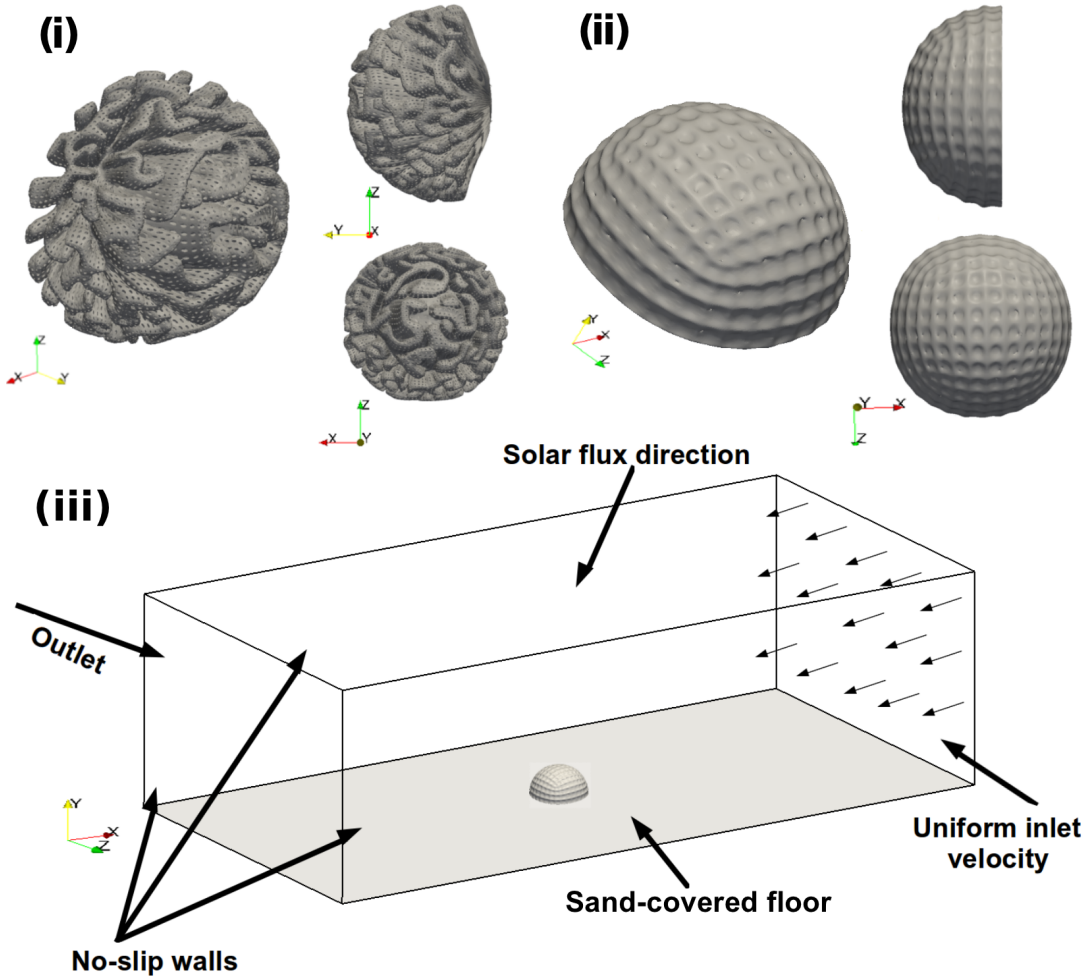

Figure 3.15. Conceptual representations of geometrical characteristics for both model species, *(i) P. sinensis* and *(ii) L. purpurea*, and *(iii)* the experimental setup used by Jimenez *et al.*(2011). Each corals consisted of hemispherical dimples with approximately 400,000 polyhedral computational cells.

0.44 and 0.27, respectively. These morphological attributes of polyps will directly impact a coral's A/V ratio. Despite obvious allometric changes in form during growth (Porter, 1976), the A/V ratio for a smooth coral surface assumes a minimum dependent on the magnitude of the critical dimension. This is the dimension that remains after the surface area is divided by the volume. For instance, a disk-shaped coral with living tissue, $A/V = \pi r^2/\pi r^2 h = 1/h$, and the height of the disk, h, is the critical dimension.

3.3.2 Surface area and volume estimations

The A/V ratio is an essential parameter in determining the thermal and mechanical properties of differently shaped and sized morphologies and has many other important implications in biology (e.g. metabolisc scaling with body size). Indeed, the relationship between coral body size and metabolic rate has been of particular interest to ecologists and marine scientists (Gould, 1966; Loya et al., 2001; Patterson, 1992a). Monitoring of the surface area and volume of corals is also useful for assessing growth, and can thereby provide insight into the health of coral reef ecosystems (Vago et al., 1994).

The suite of image analytical techniques used to estimate the physiological parameters of corals (mainly surface area) by coral biologists has advanced significantly in the last decades (Edmunds and Gates, 2002; Holmes, 2008; Jones et al., 2008). This suite of techniques includes wax dipping which provides very good estimation of the surface area of coral skeletons along with external coralites, regardless of the morphological complexity of the coral colony being studied; whereas X-ray computed tomography (CT) scanning provides the highest resolution surface area estimates by detecting surface features smaller than 1000 μm^2 (Veal et al., 2010). In contrast to these previously developed methods, here I estimate both the surface area and volume of coral models simultaneously using a cell looping technique that calculates and increments cell area and volume using a mesh-based implementation. This method has low error rates associated with complex morphologies. The theoretical calculations of surface area and volume of a simple hemispherical and cylindrical shape coral were validated against our numerical estimation.

3.3.3 Numerical simulations

The magnitude of net irradiance absorbed by an area of coral surface is a function of the coral's spectral properties such as reflectivity and transmissivity which, in turn, is determined predominantly by its darkness and orientation to the heat source's position. The absorptivity value for both coral species studied here were set at 0.5 following the experimental results of Jimenez *et al.* (2011). The thermal conductivity of seawater was 0.62 W m^{-1} K^{-1}, the tissue (mesoglea) was set to approximately 0.22 W m^{-1} K^{-1} (Joshi, 2013), and the skeleton (aragonite) was set to 2.1 W m^{-1} K^{-1} (Ong et al., 2012). The heat balance of the coral then modelled as a function of the losses from convection into the surrounding water, conduction from the tissue into skeletal layers, and the emission of heat radiation. These computed values of absorbed net irradiance were subsequently converted into volumetric heat flux values via the energy term (Equation 2.33), thereby taking into account both the gains as losses of heat at the coral's surface.

Boundary and initial conditions were also set to closely resemble the experimental conditions set by Jimenez *et al.* (2011). Consequently, fixed-value boundary conditions for superficial velocity of 0.01 m s^{-1} was applied at the inlet. A zero-gradient boundary condition constrains the normal gradient of the boundary patch to zero, while the slip boundary condition sets the normal velocity component to zero. The pressure at the inlet of the apparatus was fixed at the zero gradient condition. The pressure at the outlet was fixed at the reference pressure, while the outlet velocity was fixed at the zero gradient. The velocity and pressure at the domain sides was fixed at the slip boundary condition. The initial and boundary conditions for velocity, pressure, and temperature are shown in Table 3.9.

Table 3.9. Initial and boundary conditions used to model conditions of the apparatus used by Jimenez *et al.* (2011).

Parameter (units)	Initial value	Surrounds	Floor	Inlet	Outlet
p (kg m^{-1} s^{-2})	0	S	ZG	ZG	FV
u (m s^{-1})	0.01	S	ZG	FV 0.01	ZNG
T (K)	298	S	FV	FV	ZG

*S: slip, ZG: zero gradient, ZNG: zero normal gradient, FV: fixed value

The governing equations of fluid flow and heat transfer along with the aforementioned boundary conditions were solved numerically using the control volume in the computational domain using the Finite Volume Method (FVM) (Ferziger and Perić, 1999). The pressure-velocity coupling were resolved using the SIMPLE (semi implicit method for pressure-linked equations) algorithm which calculates pressure based on the velocity components by applying an iterative procedure coupled with the Navier-Stokes equations. The resulting system of algebraic equations is solved using the Gauss-Seidel iterative technique, with successive over-relation to improve the convergence time. A grid sensitivity analysis based on Richardson Extrapolation which aims to reduce truncation error and determine grid independent solutions were performed previously (Ong et al., 2012). The mesh near the coral was finer than anywhere else in the domain in order to adequately capture the momentum and thermal boundary layers. I used two types of grids, predefined block structured hexahedral and polyhedral, to represent both computational and coral domains with approximately 900,000 cells each with a constant time step. Further refinement of number of cells would likely have had little impact on the overall results. To simulate the effects of irradiance across the integrated colony due to polyp depth, I implemented the ray-tracing

technique where the intersecting facet of each polyhedral cell on the coral surface was determined using Radiance (Ward, 1994c).

3.3.4 Results

3.3.4.1 Analysis of polyp depths (PD) and surface area to volume (A/V) ratios

The predicted surface areas and volumes from the proposed model agreed reasonably well with the theoretical results (Table 6.4) exhibiting low root-mean-square errors (RMSE) between the two measurements.

Table 3.10. Comparison of the actual and estimated surface area and volume

Shape	Size (m)	Actual		Model		RMSE	
		A (m^2)	V (m^3)	A (m^2)	V (m^3)	A (m^2)	V (m^3)
Hemisphere	0.5 ϕ	0.39	0.0327	0.41	0.0331	0.020	4×10^{-4}
Cylinder	0.3 ϕ & 0.3 h	0.283	0.0106	0.262	0.0123	0.021	0.002

The surface area was defined as the entire area of living coral tissue; the volume was the volume of the entire skeleton plus tissue. Small polyps break up the smooth surface, thereby increasing the coral surface area. For massive or rounded coral species whose bases contact the reef substrate, only the upper living surface was used in the calculation of their A/V ratios. The A/V ratio of each of the coral species is plotted here against their polyp depths (Fig. 3.16). These points yield curves that are best represented by exponential functions, where *L. purpurea*: $A/V = 0.33\cdot\exp(0.13\times PD)$ and *P. sinensis*: $A/V = 0.25\cdot\exp(0.21\times PD)$. Note that in general, high A/V ratios tend to have deep polyps, and vice versa.

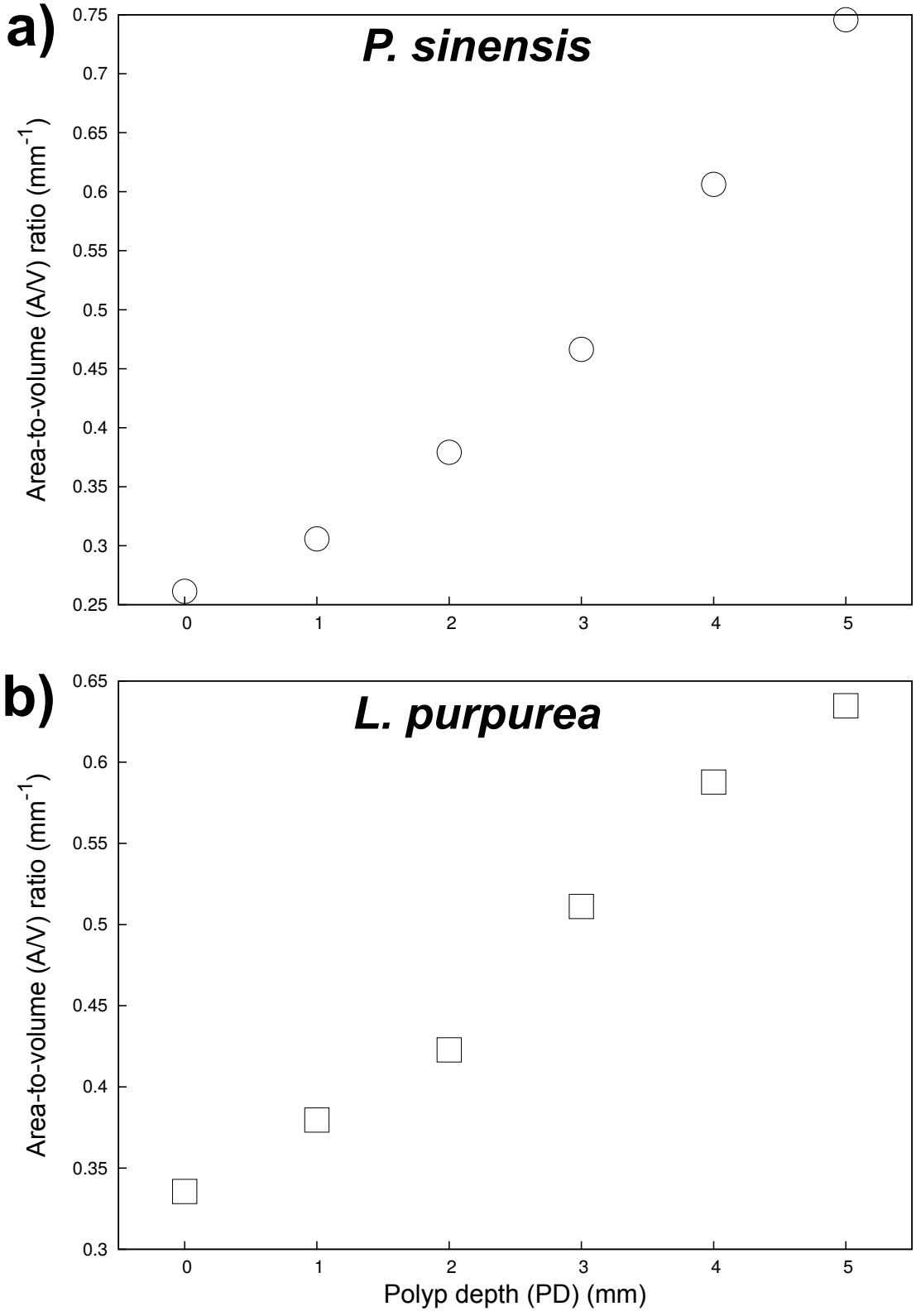

Figure 3.16. The surface area to volume (A/V) ratio against polyp depth (PD) of: *(a) P. sinensis* and *(b) L. purpurea*. These points are most closely described by exponential curves.

3.3.4.2 Coral thermal dynamics and their relationship to PD and A/V ratios

The effects of maximum irradiance or light capture across the colony due to PDs showed that smaller PD colonies were more suited for light interception (Fig 3.17). The difference in irradiance levels between 1 mm and 5 mm PD for *L. purpurea* and *P. sinensis* were 1.2 and 1.4 W m^{-2}, respectively, which is unlikely to cause any significant contributions to the overall surface warming of the colonies.

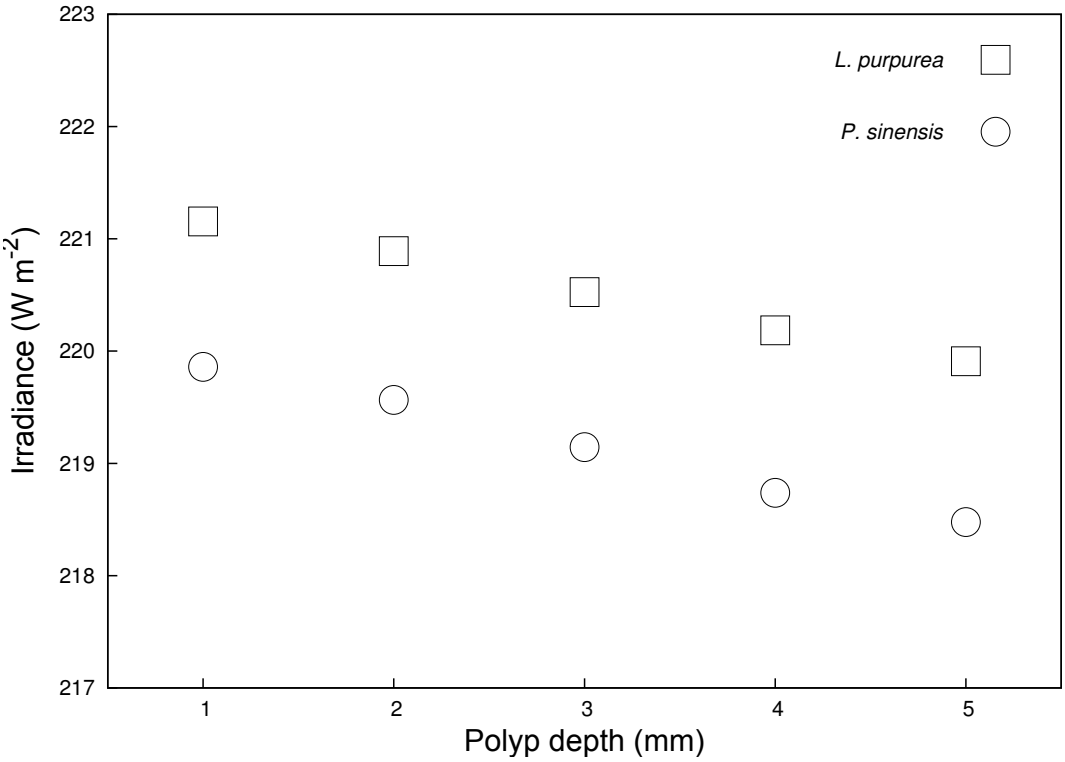

Figure 3.17. Irradiance levels at the microscale polyps due to polyp depth (PD) for *P. sinensis* and *L. purpurea*.

The experimental results of Jimenez *et al.* (2011) and the results of our models were broadly consistent (Fig. 3.18). The greatest differences in temperature rise between 5 mm PD and a smooth surface (0 mm PD) for *L. purpurea* and *P. sinensis* were 0.18°C and 0.19°C, respectively. Similarly, species having large PD and a high A/V ratio were associated with higher surface warming (Fig. 3.19).

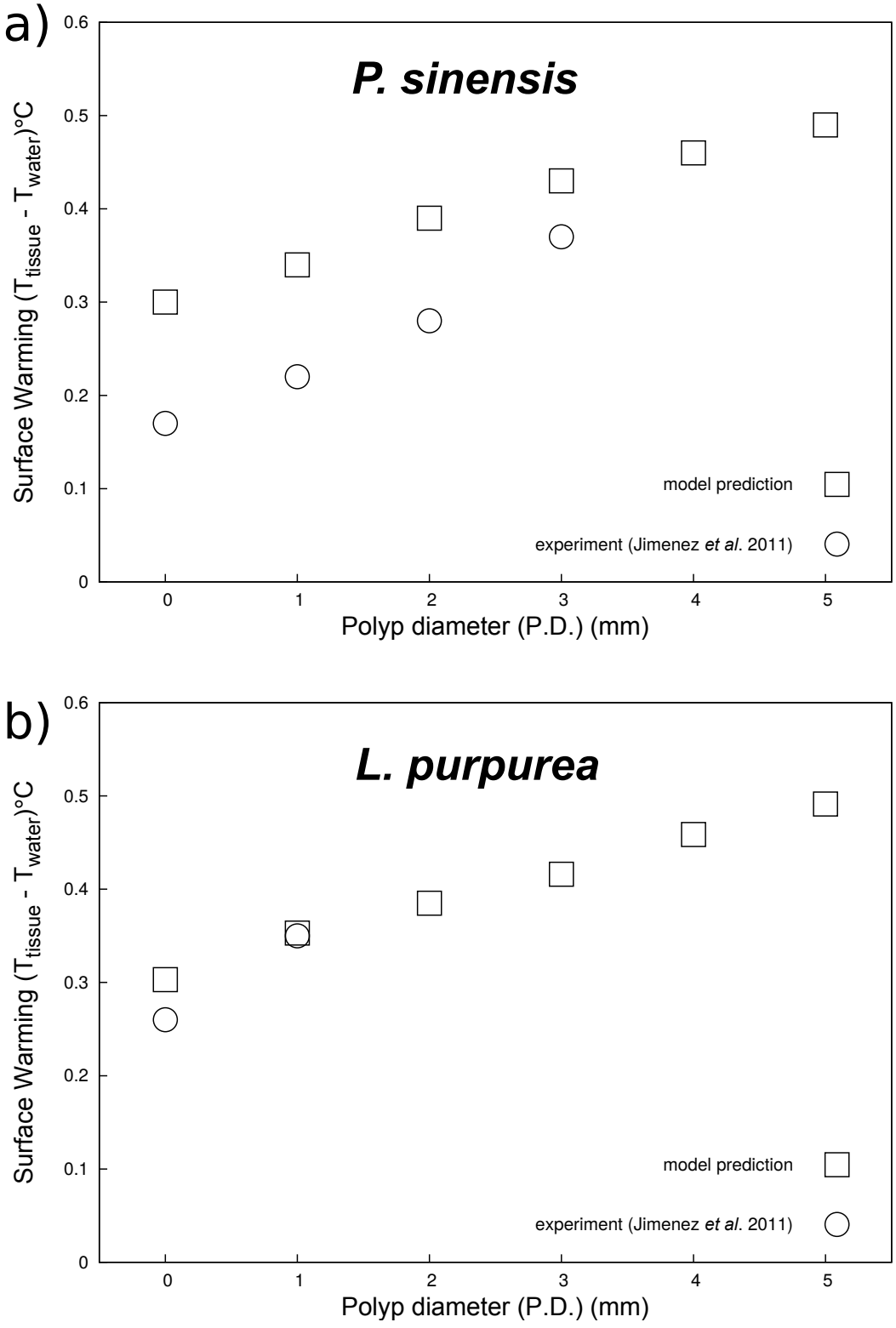

Figure 3.18. Comparisons of observed and modelled warming of polyp surfaces over: *(a) P. sinensis* and *(b) L. purpurea* under a fixed inlet flow of 0.01 m s^{-1} heated to 430 W m^{-2}.

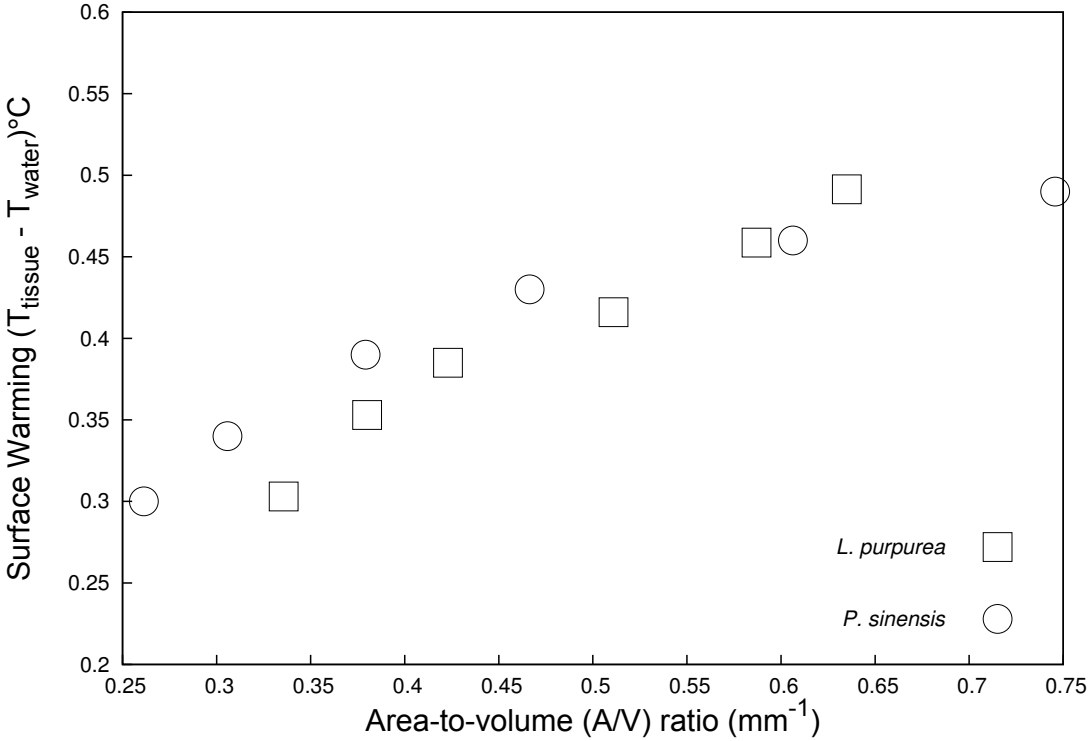

Figure 3.19. The A/V ratio of *P. sinensis* and *L. purpurea* plotted against surface warming under a fixed inlet flow of 0.01 m s^{-1} heated to 430 W m^{-2}.

3.3.4.3 Boundary layer thicknesses

The equilibrium surface warming in *L. purpurea*(∼2 mm PD) and *P. sinensis*(∼1 mm PD) at a flow rate of 0.01 m s^{-1} and ∼430 W m^{-2} were 0.39°C and 0.34°C, respectively (Fig. 3.20). The effective TBL thickness (δ_T) and MBL thickness (δ) of both species increased almost linearly with increasing PD (Fig. 3.20). Temperature differences at the surfaces of these two corals resulted from variations in the thickness of the TBL. In this study, however, the TBL thickness of these two species did not differ substantially. It appears, therefore, that these corals had similar efficiencies regarding convective heat transfer despite their differences in morphology (Fig. 3.21). TBL thickness ranged from 1.0 to 2.5 mm, whereas MBL thickness was approximately 1.5 and 1.8 times thicker in *L. purpurea* and *P. sinensis*, respectively, which indicates viscous diffusion is a more dominant process in this case than thermal diffusion (Fig. 3.22).

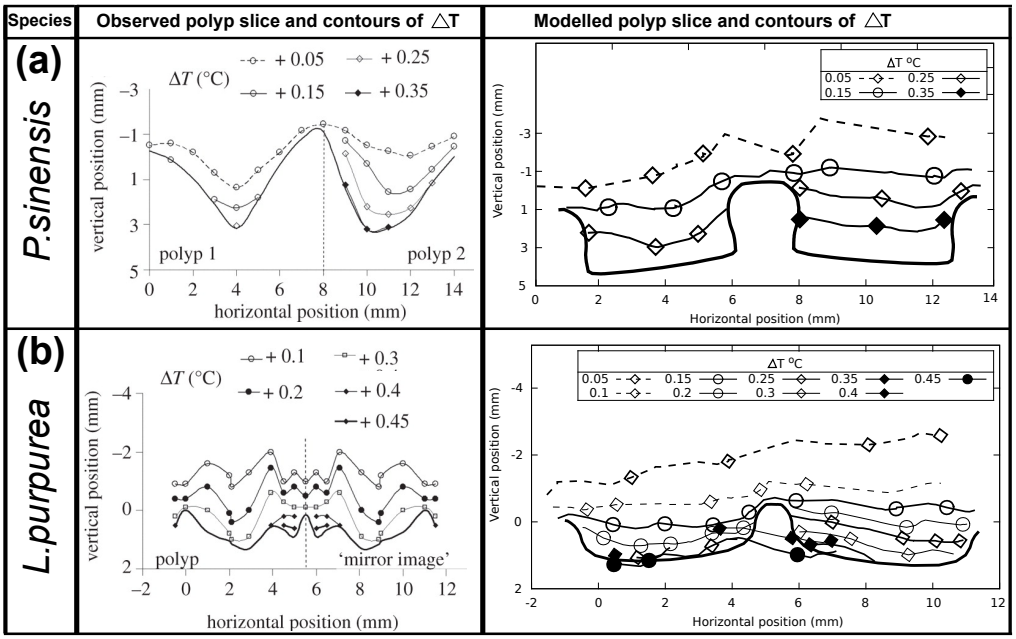

Figure 3.20. Comparisons of observed and modelled contour maps of surface warming over two neighbouring polyps for *(a) P. sinensis* and *(b) L. purpurea*, under flow of 0.01 m s^{-1} heated to 430 W m^{-2}. Observed values obtained from Jimenez et al. (2011).

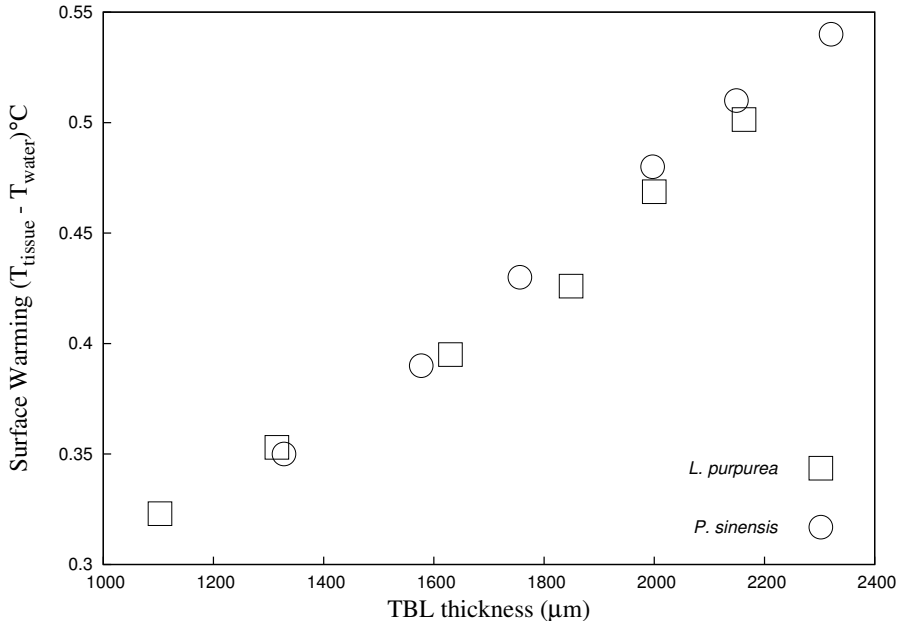

Figure 3.21. Coral surface warming plotted against the thermal boundary layer thickness (μm) under a water flow of 0.01 m s^{-1} heated to 430 W m^{-2}.

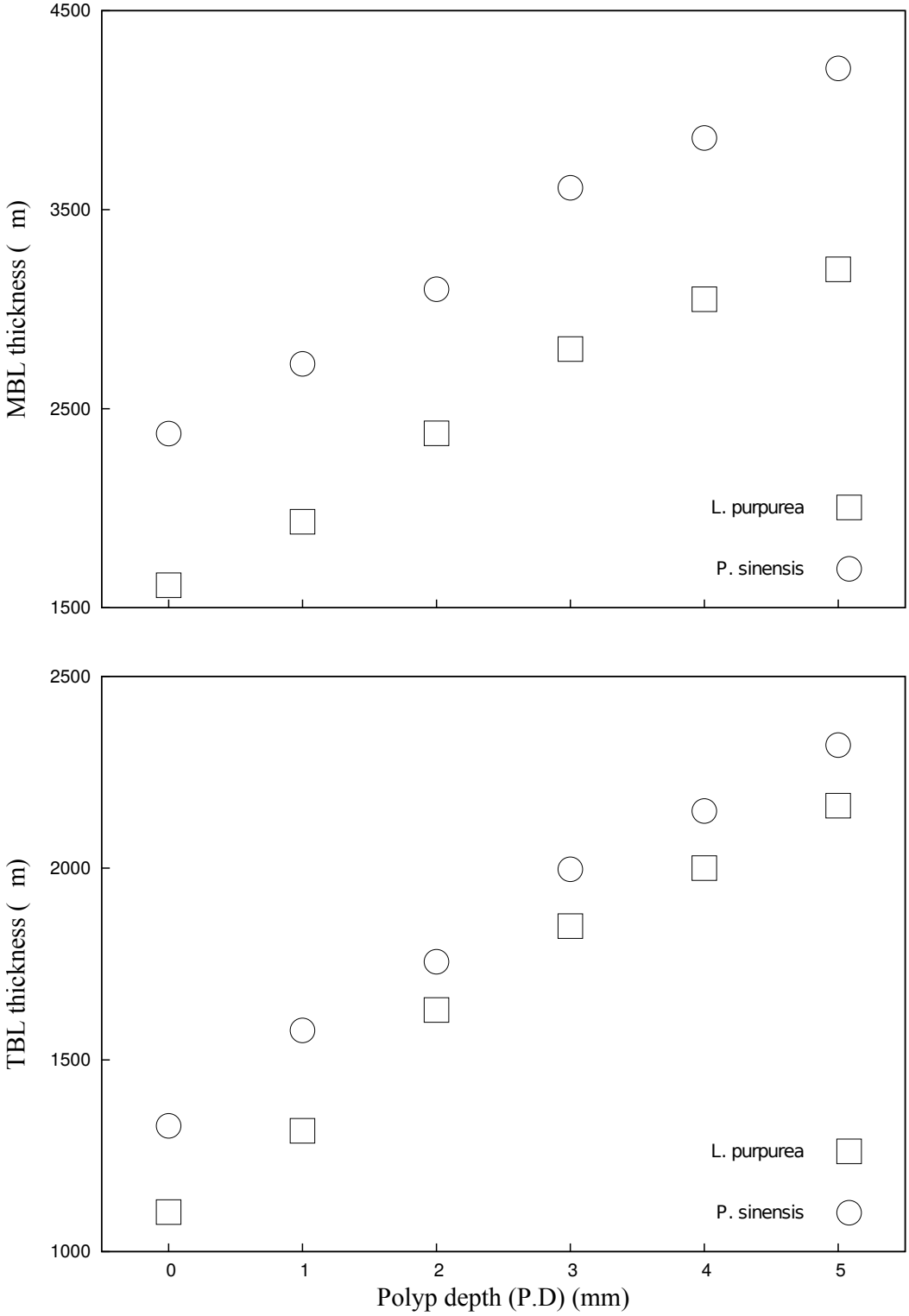

Figure 3.22. The thicknesses of: *(a)* momentum and *(b)* thermal boundary layers plotted against corals (MBL and TBL, μm) over *P. sinensis* and *L. purpurea* under a fixed inlet flow of 0.01 m s^{-1} heated to 430 W m^{-2}.

3.3.5 Discussion

The interspecies differences in coral surface warming modelled here can be attributed to variation in the polyp depth (PD), regularity and/or uniformity, and area-to-volume (A/V) ratio. Polyp depth and polyp spacing had a direct relation to the heat transfer enhancement. Decreasing the polyp depth yields less variation in the heat transfer coefficients across the depth and diameter of the polyp, which in turn, may alter the flow characteristics and increase the heat transfer coefficients. A small increase in polyp diameter and depth can cause an increase in surface area on a micro-topological scale that can be functionally related to the overall A/V ratio. In our model increasing PD was associated with an exponential increase in the A/V ratio which in turn led to a higher surface warming. This result is consistent with a similar report by Ong *et al.* (2012), where the surface warming of a branching coral with a higher A/V ratio was greater than that of a hemispherical coral with a lower A/V ratio. These observations are also consistent with the notion that heat transfer is directly proportional to surface area, whereas heat capacity is proportional to volume. Hence, the A/V ratio would be expected to influence heat accumulation and dissipation. Moreover, our simulation results suggest that while differences exist in surface warming between smooth and dimpled surfaces with varying PD (up to 5 mm), they are not substantially different ($\sim$0.18-0.19°C) and that these differences can be largely attributed to increasing A/V ratios. Therefore, with respect to heat transfer and assuming that heat generated due to physico-chemical conversions is trivial, physiologically integrated massive colonies with smooth-surfaced are likely to replicate similar thermal profiles compared to colonies with polyp-surfaced.

Similarly, species with smaller PDs are likely to better at light interception and capture because of the increase in surface area. This finding also agrees well with theories and field observations that colonies with high A/V ratios typically occur in deep water or other low-light environments and often display more "open" geometries that should also increase the efficiency of light capture, the irradiance intercepted per unit volume. Furthermore, many small polyps should also increase the photosynthetic surface area more than a few large ones, and are therefore favoured the branching morphology with a greater A/V ratio. For massive or flat plate-like species whose bases contact the reef or seafloor, only the upper living surface tissue is used in the calculation of their A/V ratio, hence is less effective in light interception and capture. However, from a biological standpoint, larger-polyped species that have smaller A/V ratios should maximise the efficiency at capturing prey items due to the bigger projected surface area, hence may procure nutrients and energy through symbiosis. The mass diffusive transport in production of energy is affected by flow regime and colony shape and size (A/V ratio) which can be determined from the Sherwood-Reynolds (Sh-Re)

plots; likewise, an analogous principle can be applied to examine heat transfer performance using the empirically derived relationship of the Nusselt-Reynolds (Nu-Re) plots.

Temperature differences may also be attributed to variations in the thickness of the TBL. However, in this study, various TBL thicknesses were associated with similar efficiencies of convective heat transfer. The convection coefficient can be expressed as an inverse relationship of the thickness of the TBL ($h = k/\delta_T$), rearranging Equations 2.3 and 2.2, the warming can be written as:

$$\Delta T = \frac{\delta_T \, I \, \alpha}{k} \tag{3.7}$$

Therefore, for a given irradiance (I), the slope of the relationship between warming (ΔT) and TBL thickness (δ_T) (Fig. 3.21) should be proportional to the coral's absorptivity (α), and inversely proportional to the thermal conductivity of the medium ($k_m = (1-\phi)k_c + k_f$). Thus, thermal properties (conductivity and heat capacity) of both tissue and skeleton as well as the morphological traits (size and shape of the colony) may affect the thermal dynamics in coral microenvironments.

Furthermore, because morphological variation in coral aggregations can be strongly influenced by light/irradiance and water flow rates (Anthony et al., 2004; Berkelmans et al., 2004; Helmuth et al., 1997), the concept of coral thermal microenvironments has profound implications not only in the context of thermal stress but also in relation to many temperature-controlled processes, such as rates of metabolism and growth. For example, skeletons of massive *Porites sp.* are widely used as proxies of past and present SST (Barnes and Lough, 1993, 1999; Barnes et al., 1989). Their rates of linear extension increase by 27% of the mean with each 1°C warming (Lough and Barnes, 2000). However, this relationship between SST and coral growth along spatial and temporal gradients may over-estimate the effects of temperature in coral skeletons where microenvironmental temperatures systematically deviate from SST values. This relationship is expected to become more complex given the expected dependence of coral surface temperatures and pigmentation and area of percolation through openings and increased porosity due to grazers or predators (Ong et al., 2012). By understanding better these relationships between metabolic or growth rates with colony surface warming, the thermal microenvironment of corals may help refine predictions of the effects of climate change on corals.

In the past, gradients of boundary layer conditions for corals have been measured using micro-sensors under laboratory conditions. In contrast, the CFD methods presented here have allowed to generate a more complete representation of boundary layers that could affect the surface temperatures of these corals. Although, laminar boundary layers can readily be measured experimentally, in the presence of turbulence, predicting turbulent boundary layer thicknesses is

more difficult due to the time-dependent variation of the flow properties and smaller thickness and are thus harder to observe experimentally. In addition, the heat transfer-based CFD techniques used here are analogous to mass transfer approaches. As a result, these methods could also be used to estimate the concentration boundary layer for evaluating the diffusion flux of dissolved nutrient uptake by a coral. These CFD type models, therefore, may have much broader application to many different problems related to coral morphology and physiology under a wide range of environmental conditions.

In conclusion, I have shown that numerical results from CFD can help resolve energy transport and TBL conditions. These methods compare well with the experimental study of Jimenez *et al.* (2011). From a heat transfer perspective, physiologically integrated smooth-surfaced massive colonies can be appropriate for modelling the thermal profiles of colonies consisting of modular polyps. Furthermore, the differences in morphological traits between the two species considered here appear equally effective in terms of light modulation at the colony with polyps achieving similar irradiance levels.

3.4 Summary

In this chapter I developed and presented a comprehensive set of CFD validation simulations against the existing experimental data from the literature. The initial simulation predicted the coral surface warming in the steady state and transient irradiance scenarios under a steady laminar and turbulent flow under a controlled laboratory experiments. It also explored the effects of coral surface architectures between smooth and polyped on the overall thermal dynamics in the coral microenvironments.

The results from this chapter showed that coral bleaching predictions should not rely simply upon satellite imagery of SST. Instead, there is much to learn by modelling flow dynamics and heat transfer even within single coral colonies to improve bleaching predictions.

Chapter 4

Solar load model for measurement of spectral irradiance

A subset of the work presented in this chapter is published as follows:

- King, A., B. Mullins, and R. Ong (2011). Prediction of surface warming in corals using coupled irradiance and computational fluid dynamics modelling. *9th Australian Heat and Mass Transfer Conference - 9AHMTC.*

This chapter implements a ray tracing method to quantify the global horizontal irradiance (I_{gh}) due to the direct normal irradiance (I_{dn}) and diffuse horizontal irradiance (I_{dh}). It then uses the resulting data to determine the volumetric heat flux on coral surface to calculate the surface warming due to solar radiation and percolation flow through a porous coral using our previously established computational fluid dynamics (CFD) model.

Analysis of the semi-diurnal sun elevation angles and solar irradiance of the ray-tracing model was conducted against the sky-scanner data for calm or lightly rippled sea-states. The contributions of specific wavelengths including the ultraviolet radiation (UVR, 280 to 400 nm) and photosynthetically active radiation (PAR, 400 to 700 nm) is also included. Furthermore, the variation in downwelling irradiance levels due to water clarity or turbidity, tide, and clouds are investigated.

The technique presented in this chapter considers the basic concept of direct sunlight and diffuse skylight passing through the ocean surface and underwater environment. The analysis of light transmissions due to breaking waves, wakes around corals, splashes from bodies that impact the coral surface are all assumed to be trivial with respect to the overall volumetric heat flux in the CFD energy

equation, and hence are not considered further here. Moreover, to test the solar load model's capabilities of handling diffuse and specular inter-reflection of the light and the material properties, the light distribution of the branching and massive coral surfaces were measured and compared against experimental observations. In addition, the effect of exteriors properties such as coral pigmentation and tissue thickness in modulating the light field within the coral tissues is also investigated.

4.1 A Brief description of the solar load model

The model implementations and mathematical governing equations and further details about the model are given in the Chapter 2 and Appendix 2.

The model was implemented using the backward ray-tracing suite of Radiance codes. Firstly, the scene description for the CIE standard sky distribution depending upon the position of the sun at the given month, day, and time on a 24-hour clock was generated using the GENSKY command. The sky radiance distribution model has the capacity to produce an accurate sky description which can vary from clear to overcast. Here, the state of the sky is denoted by the fraction of the sky obscured by clouds, for instance, cloudy sky had more than 70% cloud cover.

The spectrum from visible to ultraviolet light correspond to the wavelength range of 280-700 nm and a colour range of violet to red. The photometric equivalent of irradiance is illuminance, measured in lumen/m^2 (lux). To calculate the irradiance based on the given coordinate of a point and a vector direction of points and directions, RTRACE traces illuminance from the standard input through the generated scene based on the wavelength traced. The spectral RGB irradiance can be computed as follows:

$$\text{irradiance} = 0.265 \times R + 0.67 \times G + 0.065 \times B \tag{4.1}$$

The attenuation effects of solar irradiance in the underwater environment suggest that not only the intensity of downward irradiance decreases with depth but also the spectral quality. Here I implemented the standard of loss of visible light wavelength in coastal turbid water (Jerlov, 1976) as previously shown in Table 2.1. The local fractions of red green blue (RGB) values of light at each visible spectrum were calculated, then multiplied by the proportion of the ito obtain the remaining luminous absorbed by the colony surface. The calculated RGB values of light was then converted to the total irradiance per meter of water depths.

4.2 Converting photon irradiance to energy irradiance

Light has a wavelength and a frequency that can be considered as a stream of particles, photons, or quanta. The photometric units of light is in moles per square meter per second (mol m^{-2} s^{-1}), where moles refers to the number of photons (1 mol of light = 6.02×10^{23} photons, Avogadro's number). This light measurement term is known as photon irradiance.

Quanta and energy units can readily be interconverted, provided that the wavelength of the light is known. The energy of a photon is related to its wavelength as follows:

$$E = \frac{hc}{\lambda} \tag{4.2}$$

where c is the speed of light (3×10^8m s^{-1}), h is Planck's constant (6.63×10^{-34}J s), and λ is the wavelength of light, usually in nm (1 nm = 10^{-9}m). To solve for the $h\lambda$, the energy of a photon can be written as:

$$E = \frac{1,988 \times 10^{-16} J}{\lambda} \tag{4.3}$$

A photon of 400 nm light contains 4.97×10^{-19} J and a 700 nm photon contains 2.84×10^{-19} J.

For example, 5 μmol of 400 nm light falling on 1 m^2 s^{-1} every second, or a photon irradiance of 5 μmol m^2 s^{-1}. To convert photon irradiance to energy irradiance, firstly, μmoles is converted to moles (1 μmol = 10^{-6}mol): 5 μmol m^2 s^{-1} $\times$ 10^{-6}mol μmol^{-1} results in 5×10^{-6}mol m^2 s^{-1} of photons, or quanta. Calculating the number of quanta from Avogadro's number gives: 5×10^{-6} mol quanta m^2 s^{-1} $\times$ 6.02×10^{23} quanta mol^{-1} = 3×10^{18} quanta m^2 s^{-1}. Each photon or quantum of 400 nm light contains 4.97×10^{-19} J . Thus, 4.97×10^{-19} J quantum^{-1})$\times3\times10^{18}$ quanta m^2 s^{-1} yields 1.5 J s^{-1} m^{-2}. Since 1 J s^{-1} = 1 W; thus, the energy irradiance of 5 μmol of 400 nm is 1.5 W m^{-2}, and, 5 μmol of 700 nm is 0.8 W m^{-2}.

4.3 Solar heat gains and underwater attenuation coefficients

An understanding of the role of solar radiation in coral bleaching is often hindered by the lack of measurements of the contribution of spectral broadband wavelengths in solar radiation, namely ultraviolet radiation (UVA, 315 to 400 nm; and UVB, 280 to 315 nm) and photosynthetically active radiation (PAR,

400 to 700 nm). Unlike, sea surface temperature (SST), which can be monitored remotely using satelites and continuously recorded using in-situ sensors, solar radiation measurements above and below water demand expensive instrumentation, regular calibration, and intensive mainentance (Dunne and Brown, 2001). The interpretation of solar radiation data is also a great deal more complex because it is much more variable than SST in time and space. Temporally, whilst SST changes relatively slowly, underwater solar radiation may vary rapidly due to wave focusing effects and changes in cloud cover. Spatially, SST is uniformly experienced by the coral colony, whilst solar radiation is very different depending on the vertical angle and compass direction of the coral surface, and the underwater light field. The light field (intensity and wavelength) is modified by factors such as the water depth, water quality (suspended and dissolved matter), above-surface weather, and orientation of the direct solar radiation. In shallow water the tidal regime and sea level anomalies play a major role in controlling the water depth and the angle of sunlight reflectance (Alados-Arboledas et al., 2000; Dunne and Brown, 1996, 2001).

The solar load model was implemented based on the backward ray-tracing algorithm in Radiance (Ward, 1990, 1992, 1994a,b,c; Ward and Heckbert, 1992; Ward and Rubinstein, 1988; Ward et al., 1988; Ward and Shakespeare, 1998), that was used as a practical means of quantifying daylight irradiance and applying it in the solar load model as a heat source in the CFD energy equations. Radiance is based on physically realistic and true behaviours of light and is capable of simulating the specular daylighting luminance of the sky by using irradiance caching to efficiently account for the flexible diffuse interreflection and transmittance between surfaces of complex geometries (Mardaljevic, 1995, 2000; Reinhart and Walkenhorst, 2001). The model implemented a solar calculator utility that was used to construct the sun's location in the sky for a given time of day, date, and position. Here, we perform a number of validation studies largely based on the direct and diffuse illuminances under multiple sky conditions simulated with Radiance against the values of sky-scanner data.

4.3.1 Validation of surface solar irradiance

The experimental study of Brown *et al.* (1994) (Brown et al., 1994) took place on intertidal reef flats along the southeast coast of Phuket, Thailand (Figure 4.1). Brown *et al.* (1994) measured the solar irradiance for typical clear sky conditions at Phuket Marine Biological Centre (PMBC) on 4 March 1993 using a Macam Photometric SR 9910 double-grating spectroradiometer fitted with a teflon cosine-corrected 2π collector (Brown et al., 1994). The spectroradiometer was calibrated before use at the ambient temperature (29°C), and the scans ranged from 280 to 700 nm (Brown et al., 1994).

Measurements of solar irradiance were conducted for three variously oriented surfaces (Brown et al., 1994):

- 'horizontal surface' the plane of the cosine collector was oriented parallel to the earth's surface
- 'inclined irradiated surface', at 50° elevation to the horizontal (zenith angle 40°) and 254° compass bearing (west facing)
- 'inclined shaded surface', at 50° elevation to the horizontal and 74° compass bearing (east facing)

Furthermore, the solar load model was compared against the hourly solar elevation data at three different times of the year in order to quantify the effects of seasons, latitude, and time of day on the solar elevation angles and irradiance levels. The measurements of solar elevation angles used here took place at Heron Island (23°26′S) during 21 June, 21 September, and 21 December. The data were provided by the Geoscience Australia: National Mapping Division (http://ga.gov.au/).

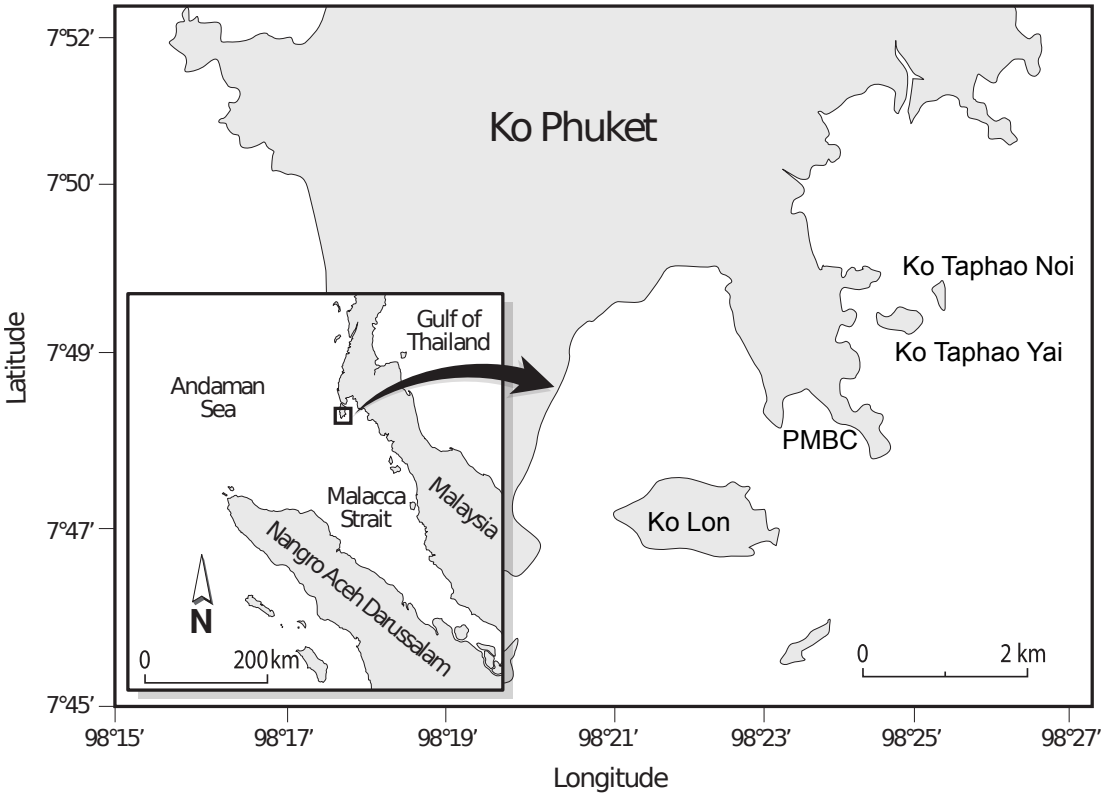

Figure 4.1. Location of southeast coast of Ko Phuket, Thailand, showing the surrounding intertidal reef flats and the location of the Phuket Marine Biological Centre (PMBC)

4.3.1.1 Results and discussions

The semi-diurnal measurements of the global horizontal irradiance levels and solar elevation or altitude angles for PAR, UVA and UVB between the model and the spectroradiometer scans are shown in Figures 4.2 and 4.3. The inclined irradiated and shaded surface irradiance measurements for UVA and PAR are shown in Figures 4.4 and 4.5. There were no available spectroradiometer scans of inclined irradiated and shaded surface irradiance levels for UVB. However, differences in irradiance on differently oriented surfaces were likely to have been trivial and are ignored here.

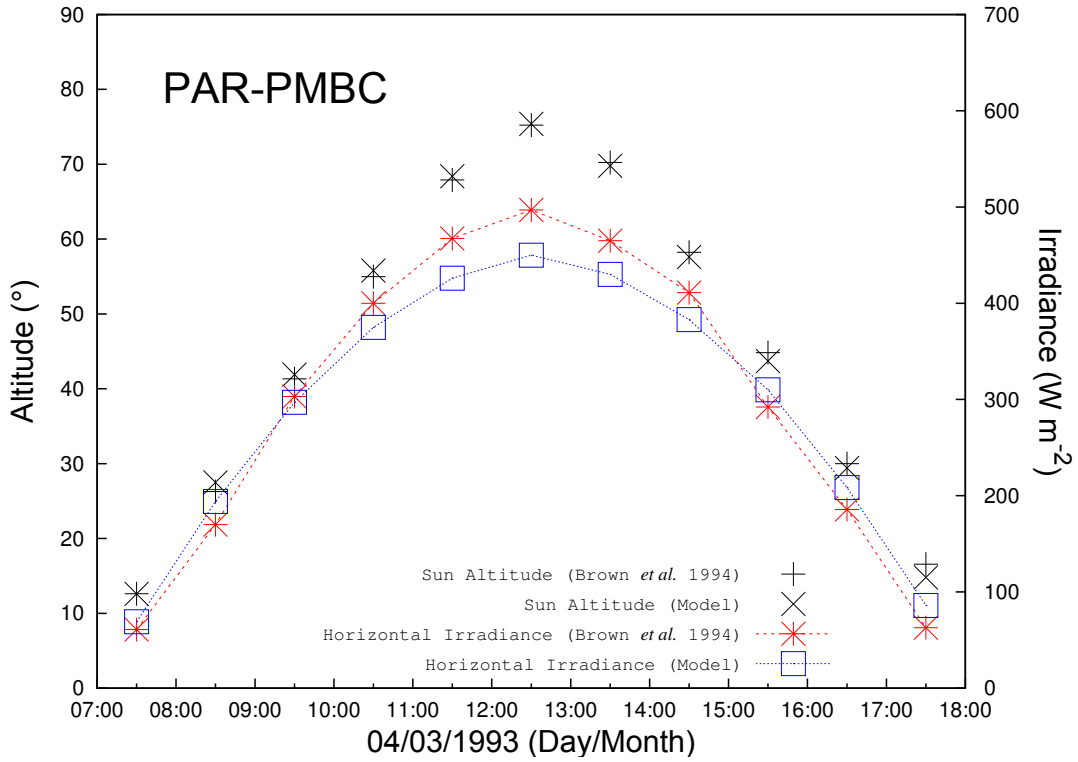

Figure 4.2. Global horizontal irradiance of PAR and sun altitude for typical clear sky conditions at PMBC (4 March 1993)

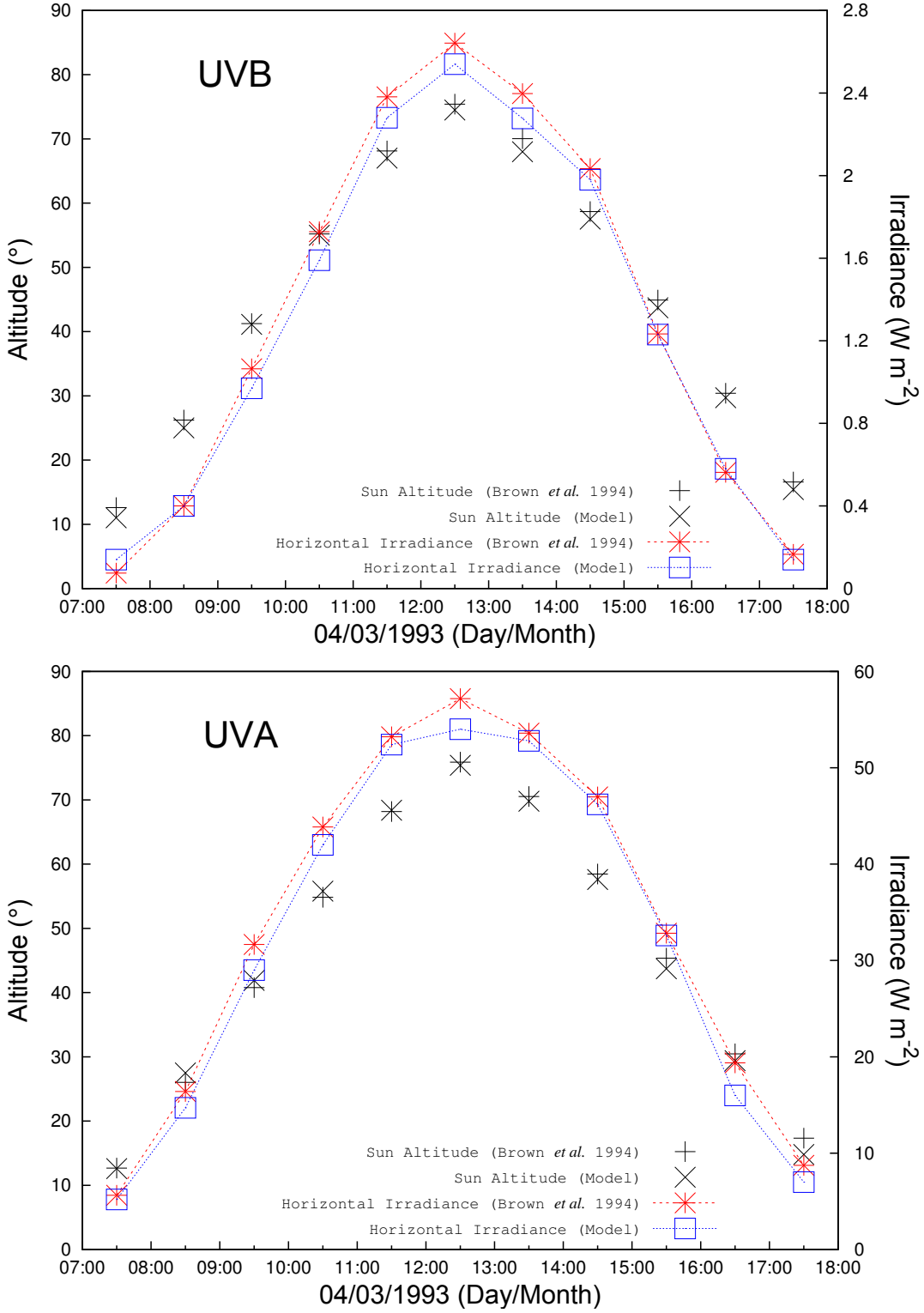

Figure 4.3. Global horizontal irradiance and sun altitude for a clear sky condition on 4 March 1993 at PMBC for short-wave UVB (280 to 315 nm) and long-wave UVA (315 to 400 nm)

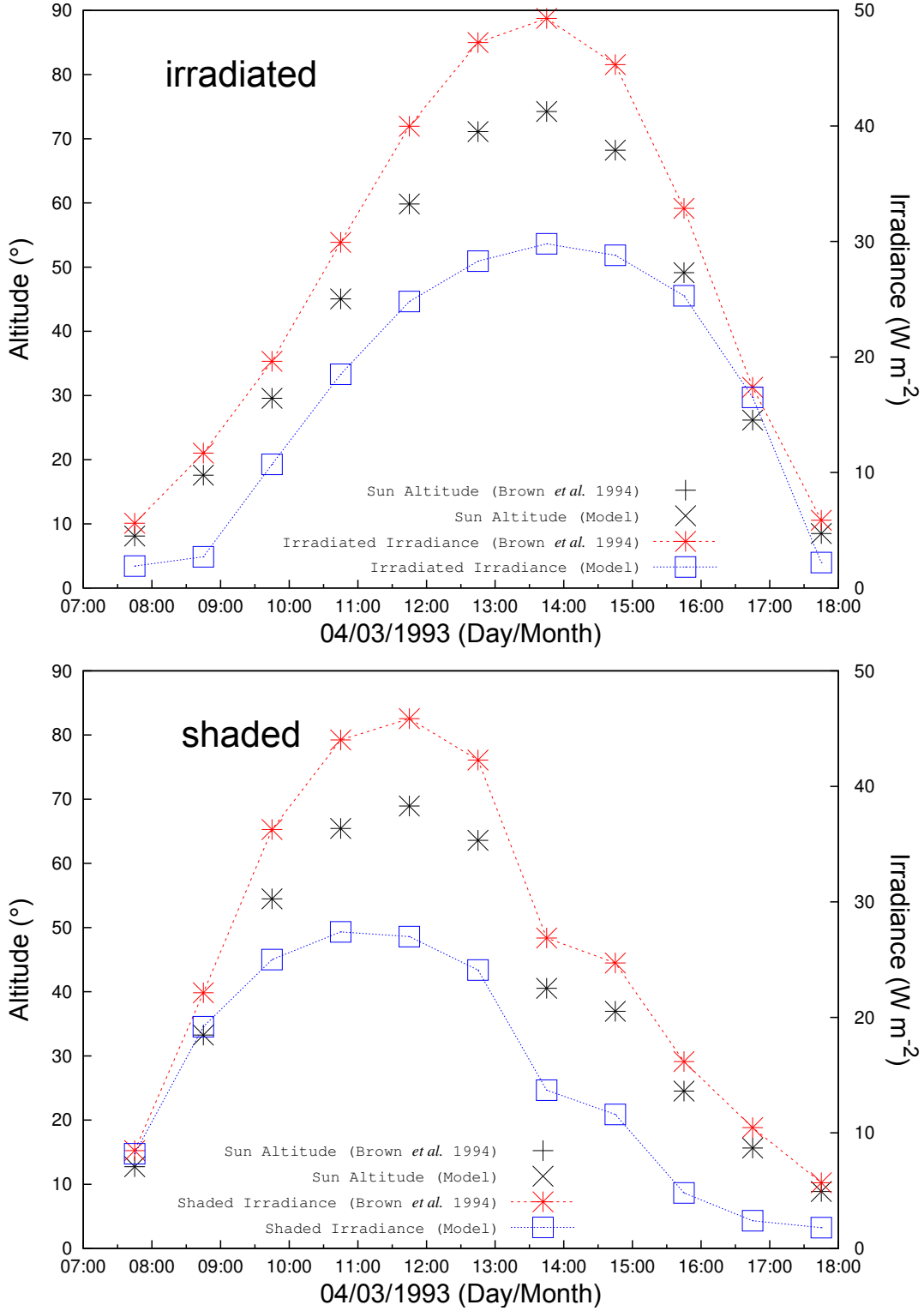

Figure 4.4. Inclined irradiated and shaded irradiances and sun altitude for typical clear sky conditions on 4 March 1993 at PMBC for long-wave UVA (315 to 400 nm)

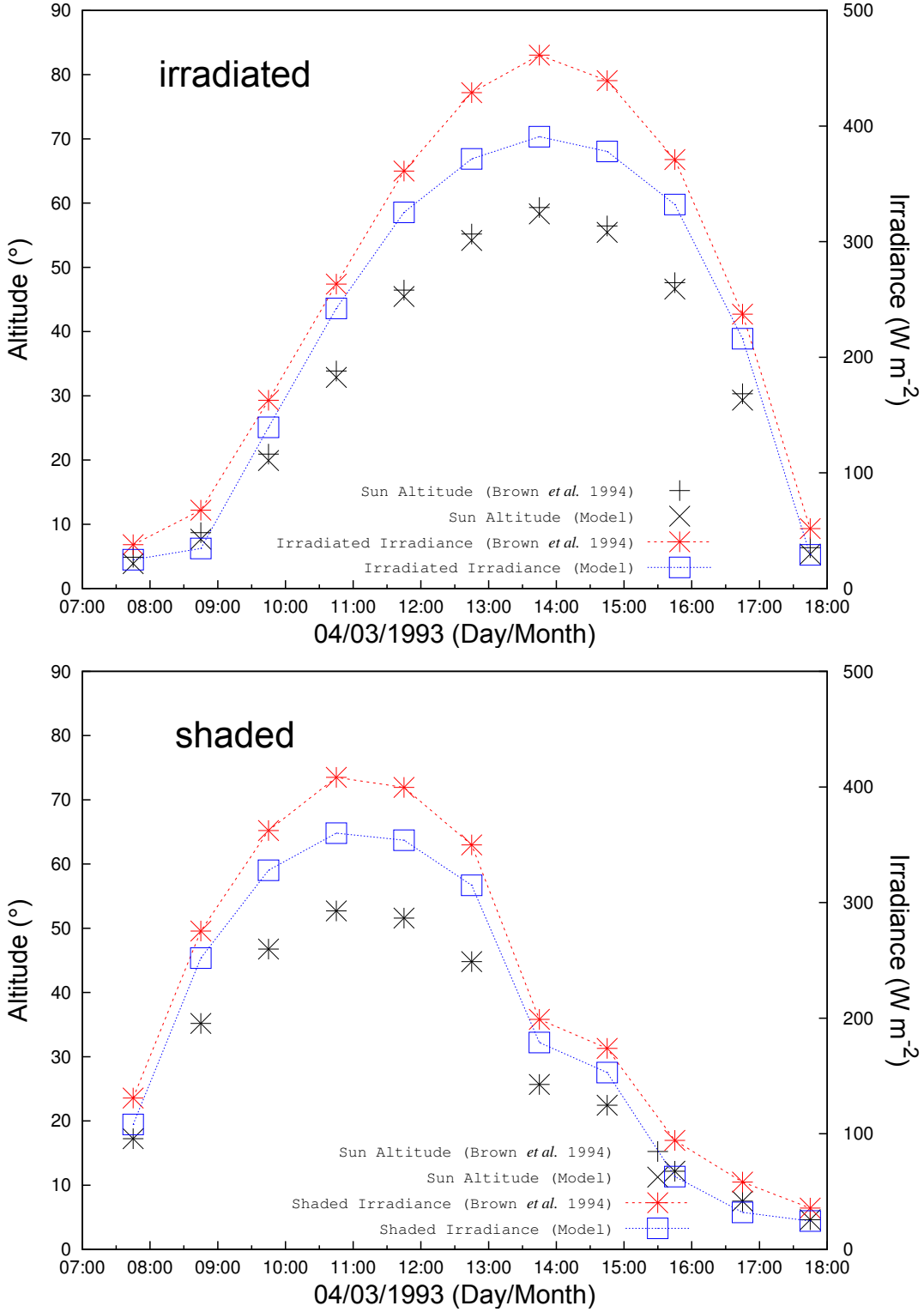

Figure 4.5. Inclined irradiated and inclined shaded irradiances and sun altitude for typical clear sky conditions on 4 March 1993 at PMBC for PAR (400 to 700 nm)

Validations against measurement data showed that the solar load model results agreed very well with experiments, especially for the global horizontal irradiance. The horizontal surface received almost identical levels of UVR in the afternoon as the inclined irradiated surface for solar elevation angles of 65° or less. The measurements also showed stronger irradiation on the inclined irradiated surface than on the horizontal surface for PAR with a maximum difference of ∼20-25% (Brown et al., 1994).

Solar irradiance has many potential targets and mechanisms, for examples, providing radiative heat, desiccating, benefiting or damaging wavelength-related photosystems or cells. The measurements of irradiance on differently oriented surfaces were almost identical with respect to UVR between the horizontal and inclined irradiated surfaces. These empirical results concur with Schauberger (1990) whose work included comprehensive short wavelength UVR irradiance profiles for a single sun altitude angles of 66° (Brown et al., 1994).

Our findings are also consistent with the theoretical physical effects of the differently angled surfaces with respect to an energy beam (Lambert's cosine law), the orientation of the plane of the surface to the natural horizon, and the wavelength-dependent atmospheric scattering of solar radiation. These all determine that an inclined irradiated surface will receive increased direct irradiance but reduced diffuse irradiance compared with a horizontal surface during the afternoon (Brown et al., 1994).

Figures 4.6 and 4.7 show the effect of seasons, latitude, and time of day on the elevation solar angles and irradiance levels, respectively. Between sunrise and sunset, the elevation angle of the sun increases from an angle of zero degrees at sunrise to its highest point at around noon, and then decreases to zero degrees at sunset.

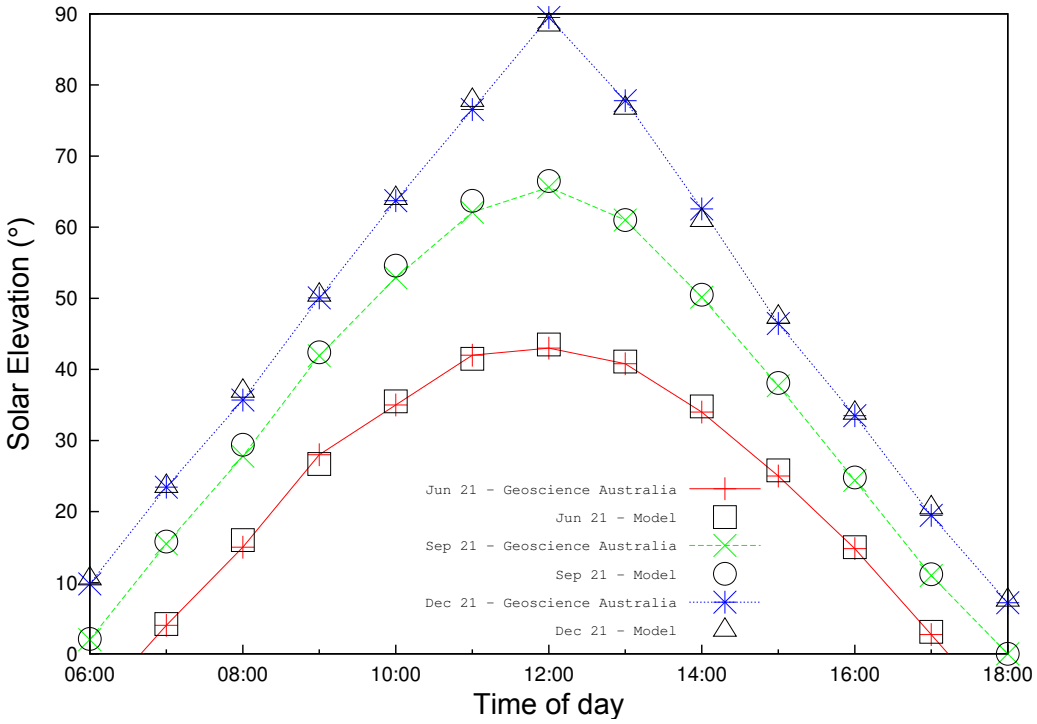

Figure 4.6. Validation of ray-tracing simulation and experimental diurnal solar elevation over the course of three days for a Heron Island, GBR.

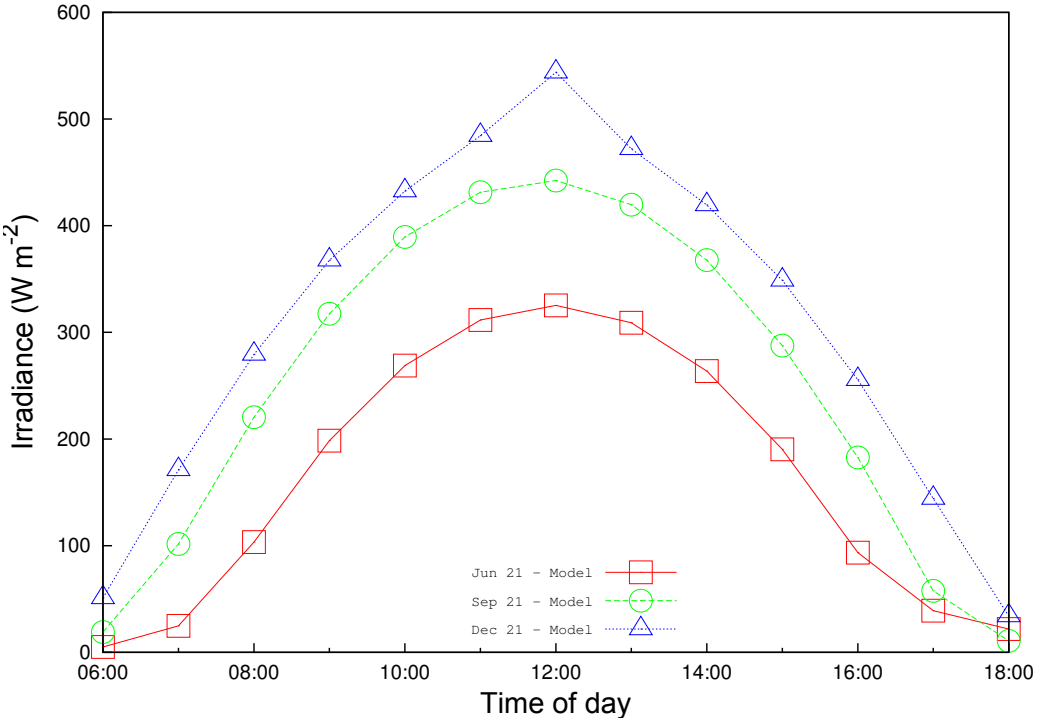

Figure 4.7. Model results of semi-diurnal irradiance levels over the course of three days for a Heron Island, GBR.

4.3.2 Variation of attenuation coefficients

The attenuation of downward solar irradiance in a shallow water suggests that not only the intensity of downward irradiance decreases with increasing depth but also the distribution of spectral RGB quality. The attenuation of light in different ocean regions with variations in their properties governing scattering and absorption was previously shown in Table 2.1. The absorbance and reflectance of direct sunlight varies greatly with the elevation angle of the sun, cloudiness and sea-state. The amount of reflectance of direct sunlight related to the suns elevation angle for a smooth ocean surface was previously shown in Table 2.3. The local fractions of red green blue (RGB) values of light at each visible spectrum were calculated, then multiplied by the proportion of the loss of light to obtain the remaining luminous absorbed by the colony surface. The calculated spectral RGB fractions due to loss of lights per meter were then converted to attenuated irradiance.

Here we analysed the surface solar irradiance data obtained previously in order to determine the contributions of turbidity and tides to variation in downwelling global spectral irradiance at each of 5 m depths.

4.3.2.1 Cloud cover

Cloud cover affects both the quantity and quality of light reaching the ocean surface by reflecting, absorbing, and transmitting the incoming solar radiation. The study of A. Salih (unpublished) was used to validate the model in accounting for the effect of cloud cover on the irradiance curves. The study was conducted on 2 September 1998 at One Tree Island, Great Barrier Reef (23°30'S, 152°06'E). The metadata of cloud cover for an average semi-diurnal hours was obtained from the Bureau of Meteorology of Australia (http://bom.gov.au/climate/averages/climatology/gridded-data-info/metadata/md_ave_cloud.shtml)

The model results were in reasonable agreement with the measured irradiance and the sun's altitude angle measurements due to the presence of clouds at One Tree Island, Great Barrier Reef (Figure 4.8).

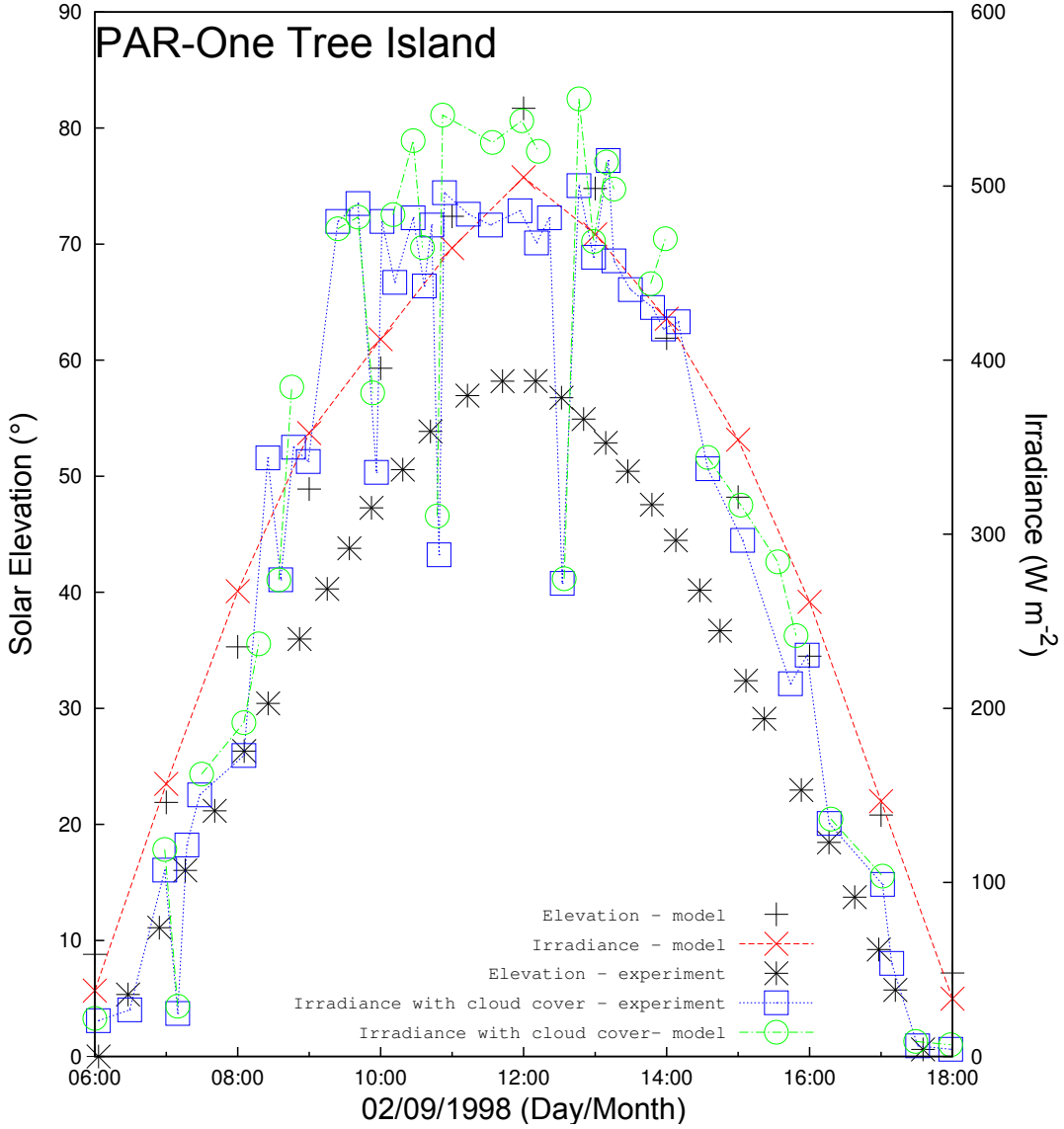

Figure 4.8. Global horizontal irradiance of PAR and sun altitude at One Tree Island (2 September 1998) with the presence of cloud cover

4.3.2.2 Turbidity or water clarity

The work of Dunne&Brown (1996) (Dunne and Brown, 1996) was used to validate the model in terms of the effects of water clarity or turbidity on irradiance per meter depth. Their experiments measured the downwelling global spectral irradiance of solar radiation underwater using scanning spectroradiometry in shallow tropical waters at three locations, including PMBC (Dunne and Brown, 1996).

The ocean water turbidity (inverse of clarity) has been classified into fourteen categories often referred to as Jerlov Water Types (Jerlov, 1976). Previous experiments have identified that the seawater at Ko Phuket was turbid and highly coloured (Brown et al., 1994; Dunne and Brown, 1996, 2001), hence, the water in this study was denoted as Oceanic II Jerlov type (refer to Chapter 2 Section 6).

Vertical attenuation coefficients at any sea surface height can be readily estimated using Table 2.1. To characterise the attenuation coefficients due to turbidity for UVR and PAR (280-700 nm), and $K_d(z, \lambda)$, Table 4.1 reports the fractions of spectral irradiance associated in red, green, and blue portions of the wavelength spectrum per meter of water depth.

Table 4.1. Fraction of spectral RGB due to turbidity in one meter of the least clear Oceanic Jerlov water

λ (nm)	violet (300-400)			blue-green (460-540)			yellow (570-590)			orange (590-620)			red (700)		
	R	G	B	R	G	B	R	G	B	R	G	B	R	G	B
sRGB	127	0	255	127	0	255	127	0	255	127	0	255	127	0	255
Frac. (%)	0.142	0	0.5	0	0.4	0.5	0.286	0.4	0	0.286	0.2	0	0.286	0	0
Spectral light remaining in one meter of the least clear oceanic Jerlov type water															
%	0.053	0	0.185	0	0.024	0.03	0.200	0.280	0	0.157	0.110	0	0.074	0	0

Based on the above table, the total fraction of the red, green, and blue spectrum in one meter of the least clear oceanic Jerlov type water were 0.484, 0.304, and 0.215, respectively. These spectral values were then applied in the previous Equation 4.1:

$$\text{irradiance} = 0.484 \times R + 0.304 \times G + 0.215 \times B \tag{4.4}$$

The pattern of observed irradiance attenuation at PMBC between the Jerlov theoretical calculation, experimental data, and the solar load model results is shown in Figure 4.9.

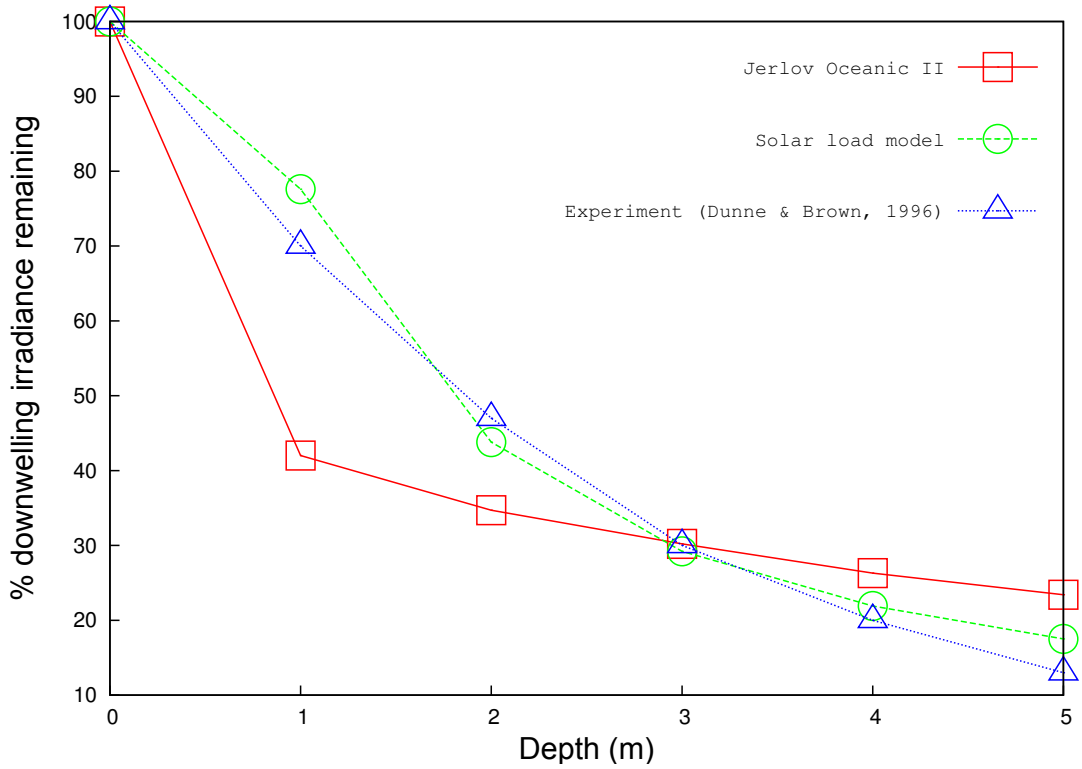

Figure 4.9. Percentage of below water PAR at depths of 1, 2, 3, 4, and 5 m due to turbidity.

4.3.2.3 Tides

The downward flux of solar radiation due to water depth previously was given in Equation 2.40 and Table 2.2 (Paulson and Simpson, 1977):

$$\frac{I_z}{I_0} = R^{(z/\zeta_1)} \tag{4.5}$$

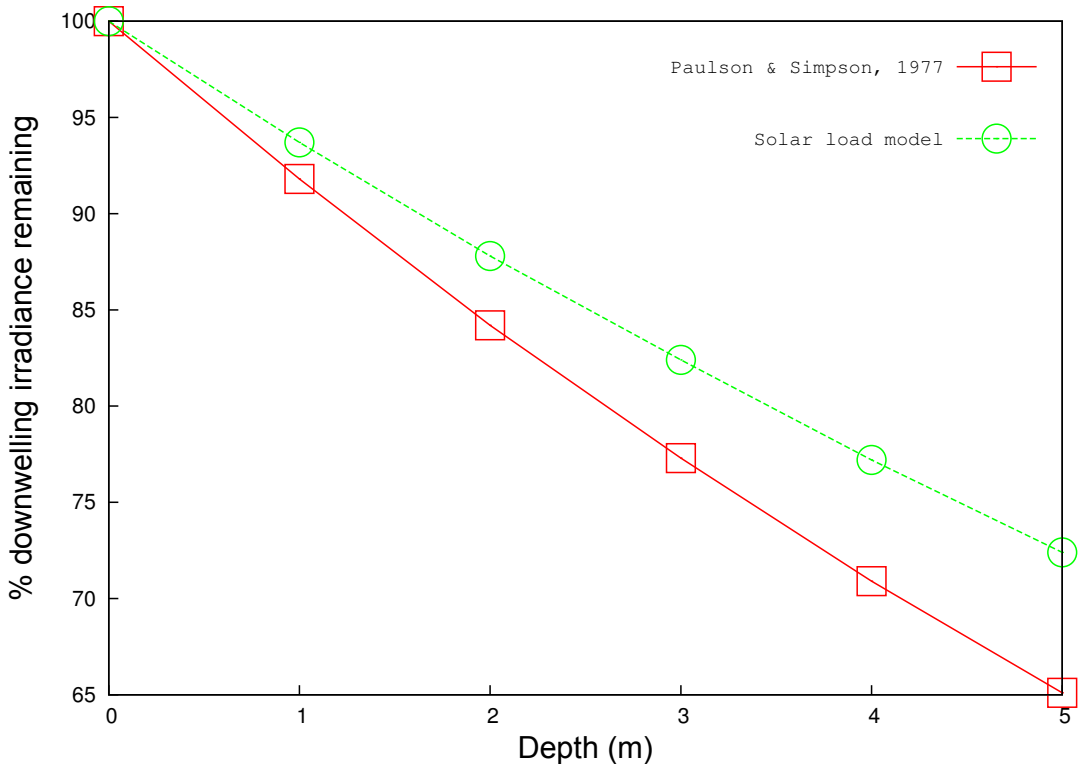

Figure 4.10. Percentage of below water PAR at depths of 1, 2, 3, 4, and 5 m due to tides

The observed irradiance attenuation between the theoretical model of Paulson & Simpson (1977) (Paulson and Simpson, 1977) and the model is shown in Figure 4.10.

4.3.2.4 Sea-state

The directional orientation of sunlight penetrating the water surface varies according to the angles of surface water movements such as smooth or choppy. Values associated with the change in sunlight reflectance with the Sun's elevation angle are listed in Table 2.3.

The measured values of reflectance for both smooth and rough water surfaces based on Fresnel's law (Weinberg, 1976) is shown in Figure 4.11.

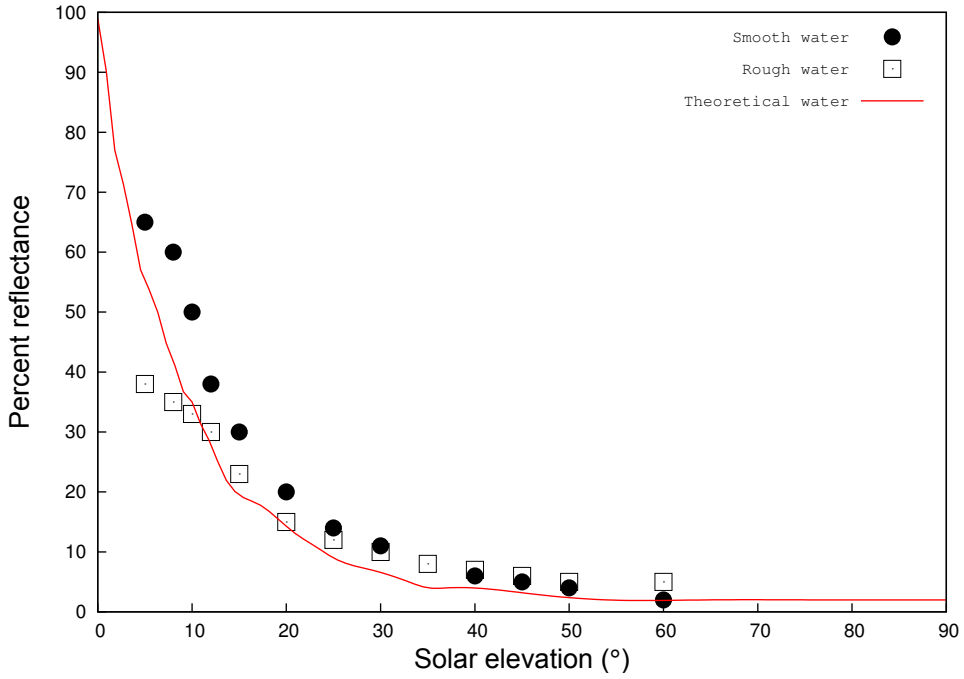

Figure 4.11. Theoretical percentage of sunlight reflected off different water surfaces.

4.3.2.5 Summary

The amount of attenuated irradiance at 1 m below water surface due to water turbidity, cloud cover, tides, and sea-state (calm or choppy) were approximately 75%, 15%, 7%, and 3%, respectively. This findings conformed to a similar experimental study conducted by Anthony *et al.* (2004), where they analysed the contributions of turbidity, clouds, and tides at 1.5 m below water surface were 74-79%, 14-17%, and 7-10%, respectively (Anthony et al., 2004).

It would be possible to devise a more complex model by adding more realistic spatial secondary gradients (such as, cloud thickness, cloud turbidity, inter-reflection of the light between coral branches in branching corals, etc) into the ray-tracing algorithm for quantifying the irradiance as a function of water depth and solar refractions. Although crude, this model has approximated satisfactorily variations in irradiance levels.

Furthermore, the results shown here supports the hypothesis that areas with high turbidity (Goreau et al., 2000; Meesters et al., 2002) and large amounts of cloud cover (Mumby et al., 2001) at the water current-exposed site tend to exhibit less bleaching as compared to the sheltered site (Bayraktarov et al., 2013).

4.4 Validation of micro-scale irradiance

Previously, I demonstrated the potential of the solar load model's ray-tracing algorithm for predicting illumination energy that results from incident solar radiation. Here, the net irradiance received at the water surface was then absorbed by the coral surface area depending on the host's pigmentation (absorptivity and emissivity values). The sun position vector and other illumination parrameters may be applied to the coral surfaces to compute the absorbed net irradiance and subsequent heat flux via a source term in the energy equation. In this study, the absorptivity and emissivity values under visible light (PAR, 400-700 nm) were set to be 0.3 and 0.8, respectively; and 0.01 under UVR (280-400 nm).

In coral species where colony architecture is influenced by light, changes in colony morphology may directly result in variation of absorption and scattering of irradiance levels at the colony level and at the subtissue level through changes in pigmentation (Anthony et al., 2005; Kaniewska et al., 2008, 2011; Muko et al., 2000). To investigate the relative contributions of morphology (at colony and tissue scales) in modulating light levels, the experimental study of Kaniewska *et al.* (2011) (Kaniewska et al., 2011) was used. In this study, the effects of microscale properties of tissues (pigmentation and tissue thickness) on the regulation of irradiance levels within the massive and branching morphologies were also investigated.

Irradiance distribution experimental measurements were conducted in-situ for two coral species with contrasting colony morphologies: *Stylophora pistillata* (branching, ∼30 cm diameter, ∼80 mm height, ∼1 mm polyp size) and *Lobophyllia corymbosa* (massive, ∼30-40 cm diameter), at Heron Island (23°27.625'S, 151°55.759' E), southern GBR, Australia. The experiments used six irradiance points on each colony in order to account for irradiance variation across colony surfaces: three irradiance points on the top of the colony and another three points on the side of the colony (0, 1, and 2 cm) (Kaniewska et al., 2011). To provide a reasonable validations for the experiments, the field data of 3D isosurface irradiance were sampled according to the specified experimental points and exported to graphing packages. The downwelling irradiance was measured with light loggers and spectrometers as photosynthetically active radiation (PAR; 400-700 nm, μmol photons m^{-2} s^{-1}). This was then converted to irradiance (W m^{-2}) using a conversion factor of 4.44 W s μmol $photons^{-1}$ derived from theoretical calculations between 400-700 nm.

4.4.1 Results and discussions

Simulated light distributions across two coral species underscored the differences in colony surface irradiances, showing a slight increase at the amount of PAR

at the surface of branching *S. pistillata* as compared to massive *L. corymbosa*. For *S. pistilata*, the frequency distribution of 14 irradiance ranges (25-800 μmol photons$\cdot$m$^{-2}\cdot$s^{-1}) at the coral surface exhibited a shift toward lower irradiance, where the modal range was 50-150 μmol photons$\cdot$m$^{-2}\cdot$s^{-1}. On the other hand, *L. corymbosa*, tend to shift toward higher irradiance, where the modal range was 400-600 μmol photons$\cdot$m$^{-2}\cdot$s^{-1}. The light distributions are presented as percentages across irradiance categories of the total whole colony PAR level (Figure 4.12). The illustrations depict a distribution map of irradiance levels at top and side views in the colony for each species shown in Figure 4.13.

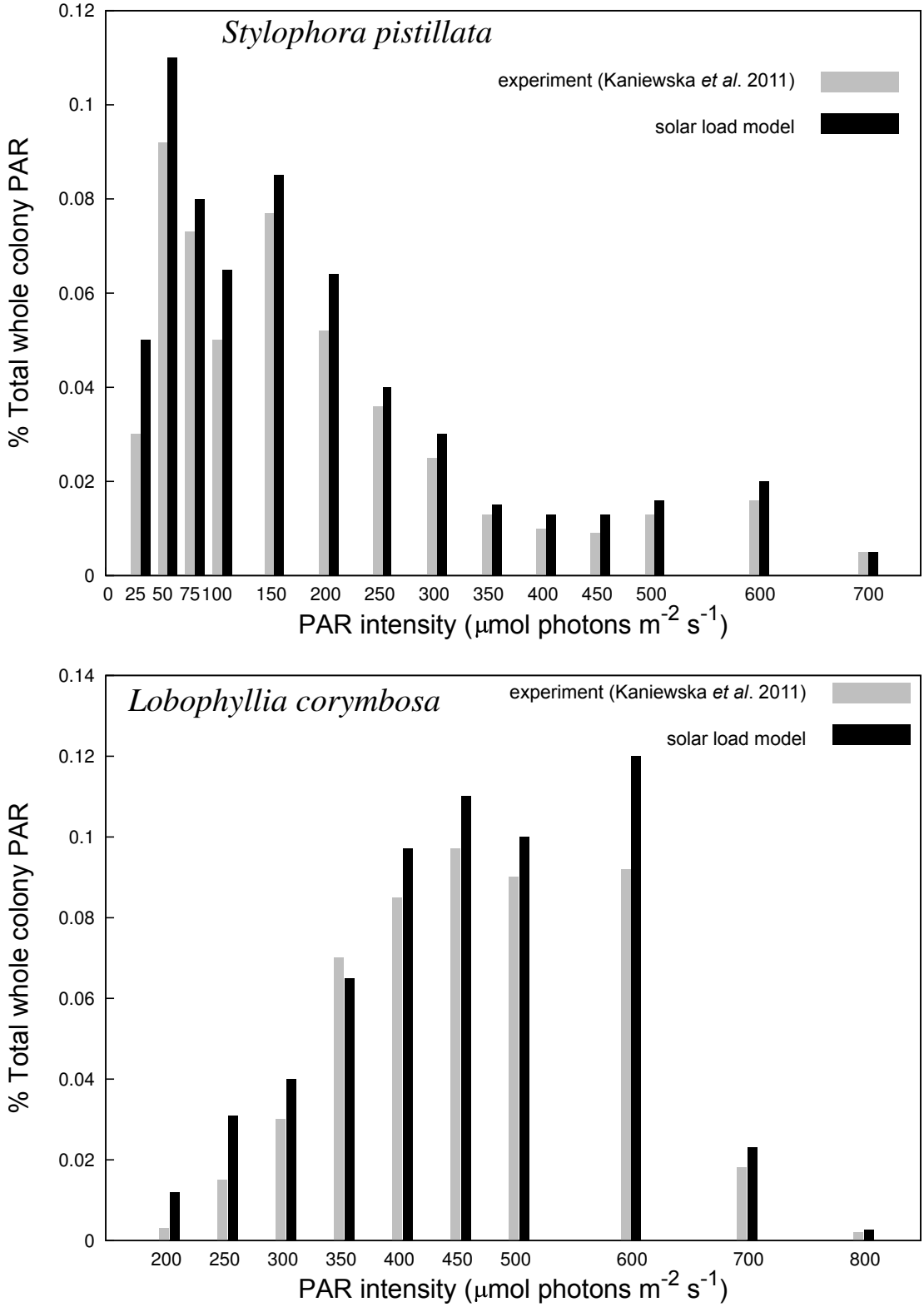

Figure 4.12. PAR distributions, 2 mm into the coral tissue for coral surface irradiance. The light distributions were obtained using the mean daily maximum irradiance for *Lobophyllia corymbosa* and *Stylophora pistillata*.

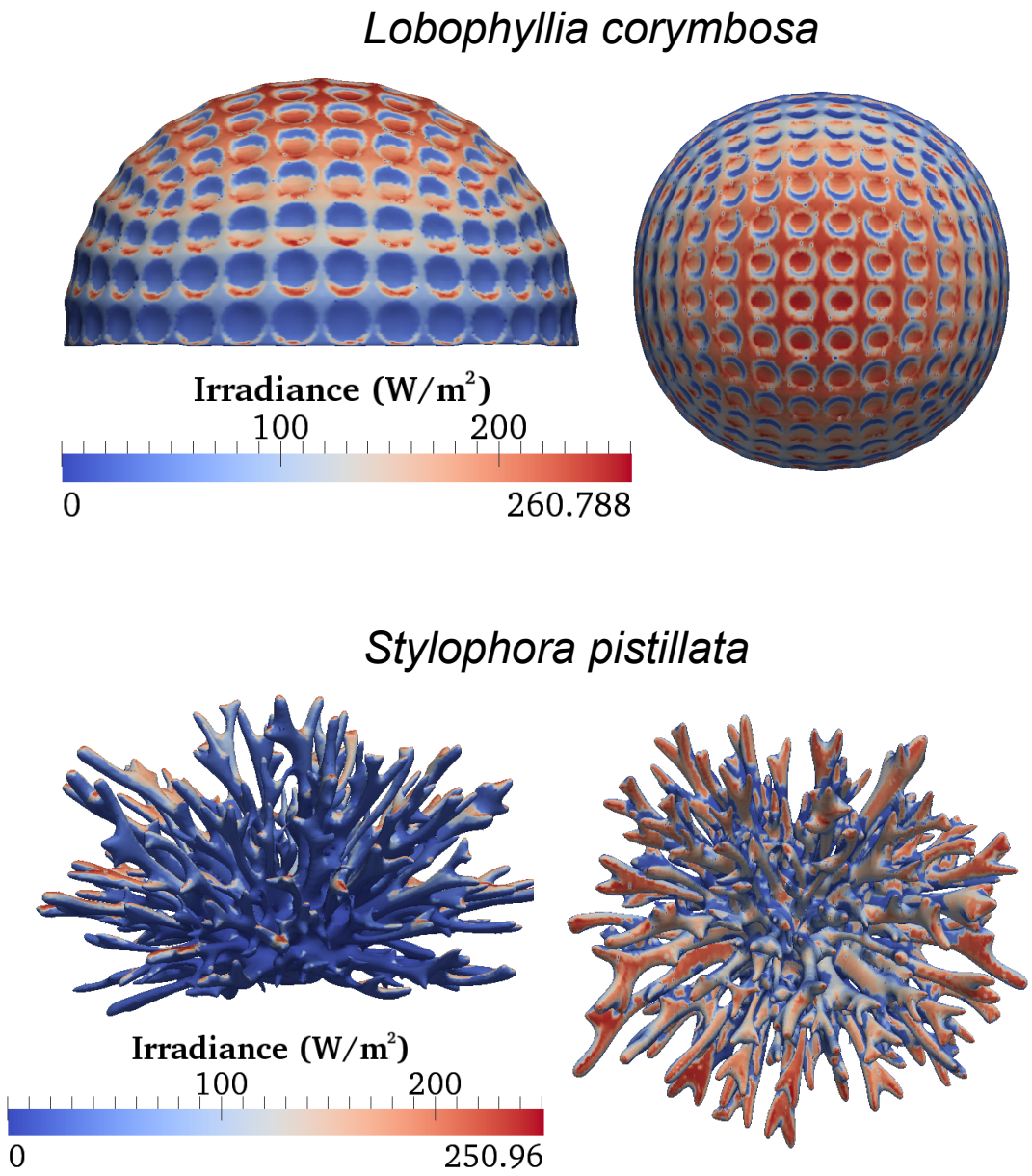

Figure 4.13. Model representations and illustrations of a distribution map of irradiance categories for *Lobophyllia corymbosa* and *Stylophora pistillata*.

Although, there is a difference of the amount of irradiance received between branching and massive colony architectures, however, the thermal effects on the overall coral surface warming is trivial compared to other morphological properties, such as permeability of the tissue layer and skeletal matrix. Furthermore, our results demonstrated that changes to microscale tissue properties (tissue thickness and pigmentation) can modulate the external light environment. The dose

of modal irradiance received on the coral surface due to tissue darkness or pigmentation was more pronounced than for tissue thickness. The results show that corals with thicker tissue received slightly lower irradiance. While these modelled results are consistent with the hypothesis that reduced thickness of the tissue might provide greater photoprotection when corals are exposed to heat (Dimond et al., 2012; Hoegh-Guldberg, 1999b; Kaniewska et al., 2011; Loya et al., 2001), however, these small increases in photo-protection are unlikely to be biologically meaningful. The magnitude of irradiance received in both coral species increased linearly with increasing pigmentations. The irradiance levels in massive coral (*L. corymbosa*) was notably greater compared to the branching coral (*S. pistillata*), which is partly due to the branching morphology versus self-shading due to tissue thickness and tissue properties (Figure 4.14) (Kaniewska et al., 2011).

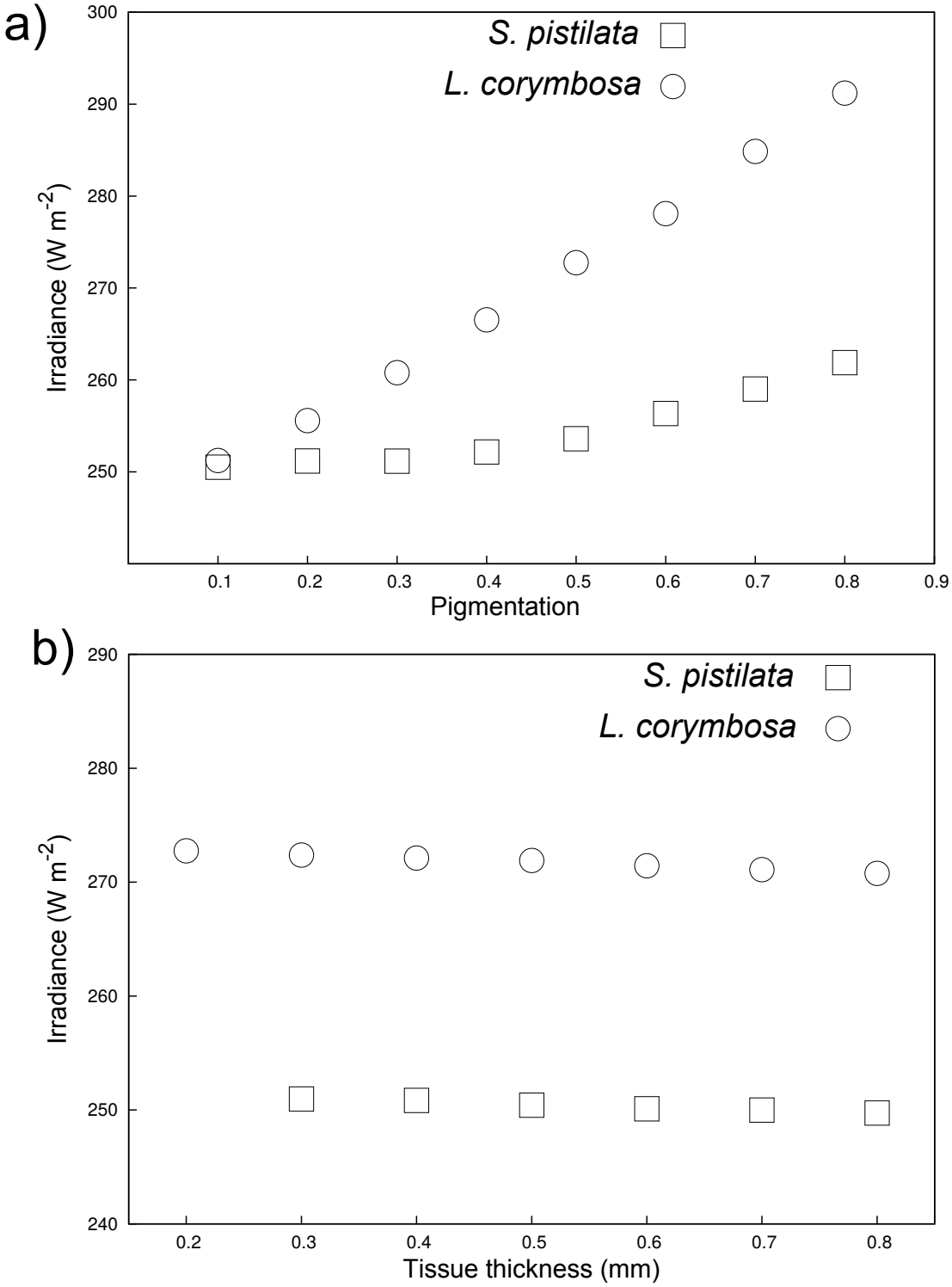

Figure 4.14. The effects of pigmentation and tissue thickness on irradiance distribution for the branching coral *Stylophora pistillata* and the massive coral *Lobophyllia corymbosa*.

4.5 Summary

This chapter utilised the ray-tracing technique to estimate the quantity (irradiance intensity) and quality (wavelength spectrum) of variation in the light field above and below the water surface before subsequently reaching the coral surface. It also analysed the contributions of water turbidity or clarity, cloud cover, tides, and sea-state to variations in irradiance. Furthermore, this thesis analysed the frequency distribution of microscale irradiance across the massive and branching coral species.

Chapter 5

Physical processes on a reef flat

5.1 Introduction

During January-March 1995 on a near-shore shallow reef flat in the Andaman Sea (7°48'N, 98°25'E) colonies of massive coral, *Goniastrea aspera*, bleached on their western sides. During mid May of the same year bleaching began to appear on the eastern faces of the same coral colonies (Brown et al., 2002, 2000). The study indicated that the east surface were not exposed to more solar radiation than the west at the time of differential bleaching was first observed (14 May). This phenomenon also could not be accounted for by genetic differences in zooxanthellae genotypes from the east and west faces of the same colonies leaving the authors to speculate that the west side of *G. aspera* colonies were more thermotolerant because previously they had been exposed to more solar radiation. Arguably, however, since their genotypes did not vary significantly, thus it is most likely that there was no shift genetically although the impact of plasticity could not be ruled out at this stage. Therefore, the "experience-mediated tolerance" hypothesis, suggested by Brown *et al.* (2000), cannot be used solely as the main cause for the differential bleaching pattern. However, the task of identifying the precise causes of the propagation of directional bleaching observed in the validation case study is likely to be complex, especially because the data coverage for the region in which this differential bleaching was observed is sparse and are predominantly for large spatial and temporal scales. Despite the challenges of understanding this differential bleaching empirically, this thesis may provide an indication of the cause of this bleaching pattern by modelling the thermal stress in coral microenvironment.

Firstly I examine the driving mechanism of reef flat currents in the Andaman Sea and establish the influence of the Indian monsoon on reef flat circulation patterns. The modelling approach used aims to employ the ray tracing scheme developed in previous chapters to solve the radiative transfer process of natural

daylight illumination conjointly incorporating the dynamical processes of thermal microenvironment in *G. aspera* colonies with calm to lightly rippled ocean surfaces. The radiative transport process was implemented using a hybrid approach of Monte Carlo ray tracing suite of codes based on known light behaviour, Radiance (Ward, 1994c), with spatially spectral dependent absorption and scattering coefficients of seawater and coral colonies which in turn computes radiant energy falling on coral surfaces according to the Sun's location and atmospheric conditions by interpolating the three component values RGB. In the model of the physical system, the data values representing a single physical parameter - i.e. cloud cover, atmospheric pressure, sea turbidity, SST, sea surface current and alignment, and wind velocity and stress direction - are grouped together to make up a qualitative field that determines the mean variation of the vertical attenuation coefficient of light and a single scattering albedo.

The modelling tools developed in this work can be used to explore the full range of parameters that could trigger asymmetric bleaching scenarios. The case study of Brown *et al.* 2000 was used as a conceptual study, however, the validated results can be widely applied to understand other reef system and other conditions.

5.2 Study site

The validation study was conducted in intertidal reef flats along the southeast coast of Ko Phuket, Thailand, 8°N; 98°20'E, on the border between the Andaman Sea and the Strait of Malacca (Figure 5.1). The reef flats are approximately 200 m wide with a shallow gradient from shore seawards and are characterised by moderate cover (40 to 70 %) of live corals, dominated by massive species of the general *Porites* and *Goniastrea* (Brown et al., 1994). Corals occurring in shallow reef flat areas are often simultaneously exposed to maxima seawater temperatures and supra-optimal irradiances, especially during mid-day spring low tides (Coles, 1997). Constant water flow benefits coral survival (Jokiel, 1978), calcification (Dennison and Barnes, 1988), and photosynthesis (Lesser et al., 1994), while reducing photoinhibition and bleaching (Nakamura et al., 2005).

Ideally, the oceanographic and meteorological data would be obtained from a nearby station. However, the data coverage in this region is very sparse, with the only permanent available station is a tidal station (Ko Taphao Noi, 7°50' N, 98°25.5' E). Although some data do exist, they are predominantly available on large spatial and temporal scales (i.e. intermittent in-situ data provided by Brown *et al.* (1994) (Brown et al., 2002, 1994, 2000; Dunne and Brown, 1996, 2001) and satellite altimetry data). Therefore, it is necessary to extrapolate data as a proxy for single values representing conditions on the reef flat.

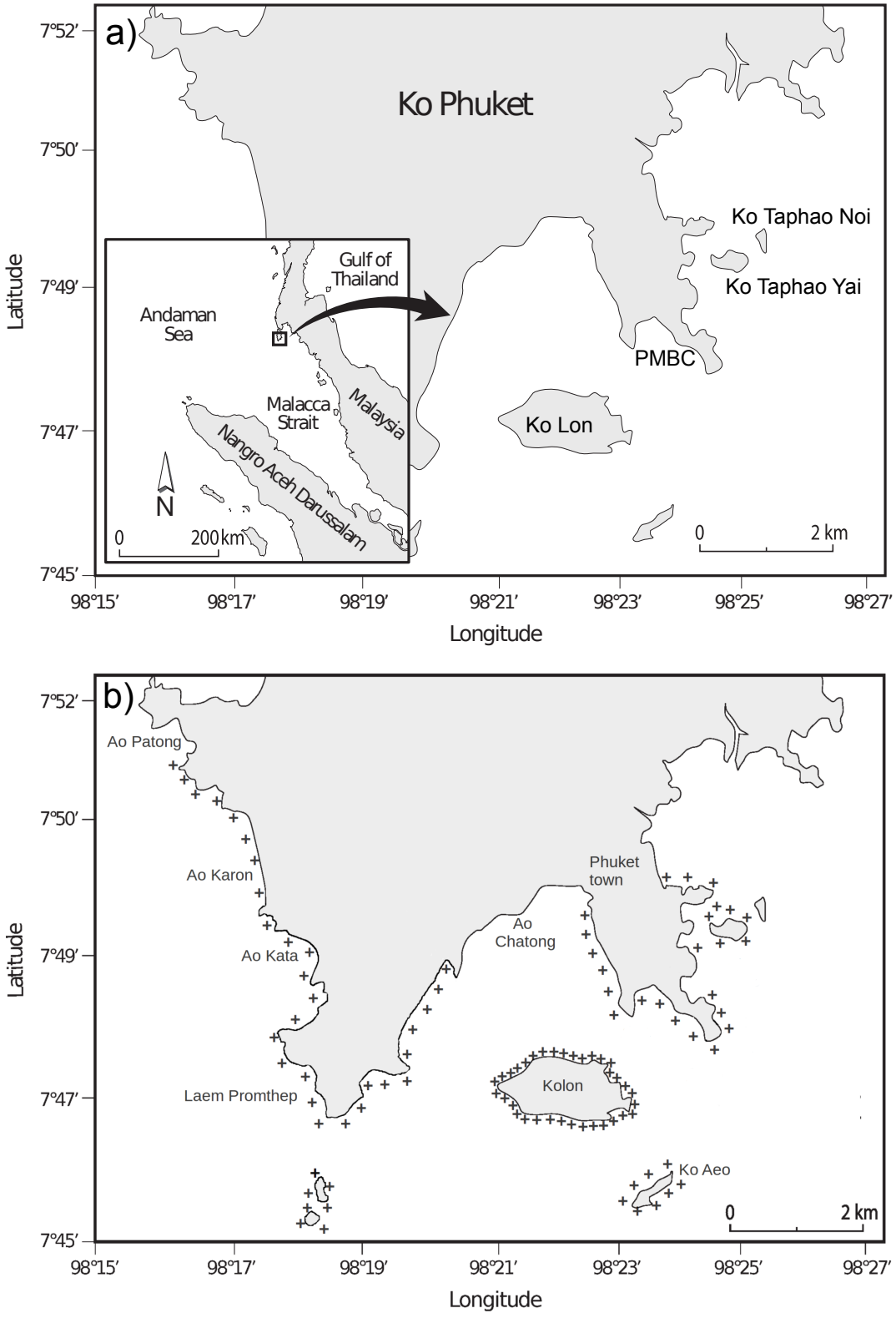

Figure 5.1. Map of the study site where intracolony variation in bleaching patterns were observed. a) Southern part of Ko Phuket. b) Locations of coral reef development around reefs

5.2.1 Description of the reef flat

The distribution of emergent reef flats around Ko Phuket is shown in Figure 5.1. On the exposed west coast of Ko Phuket, intertidal reef flats are sparse and occur only in the most protected corners of deep bays; meanwhile, on the east coast, intertidal reef flats are common in sheltered bays where saltation is not too excessive (Ditlev, 1978). The climate is humid monsoonal, with mean monthly temperature ranges from 29°C in April to 27°C in September (Brown et al., 2002; Dunne and Brown, 1996).

Water flow in many reef flat systems is tidally influenced, resulting in a strong semi-diurnal or diurnal flow pattern (Kraines et al., 1998; Storlazzi et al., 2004). Mesotidal areas - such as in the Andaman and Nicobar Islands and along the north/northwest coast of Sumatra - feature a spring tide range of 1-2 m, while macrotidal ranges are found along the coast of Thailand (∼3 m) and the Mergui Archipelago (>5 m) of Myanmar (Gibson et al., 2007). The monthly sea level fluctuations during 1940-2010 is given in Figure 5.2. The lowest low tides always occur around 06.00 and 18.00 h when insolation is comparatively low. A period of negative sea-level anomalies in 1994-1995 extended over 9 months from May 1994 to January 1995 whereas the more pronounced negative anomalies of 1997-1998 persisted over 11 months from July 1997 to May 1998 (Dunne and Brown, 2001; Gibson et al., 2007). Such negative sea-level anomalies are a regular feature in the Andaman Sea and Indian Ocean (Webster et al., 1999).

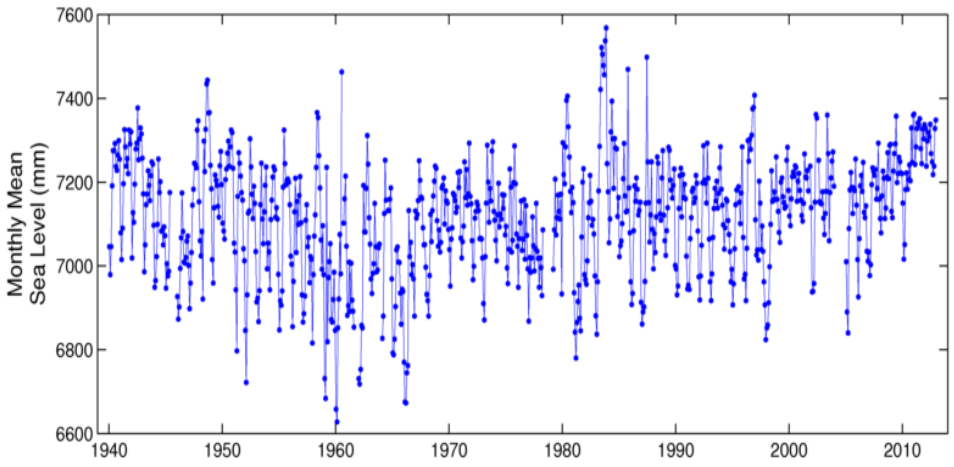

Figure 5.2. Monthly mean sea level of the Ko Taphao Noi tide station during 1940-2010. The data was obtained from Tides and Currents NOAA (http://tidesandcurrents.noaa.gov/sltrends/sltrends_global_station.htm?stnid=545-001).

Circulation of the Indian Ocean is strongly influenced by the seasonal reversal of the monsoon winds and their effect on ocean currents (Gibson et al., 2007; Tomczak and Godfrey, 2003). The current in the Straits of Malacca flows northward during the southwest monsoon. Water is pressed into the east of Ko Phuket, and escapes as a strong coastal current along the east side of Ko Phuket and around its southernmost point (Ditlev, 1978). During the northeast monsoon the current is much weaker and flows southward (Ditlev, 1978). This general trend is complicated by strong tidal currents. The water around the site is typically turbid based on (Brown et al., 1994) and are predominantly type II waters (Jerlov, 1976). Figure 5.4 shows a geomorphological map of typical fringing reef with a distinct topographical zonation: moat, reef flat, reef crest, reef edge and reef slope. The reef flat is usually wide, ranging from 20-300 m.

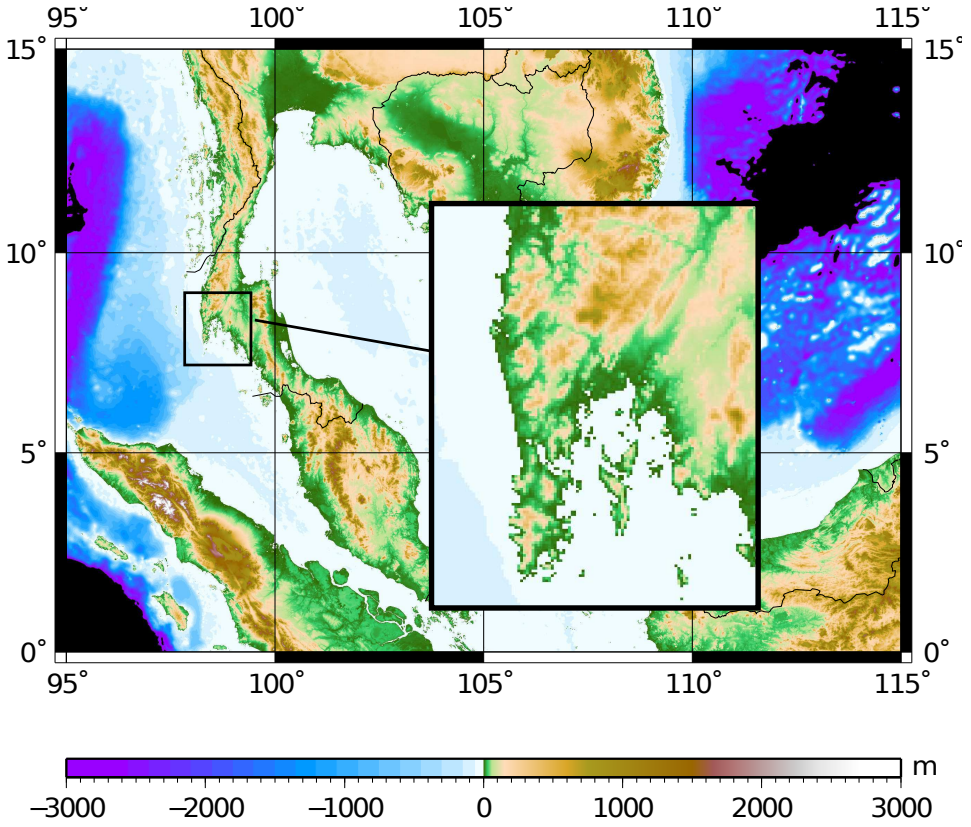

Figure 5.3. A low-resolution bathymetry map of the location. The bathymetric data was obtained from the ETOPO1, which is a 1 arc-minute global relief model of ocean bathymetry. It was provided from the National Geophysical Data Centre (NGDC), http://www.ngdc.noaa.gov/mgg/global/global.html. The bathymetric data was extracted from ETOPO and plotted using the Generic Mapping Tools (GMT, http://gmt.soest.hawaii.edu/).

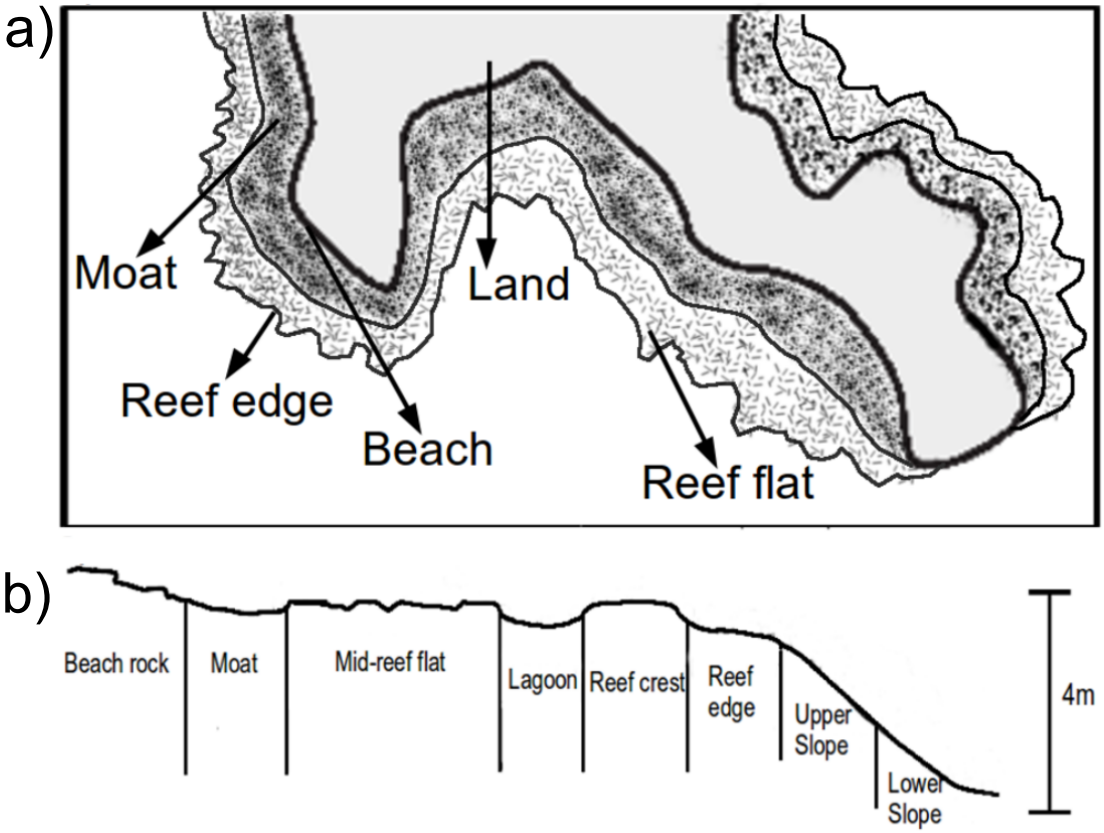

Figure 5.4. a) Geomorphological map of typical fringing reef. b) reef flat anatomy. Adapted from the Center for Coastal Monitoring and Assessment (CCMA, http://ccma.nos.noaa.gov/default.aspx).

5.2.2 Coral cover

Fringing reefs are the dominant reef form at all sites within the Andaman Sea and the coral reefs are not only extensive and largely undisturbed but also boast a relatively high diversity of corals (Gibson et al., 2007). In the Andaman and Nicobar Islands the width of reef flat is considerable, ranging from 200 to 500 m (Gibson et al., 2007). Common coral species found in this zone are *Acropora aspera*, *Porites lutea*, *Goniastrea pectinata*, *Goniastrea retiformis*, *Goniastrea aspera*, *Coeloseris mayeri*, *Favites* spp., *Platygyra sinensis*, *Platygyra pini*, *Favia speciosa*, *Montipora digitata*, and *Pocillopora damicornis* (Phongsuwan, 2002).

5.3 Metocean data during differential bleaching conditions

Fringing reef circulation and current patterns are controlled by the interactions of wind, tide, and wave processes with the reef structure. A comprehensive review of the oceanogaraphy of the Andaman Sea is provided by Varkey *et al.* (1996) (Varkey et al., 1996) and Potemra *et al.* (1991) (Potemra et al., 1991), which described surface circulation in the Andaman Sea as a double gyre with anti-clockwise flow during the northeast monsoon and clockwise flow in the southwest monsoon.

The climate and circulation of the equatorial Indian Ocean is strongly influenced by two monsoonal seasons associated with the dynamics of wind-forced intraseasonal zonal current variability, this phenomenon is known as the Indian Ocean Dipole (IOD) (Rao et al., 2002; Saji et al., 1999; Vinayachandran et al., 1999). The IOD is represented by a simple index consists of time series that describes the difference in SST anomaly between the tropical western Indian Ocean and the tropical south-eastern Indian Ocean, this index is referred to as the dipole mode index (DMI) (Saji et al., 1999). The dipole mode is strongly affected by the monsoonal circulation. The relationship of the DMI to the Indian monsoon variability remains unclear, however, it is clear that the dipole mode has important implications for climate variability in the Indian Ocean (Saji et al., 1999).

The sea surface height (SSH) in the region exhibits high annual variability with considerable anomalies in some years. These anomalies are primarily a result of ocean-atmosphere-land interactions in the Indian Ocean which occur primarily as a result of a reversal in the temperature gradient between east and west basins of the Indian Ocean. During this process, there is substantial warming in the western basin of the Indian Ocean with higher SSH, deeper thermocline and reduced upwelling. In contrast, SSH is depressed in the eastern Indian Ocean and the position of the thermocline is raised with resultant enhanced upwelling (Gibson et al., 2007; Webster et al., 1999).

Estimations for individual variables - heat fluxes, cloud cover, atmospheric pressure, sea turbidity, SST, Dipole Mode Index (DMI), sea surface current and alignment, and wind velocity and stress - were grouped together (Figures 5.5, 5.6, and 5.7). These data sets were obtained from various remote sensing instruments, NCEP-NCAR Daily Reanalysis (http://www.esrl.noaa.gov/psd/data/gridded/data.ncep.reanalysis.html), NOAA Reynolds OI SST (http://www.esrl.noaa.gov/psd/data/gridded/data.noaa.oisst.v2.html), NOAA OSCAR (http://www.oscar.noaa.gov/), and NOAA NCDC (http://www.ncdc.noaa.gov/).

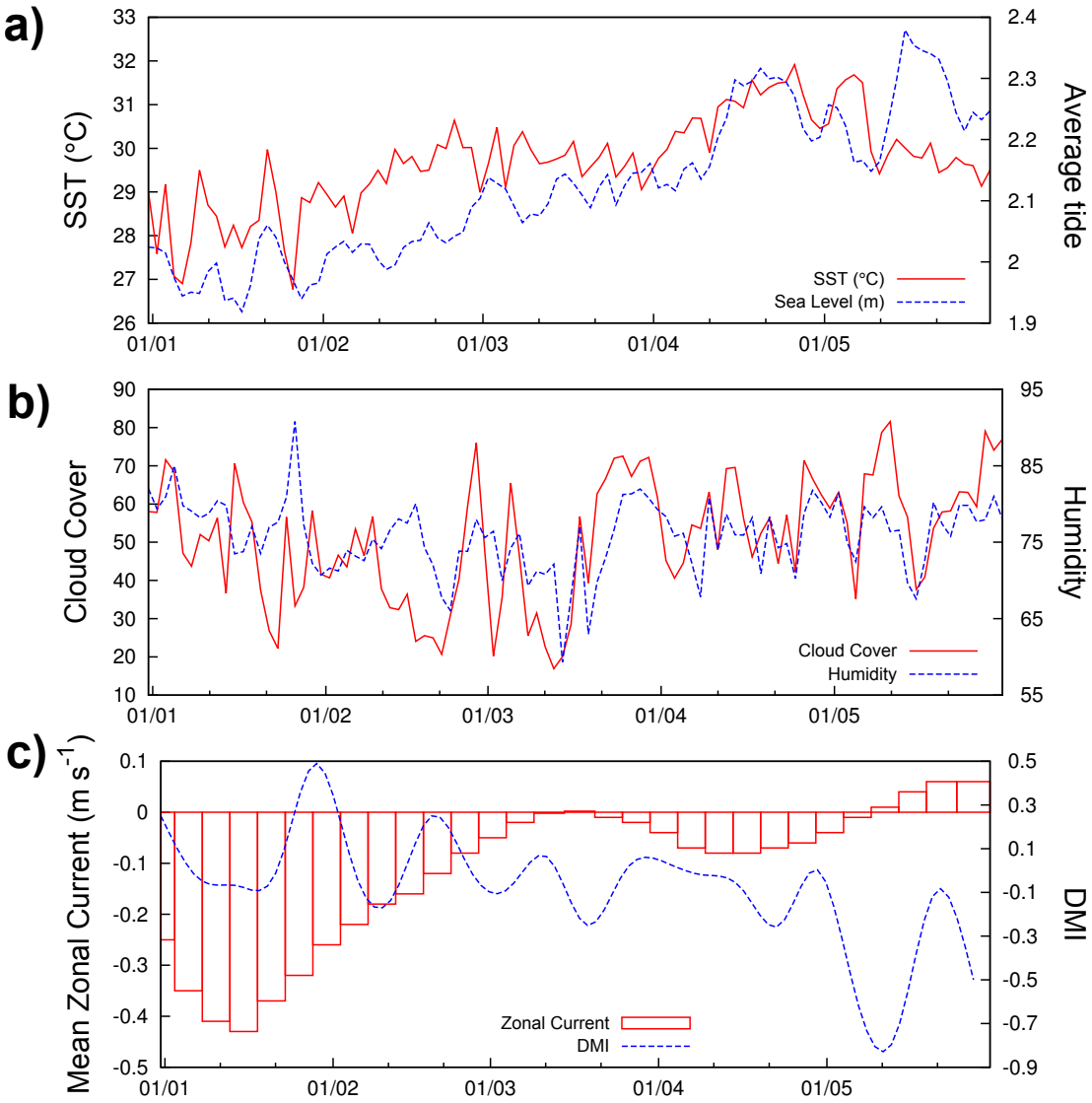

Figure 5.5. **a:** Daily time series of observed SST and daily time series of sea level. **b:** Daily time series of observed cloud cover and humidity. **c:** Time series of 5-day mean zonal surface current (U) within domain 6.5°-8.5°N, 94.5°-100.5°E. Data was obtained from NOAA Reynolds OI SST (http://www.esrl.noaa.gov/psd/data/gridded/data.noaa.oisst.v2.html) and NOAA OSCAR (http://www.oscar.noaa.gov/).

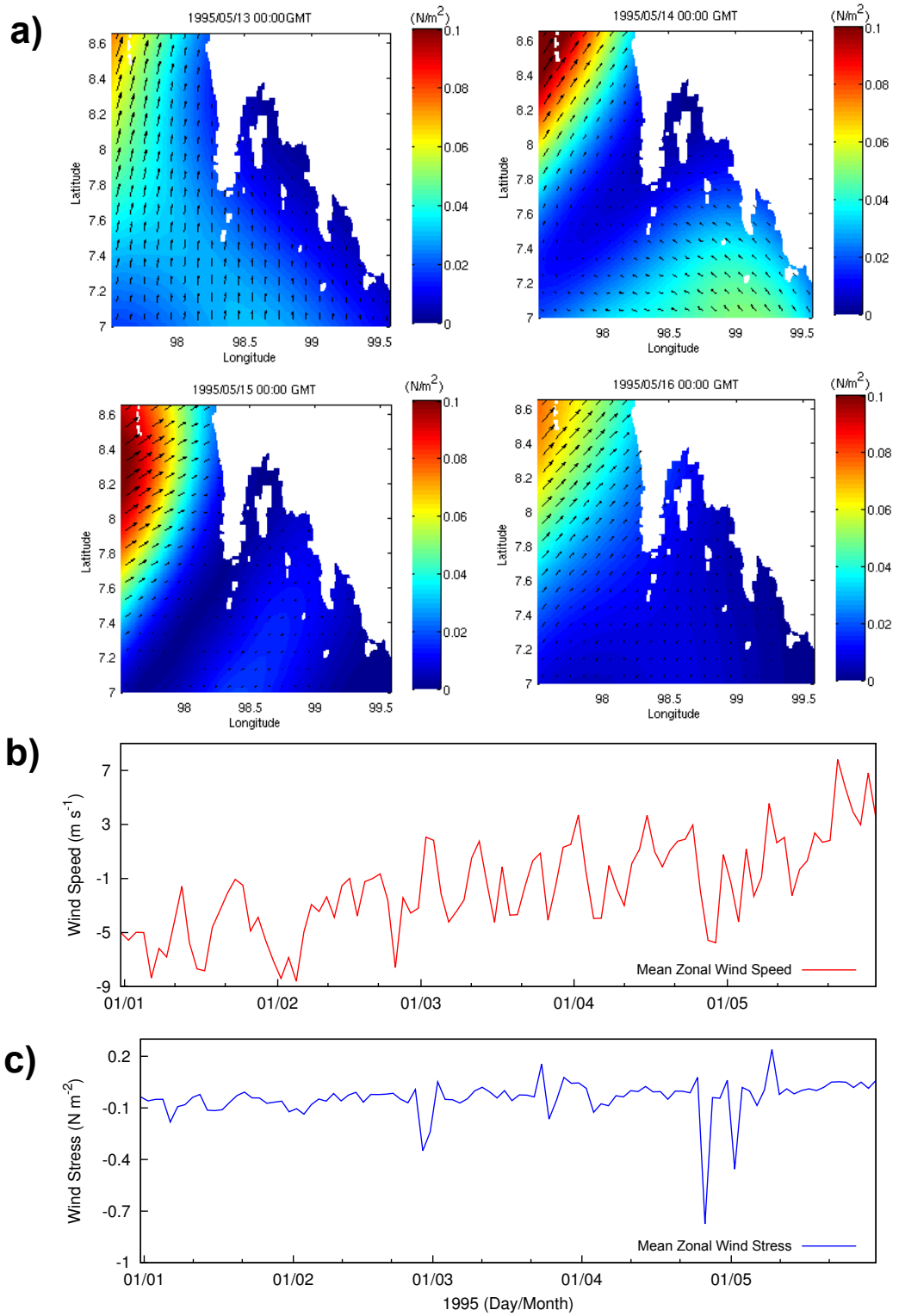

Figure 5.6. **a:** Wind stress distributions during the monsoon onset on 13, 14, 15, and 16 May 1994. **b** and **c:** Daily time series of blended mean zonal wind speed and wind stress, respectively. Data was obtained from NOAA/NCDC (http://www.ncdc.noaa.gov/).

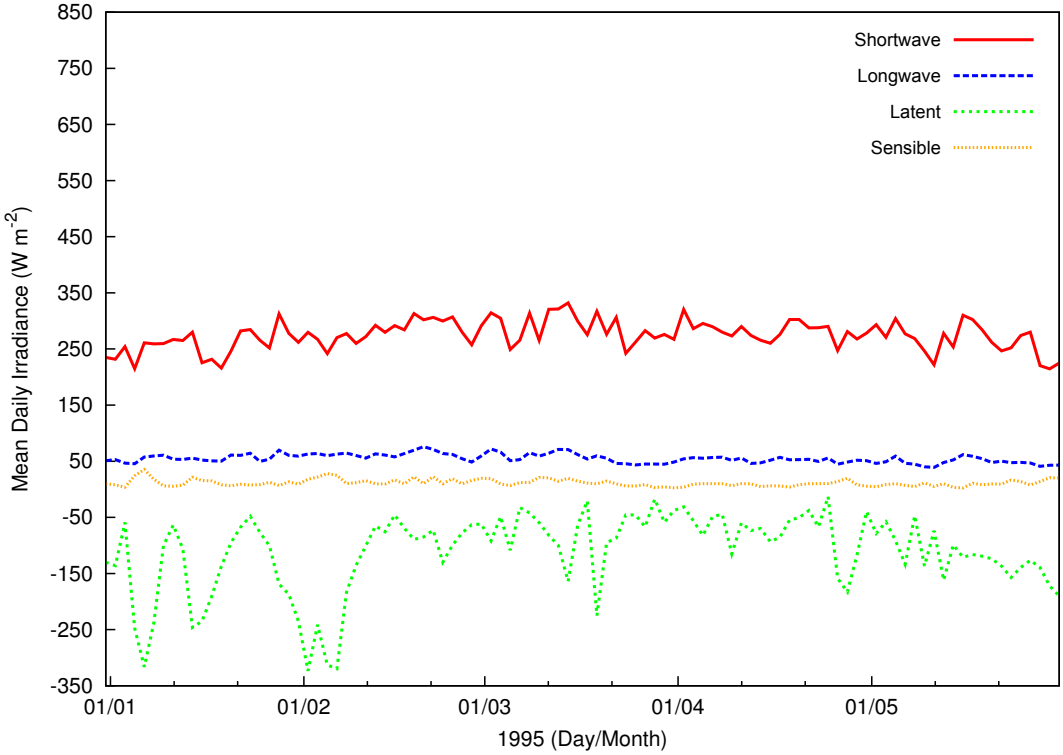

Figure 5.7. Daily time series of observed daily heat fluxes during January-May 1995. Data was obtained from NCEP-NCAR Daily Reanalysis (http://www.esrl.noaa.gov/psd/data/gridded/data.ncep.reanalysis.html).

5.4 Model description

I used a combination of numerical models to investigate the momentum and heat balances established on the nearshore shallow reef flat in the vicinity of Ko Racha Noi, Thailand. The model is divided into three stages: firstly, a coupled model of ROMS-SWAN is used to investigate the 2-D hydrodynamic nearshore currents based on the available oceanographic data; secondly, the solar irradiance load model is used to quantify the amount of semi-diurnal surface irradiance and the variation of irradiance levels due to turbidity, cloud cover, water depth (tides), and sea-state; finally, CFD simulation is implemented to solve for the coral tissue/surface warming based on coupled dynamics of water flow, heat transfer and irradiance levels in and around corals. Coral surface warming is defined as a deviation from the ambient water temperature under a constant seawater flow and solar irradiance.

5.4.1 ROMS-SWAN coupled model

A coupled model of ROMS (Regional Ocean Modelling System, (Shchepetkin and McWilliams, 2005)) - hydrodynamic model and SWAN (Simulated Waves Nearshore, (Booij et al., 1999)) - wave model, was implemented to study the circulation throughout these fringing reef flats. ROMS used for this study was a version with model coupling and nesting (Warner et al., 2010). The model was coupled with MCT (Model Coupling Toolkit), which allowed two-way coupling among multiple sub-models (Warner et al., 2008). The model implemented for this study was a 3-D barotropic model, thus, the temperature and salinity values were constant and invariable with respect to time and depth.

The model required a horizontal spatial resolution of 100-200 m in order to simulate wave-current interactions in shallow waters. Yet, the model domain needed to be sufficiently large enough to account for monsoon winds. In order to meet these requirements, the model consisted of three domains with different spatial resolutions. The largest domain (Parent domain) had a spatial resolution of approximately 5 km, smaller regional domain (child domain 1) had a spatial resolution of 1 km, and the smallest domain (child domain 2) had a spatial resolution of approximately 200 m (Figure 5.8). The child domains 1 and 2 were nested into the parent domain and allowed two-way nesting (Figure 5.8). The child domain 2 included an island called Ko Racha Noi or Ko Racha Yai and its fringing reefs, the region of my interest located on the west of the island (98° 14'60" E, 7° 28'48" N). ROMS and SWAN were specified for the same grid size and spacing.

The model was run for 31 simulation-days starting at 00:00 GMT, April 20, 1995. The first 2 days of model outputs were used as spin-up and were discarded; the rest was used for data analysis. The model used time splitting between slow-moving baroclinic mode and fast-moving barotropic mode. The baroclinic time step for parent grids and child grids was 60, 30 and 10 s, respectively. Whereas, the baroclinic time step was 30 times smaller than each baroclinic time step. Time step for SWAN was 10 minutes for all domains. Both models were coupled every 1800 seconds (i.e. 30 minutes). The number of vertical layer distribution was selected as a standard 20.

The input parameters that are required to implement the models were: (1) bathymetry variables, (2) forcing data, and (3) open boundary data. Bathymetry data were obtained from the General Bathymetric Chart of the Ocean (GEBCO), which provides bathymetry with a spatial resolution of 30 arc seconds (IOC, 2003) (Figure 5.9). Unfortunately, there was no other readily available finer-resolution bathymetry data at this stage. As a result, the model results were compromised in particular for shallow waters. Bathymetry was smoothed to avoid pressure gradient force (PGF) error. Forcing data were obtained from NOAA Climate

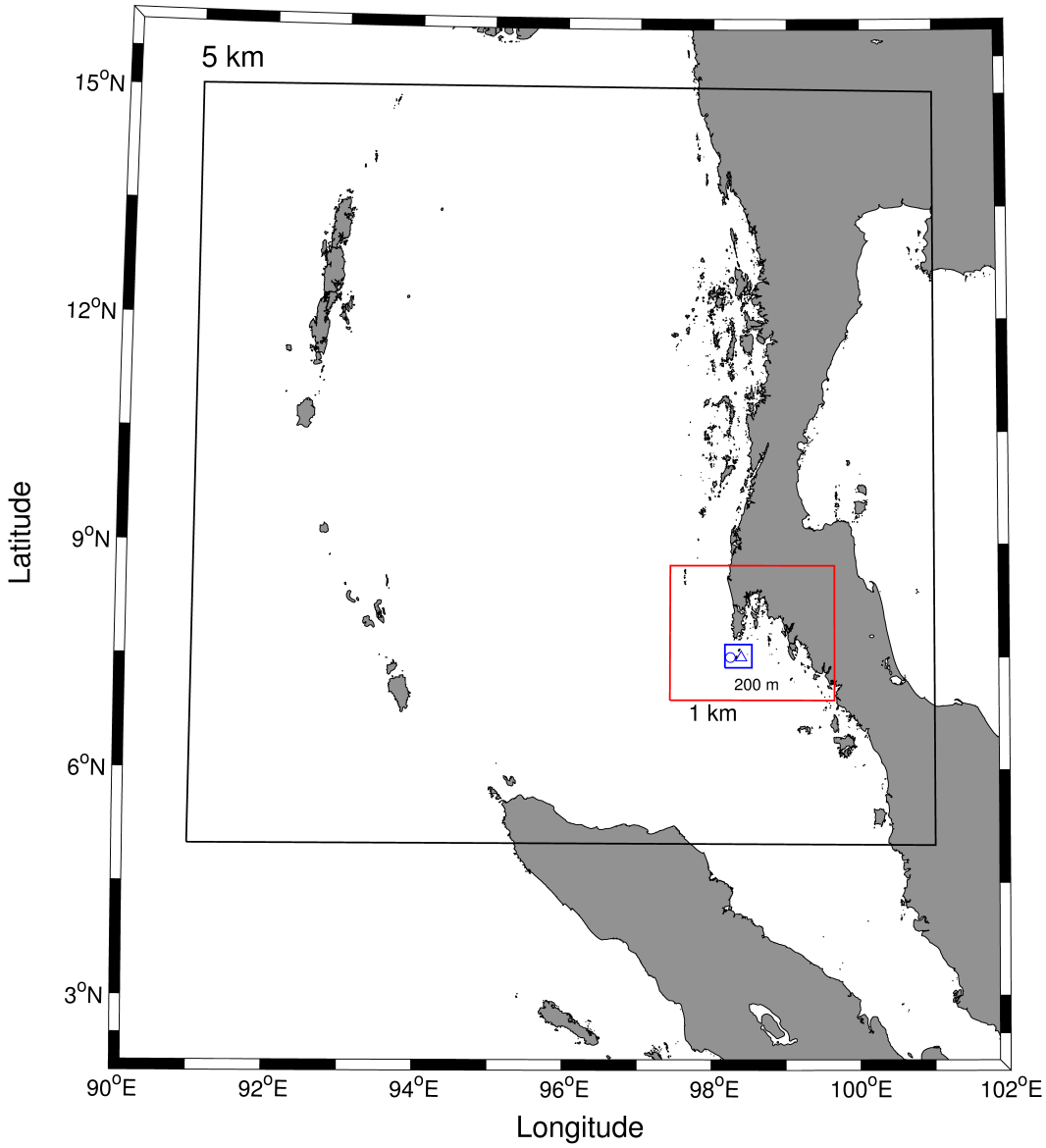

Figure 5.8. Model domains. The black line represents the parent domain. The red line a child domain and the blue line another child domain.

Forecast System Reanalysis (CFSR) outputs which provide forcing data with 0.5 degree spatial resolution (Saha et al., 2010). Wind stress and mean sea level pressure were included in the model (Figure 5.6). Open boundary data included wave parameters (height, period, direction and directional spreading) along the open boundaries (North, West and South) and also tidal constituents along the boundaries to impose tides and waves. Wave data were obtained from NOAA

Wave Watch III (Tolman, 2002) reanalysis and tidal constituents were obtained from outputs of an inverse tidal model developed by a group at Oregon State University (Egbert and Erofeeva, 2002).

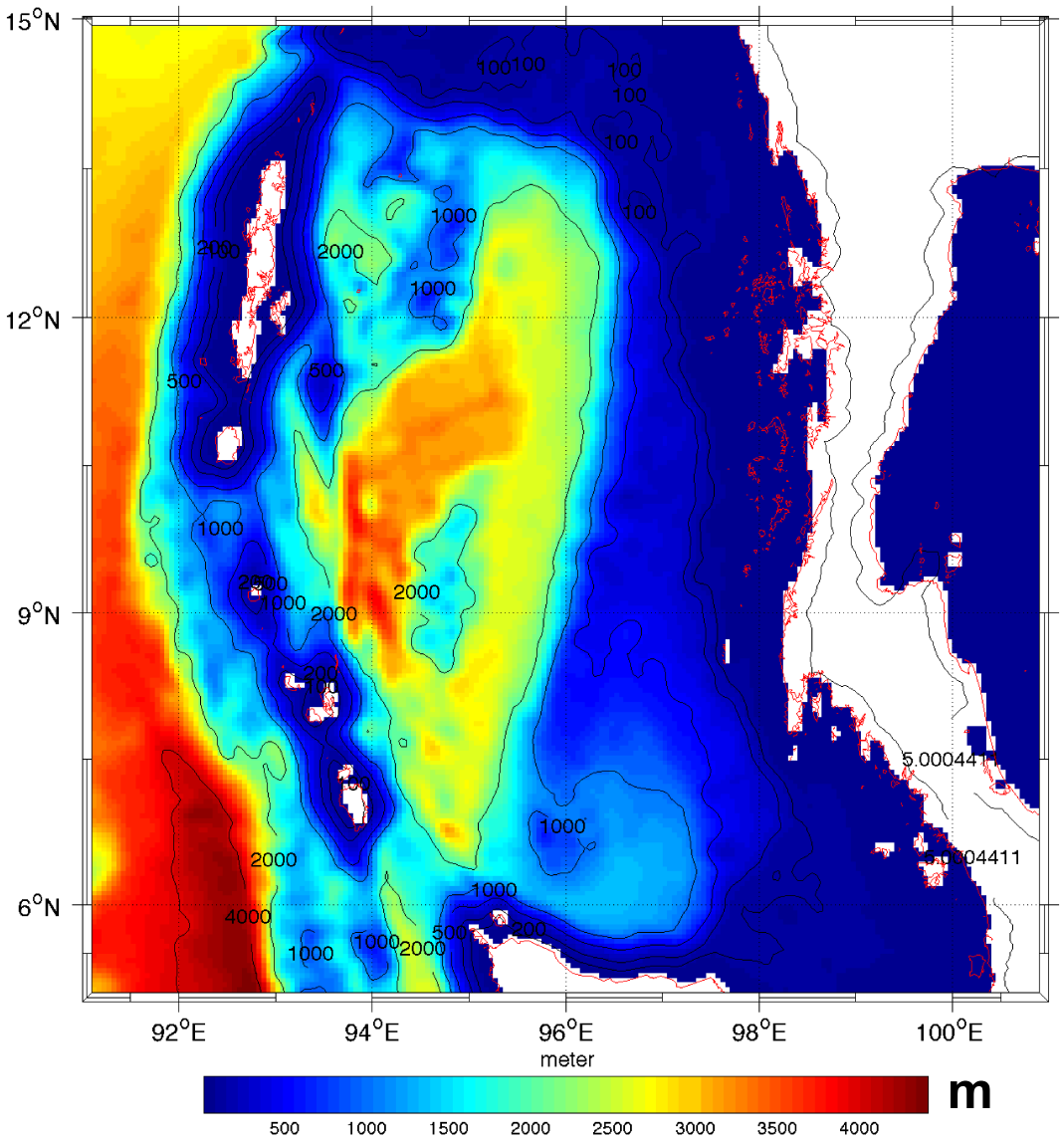

Figure 5.9. A global 30 arc-second grid of bathymetry. Data obtained from GEBCO, http://gebco.net/data.

5.4.2 Solar irradiance load model

The amount of irradiance and spectral quality entering the ocean surface is closely related to the azimuth and elevation angles of the sun. Previously, I have discussed the solar ray-tracing mechanisms in predicting surface irradiance and variation of irradiance due to turbidity, cloud cover, water depth (tides), and sea-state (Chapter 4). Here, I focus mainly on PAR because various field experiments (Brown et al., 1994; Fitt and Warner, 1995; Hoegh-Guldberg, 1999b), indicate that it has a much greater influence on bleaching compared to the shorter wavelengths of UVR (Dunne and Brown, 2001). Additionally, at the observed study site at Ko Phuket the seawater is turbid and highly coloured so the shorter wavelengths of UVR are strongly attenuated close to the water surface (Dunne and Brown, 2001). We denote the state of the sky by using the fraction of the sky obscured by clouds. The contribution of secondary atmospheric variables such as sky turbidity, water vapour content, and cloud type to the overall amount of irradiance is likely to be negligible.

Coral optical properties: The light absorbing and emissivity capacity of *G. aspera* was defined as the thermal absorptance and emittance values in the spectral range 280-700 nm (UVR and PAR). The values were obtained from previous laboratory experiment conducted by Jimenez *et al.* (2008) (Jimenez et al., 2008), wherein the absorptivity and emissivity values of coral tissue were set as 0.3 (light grey) and 0.8 (grey body), respectively; whereas for UVR, I set both the absorptivity and emissivity values as 0.01 (Veal et al., 2010). The irradiance results of each cell of the coral surface were then converted to a volumetric heat flux term (φ_{qv}), then imported for CFD simulation.

5.4.3 CFD model

Here I am only concerned with the along-shore (U'_x) and across-shore (U'_y) small-scale spatial flow scales of approximately 50 m, hence the effects of vertical flow (U'_z), i.e., thermal stratification and tidal mixing, are not covered here. The simulations were run for 12 afternoon time for each day starting from 01 May to 20 May 1995, based on the model output currents and tides from the coupled ROMS-SWAN model and the irradiance data from the ray-tracing model, as the input basis for the CFD model.

This study was conducted using the open-source suite of software applications, libraries and utilities for continuum mechanics problems, known as OpenFOAM (OpenCFD Ltd., 2010). The description of the model is given in Appendix 1. This study mainly used two types of grids, predefined block structured hexahedral and polyhedral, to represent both computational and coral domains with approximately ~2,500,000 cells for the low-Re turbulence model with y^+ was set

~1.0 (viscous sublayer region).

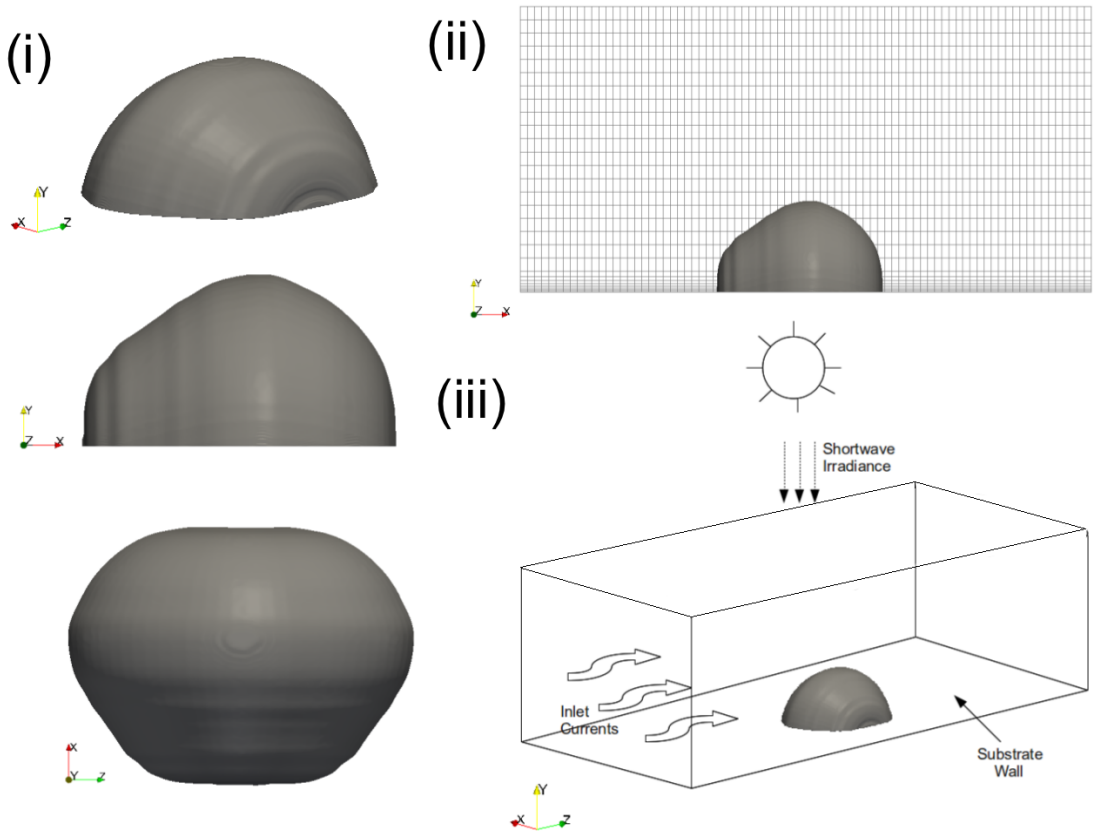

Figure 5.10. Geometric representation of simulated conditions for *G. aspera*. (i) various perspective views of the coral model, (ii) mesh model for low-Re turbulence simulation ($y^+ \sim 1$), (iii) conceptual representation of the model

All the simulations were conducted in steady-state conditions using the SIMPLE (semi implicit method for pressure-linked equations) algorithm. This method determined pressure on a staggered grid from velocity components by applying an iterative procedure coupled with the Navier-Stokes equations Ferziger and Perić (1999); OpenCFD Ltd. (2010); Versteeg and Malalasekera (1995). The schemes implemented for both convection divergence and Laplacian terms were the Gauss linear upwind cell limited least squares and the Gauss linear limited 0.5, respectively. The generalised geometric-algebraic multi-grid (GAMG), smoother Gauss-Seidel, and preconditioned bi-conjugate gradient (PBiCG) were used to discretised pressure, velocity, and temperature governing equations, respectively.

5.4.4 Turbulence generalities

The turbulent generalities, boundary conditions, and numerical schemes were similar to those found in the previous chapters. Analysis of the turbulence modelling previously shown in the Chapter 3 and the Appendix 1. Here, I selected the $k - \omega$ Shear Stress Transport (SST) model (Menter et al., 2003; Menter, 1994; Wilcox, 1998). The free-stream specification values were calculated using the formula found in Table 3.6.

5.4.5 Surface-to-subsurface velocity projection

Using the shallow water model projection (Shen and Evans, 2001), the obtained surface currents were then inferred to approximate the sub-surface currents at depth of 5 m. The accuracy limit of this projection has been validated against observations, and performed seemingly robust (Shen and Evans, 2001).

5.5 Results

The irradiance load and CFD models agreed well with the satellite and in-situ observations. Although, a better understanding of the spatial and temporal variability in bleaching patterns may be achieved by a more detailed description of the surrounding environmental parameters.

Overall, the coupled ROMS-SWAN model reproduced features of tidal currents, low-frequency currents and wave sheltering effects. However, it was difficult to resolve wave-current interactions due to coarse-resolution bathymetry and lack of in-situ data to validate the model. Thus, the following results are still preliminary. The model data were extracted for the eastern and western side of the Ko Racha Noi island to investigate differences between two sites.

5.5.1 Tidal elevation and currents

The time series of adjusted wave levels is shown in Figure 5.11. Tides in Phuket are dominated by semi-diurnal tides (M_2). The highest tidal amplitude occurring during spring tides was little less than 3 m. The model quickly captured tidal elevations following its initiation. Consecutive spring tides were asymmetric. Although there were no tide records available during the simulation period, predicted tides at the Phuket Harbour were obtained and compared to simulated water levels. The predicted tides are in good agreement with the simulated tides (Figure 5.11).

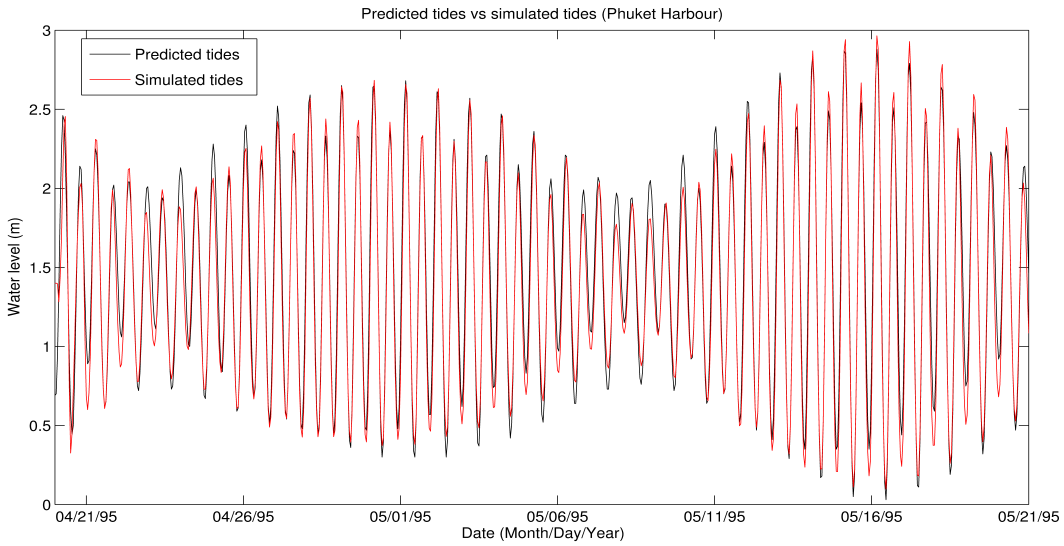

Figure 5.11. The predicted vs simulated results of tidal elevation near the Phuket Harbour.

Tidal currents were estimated based on tidal harmonic analysis based on Pawlowics *et al.* (2002) (Pawlowicz et al., 2002). The tidal ellipses of M_2 constituent is shown in Figure 5.12. Tidal currents are strong over narrow straight, between islands, over the continental shelf and over/between reefs. Near the Phuket, tidal currents were amplified and the east-west component was dominated.

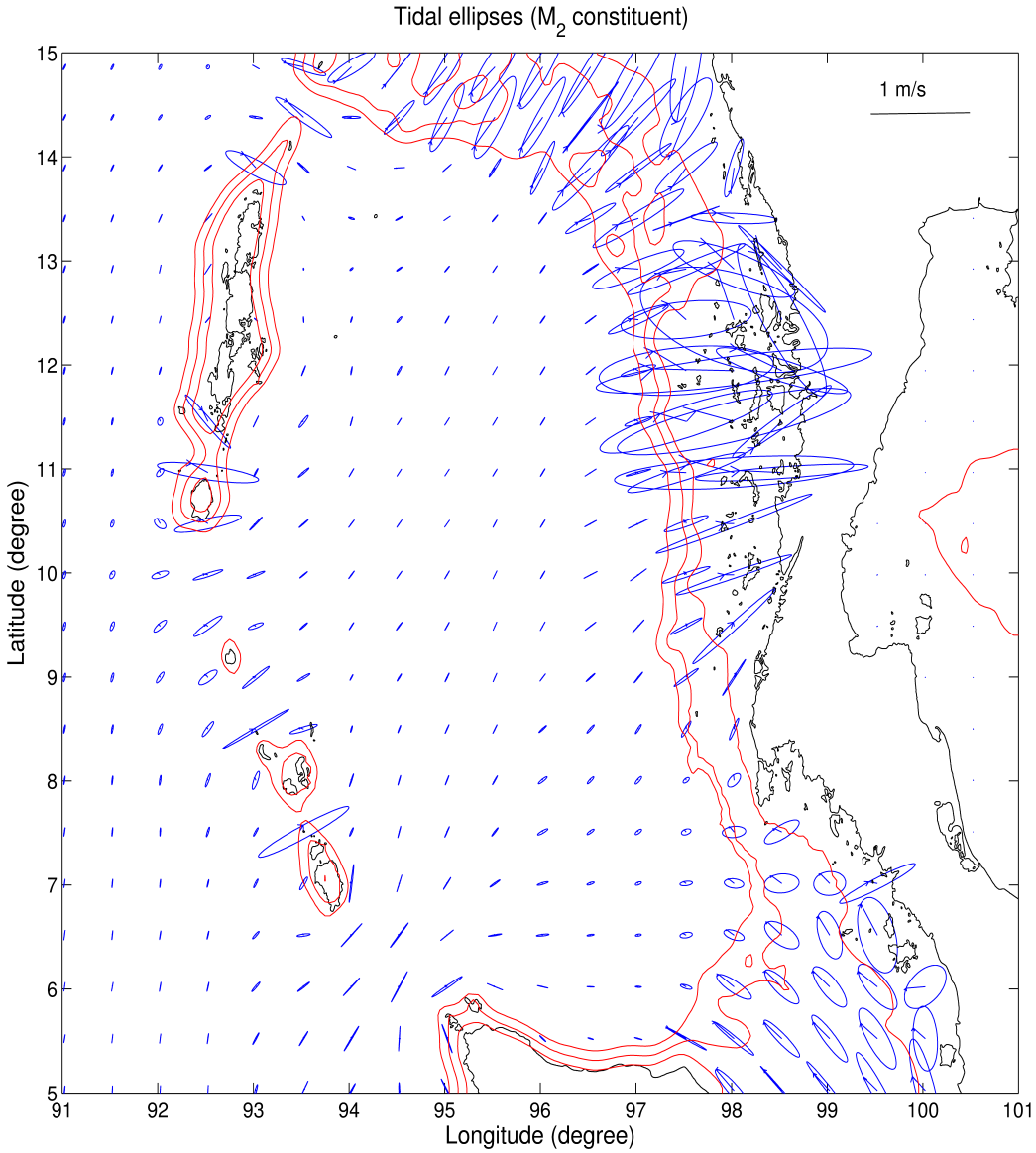

Figure 5.12. Simulated results of tidal ellipses (M_2 constituent). Isobaths of 50 m, 100 m, and 200 m are shown in red.

5.5.2 Low-frequency current

Low-frequency currents are shown as progressive vector diagrams (PVC). Currents were estimated by filtering out currents shorter than 40 hours. The PVD of wind stress (Figure 5.13) shows eastward component of wind stress since the monsoon onset. Variability of the low-frequency current is consistent with the wind

stress (Figure 5.14). The currents on the western and eastern side of the island different slightly. Both currents showed an eastward component after around 10 May 1995 following the monsoon onset. The distance the current travelled reached 10 - 15 km, which suggests that the current with aid from tidal currents could have brought colder, offshore water to the reef, which might have contributed to reduced temperatures over the fringing reefs. It should be noted that although the eastward (onshore) current was captured, the onshore current appears to be location-dependent latitudinally (Figure 5.15).

The reconstructed current for 24-hour mean zonal current from 01-20 May 1995 on the reef flat was given in Figure 5.16. The results from ROMS-SWAN current compared reasonably well against the OSCAR current data (Figure 5.17). Negative U indicated that the zonal temperature gradient close to the equator generated easterly winds, which in turn drive the westward current. Similarly, during the positive DMI and U (negative IOD event), the zonal temperature gradient near the equation generates westerly winds, which lead to eastward current. An averaged zonal current over the semi-diurnal (daylight hours) period was given in Figure 5.18.

Previously, I have shown that there are three main attenuation factors that may reduce the intensity of both the quality and quantity of light received by the coral surface, one of which is tidal height. Due to the lack of available data for diurnal tidal heights at the site location, I conducted two distinct sensitivity analyses based on the sea level data and computed the most likely best (high tide: $\simeq$85% zonal current) and worst (low tide: $\simeq$15% zonal current) scenarios (Figure 5.19). The surface-to-subsurface velocity projection was estimated using Shen *et al.* (2001) analysis which was shown in Figure 5.20.

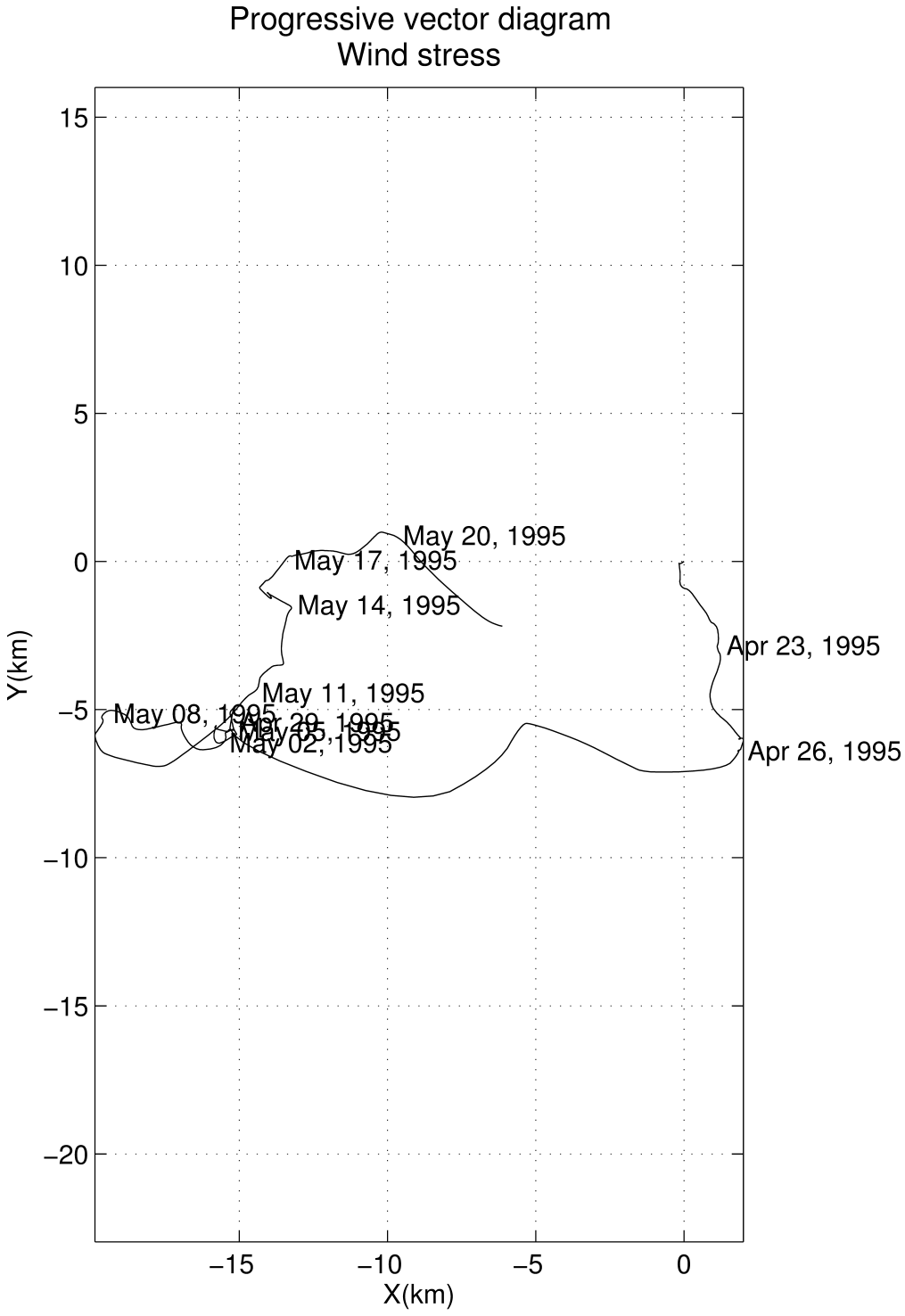

Figure 5.13. Simulated results of progressive vector diagram of wind stress.

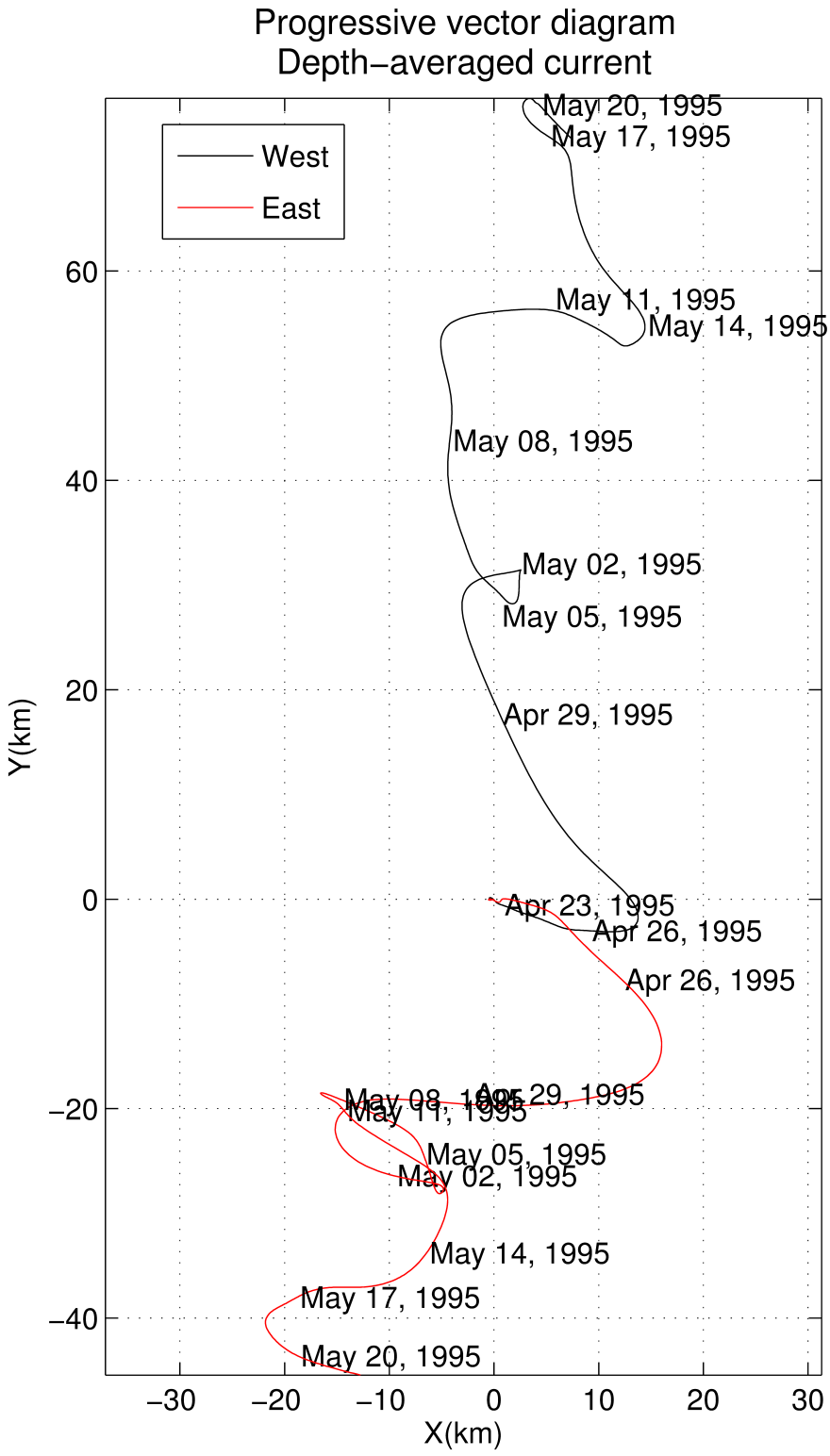

Figure 5.14. Simulated results of progressive vector diagram of depth averaged currents.

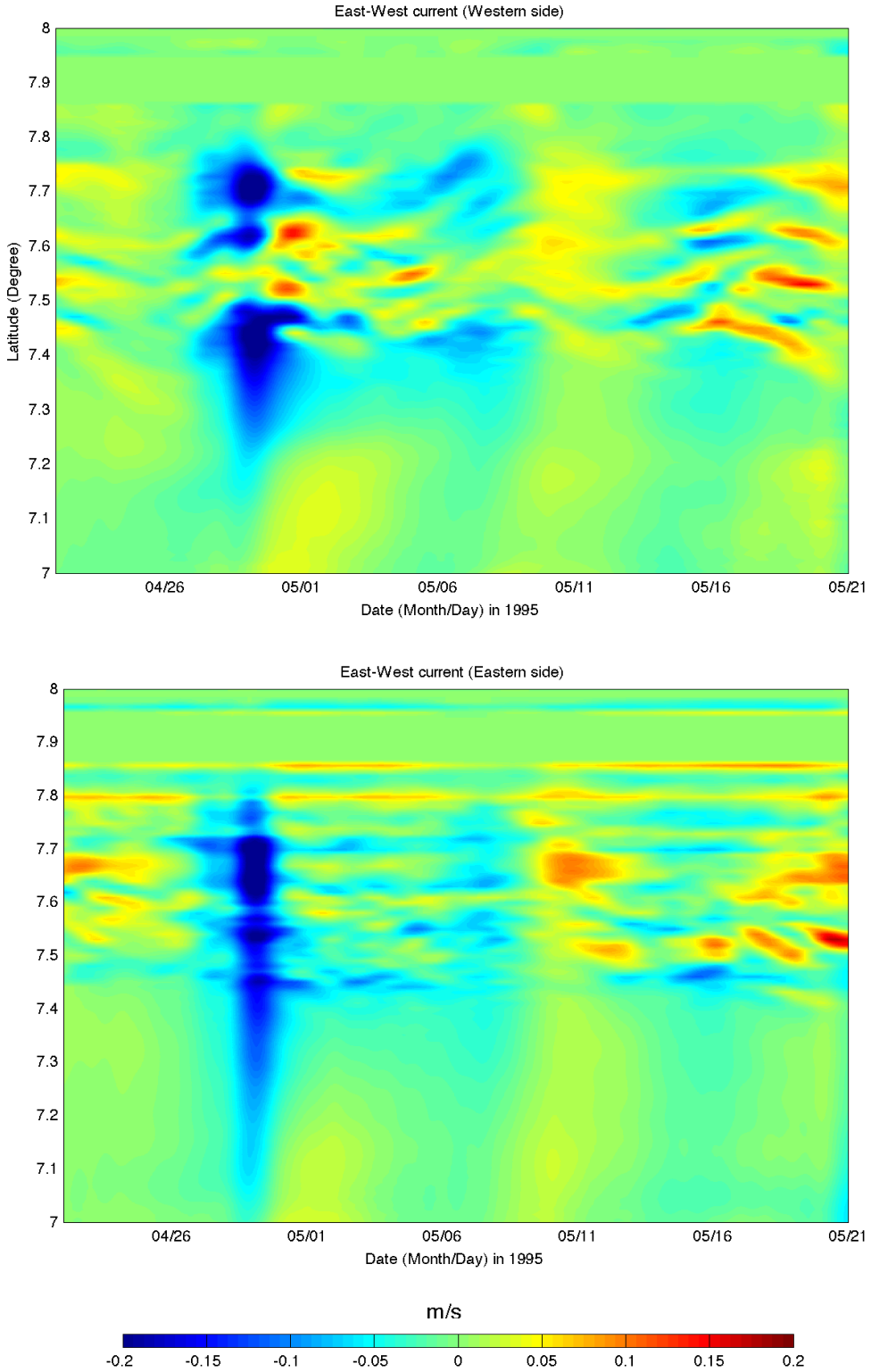

Figure 5.15. Simulated results of latitudinal difference in depth-averaged residual currents on the western and eastern sides of Ko Racha Noi island.

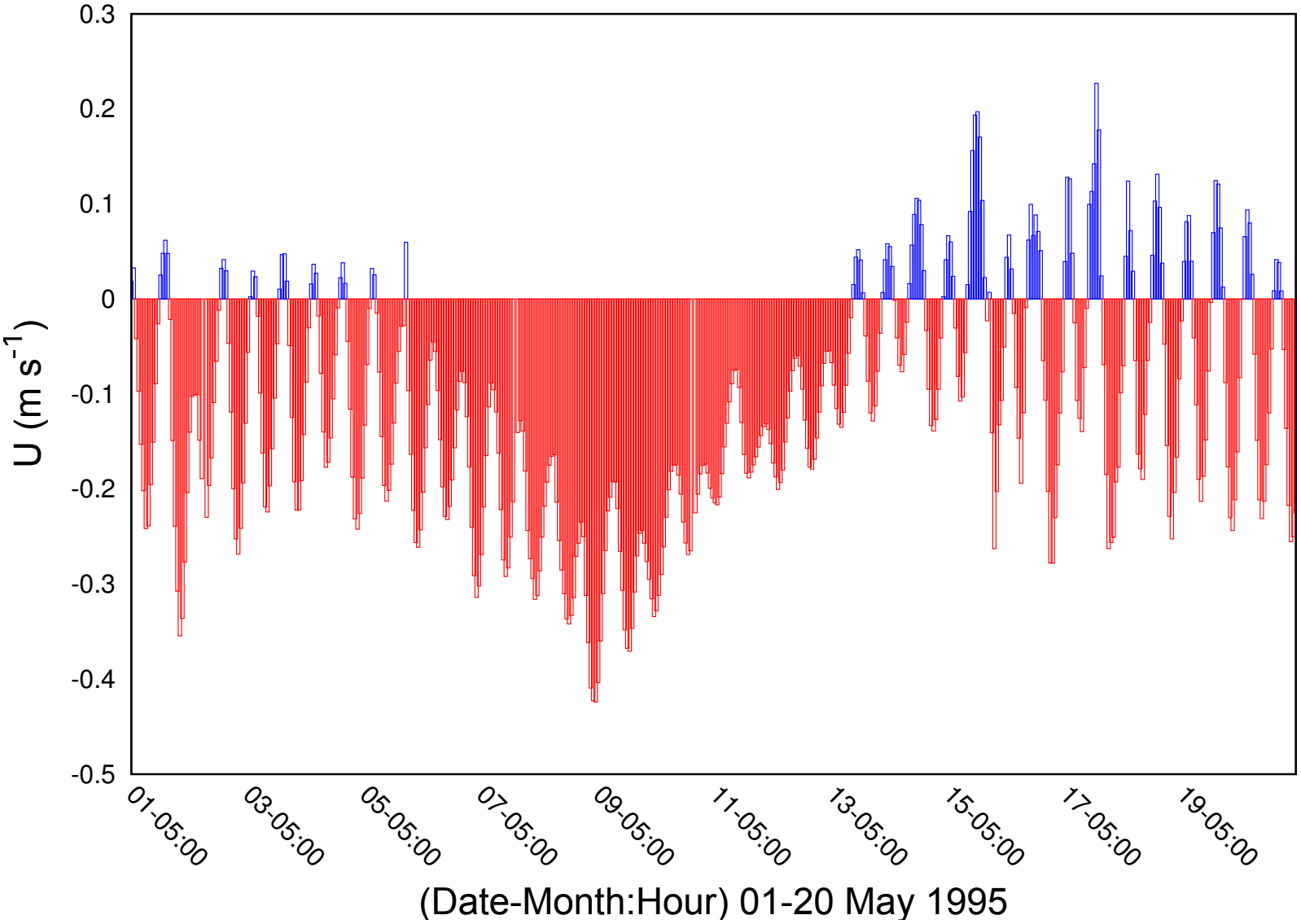

Figure 5.16. Simulated results of time series of 24-hour mean zonal current (U).

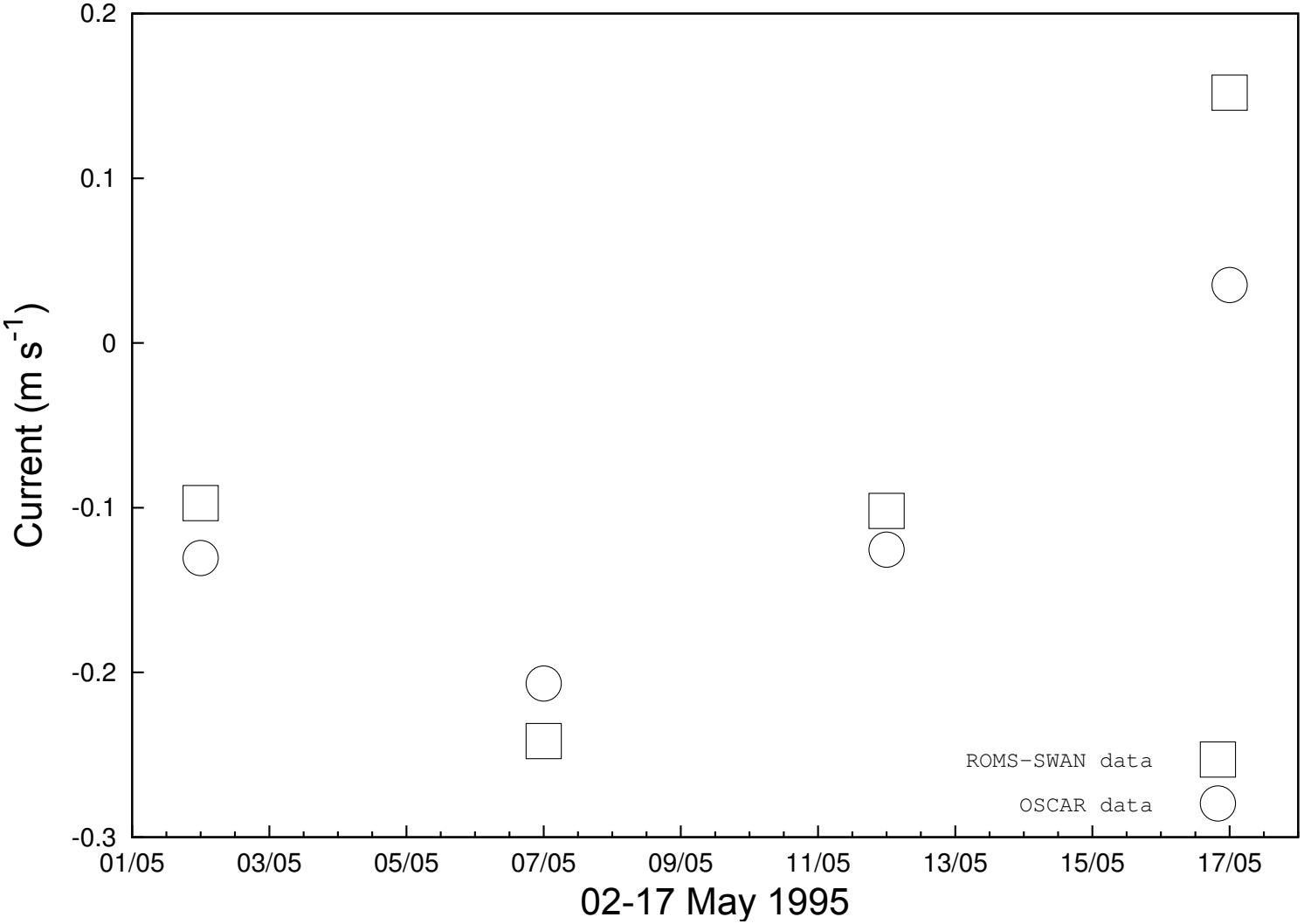

Figure 5.17. Comparison of ROMS-SWAN and OSCAR data for 24-hour mean zonal current (U) with a 5-day interval from 02-17 May 1995.

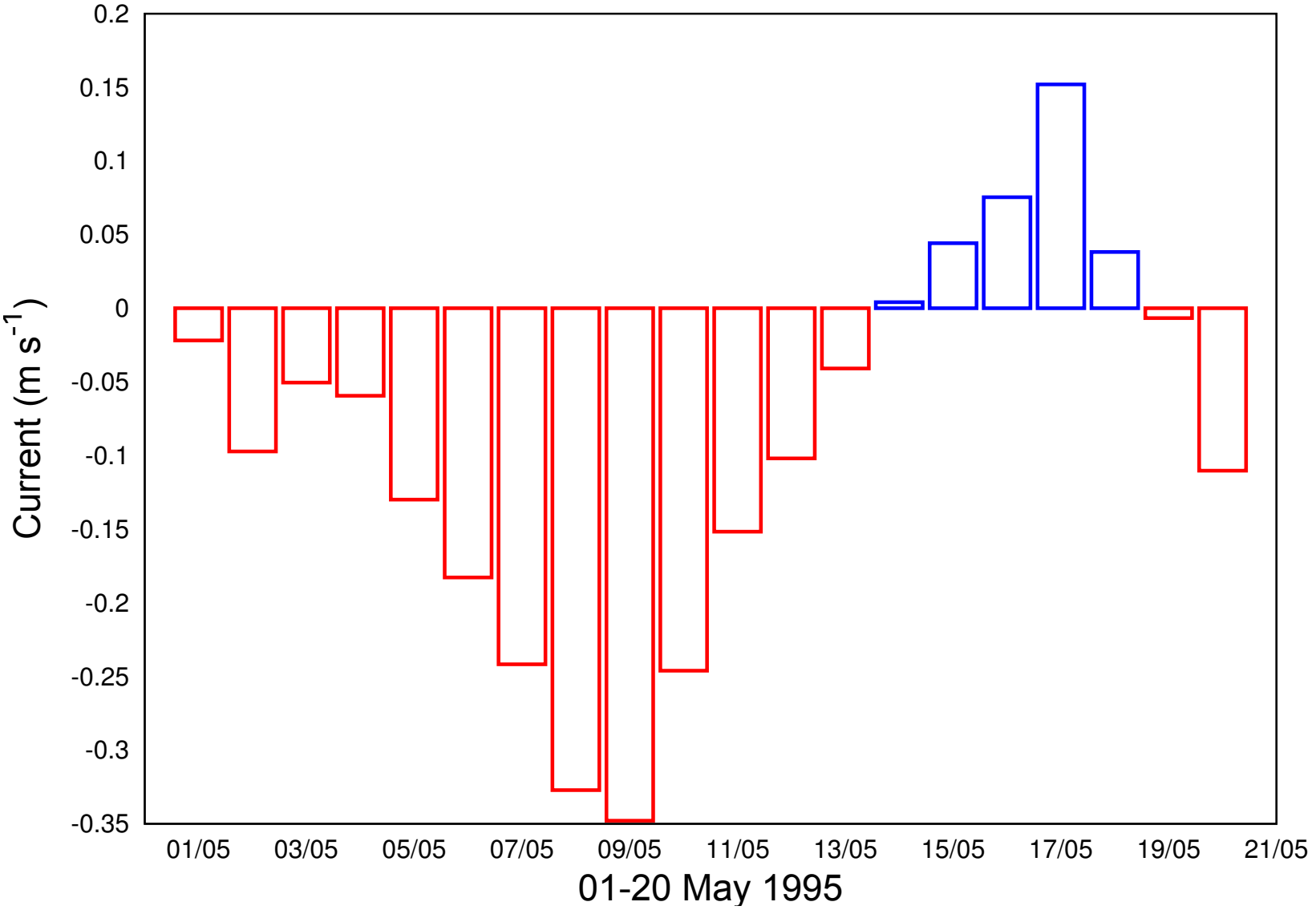

Figure 5.18. Simulated results of the semi-diurnal mean zonal current (U).

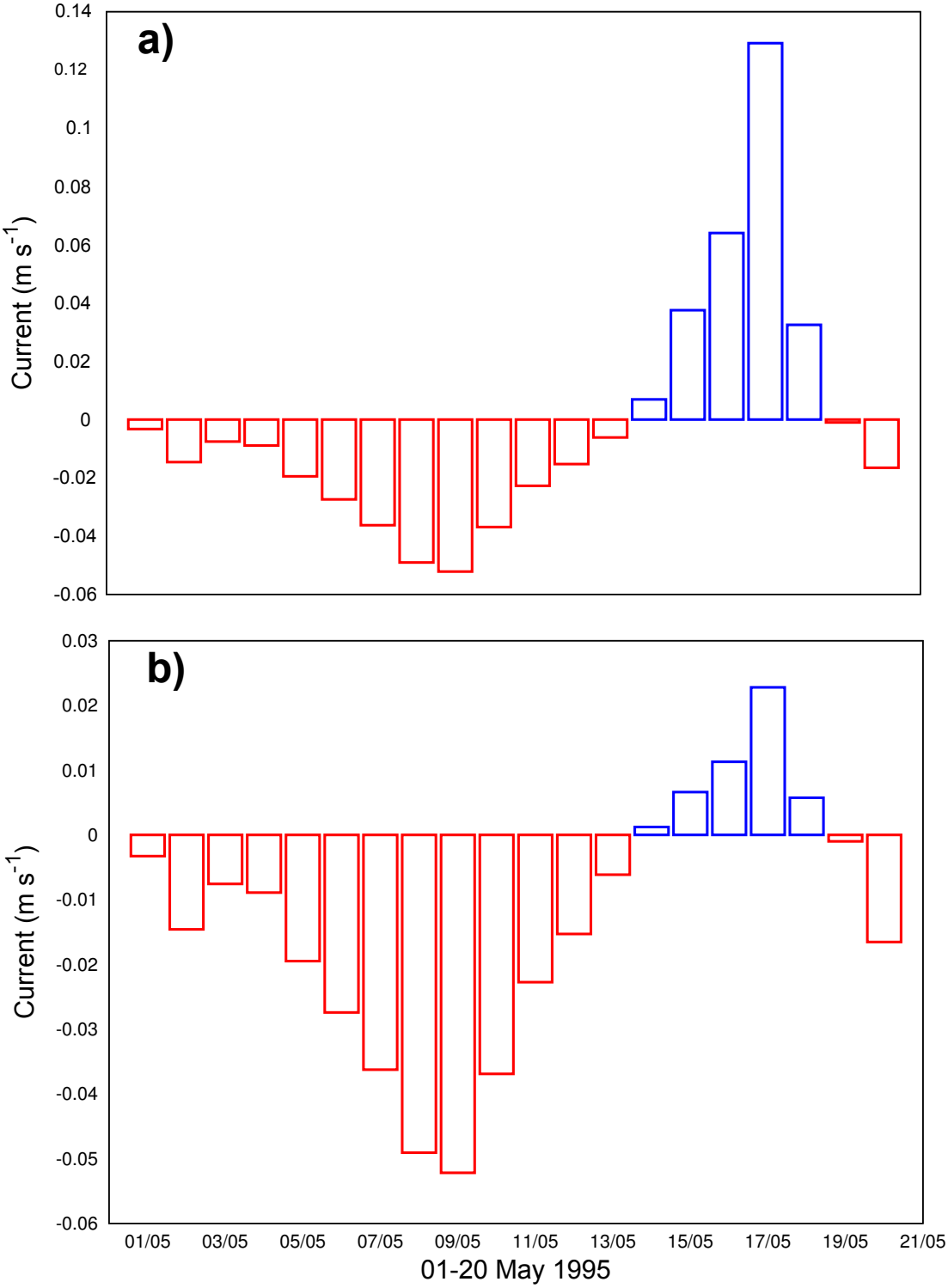

Figure 5.19. Semi-diurnal mean zonal current (U) for (a) high tide and (b) low tide

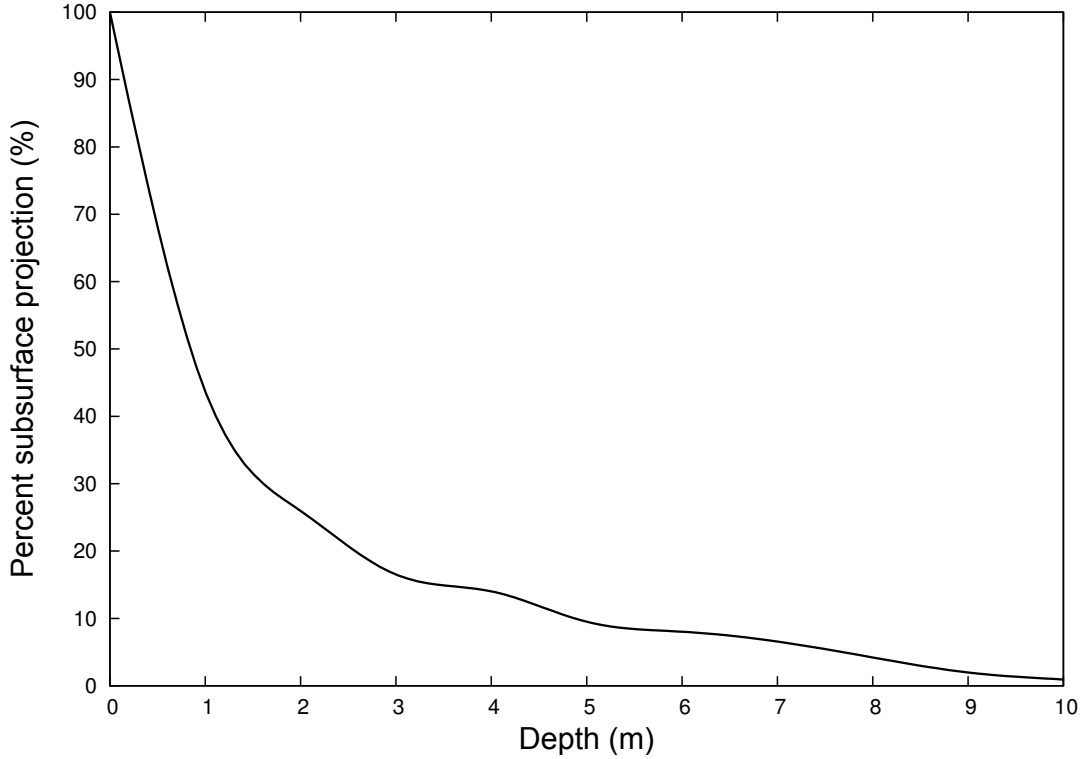

Figure 5.20. Estimated decrease in subsurface velocity with water depth using (Shen and Evans, 2001) approximation model.

5.5.3 Wave sheltering and wave-current interactions

At two locations, the eastern and western sides of the island were similar in terms of current speed/direction and wave height/direction (Figure 5.21). High wave height in late April was associated with the passage of a tropical cyclone, which induced strong currents (Figure 5.15 and 5.21). One of the noticeable differences between the western and eastern sides was wave height. Following the onset of the monsoon, wave heights on the western side became significantly higher than those of the eastern side. The dominant wave direction was from the west; therefore, the difference in wave height would have been associated with wave sheltering by the island. As a result, the wave heights on the eastern side were significantly lower. This indicates that the western side should be more prone to wave-induced mixing than the eastern side when waves propagate from the west (offshore) and that might have contributed to a reduction in thermal stress of the corals.

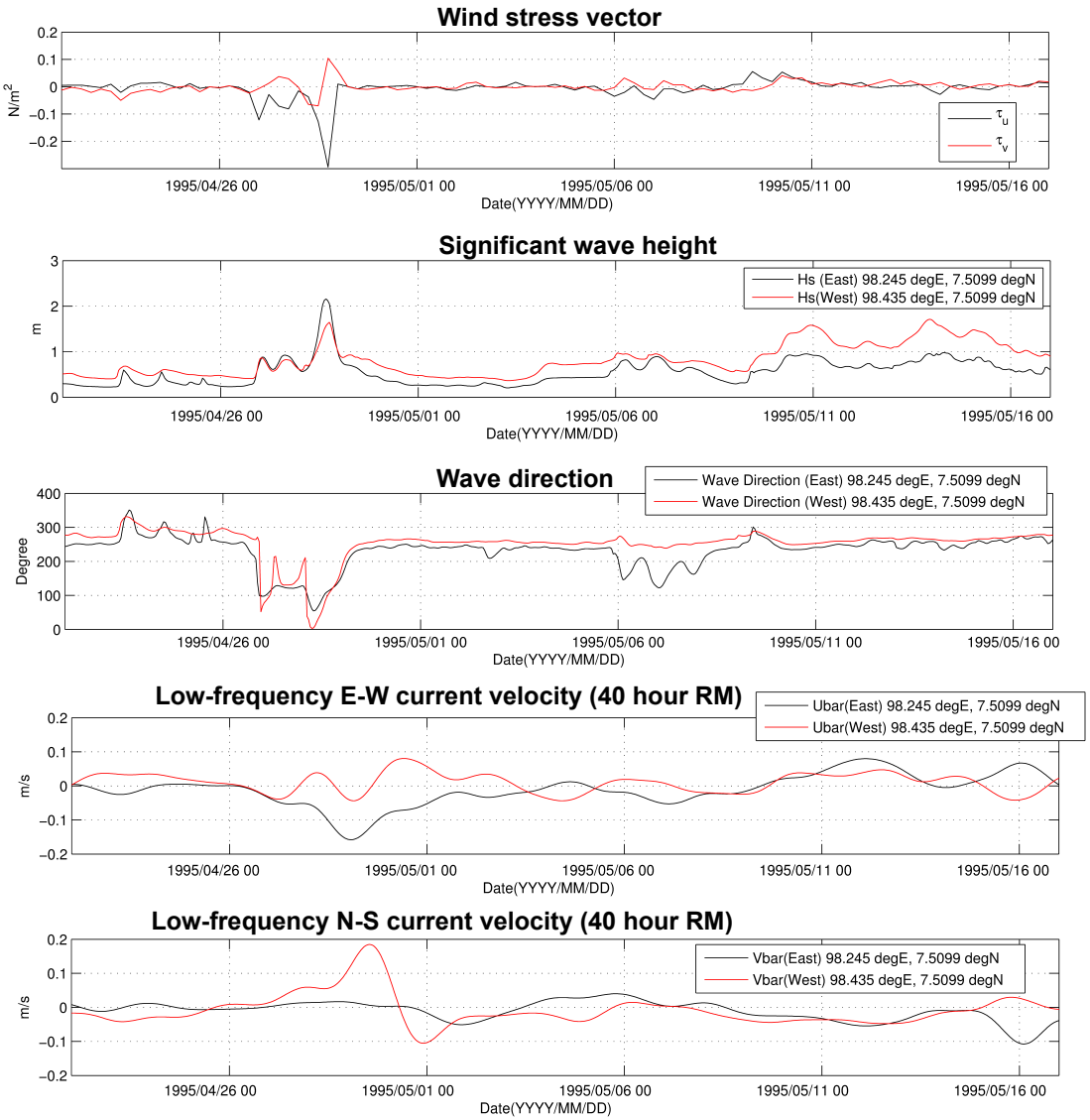

Figure 5.21. Simulated results of time series of wind, wave, and currents outputs

The model was tested with and without the wave-current interactions. Wave-current interactions were included in the model (Uchiyama et al., 2010), the lack of in-situ data and high-resolution bathymetry, it is difficult to understand wave-current and wave-wave interactions over fringing reefs. The bathymetry data from GEBCO fail to represent detailed reef topography due to a lack of resolution. As a result, validity of the discussion on wave-current interactions was therefore not included.

5.5.4 Irradiance estimation

Quantitative findings of solar irradiance were in excellent agreement with field observations (Figure 5.22 and 5.24).

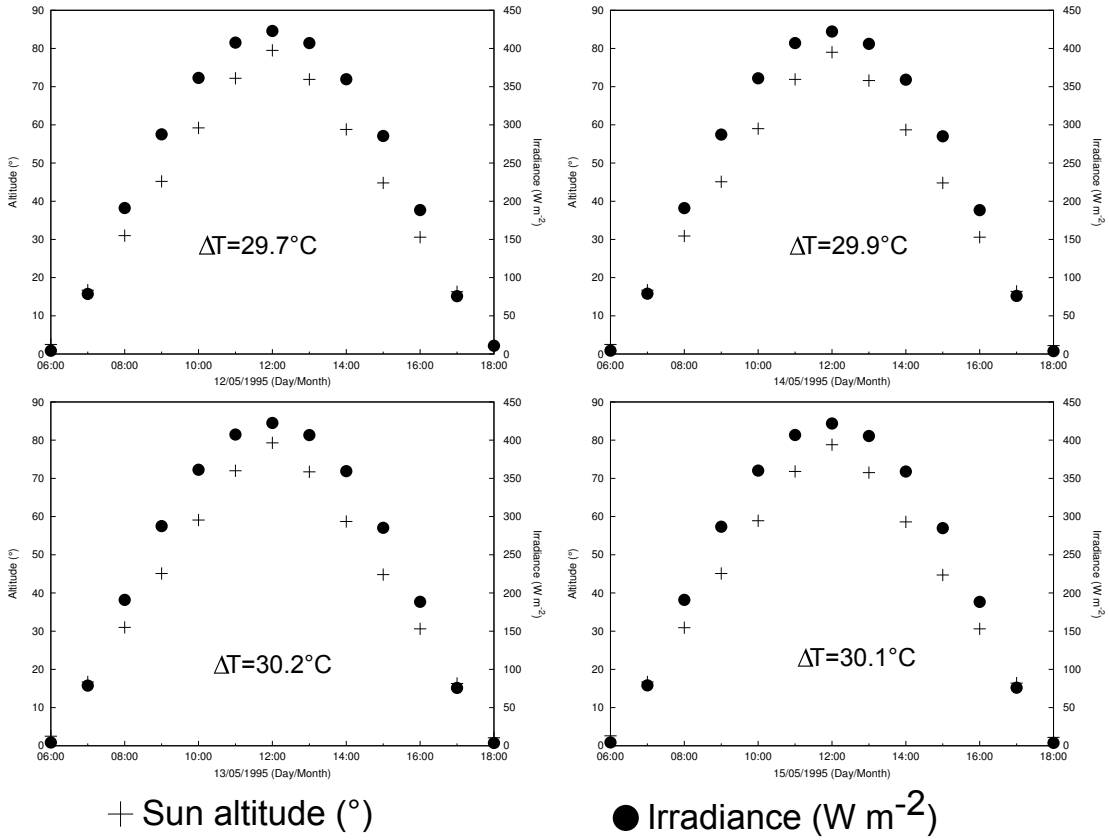

Figure 5.22. Simulated results of daily hours of direct sunlight from 12-15 May 1995 at the observed site.

The maximum daily irradiance observed by satellite (NCEP-NCAR, http://www.esrl.noaa.gov/psd/data/gridded/data.ncep.reanalysis.html) and the solar load model is given in Figure 5.23, and they reasonably agree well. The downwelling solar radiation (PAR) dose received approximately 10% greater than the eastern face of coral surface in January-March 1995. The difference in downwelling PAR received by the west and east faces declined with advancing season (Figure 5.24). By late April-May 1995, the data set shows the west faces received irradiance around 10% higher than the east faces during the time when differential bleaching was first observed (14 May 1995). The periods of high irradiances were concentrated into a short (1-4 h) timescale, often during low tides (Brown et al., 2002).

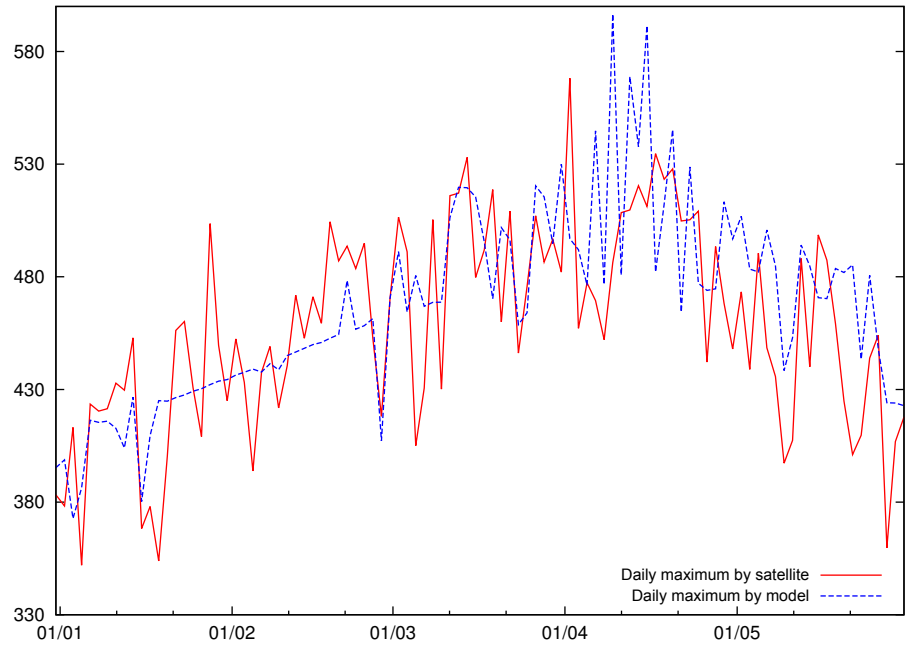

Figure 5.23. Comparison of the maximum daily irradiance data at the island (Ko Racha Noi) from the satellite (NCEP-NCAR) and the solar load model.

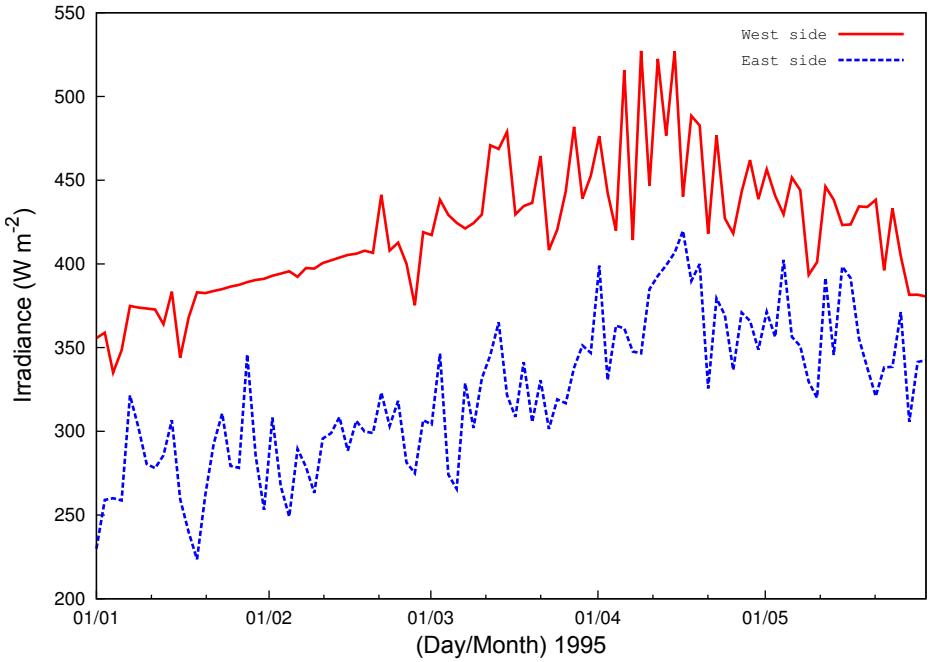

Figure 5.24. Maximum daily dose of PAR during January-May 1995 received by the west and east surfaces of *G. aspera*.

5.5.5 Flow patterns behind a single coral colony

Velocities behind the single isolated coral were significantly reduced relative to distance upstream, indicating a turbulent wake. With increasing distance downstream from the coral, the wake attenuates.

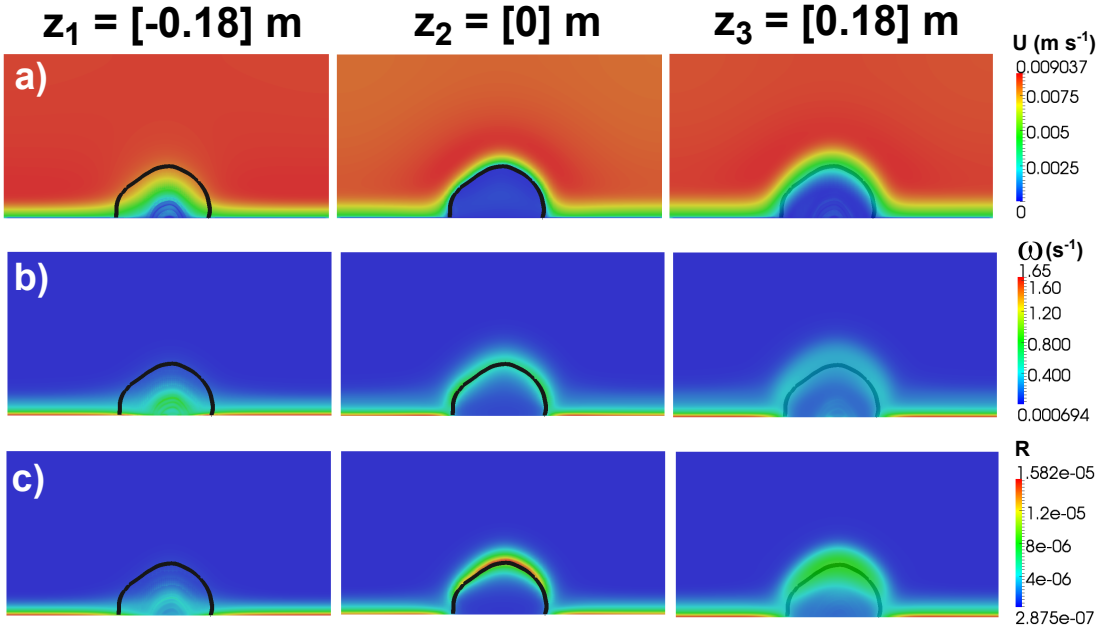

Figure 5.25. Spatial structure of a single coral colony for (a) velocity (U), (b) specific turbulent dissipation rate (ω), and (c) Reynolds stress (R) at three distances downstream (z: -0.18 m, 0 m, and 0.18 m) at 14 May 1995. The solid black line indicated the outline of coral cross-section

5.5.6 Surface warming on both sides of *G. aspera*

The variation of tidal heights on shallow reefs not only influences K_D, but also greatly alters the flow characteristics within the coral and consequently the coral surface warming, especially when the impermeable tissue layer is breached by borers and coral grazers which create pathways for percolation fluxes through a highly porous and therefore permeable coral skeleton (Figure 5.26).

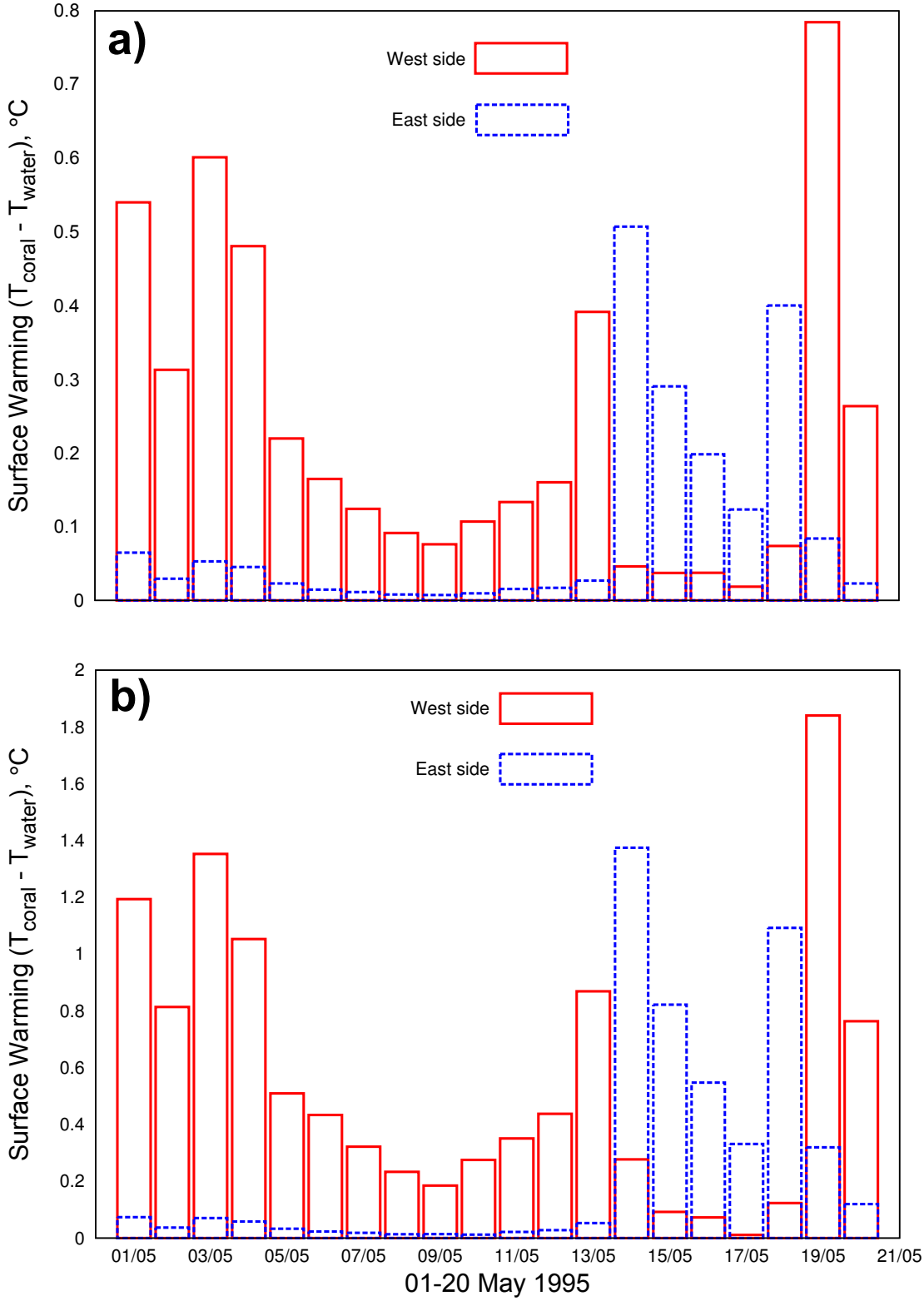

Figure 5.26. Surface warming of the west and east surfaces of *G. aspera* in response to irradiance and semi-diurnal mean zonal currents for a) high-tide and b) low-tide scenarios.

The flow penetration in coral from one face to another is significantly reduced as it passed through almost impermeable coral tissue which induces convective cooling at the downstream face of *G. aspera* colony (Figure 5.27).

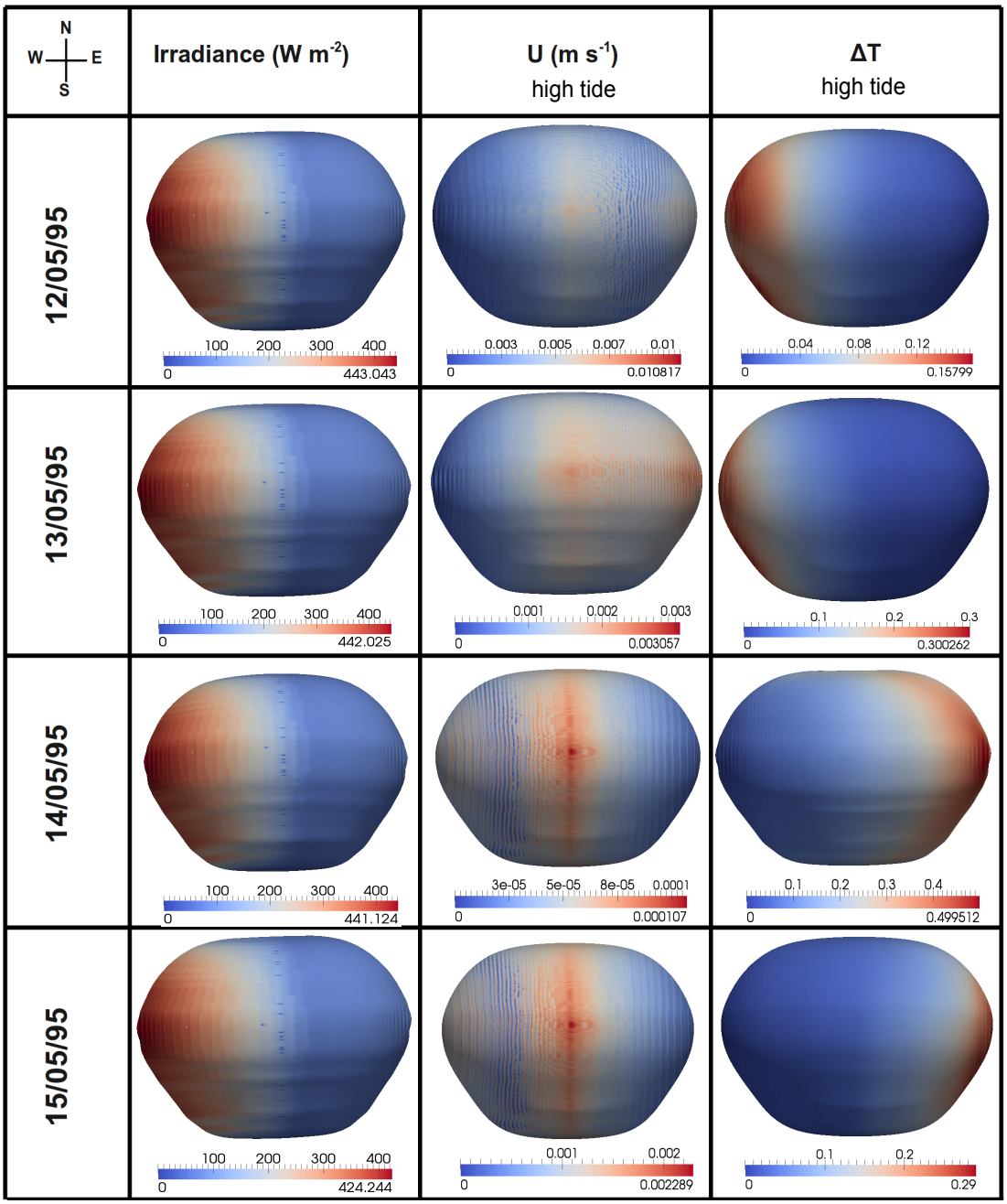

Figure 5.27. Effects of flow and irradiance for a high-tide scenario showing the differential patterns of thermal stress on the west and east sides of *G. aspera*.

5.6 Discussion

This chapter presents a coupled wave-hydrodynamic and ray-tracing and CFD model to investigate variability of waves and low-frequency currents and wave-current interactions and subsequent coral surface warming. The CFD model has been validated previously against laboratory observations to predict variation of thermal stress in coral microenvironments (Chapter 3 and 4).

The hydrodynamic model of a coupled ROMS-SWAN reproduced tides, wind-induced currents and waves reasonably well. The low-frequency currents determined eastward component following the onset of the monsoon and a wave sheltering effect showed that the western side was prone more to wave-induced mixing than that on the eastern side, thus, it may have contributed to a decrease in thermal stress of the corals on the western side. Given that the resolution of bathymetry (1 km), the wave-current interactions and the wave-wave interactions could not be examined in a great detail. Furthermore, although the simulated tides were in good agreement with predicted tides, the model results are deemed preliminary given lack of in-situ data to validate the model and requires further validation by collecting in-situ data or satellite-based data. Adding the baroclinic component (temperature and salinity) may give insight into the variability of residual currents and waves influence temperature and mixing and consequently thermal stress of coral reefs if high-resolution bathymetry and in-situ data become available. Because the hydrodynamic system was driven by the tidal constituents and wave boundary conditions at the open boundaries of the model and wind at the entire domain of the model, hence some numerical uncertainties may result due to solver schemes and the missing forcing during the tidal constituents set-up and waves. Despite uncertainties in the model set-up and low data resolution, qualitative agreements were observed between the predicted ROMS-SWAN and the OSCAR current data (Figure 5.17) with a total root-mean square error of 0.064 m/s, as well as for the estimated and satellite-based observation of the sea level. A validation study between OSCAR current and in situ data measured from moored current meters was conducted by Johnson *et al.* (2007), the results found reasonably accurate time means of zonal and meridional currents in the near-equatorial regions. Moreover, the sensitivity of surface-to-subsurface velocity inference to the measurement uncertainties was previously performed in Shen *et al.* (2001), the inferred result was found to be generally robust.

The differential bleaching pattern could not be attributed for by genetic differences in zooxanthellae genotypes from the east and west faces because at the time it was first noticed, the east surface was not exposed to a higher irradiance. Thus, since their genotypes did not vary significantly, it is most likely that there was no shift genetically although the impact of plasticity could not be ruled out. Therefore, the "experience-mediated tolerance" hypothesis, suggested by

the authors, cannot be used solely as the main cause for the differential bleaching pattern. Also, it appears that during this event, other species were bleaching and so the conditions were likely to be right on the edge of favourable for corals, thus it might not take much additional incremental stress to induce bleaching.

The characteristics of currents moving across a coral reef are governed by the dynamic balance among tide, waves, and wind effects. My preliminary analysis suggest that the low-frequency currents showed eastward component following the double monsoon onset on 14 May 1995. This finding is further supported by the works of Flatau *et al.* (2001) and Nair *et al.* (2010), which observed early onset over Andaman Sea on 14 and 15 May 1995. They indicated that the initial "bogus onset" was followed by the flow weakening and reversal and clear-sky and dry conditions over the monsoon region that appeared in mid-May and disappeared by the end of the month in the Indian Ocean and Andaman Sea. Therefore, the associated changes in water circulation during a period of calm conditions at a low wind speed and low wave height is a plausible explanation for the differential patterns of thermal stress on the eastern and western sides of *G. aspera*. Furthermore, a wave sheltering effect was quantified and the western face was more prone to wave-induced mixing than the eastern face, which may have contributed to a reduction in thermal stress of the corals on the western face.

A number of studies have established that water flow may perform a number of roles during and following episodes of coral reef bleaching (Carpenter and Patterson, 2007; Smith and Birkeland, 2007). This finding suggests that intermittent flows associated with semi-diurnal tides, and low irradiances caused by turbidity or shading, may reduce photoinhibition and bleaching during warming events. Figure 5.25 shows that the flow penetration in coral from one face to another is reasonably reduced by the almost impermeable coral tissue which restricts heat transfer to convective cooling at the downstream face of *G. aspera* colony. This pattern of differential coral surface warming on the western and eastern surfaces indicate that the higher water flow across the eastern face of the colony led to a reduction in photoinhibition which in turn enhanced the efficiency of xanthophyll cycling in the excess-energy-dissipation process (Nakamura et al., 2005) and therefore can cause the bleaching pattern. Water motion can also affect nutrient availability during photosynthesis, with some experimental and empirical studies indicating that the flux of oxygen is higher under no-flow conditions (Mass et al., 2010). Oxygen radicals produced by zooxanthella, at high irradiance coupled with no-flow conditions could damage pigments and proteins and therefore induce coral bleaching. Some findings suggested that growth rates and consequent porosity and permeability of coral skeletons in massive corals may prove to be crucial in determining their bleaching susceptibility and severity of bleaching when it occurs (Cooper et al., 2012).

5.7 Summary

The development of "ecosystem models" was divided into three stages: firstly, a coupled model of ROMS-SWAN was used to investigate the 2-D hydrodynamic nearshore currents based on the available oceanographic data; secondly, the solar irradiance load model was used to quantify the amount of semi-diurnal surface irradiance and the variation of irradiance levels due to turbidity, cloud cover, water depth (tides), and sea-state; finally, CFD simulation was implemented to solve for the coral tissue/surface warming based on coupled dynamics of water flow, heat transfer and irradiance levels in and around corals.

The field observational study of Brown *et al.* (2000) was used as an initial motivation or conceptual study to explore the full range of parameters that could trigger asymmetric bleaching scenarios. The result of this study could potentially valuable as it could be readily applied to understand other reef system and other conditions. Although there exist other potential stressors – such as a reduction in the flux of particulate matter or suspended sediment in a flow – the thermal stress variability due to flow reversal during the double monsoon onset as well as the difference of wave sheltering and wave-induced mixing effects on western and eastern coral surfaces, were most likely to invoke a differential bleaching event.

Chapter 6

The effect of allometry on thermal scaling

6.1 Introduction

Despite the significant threat of coral bleaching, bleaching variability and susceptibility within and between colonies are still not well understood. For example, colonies of the same species often exhibit very different bleaching responses at similar temporal and spatial scales. Overall, the role of the diversity and composition of symbiont populations (*Symbiodinium*) associated with thermal bleaching have received comparatively more attention than that of the role of the coral host yet it is the bleaching of the host that is of primary concern. One approach to better understanding the relationship between bleaching susceptibility and coral morphology is through the observations of the thermal exposure in coral microenvironment. While thermally induced bleaching events have been strongly correlated with seawater surface temperature (SST), few emerging studies have shown a clear difference between coral surface (tissue) temperature and SST (Fabricius, 2006; Jimenez et al., 2008; Ong et al., 2012). It is this thermal stress, induced by a combination of multiple environmental factors (i.e. irradiance, cloud cover, water quality, sediment and water flow rate) (Anthony et al., 2004; Berkelmans et al., 2004; Glynn, 1993; Hoegh-Guldberg and Salvat, 1995; Mumby et al., 2001), as well as differences in growth form and the colony biomass and tissue pigmentations (Cooper et al., 2012; Jimenez et al., 2008; Ong et al., 2012; Thornhill et al., 2011), and differences in symbiont types and the species composition of coral assemblages (Loya et al., 2001; Marshall and Baird, 2000; Rowan et al., 1997) that are most likely to trigger and determine the severity of bleaching.

Morphological variations in bleaching susceptibility are often attributed to inherent differences in growth rate (Baird and Marshall, 2002; Marshall and Baird,

2000), thermal tolerances of photoendosymbionts (Berkelmans and Van Oppen, 2006), tissue thickness, and/or marked differences in colony size and age (Loya et al., 2001). However, one of the most predominant drivers and the likely best explanation of consistent variation in bleaching susceptibility is the level of physiological integration (Baird and Marshall, 2002; Brandt, 2009; Loya et al., 2001; Marshall and Baird, 2000; Shenkar et al., 2005), which is highly linked with coral morphology that includes, but is not limited to, size, shape, and composition (i.e. taxonomy, tissue thickness, permeability, and aragonite density) of the colony. The phylogeny of the Scleractinian coral confounds morphological variations; highly complex branching, simple hemispherical, encrusting forms are non-randomly distributed among coral clades (Veron, 1995, 2000).

In general, fast growing and finely branched species, such as *Acropora* and *Pocillopora*, are highly susceptible to thermal stress and experience high rates of whole colony mortality (Baird and Marshall, 2002; Guest et al., 2012; Loya et al., 2001; Marshall and Baird, 2000). In contrast, massive corals such as *Porites* and *Faviid* are more resistant to thermal stress and more frequently experience partial, rather than whole colony mortality associated with bleaching (Baird and Marshall, 2002; Guest et al., 2012; Loya et al., 2001; Marshall and Baird, 2000; Woesik et al., 2001). Therefore, the accumulating evidence that some types of corals tend to bleach more readily than others may be defined by a possible relationship between colony morphology and bleaching.

Increasing body size exposes the structural, functional, and geometric constraints of phenotype which result in scaling effects and that in turn can have have profound influence on an organisms physiology (Edmunds and Gates, 2002; Gould, 1966; Schmidt-Nielsen, 1984). Size normalisation assumes a proportional relationship (i.e. isometry), however, the assumption of isometry is rarely demonstrated and most traits scale disproportionately with size (i.e. allometry) (Edmunds and Gates, 2002; Packard and Boardman, 1988). Therefore, the relationship between surface area and volume is fundamentally important relationship that affects an organism's metabolism and thermal regulation (Gould, 1966; Schmidt-Nielsen, 1984; Vollmer and Edmunds, 2000). Colony size also plays a role in determining patterns of mortality of bleached corals. For instance, small juvenile colonies of some species can survive better than large, mature colonies (Loya et al., 2001; Mumby, 1999; Riegl, 2002; Van Woesik et al., 2004). Consequently, repeat bleaching events might shift age distributions toward smaller colonies with lower fecundities (Done, 1999), in turn hindering the recovery of these reefs. However, this may not be true of all sites and species, and may vary according to how other environmental stressors interact with bleaching which suggested that large colonies might be more resistant than small colonies to environmental disturbances, such as nutrients and sedimentation (Bak and Meesters, 1999). These studies provide evidence that colony-level differences may indeed af-

fect bleaching susceptibility in this habitat and suggest that the impact of future thermal anomalies may be biased toward larger colonies of dominant reef-building species (Brandt, 2009).

The study of the relationship between coral bleaching and colony morphology has been dominated by laboratory, continuous field and in-situ observations, and predictive modelling studies based on remotely sensed sea conditions, particularly SST. While useful, these experiments are inevitably restricted to investigating only a few colony and locations due to their relatively high cost and difficulty in obtaining accurate measurements. In addition, predictive modelling is limited by the assumption that SST, or other such parameters, adequately represents key environmental features that are related to bleaching. An additional challenge for biological assessments of coral size is to progressively measure the surface area and volume of corals in-situ during growth. There have been several approaches to estimating the three-dimensional morphology of corals (i.e. surface area and volume). While these approaches are reliable for simple coral growth forms, estimation for complex growth forms is less certain for complex growth forms (Edmunds and Gates, 2002; Holmes, 2008; Jones et al., 2008). In contrast, numerical modelling technique, such as computational fluid dynamics (CFD) used throughout this thesis, provide a holistic approach to understanding detailed interactions between heat and fluid dynamics and coral morphology with varying permeability and thicknesses of coral tissue and skeleton. Previously, I established the potency of CFD in estimating the thermal stress of coral microenvironments under controlled laboratory conditions such that the flow regime was laminar and irradiance was fixed at an overhead 90° angle (Chapter 3). Here I assess whether corals of the same species, but that vary in size and shape, may respond differently to thermal stress due to different heat transfer rates and thermal capacities related to differences in surface area-to-volume (A/V) ratios and their relationship to thermal scaling in coral microenvironments.

6.2 Isometric and allometric scaling

The concept of isometric and allometric scaling presented in this section can be used as an aid to understanding the correlation between the size and shape of a coral with the effect of scaling. Scaling, the study of the influence of body size on form and function, provides a useful tool for exploring differences in morphology among individuals and species (Biewener, 1990; Gould, 1977). Some studies have applied the scaling principle to understand physiological parameters, such as metabolic rate (Schmidt-Nielsen, 1984), and exponential parameters, including population sizes, biomass, and population growth rates (Calder, 1996; Peters, 1986).

If two objects have the same shape, then they are termed isometric (Thompson, 1966). For example, a sphere with radius r has a surface area of $4\pi r^2$ and a volume of $\frac{4}{3}\pi r^3$, thus, the ratio of its volume to surface area A/V is $\frac{3}{r}$. Hence, A/V varies as r. Similarly, using L to represent any linear dimension, the general equations is given by:

$$A \propto L^2, \qquad V \propto L^3, \tag{6.1}$$

$$\text{or} \qquad A = k\,L^2 \quad \text{and} \quad V = k'\,L^3 \tag{6.2}$$

where k, k' are similarity ratio or factors of proportion. In isometric bodies, all corresponding linear dimensions are related in the same proportion, and all corresponding surfaces have areas that are related in the same proportion. Therefore, the final form can be written as:

$$\frac{V}{A} \propto L \quad \text{or} \quad \frac{V}{A} = \frac{k}{k'}\,L = K\,L \tag{6.3}$$

Real coral shapes usually are not isometric, instead certain proportions change in a regular fashion. To test whether corals scale isometrically or allometrically, two sets of anatomical measurements (x and y) can be fitted to the power function to determine the scaling exponent, b. The simplest way to do this is to construct log-transformed plot of morphological data and derive a linear regression of $log(y)$ on $log(x)$, taking the slope as an estimate of b. Hence, the general equation of allometric scaling can be written as:

$$y = a \cdot x^b \tag{6.4}$$

$$\log y = \log a + b \log x \tag{6.5}$$

where y is some observable quantity, x is the size or mass of the coral, a is the y-intercept and b is the slope. If the slope (b) is equal to 1, then the variables exhibit equal proportional changes, and demonstrate isometry. However, most organisms do not scale isometrically and can have a variety of forms:

1. independence ($b = 0$);
2. positive allometry ($b > 1$);
3. negative allometry ($0 < b < 1$);
4. inverse allometry ($b < 0$).

6.3 Thermal and metabolic scaling due to coral shape and size

A priori prediction of how changes in colony size or shape might affect the thermal stress at the scale of the coral microenvironment, depends on two dimensionless indices relevant to size and shape in heat transfer studies: Nusselt number (Nu) and Reynolds number (Re). Nusselt number is the ratio of convective heat transfer to conduction of a solid surface to a fluid, which can be expressed as:

$$Nu = \frac{hL_c}{k_f} \tag{6.6}$$

where, h is the heat transfer coefficient which is governed by operating parameters (size and shape of the coral colony, mass flux, and pressure) as well as physical properties of the fluid (density, specific heat, viscosity, and thermal conductivity), the characteristic length or dimension, L_c, here is defined to be equal to the height normal to the substrate, diameter, and length of right cylindrical, spherical, and plate-like coral morphologies, respectively, and k_f is the thermal conductivity of fluid. Heat transfer coefficients are related to tissue thicknesses, shapes, and sizes of coral colonies by an inverse power function because larger objects will have absolutely thicker boundary layers for the same flow speed relative to small objects. Nusselt number can be calculated locally as a function of position downstream (x) over a coral colony (Nu_x), but doing so would require calculations with surface warming of the local heat fluxes within patches of the colony. Hence, Nu_x is integrated over the entire whole, branching, or massive colonies to determine $\bar{Nu}$, the average Nusselt number.

As discussed in the previous chapter, heat transfer within and around corals occurs by three main mechanisms.

Conduction: The rate of heat conduction from the tissue into the skeleton is the product of the temperature differential between the tissue and the skeleton, the conductivity of aragonite, and the area over which the contact occurs:

$$Q_{cond} = k_s \cdot A \cdot \frac{dT}{ds} \sim \frac{k_s}{s} \cdot A \cdot (T_1 - T_2) = h_{cond} \cdot A \cdot (T_1 - T_2) \tag{6.7}$$

where $h_{cond} = \frac{k_s}{s}$, where k_s is the thermal conductivity of the aragonite and s is the measure for the object size. Another variable that affects the rate of conductive heat transfer is the area through which heat is being transferred. For instance, heat transfer through coral tissue to skeleton depends on the size of the coral. More heat will be lost from a larger area of tissue than a smaller one of the same aragonitic characteristic and tissue thickness.

Convection: The energy flow per second from the surface of the coral with temperature T_1 into surrounding fluid temperature T_2 is affected by the pattern

and rate of fluid movement around the colony, the amount of surface area in contact with the fluid, and the thermal gradient between the coral and surrounding fluid:

$$Q_{conv} = h_{conv} \cdot A \cdot (T_1 - T_2) \tag{6.8}$$

where h_{conv} is the convective heat transfer coefficient and is determined from the coral colony's size and shape with the fluid moving around the coral. These values depend on the Reynolds number, $Re = UL/\nu$ which expresses the ratio of inertial forces to viscous forces that define flow regimes as either laminar or turbulent. The characteristic of the local convective regime similarly affects the flux of heat away from the surface and is determined from Nu. Therefore, plots of Nu (ordinate) - Re (abscissa) yield information on the degree to which water motion (momentum flux) affects convective heat transfer. The relationship can be expressed as a power law:

$$Nu = a\, Re^b \tag{6.9}$$

where a and b are heat proportionality coefficients and heat exponent values, respectively, and in logarithmic form:

$$\log Nu = \log a + b \log Re \tag{6.10}$$

The curvature of the Nu vs. Re relationship was fitted in a linear format in a log-log coordinate to yield information on the a^* and b^* which are the global heat coefficient and exponent terms, respectively. These values are directly affected by the coral shape and flow regime, thus varied among colonies (Patterson, 1992b). The heat exponent, b, is the most important coefficient in determining the degree to which flow augments convective heat transfer relative to diffusion, and its numerical value indicates whether the transport is occuring through a laminar ($b \approx 0.5$) or turbulent ($b >\approx 0.6$) boundary layer around the exchange surface (Patterson et al., 1991; White, 1988). Hence, it follows that h_{conv} depends on viscosity, thermal conductivity of the fluid and coral, and also nonlinearly on the temperature difference, i.e. $h_{conv} \sim \Delta T^b$, where the power of b depends on flow conditions.

Radiation: The heat flux due to absorption of radiation, ΔQ, is proportional to ΔI, α, and the coral surface area (A). Defined as the fraction of incident radiation absorbed by the surface, α, accounts for a range of factors affecting the amount of absorbed light, such as the optical properties of both the host tissue (host pigments, tissue thickness) and the zooxanthellae (symbiont density, photosynthetic pigments). Refer to Equation 2.10.

These modes of heat transfer analysis leads to the exponential Newtonian heating or cooling behaviour since the amount of thermal energy in the body is

directly proportional to its temperature, which in turn determines the rate of heat transfer into or out of it. The heating and cooling in a coral can be represented using a simple first-order differential equation which is given by:

$$\frac{dT_{coral}}{dt} \propto T_{coral} - T_{fluid} \tag{6.11}$$

Heat transfer is directly proportional to surface area, whereas heat capacity is proportional to volume. The above equation can be rephrased in terms of $q'' = Q/A$ as

$$q'' = \bar{h}(T_{coral} - T_{fluid}) \tag{6.12}$$

where, $\bar{h}$ is the average heat transfer coefficient over the surface of the body. Without the bar, h denotes the "local" value of the heat transfer coefficient at a point on the surface. Thus, the heat accumulation and dissipation highly depend on three parameters: coral size and shape, convective heat transfer coefficient, and the coral absorptivity and emissivity.

A similar analogy to heat transfer can also be applied to mass transfer in order to determine the relation between body size and metabolic rate in coral. The Sherwood number ($Sh = h_m L_c/D$) is a dimensionless index of metabolic or mass transfer rate which can be written as:

$$Sh = \frac{h_m L_c}{D} \tag{6.13}$$

$$Sh = cRe^d \tag{6.14}$$

where h_m is the mass transfer coefficient and D is the diffusion coefficient of the dissolved species (Patterson, 1992b). Plots of $Sh - Re$ yield information on the degree to which water motion affects mass transfer, which is expressed as a power law, where c is termed the mass coefficient and d is termed the mass exponent (Patterson, 1992b).

6.4 Model assemblages and configurations

The physical models of various shape and species were used to determine the range of heat exponent values and the degree to which water motion and morphology affect heat transfer, and ultimately, the thermal microenvironments. Most of the models used in this study were scanned using a medical computed-tomography (CT) scanner with isotropic resolutions. I reconstructed the scans using an image processing package, Fiji (Ferreira and Rasband, 2012), converted to a binary stereo lithography (STL) format, and visualised using the visualisation toolkit (VTK) based software, Paraview. A few additional models were created manually with the aid of computer-aided-design (CAD) software (i.e. Blender).

From the point of view of morphology, corals can be classed into mainly two shape categories: (1) branching (mostly large branching, tabulate, or corymbose); (2) massive (mostly massive, columnar, foliose, or encrusting). Their scaling properties do not depend on most details of morphological traits, including the branching patterns. The degree of overall similarity ratios (K) between branching and massive coral morphologies were evaluated using the equation 6.3. The model assemblages and similarity ratios are shown in Table 6.1and Figure 6.1. The characteristic dimension, L, was taken to be equal to the height normal to the substrate, diameter, and length of various shapes (i.e. cylindrical, spherical, flat-plate, etc) measured in meters.

Table 6.1. Model assemblages (specified and generalised) and predicted similarity ratios.

Species	shape categories	L	K
Acropora digitifera	B	0.56	45
Acropora millepora	B	0.56	42
Pocilliopra eydouxi	M	0.91	50
massive coral	M	0.35	1.2
Fungia sp.	M	0.79	73
cylindrical branch	B	0.03	66
Goniastrea aspera	M	0.40	1.5
Montastrea annularis	B	0.48	40
Madracis mirabilis	B	0.25	43
Porites sp.	M	0.64	53
Seriatopora caliendrum	B	0.56	38
Seriatopora hystrix	B	0.49	236

To examine the effect of allometry on thermal scaling in the oral microenvironments, each model morphology was scaled in size in order to explore various magnitudes of A/V ratios. Coral morphologies were modelled for two thermal and flow regions, tissue and skeleton, each with its own thermal functions and permeabilities (Figure 2.1). The flow of water through the coral tissue and skeleton (if it occurs), should significantly influence the thermal microenvironment of the coral. In constructing these models, I have developed models that allowed us to evaluate a diverse range of scenarios. In particular, I hypothesised that there

is unlikely to be any significant permeability through intact living tissue, however, in many real life cases, the activity of borers and coral grazers will result in openings allowing percolation and increased skeletal porosity. Thus, in this work I modelled a very small percolation flow along the tissue layer (∼1-2%) and a moderate flow through the skeletal matrix (∼7-10%) (Ong et al., 2012).

The size specifications of flow chambers in laminar and turbulent flow regimes were randomly set at 15 cm h (height) × 10 cm w (width) × 25 cm l (length), and 15 m h × 10 m w × 25 m l, respectively. The direct sunlight measured at 12 noon with a steady-state unidirectional flow of seawater maintained at 0.01 m s^{-1}, and the seawater temperature at 26°C. The choice of the solar position for global irradiance was somewhat arbitrary, with emphasis on using the ray-tracing model. Here I set the solar position to have an azimuth angle of 35° and an elevation angle of 86°, with the maximum irradiance of ≈ 500 W m^{-2}.

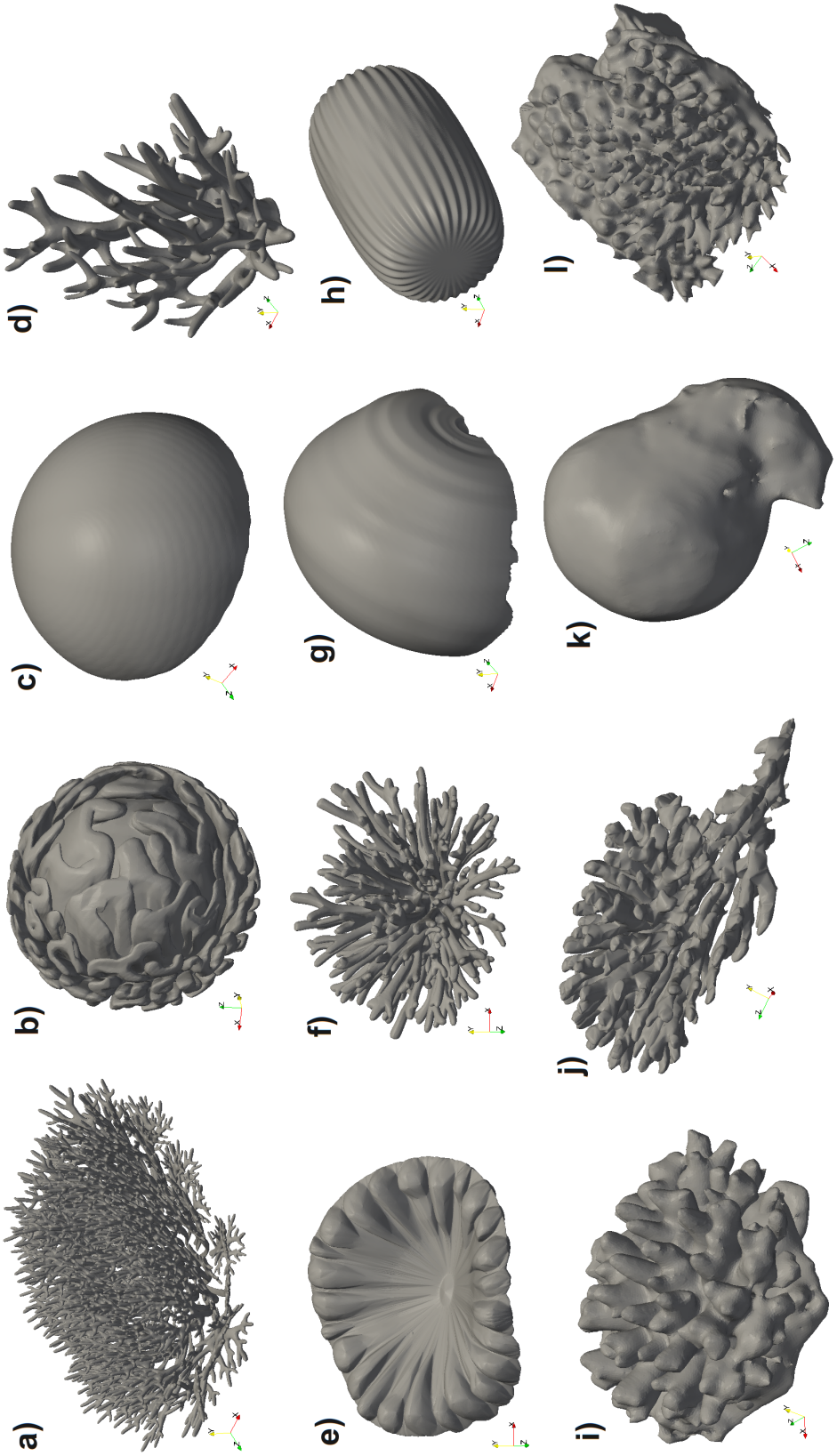

Figure 6.1. Models of coral species studyied here: (a) *Acropora millepora*, (b) *Pocillopra eydouxi*, (c) massive coral, (d) *Seriatopora hystrix*, (e) *Fungia sp.*, (f) *Seriatopora caliendrum*, (g) *Goniastrea aspera*, (h) cylindrical branch, (i) *Montastrea annularis*, (j) *Madracis mirabilis*, (k) *Porites sp*, (l) *Acropora digitifera*

6.5 Model boundary conditions

This study mainly used two types of grids, predefined block structured hexahedral and polyhedral, to represent both computational and coral domains with approximately 900,000 cells for laminar flow simulations. In turbulent simulations, it was necessary to place the grid line closest to the wall at an appropriate distance in order to resolve the boundary layers within the first layer of cells and the second layer consists only of flow with turbulent characteristics. To run the low-Reynolds turbulence cases, the y^+ ~1.0 (viscous sublayer region) with ~2,500,000 cells.

The initial and boundary conditions for laminar and turbulent simulations were shown in Table 6.2 and 6.3. To impose boundary layers in the viscous sublayer region and to accommodate convergence, the initial conditions of k and ω at the wall are specified differently from the free-stream conditions. We estimated the turbulence intensity, I, and length scale, l to be ~0.05-0.1% and ~50% of coral diameter, respectively.

Table 6.2. Initial and boundary conditions for laminar simulations

Parameter	Initial Value	Surrounds	Seafloor	Inlet	Outlet
p_{ref}	0 Pa	S	ZG	ZG	FV
u	0.01 m s^{-1}	S	FV 0.01 m s^{-1}	FV	ZNG
T	26°C	S	FV	FV	ZG

Table 6.3. Initial and boundary conditions for turbulent simulations

Parameter	Seafloor	Inlet	Outlet
k (m^2s^{-2})	10^{-10}	TIKEI	IO
ϵ (m^2s^{-3})	FV	TMLDRI	IO
ω (s^{-1})	$\frac{60\nu}{\beta_1 y^2}$	TMLFI	IO
ν_t (m^2s^{-1})	C	C	C
u (m s^{-1})	(0 0 0)	FV	IO
T (K)	FV	FV	ZG

*SP: symmetry plane, ZG: zero gradient, ZNG: zero normal gradient, FV: fixed value, C: calculated, TIKEI: turbulent intensity kinetic energy inlet, TMLDRI: turbulent mixing length dissipation rate inlet, TMLFI: turbulent mixing length frequency inlet

6.6 Surface area and volume estimations

One of the main challenges for biological assessment of coral reefs over large temporal and spatial scales is the ability to extrapolate data obtained at the microsensor scale to tissue biomass, coral surface area, colony weight and volume (Holmes, 2008). To be able to measure the surface area and volume of coral colonies is also essential in order to monitor colony growth and how it may indicate the state of ecosystems at different scales. Determining surface area and volume of corals is essential to understanding their interaction with external and internal physical and biological processes. There have been several approaches proposed to estimate three-dimensional morphological coral properties (mainly surface area, refer to Table 1.1) with various accuracies and environmental scale measurements. While these methods are reliable for simple coral growth forms, large errors are introduced when applying them to more complex growth forms (Edmunds and Gates, 2002; Holmes, 2008; Jones et al., 2008).

Here, I quantify both the surface area and volume of coral models utilising a cell looping technique that calculates and increments cell area and volume over a mesh-based representation with low errors associated with complex morphologies. The theoretical calculations of surface area and volume of a simple hemispherical and cylindrical shape corals were validated against the model.

6.7 Results

6.7.1 Previously validated cases and estimated A/V ratios

The predicted surface areas and volumes from the proposed model agreed reasonably well with the theoretical results (Table 6.4) with low root-mean-square error (RMSE) between the two measurements. In the previous chapters, the validation studies of laminar and turbulent flows in coral thermal microenvironments were investigated (Chapter 3 and 5). The results of global horizontal irradiance agreed well with the spectroradiometer data scans of Brown *et al.* (1994) (Brown et al., 1994), and was shown in the Chapter 4 (Figure 4.3, 4.4, 4.2, and 4.5).

6.7.2 Predicted heat exponents from $Nu - Re$ plots

The heat coefficient and exponent values were estimated from the slopes of the theoretical $Nu - Re$ functions of the whole, branching, and massive colonies for both laminar and turbulent flows (Figures 6.2, 6.3, and 6.4). The $\bar{Nu}$ indicates the average behaviour of heat transfer relative to diffusion and boundary layer thickness. The $\bar{Nu}-Re$ data were fitted to an expression of the form: $\bar{Nu} = aRe^b$,

Table 6.4. Comparison of the actual and estimated surface area and volume

Shape	Size (m)	Actual		Model		RMSE	
		A (m^2)	V (m^3)	A (m^2)	V (m^3)	A (m^2)	V (m^3)
Hemisphere	0.5 ϕ	0.39	0.0327	0.41	0.0331	0.020	4×10^{-4}
Cylinder	0.3 ϕ & 0.3 h	0.283	0.0106	0.262	0.0123	0.021	0.002

where the slope, b, and the intercept, a, were obtained by regressing the least-squares linear function from these log-log plots (Table 6.5).

Table 6.5. Global heat proportionality coefficient ($\bar{a}$) and exponent ($\bar{b}$) values from $\bar{Nu} - Re$ plots

Constants	Whole colonies		Branching		Massive	
	Laminar	Turbulent	Laminar	Turbulent	Laminar	Turbulent
$\bar{a}^*$	0.39	1.49	0.27	1.22	0.47	1.75
$\bar{b}^*$	0.58	0.85	0.58	0.91	0.57	0.77
R^2	0.77	0.77	0.75	0.75	0.86	0.79

Note that the heat exponents for laminar flow result in lower values for the heat exponent compared to turbulent flow, thus, colony shape and size and the flow regime have a direct impact on the value of heat exponents obtained.

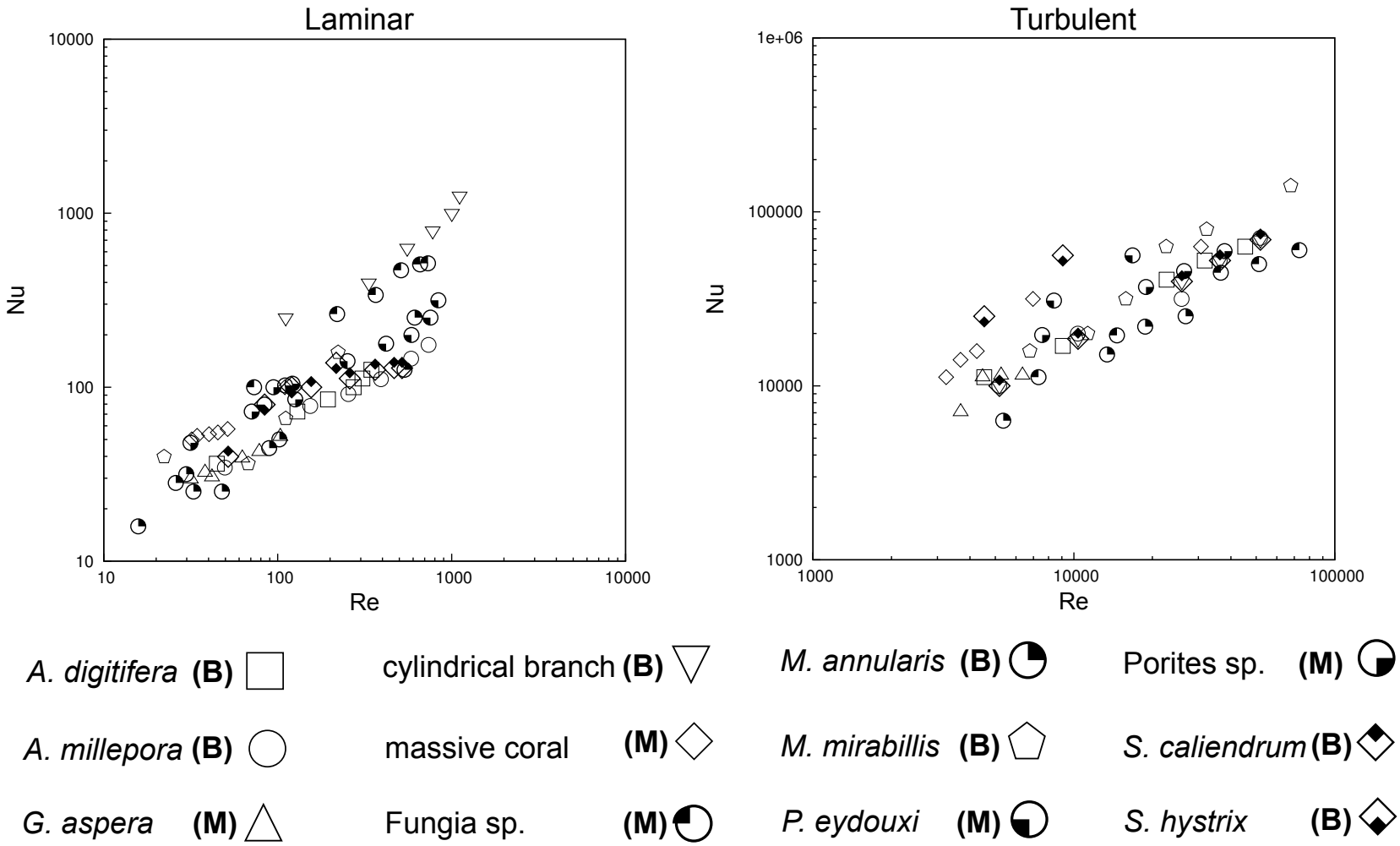

Figure 6.2. $Nu - Re$ plots of whole colonies for both laminar and turbulent flows

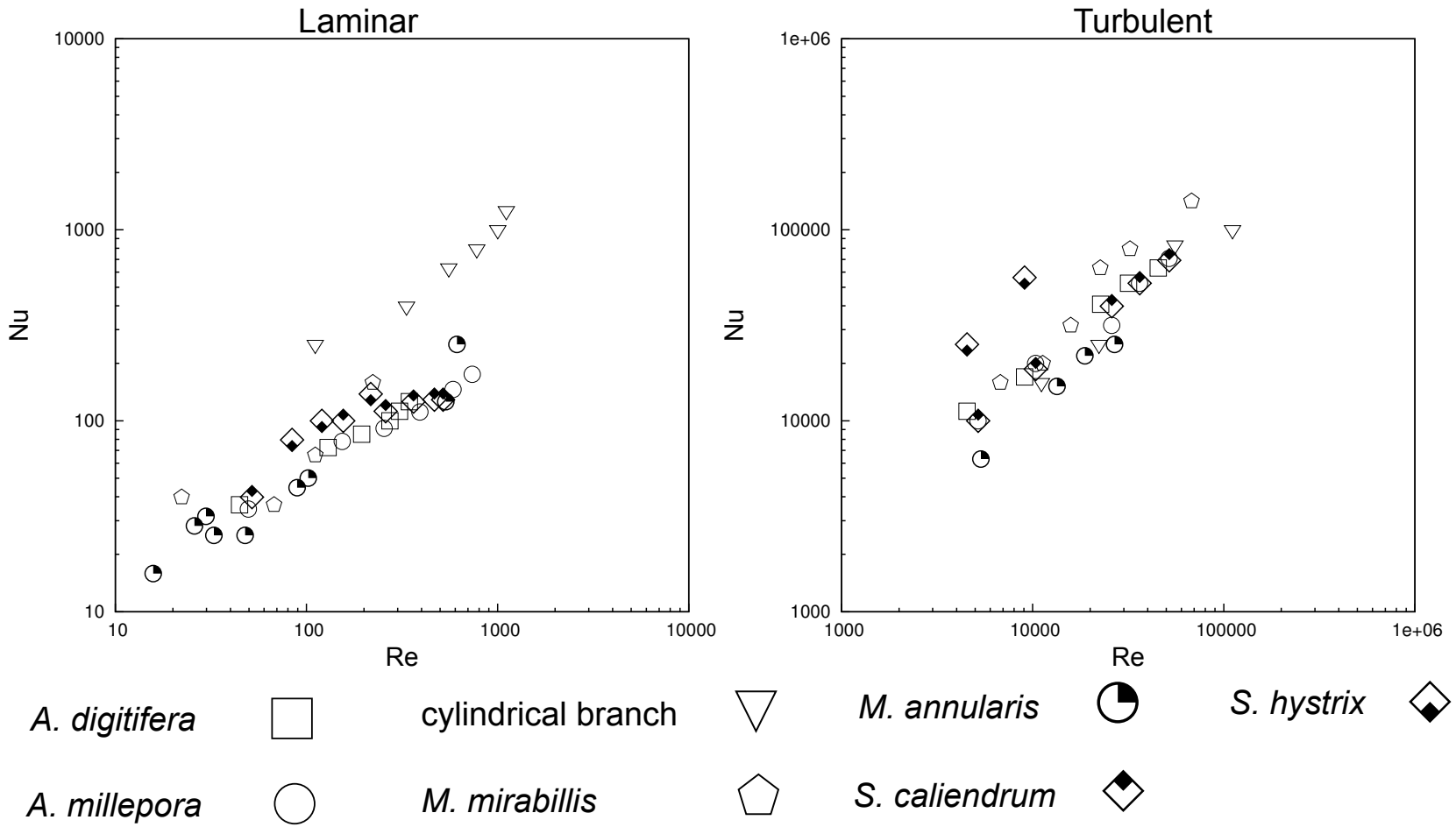

Figure 6.3. $Nu - Re$ plots of branching corals for both laminar and turbulent flows

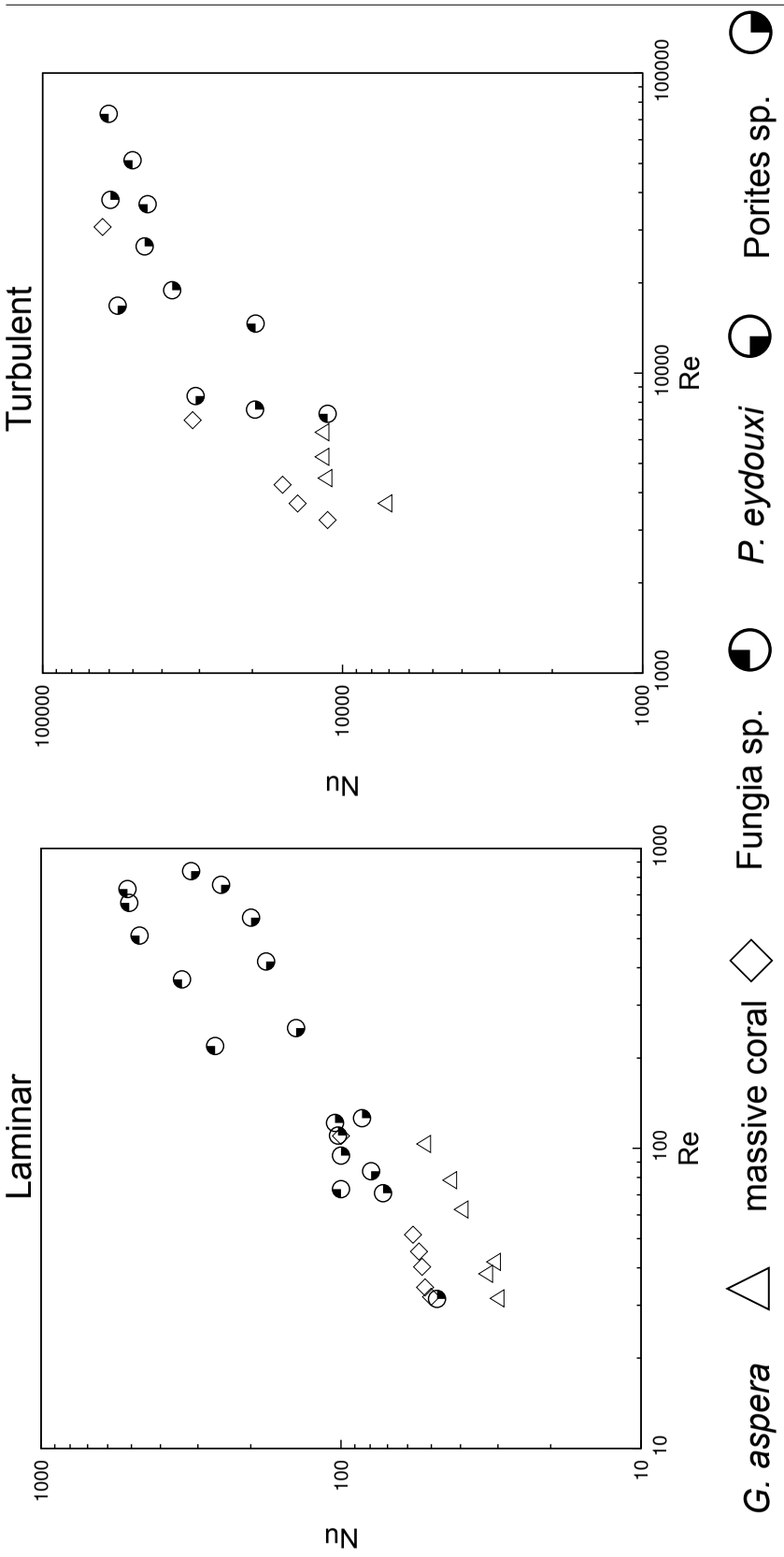

Figure 6.4. $Nu - Re$ plots of massive corals for both laminar and turbulent flows

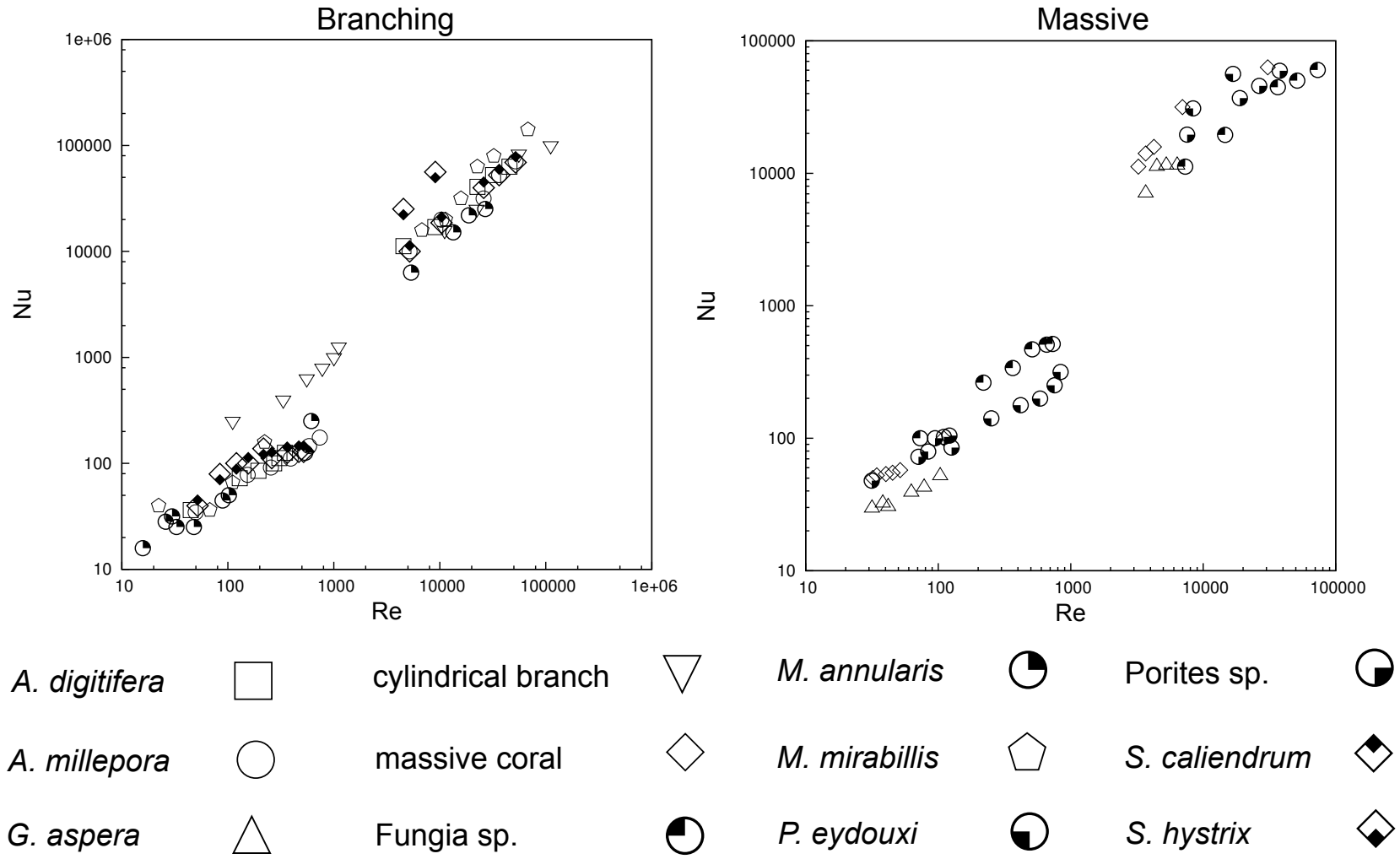

Figure 6.5. $Nu - Re$ laminar and turbulent plots for branching and massive corals

6.7.3 Allometric thermal scaling and predicted warming

Dimensionless analysis of heat transfer in relation to coral morphology provides a powerful alternative to traditional allometric methods in investigations of the effect of shape and size on heat transfer rate. The functional relationship between the magnitude of coral surface warming for a given colony shape and size, and water flow velocity can be written as:

$$\Delta T = C\ A/V^{m}\ Re^{\bar{b^*}}\ \frac{I}{I_0} \tag{6.15}$$

where the term $(\frac{I}{I_0})$ is defined as normalised irradiance intensity and the initial irradiance, I_0, was $\approx$ 500 W m^{-2}. The heat scaling exponents b were previously obtained from $Nu - Re$ plots shown in the Table 6.5.

The constants (C and m) for each of the colonies and flow regimes are obtained by regressing the log-log plots of the generalised allometric thermal scaling against the A/V ratio $\left(\frac{\Delta T}{Re^{b^*}} - A/V\right)$. These plots of whole, branching, and massive colonies for both laminar and turbulent flows are shown in Figures 6.6, 6.7, and 6.8, respectively.

Table 6.6. Global allometric model constants obtained by regressing the generalised allometric thermal scaling plots $\left(\frac{\Delta T}{Re^{b^*}} - A/V\right)$

Constants	Whole colonies		Branching		Massive	
	Laminar	Turbulent	Laminar	Turbulent	Laminar	Turbulent
C	7.94×10^{-3}	1.58×10^{-5}	3.89×10^{-3}	3.98×10^{-6}	4.17×10^{-2}	1.00×10^{-4}
m	0.27	0.65	0.39	0.86	-0.02	0.41
R^2	0.31	0.35	0.99	0.99	0.1	0.94

The local heat coefficients and exponents (a and b) and the allometric constants (C and m) for each geometrical shapes relating Re and A/V ratio to thermal scaling are shown in Table 6.7.

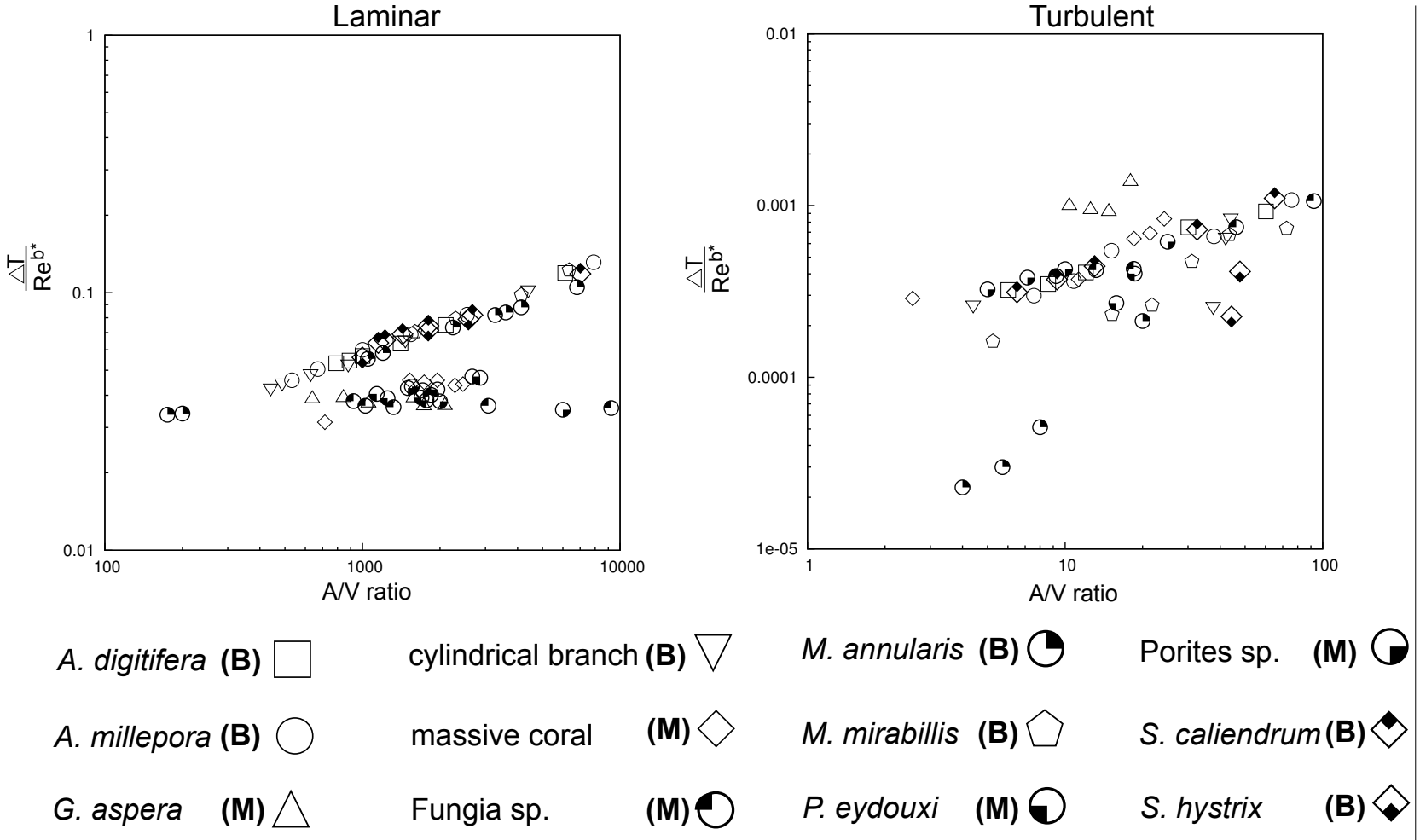

Figure 6.6. Allometric model constants $\left(\frac{\Delta T}{Re^{b*}} - A/V\right)$ of whole colonies for both laminar and turbulent flows

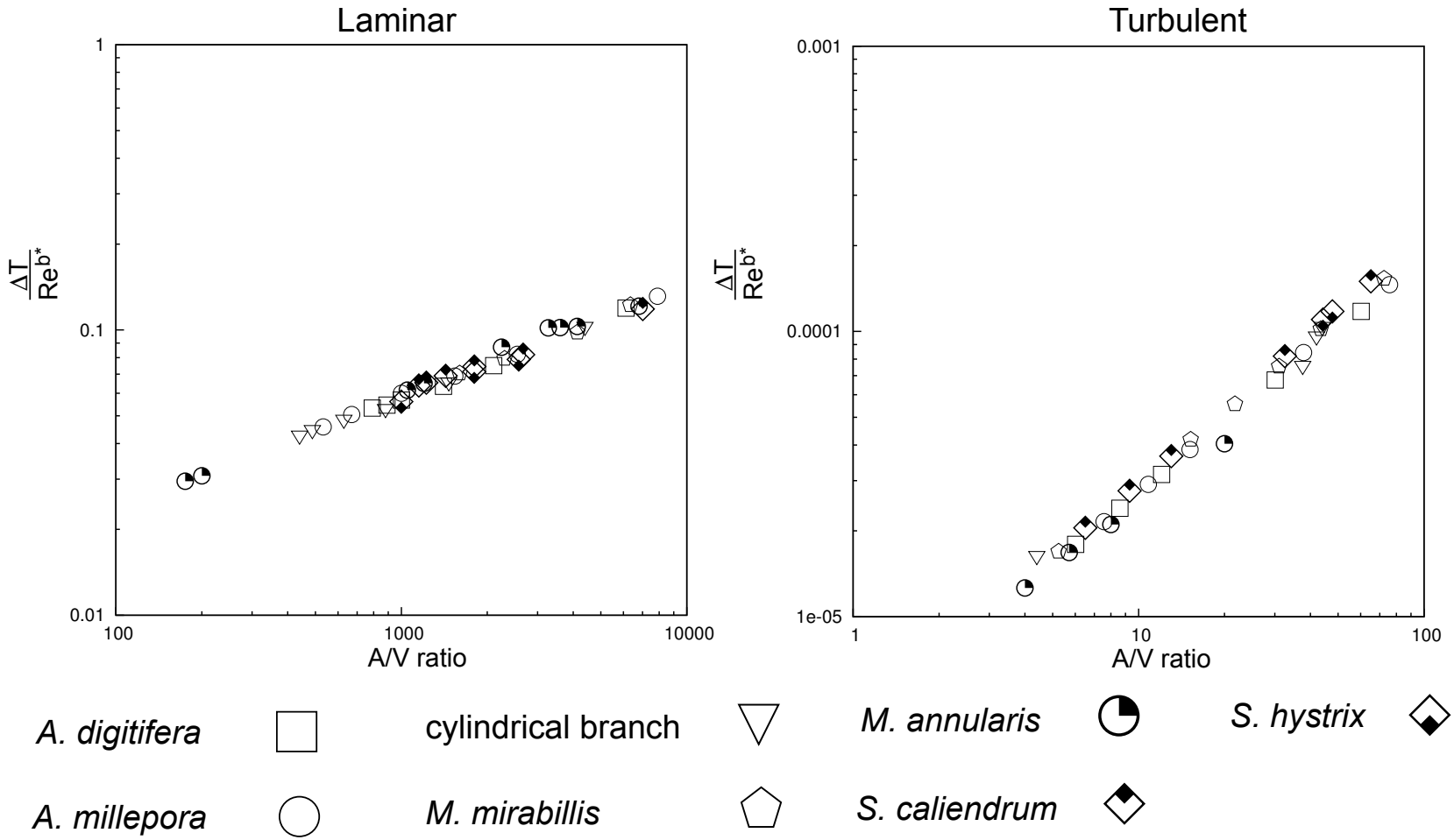

Figure 6.7. Allometric model constants $\left(\frac{\Delta T}{Re^{b*}} - A/V\right)$ of branching corals for both laminar and turbulent flows

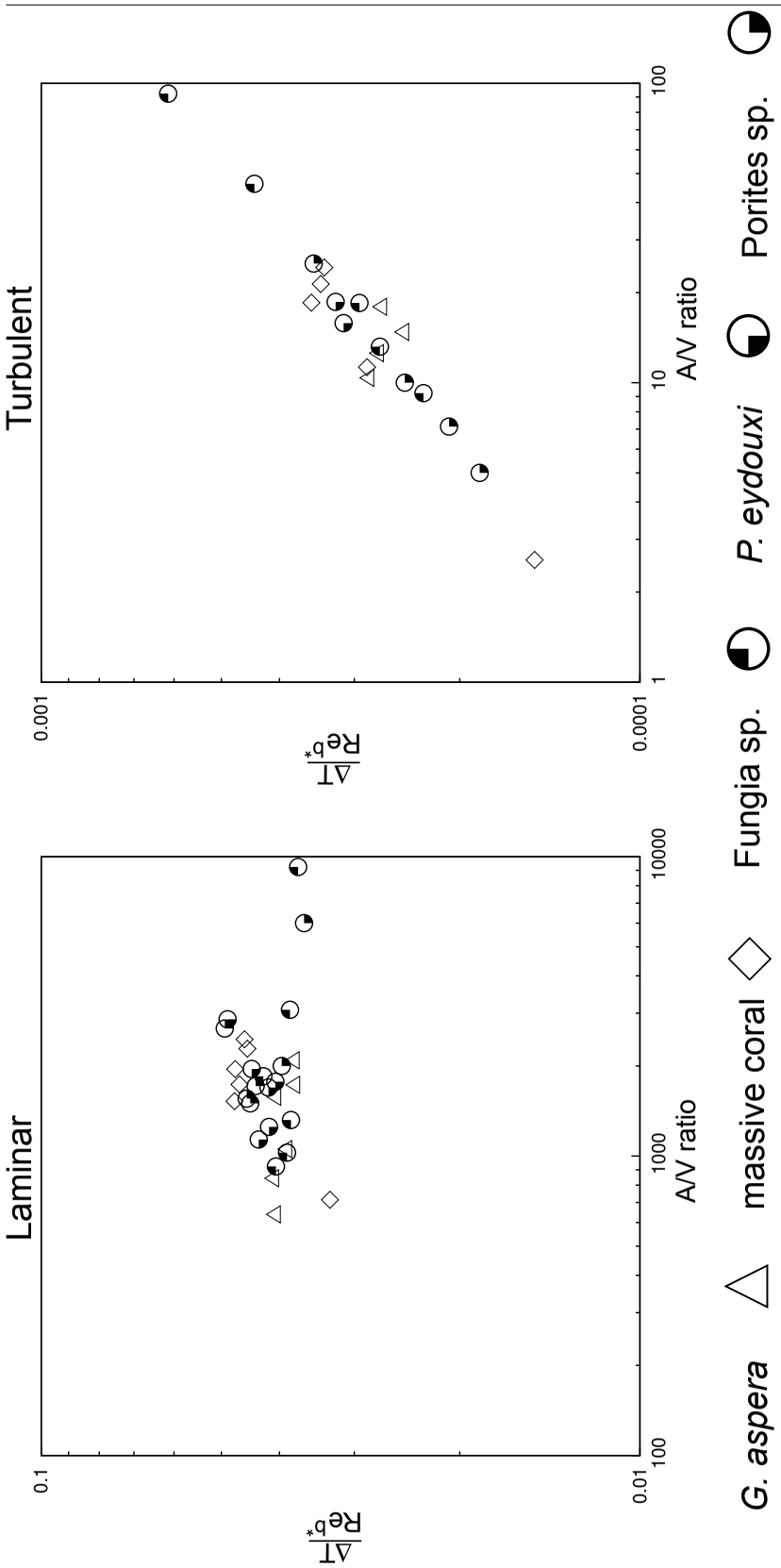

Figure 6.8. Allometric model constants $\left(\frac{\Delta T}{Re^{b^*}} - A/V\right)$ of massive corals for both laminar and turbulent flows

Table 6.7. Summary of local heat coefficients and exponents and the allometric thermal scaling constants of various shape classes in both laminar and turbulent regimes

Shape	Local a and b		Local allometric var.	
	a	b	C	m
Flat plate or mushroom (laminar)	0.68	0.72	6.45×10^{-3}	0.12
Flat plate or mushroom (turbulent)	1.16	0.75	1.17×10^{-4}	0.40
Cylinder (laminar)	0.96	0.68	1.14×10^{-3}	0.48
Cylinder (turbulent)	0.68	0.87	7.94×10^{-6}	0.74
masive - hemispherical (laminar)	0.83	0.56	5.75×10^{-3}	0.28
massive - hemispherical(turbulent)	1.52	0.75	1.35×10^{-4}	0.36
massive - *G. aspera* (laminar)	0.75	0.47	1.18×10^{-1}	-0.16
massive - *G. aspera* (turbulent)	0.96	0.83	1.99×10^{-4}	-0.09
massive - *Porites* (laminar)	0.89	0.53	1.82×10^{-1}	-0.16
massive - *Porites* (turbulent)	1.63	0.69	2.51×10^{-4}	0.32
encrusting - *P. eydouxi* (laminar)	0.83	0.55	1.54×10^{-2}	0.14
encrusting - *P. eydouxi* (turbulent)	1.10	0.86	2.51×10^{-5}	0.57
columnar - *S. hystrix* (laminar)	0.79	0.58	4.57×10^{-3}	0.36
columnar - *S. hystrix* (turbulent)	0.15	1.16	7.94×10^{-11}	3.12
columnar - *S. caliendrum* (laminar)	0.80	0.50	1.99×10^{-2}	0.23
columnar - *S. caliendrum* (turbulent)	0.89	0.84	1.00×10^{-5}	0.80
tabular - *A. millepora* (laminar)	0.58	0.57	3.98×10^{-3}	0.38
tabular - *A. millepora* (turbulent)	0.98	0.81	1.29×10^{-5}	0.73
digitate - *M. mirabilis* (laminar)	0.69	0.58	3.71×10^{-3}	0.40
digitate - *M. mirabilis* (turbulent)	0.22	1.03	9.12×10^{-7}	0.95
digitate - *M. annularis* (laminar)	0.44	0.65	1.66×10^{-3}	0.47
digitate - *M. annularis* (turbulent)	0.49	0.89	6.02×10^{-6}	0.70
digitate - *A. digitifera* (laminar)	0.61	0.58	3.63×10^{-3}	0.40
digitate - *A. digitifera* (turbulent)	1.14	0.79	1.86×10^{-5}	0.70

The analytical equation 6.15 of surface warming is compared against the previous experimental and simulation works (Figure 3.4 and 3.5) and is shown below.

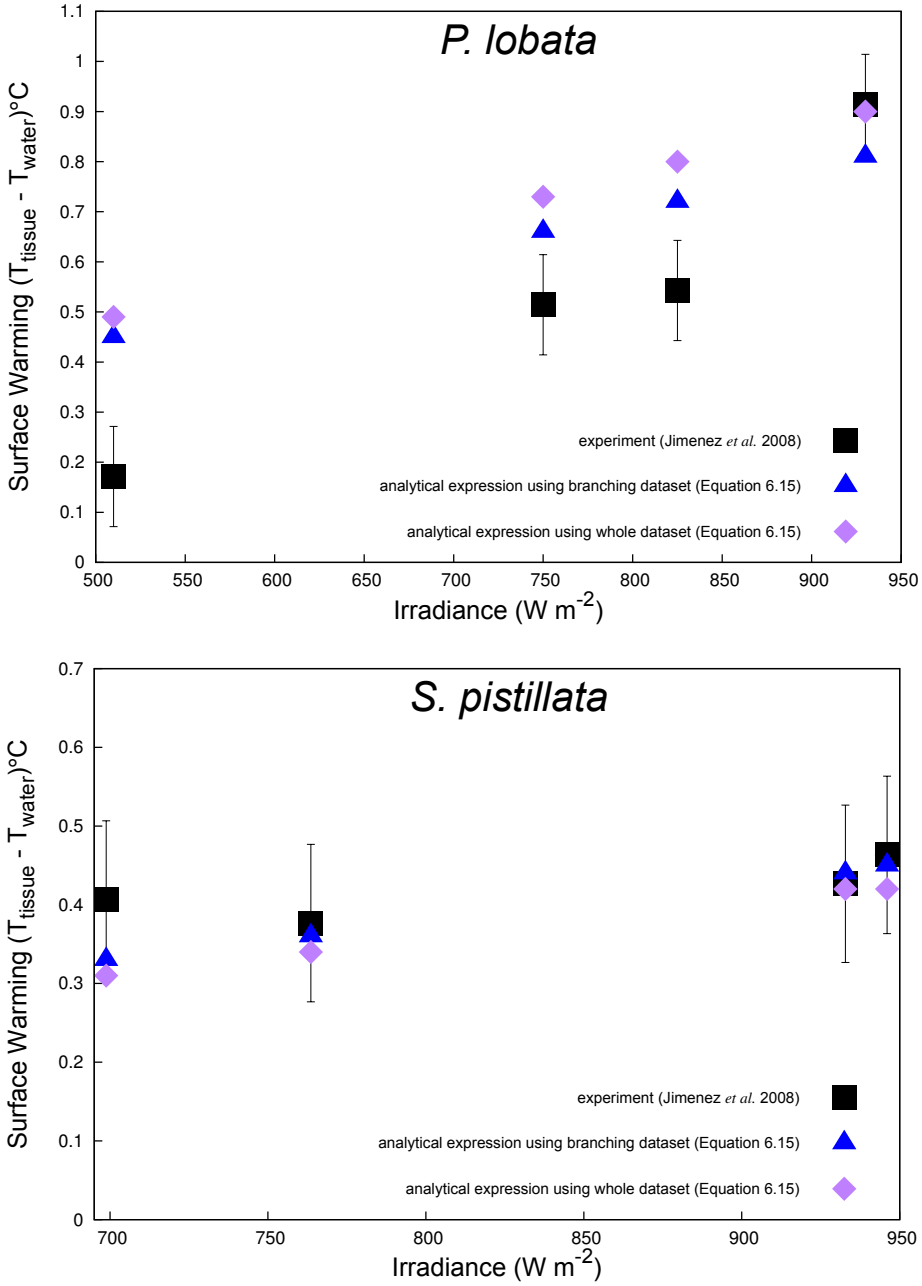

Figure 6.9. Comparisons of analytical vs simulated and experimental surface warming of a hemispherical coral *P. lobata* and a cylindrical branch of *S. pistillata*

The analytical correlation of surface warming was also validated against the previous (Figure 3.13 and 3.12) experimental and simulations using $k-\omega$ SST (Figure 6.10). I then compared the simulated and predicted surface warming values for the whole, branching, and massive colonies shown in Figure 6.11, 6.12, and 6.13, respectively.

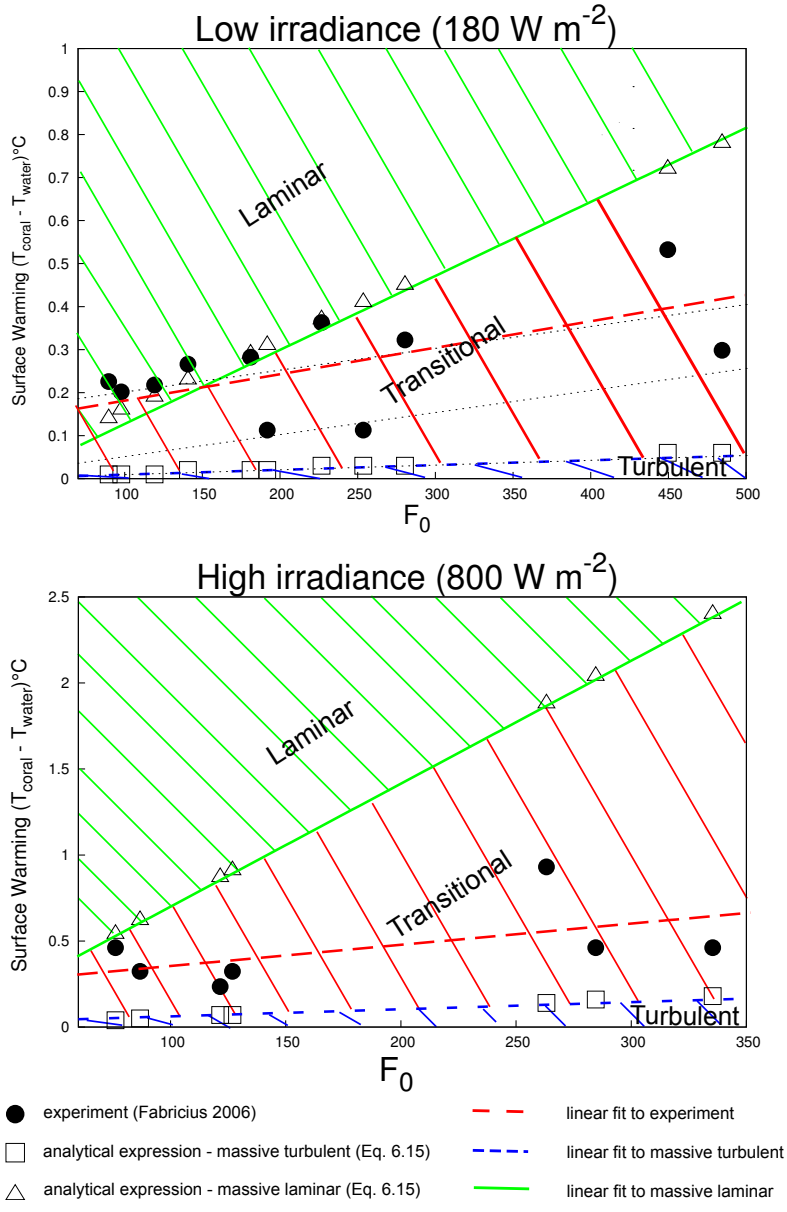

Figure 6.10. Effects of flow, irradiance, and pigmentation on *F. matthaii* surface warming at low and high irradiance for analytical vs simulated and experimental works

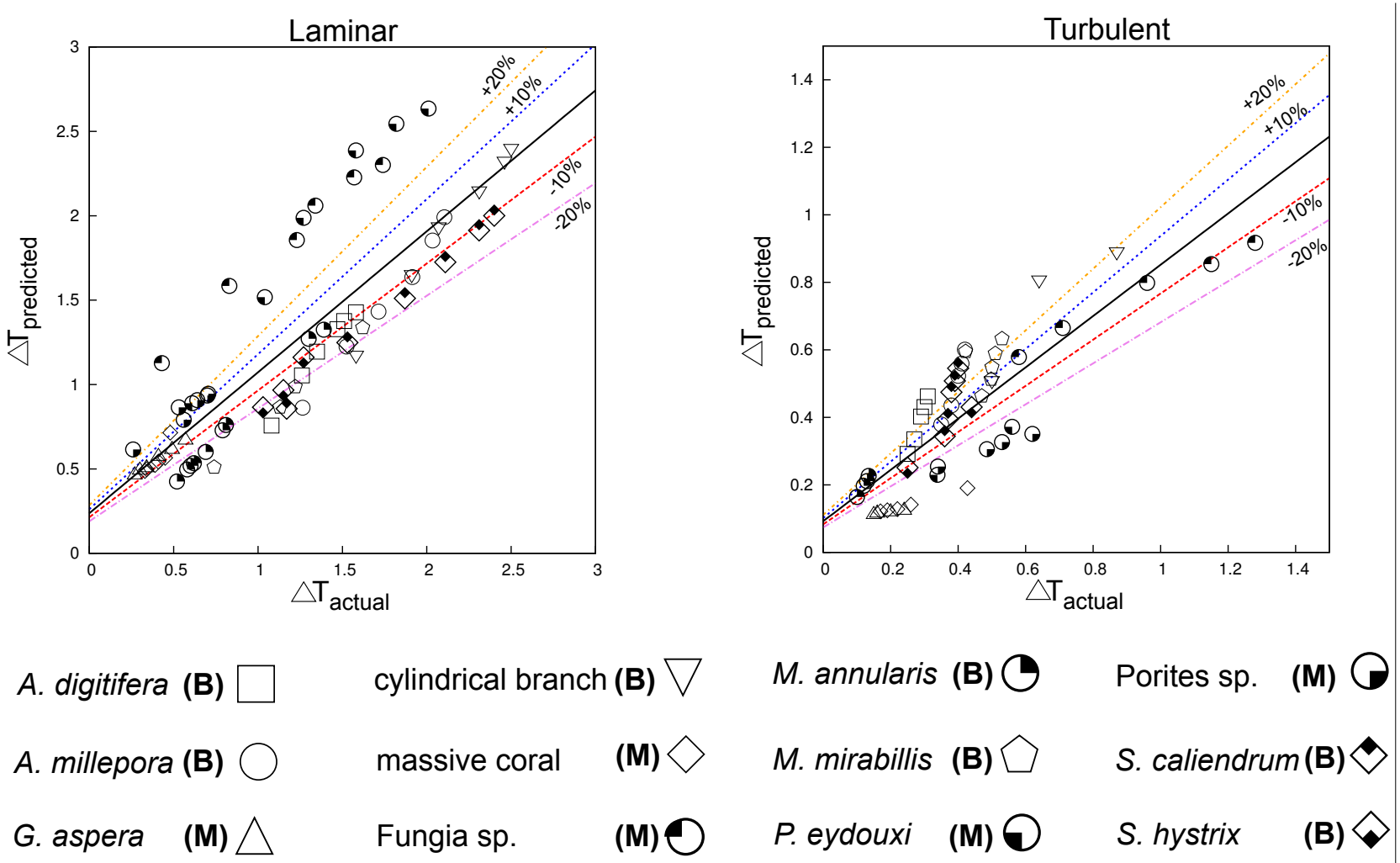

Figure 6.11. ΔT simulated vs predicted plots of whole colonies for both laminar and turbulent flows

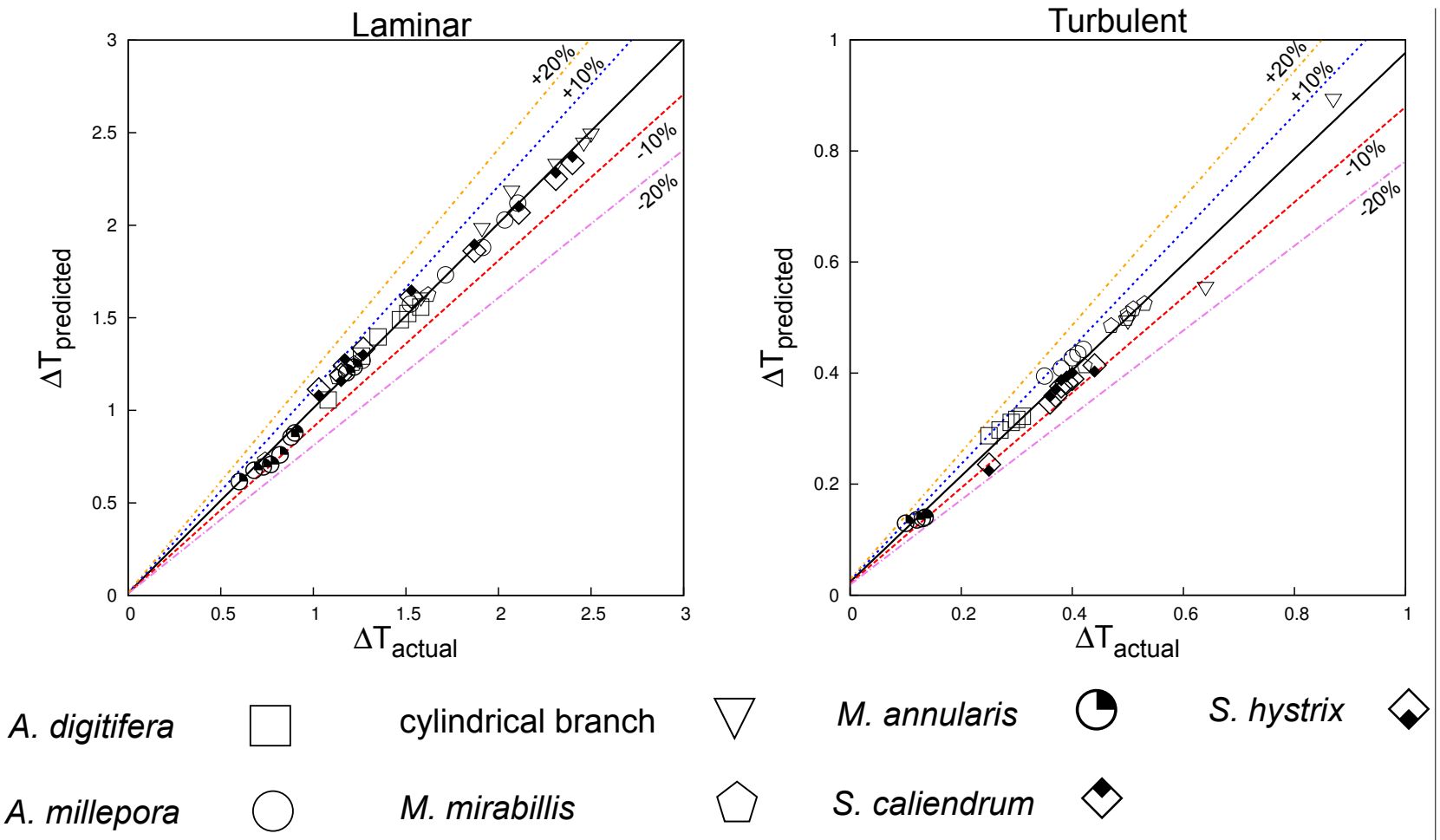

Figure 6.12. ΔT simulated vs predicted plots of branching corals for both laminar and turbulent flows

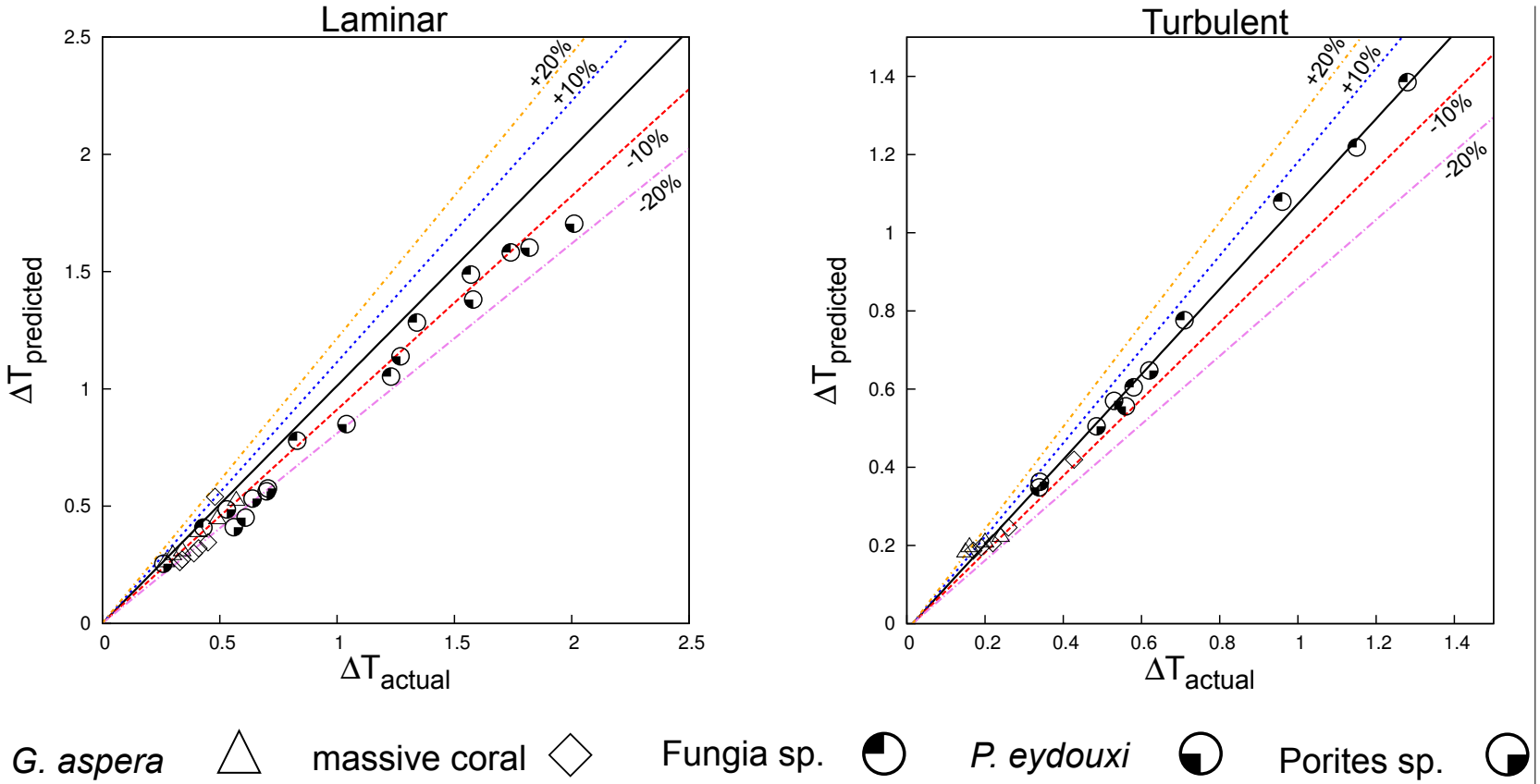

Figure 6.13. ΔT simulated vs predicted plots of massive corals for both laminar and turbulent flows

6.8 Discussion

Understanding the interacting effects of internal and external factors on thermally induced coral bleaching - such as a coral's tolerance and adaptation, the size structure of coral populations, community shifts coral species composition toward more tolerant coral species with decreasing diversity, and difference in growth rates - is critical for understanding the risks to coral colonies and their communities to coral bleaching. Much attention has been paid recently to the diversity and composition of the symbiont populations hosted by reef-building corals, specifically as it relates to the range of bleaching responses exhibited among corals exposed to similar level of stress (Baird et al., 2009; Baker, 2003). Although variability of symbiont communities may explain, in part, why bleaching susceptibility can vary among the colonies, it is unlikely that the physiological tolerances of the symbiont populations are the major factor influencing susceptibility differences in various coral shapes (species) and sizes.

My model provides a theoretical, mechanistic basis for understanding the role of allometry in thermal scaling due to coral morphology (A/V ratios) and flow velocity (Re) from the heat (and to some extent, mass or metabolic) transfer framework. The study of thermal microenvironments of corals in response to environmental variables can enhance the understanding of the mechanisms responsible for bleaching. The thermal microenvironment can also significantly affect many other temperature controlled processes, such as coral metabolism and growth. Thus, the CFD models and techniques presented here have the potential to facilitate a better understanding of how irradiance and flow are related to patterns of coral bleaching and how this might vary among coral species, individual corals, and locations of individual coral colonies on the reef.

6.8.1 Morphology and symbionts on bleaching susceptibility

The present study examines variations of thermal dynamics within and between coral colonies related to coral morphology, water flow, and irradiance intensity level. The general result indicate that in order to maintain thermal equilibrium, it is easier for larger size corals due to their lower A/V ratios compared with smaller corals. This observation is consistent with expectations from heat transfer theory that heat loss should increase with increasing surface area and decrease with decreasing volume. However, there are numerous combinations of coral morphology and physiology, thermal adaptation, metabolic rate, partial bleaching or mortality, and many other environmental factors (i.e. weather conditions, flow currents in the regions, etc), that may differentially affect a coral's propensity to bleach.

Previous studies have highlighted a link between coral surface warming and irradiance intensity, flow velocity, and tidal regime. These studies have also documented and provided the variation in thermal exposure for hemispherical and branching corals (Fabricius, 2006; Jimenez et al., 2008, 2012, 2011; Ong et al., 2012, 2011, 2012). In turn, observations from these studies may help explain the large differences in bleaching susceptibility between coral taxa with different growth forms (Baird and Marshall, 2002; Loya et al., 2001; Marshall and Baird, 2000). A previous computational study also reported a single preliminary data set on the temperature dynamics in the hemispherical corals, *P. lobata* and *C. serailia*, and the branching coral, *S. pistillata*. This study confirmed expectations of the effects of A/V ratios given heat loss should increase with increasing surface area and decrease with decreasing volume. Typically, massive corals have a considerably greater volume to mass ratio, and as I observed here, hemispherical corals heated at a slower rate, taking nearly twice as long to equilibrate. In this case, the effect of faster cooling resulting from different A/V ratios was over taken by thermal mass effects (Ong et al., 2012). These findings are consistent with previous evidence of interspecific variation in coral thermal environment and may result from variation in convective heat transfer and/or thermal properties influenced by the coral morphology and skeletal matrix (Jimenez et al., 2008, 2012, 2011).

6.8.1.1 Shape and size on thermal and metabolic rates

Many literatures have clearly identified the link between the differential bleaching susceptibility and colony morphology. Surveys conducted over a broad range of habitats and biogeographic regions have showed that branching and pocilloporid corals were among the most susceptible and suffer higher mortality rates than species with massive and encrusting morphologies (Brown and Suharsono, 1990; Fisk et al., 1985; Fujioka, 1999; Glynn, 1993, 1983, 1988, 1990a; Harriott, 1985; Hoegh-Guldberg and Salvat, 1995; Jokiel and Coles, 1990; Loch et al., 2002; Loya et al., 2001; Marshall and Baird, 2000; McClanahan and Maina, 2003; Oliver, 1985; Wilkinson, 2000; Yamazato, 1981). Massive and encrusting coral colonies also experienced frequent bleaching during periods of elevated temperature, however they also often demonstrated a high rate of survival (Loya et al., 2001; Nakamura et al., 2001). There have been many theories involving differential mass transfer in accordance with coral morphology, but the most likely hypothesis stated that since high SSTs and high solar irradiance cause the development of superoxides and oxygen radicals, removal of these by-products may be essential to ensure colony health through higher metabolic rates that is directly related to mass-transfer efficiency and colony shape and size (Baker et al., 2008; Loya et al., 2001).

The nature of allometric relationship between metabolic rate and body size and shape in aquatic invertebrates and algae resulting in mass transfer exponents (Equation 6.14, $Sh = cRe^d$), has been examined (Patterson, 1992b). Derivation of mass exponents for various coral morphologies (shape and size) are directly analogous to the allometric trend of thermal scaling using Nu-Re, as described above. The Sh-Re plot is generally used to investigate how changes in flow speed, exchange surface geometry, and fluid flow affect the degree to which convective loss or gain of material augments diffusive fluxes (White, 1988). Estimating metabolic rate is essential because it is linked to the rates of many other biological activities, and the rate of these metabolic processes can be explicitly estimated by the rate of heat production (Glazier, 2005). Patterson's observation demonstrated that the mass transfer of flat organisms was higher than the mass transfer of thinning cylinders under laminar or turbulent flow, which theoretically suggests that under a unit-flow regime, flat colonies should have a higher mass transfer than branched colonies (Baker et al., 2008; Loya et al., 2001; Patterson, 1992b).

Size may also play a major role in determining patterns of thermal and metabolic susceptibilities. Many studies have showed contradictory data with regards to the colony size, for instance, the greater bleaching extent that was recorded on larger colonies supports the hypothesis that with increased frequency of bleaching, shifts may occur toward dominance by smaller, less-fecund coral populations (Brandt, 2009; Done, 1999). In contrast, another study found that larger colonies on the GBR were less affected by bleaching and predicted that the long-term effect of warm temperatures on coral communities would show large colony dominance (Brandt, 2009; Edmunds, 2005). However, majority of the studies supported the hypothesis that small juvenile colonies of some species can survive better than large, mature colonies (Loya et al., 2001; Mumby, 1999; Riegl, 2002; Van Woesik et al., 2004). Done (1999) further stated that repetitive bleaching events might shift the age distribution toward smaller colonies with lower fecundities (Done, 1999). From the thermal dynamics model, I showed that smaller colonies resulting in higher A/V ratios, which in turn lead to lesser cooling due to water flow. However, the thermal patterns are not only dependent on the size and shape of corals, but also the interactions between other environmental stressors. Furthermore, these discrepancies in bleaching susceptibility between studies may reflect differences in regional differences such as water flow and weather conditions in the physiology of the corals or/and their hosted symbiont populations. Given the stronger water flow which increases mass transfer, has an advantage for smaller colonies since they can eliminate toxins more efficiently through diffusion. On the other hand, Bak and Meesters (1999) suggested that large colonies may be more thermally resistant than small colonies to environmental disturbances, such as nutrients and sedimentation, with greater potential for continued gamete output and reproductive success post-disturbance (Bak and Meesters, 1999; Baker

et al., 2008). Moreover, the diffusion over short distances is very fast, and oxygen can rapidly reach all parts of coral microenvironment. Over longer distances, diffusion process is slower, and diffusion alone is inadequate for supplying oxygen to a large colony. The principle of convective mass transport, therefore becomes essential as the size of the colony increases.

6.8.1.2 The role of symbiont in thermal acclimatisation

Symbiont zonation provides a simple hypothesis to explain these bleaching patterns. Bleaching was disproportionately common in what seems to be the upper limit of *Symbiodinium C*'s 'adaptive zone': low-irradiance parts of corals in shallower water, and high-irradiance parts of corals in deeper water. Slight increases in temperature and irradiance might push these symbioses, but not others, beyond some physiological limit, resulting in bleaching (Rowan, 2004; Rowan et al., 1997).

From the biological standpoint, thermal bleaching is often associated with photoinhibition in which the process of accumulation of oxidative stress at photosystem II in the symbionts (Iglesias-Prieto et al., 1992). Different clades, within the symbiont genus *Symbiodinium* apparently exhibit different tolerances to thermally induced stress (Warner et al., 1996). Many literatures during the early stage of coral reef symbiont studies have viewed that each coral species encompasses one symbiotic dinoflagellates (Trench, 1993), in which host taxa alone are adequate units of biodiversity, environmental variability is accommodated largely by physiological acclimatisation (Brown, 1997; Iglesias-Prieto and Trench, 1994), and bleaching variability is often not understood (Lesser et al., 1990). Rowan *et al.* (1997) hypothesised that polymorphic symbiont communities and directed shifts in symbiont populations following extreme environmental change suggest that similar shifts may occur over annual cycles of environmental variation (Gates, 1990) which underlie the broad distribution (Goreau, 1959) and bleaching ecology of these corals (Rowan et al., 1997).

In all other species, dominance by a single clade was thermally senstitive or tolerant, extensive bleaching occured in a large proportion of colonies, or low levels of bleaching occured in a small proportion of colonies, respectively; which indicated that there is still much to investigate between the ecological manifestation of bleaching on coral colonies and their associated symbiont communities (Baker et al., 2008; Brandt, 2009). For mutualisms in general, the ability to acclimatise with environmental change through changes in symbiont community composition reflects the selective advantage of hosting several distinct symbionts (Leigh and Rowell, 1995; Rowan et al., 1997; Smith, 1999).

6.8.2 $Nu - Re$ and allometric thermal scaling

The empirically derived relationship between $\bar{N}u$ and Re given in Equations 6.9 and 6.10 is the most powerful mean of examining the effects of allometric scaling on heat transfer performance. The results of this study are also consistent with the results from various others that have studied heat transfer principles (Bejan and Kraus, 2003; Incropera, 2011; Lienhard, 2011), and are analogous to mass transfer observations (Patterson, 1992a,b; Patterson and Sebens, 1989; Patterson et al., 1991), that investigated the effects of flow and allometric scaling on thermal dynamics in coral microenvironment. On theoretical grounds, for flow past an immersed object such as a flat plate, sphere, or cylinder, one might expect $\bar{N}u$ or $\bar{S}h \propto Re^{0.5}$ where the boundary layer is locally laminar and $\bar{N}u$ or $\bar{S}h \propto Re^{(0.67-0.85)}$ where turbulent dissipation is occurring (Patterson et al., 1991; White, 1988). Coral shape and size and flow regime have a direct effect on the value of global heat coefficients and exponents obtained that are presented in Table 6.5 encompasses the range predicted for each of the local heat exponents and allometric coefficients shown in Table 6.7. In most cases, increases in colony size and/or flow speed markedly increase the rate of heat transfer between the coral and the environment. If the primary heat exponent, b, relating changes in Re with $\bar{N}u$ is equal to $\approx$0.5, then heat transfer is most likely governed on average in the laminar regime. In other words, increases in flow speed or colony size lead to an increase in the relative importance of convective advective mixing and diffusive transport in regulating the coral thermoregulation. The linear regression of allometric curve fits is the most appropriate for studies utilising my approach, where the spatial extent and Re dependence of flow separation phenomena were not characterised.

The dimensionless analysis of allometric thermal scaling variables can be readily determined using Equation 6.15 given the degree of heat exponents (b^*) are quantified along with the flow speed (Re) and coral shape or size based on A/V ratios. Log-log plot of $\left(\frac{\Delta T}{Re^{b^*}}\right)$ (ordinate) - A/V (abscissa) yield information on the allometric thermal constants, where C is the intercept and m is the slope of the plot.

6.8.3 Effect of flow on thermal and metabolic performances

Flow regimes in coral reefs are extremely variable at scales, ranging from those of single branching corals to coral colonies or even up to whole reefs (Monismith, 2007; Shashar et al., 1996). Recent works have highlighted how flow-mediated heat transfer (and mass transfer) may prevent thermally-induced bleaching (Fabricius, 2006; Jimenez et al., 2008; Nakamura et al., 2001; Ong et al., 2012). Theoretically, convective heat (and mass) transfer is modelled using dimensionless

numbers such as the Nusselt number (Nu) and the Sherwood number (Sh), which depend on the Reynolds number (Re) that defines the kind of flow regimes. Therefore, it follows that convective heat transfer (h_{conv}) depends on viscosity, thermal conductivity and also nonlinearly on the temperature difference, i.e. $h_{conv} \sim \delta T^x$. The exact power x depends on the flow conditions, e.g. for free convection around a horizontal plate, it changes from $x = 0.25$ for laminar flow to 0.33 for turbulent flow (Incropera, 2011).

The momentum governing equations for both laminar and turbulent flows through a porous medium have the flow sink term (refer to Appendix 2 and Chapter 3), S_i, which is composed of two parts, viscous and inertial loss terms, creating a pressure drop that is proportional to the velocity and square of the velocity, respectively.

$$S_i = -(\nu D_{ij} + \frac{1}{2}|\mathbf{U}|F_{ij})\mathbf{U} \tag{6.16}$$

where D_{ij} and F_{ij} are represented as the scalars D and F, which are termed the Darcy Forchheimer coefficients and can be written as:

$$D = \frac{150(1-\phi)^2}{d^2\phi^3} \tag{6.17}$$

$$F = \frac{1.75(1-\phi)}{d\phi^3} \tag{6.18}$$

where d is the coral diameter. The viscous and inertial or kinetic energy loss terms play major roles in the laminar and turbulent regimes, respectively. Therefore, an increase in water speed combined with enhanced convective thermal properties in coral morphology (tissue and skeletal matrix permeability values) may lead to a stronger cooling effect from solar heating, which is consistent with the findings observed previously (Chapter 3).

The importance of flow-modulated metabolism to coral primary production has been covered in numerous laboratory studies (Finelli et al., 2006; Patterson, 1992a; Patterson et al., 1991; Smith and Birkeland, 2007; Ulstrup et al., 2005; van Woesik et al., 2012). The primary production of an intracellular photosynthetic symbiont also may be affected by the overall shape of the corals in which it is embedded (Patterson, 1992a). Increased colony size leads to increased Re for a given flow speed, which will shift the heat and mass transfer processes further up the Nu/Re and Sh/Re curves (Patterson, 1992a). Increased water motion also enhances respiration and primary production (Patterson, 1992a; Patterson et al., 1991). Furthermore, water flow also increases mass transfer of inorganic nutrients (Atkinson and Bilger, 1992) and dissolved gases across the diffusive boundary layer between the aquatic environment and the coral surface, which may reduce oxidative stress as well as limiting photoinhibition (Lesser et al.,

1994), which consequently minimises bleaching (Finelli et al., 2006; Nakamura et al., 2005). Increase in water-flow rates across corals may also reduce the likelihood of bleaching through the reduction in the oxygen radical accumulation in corals under thermal stress. Therefore, the effect of water motion should be critically examined for coral physiology because it can modify the metabolic rates of corals to a degree previously associated only with changes in light intensity (McClanahan et al., 2005; Nakamura et al., 2001; Patterson, 1992a; Patterson et al., 1991), and its exposure to light can have a profound impact on its susceptibility (Jokiel and Coles, 1990), even within a colony (Brown and Dunne, 2008).

6.8.4 Further modelling work

Our understanding of the thermoregulation capacity between coral morphology and other internal or external environmental factors is still in its infancy, however the preliminary observations presented here leave no doubt that these relationship are labile, complex, and physiologically diverse. Here, I address some of the further modelling works that would be very valuable to be conducted in parallel with my model.

High variability in coral morphology is a well-known trait in Scleractinian coral species, which may include variation in overall colony growth form as well as corallite architecture observed both inter and intra colonies (Brakel, 1979; Dustan, 1975; Goreau, 1963; Graus and Macintyre, 1982; Jaubert, 1977; Kaandorp et al., 2005; Muko et al., 2000; Veron and Pichon, 1976). These morphological attributes may contribute to their survivorship in a variety of environmental conditions (Kaandorp et al., 2005; Lasker, 1981; Lesser et al., 1994; Porter, 1976) and can influence the distribution, abundance, and evolutionary success of a species (Jackson, 1979; Johnson et al., 1995; Klaus and Budd, 2003). Morphological variation is caused by the combined effects of genetic polymorphism and phenotypic plasticity; however, in my model, I omitted the ability to integrate these effects and hence its alignment with morphological diversification. The potential of computational modelling in coral growth and morphogenesis, in particular, HIRAG (Hydrodynamically Influenced Radiate Accretive Growth) and PORAG (Polyp Oriented Radiate Accretive Growth), have been gaining ground in recent years due to their structured implementation details and alleviation to be integrated with CFD in parallel schemes (Kaandorp, 1999; Kaandorp and Sloot, 2001; Kaandorp et al., 2005; Merks et al., 2003a,b). Their coral growth programs utilised a Laplacian growth process by implementing real time-scales of growth and transport, and the geometric description of the morphology is absent, instead the growth form is represented by a cluster of solidified lattice sites. However, the results still need to be validated by comparing against the estimated transport time for diffusion over the yearly skeletal extension rates. Furthermore,

profound changes in size require design modifications, including elaborate structural changes and the development of complex internal systems, which are likely to evolve over relatively long time scales (Gould, 1966, 1977; Schmidt-Nielsen, 1984).

6.9 Summary

This study demonstrates allometric scaling in thermal dynamics of various coral colonies and underscores two drivers that may determine bleaching susceptibility within or/and among coral species - i.e., prediction of heat exponents from Nu-Re data and the consequent predicted coral tissue warmings from the derived analytical relationship. Dimensionless analysis of heat and mass transfer to corals provide a powerful alternative to traditional allometric methods in investigations of the effect of size on thermal and metabolic scaling rates.

There are numerous internal and external factors that relate directly to the coral host and symbionts that may have profound impact on a colony's bleaching susceptibility. Therefore, there is no simple solution to find an universal index to measure differential coral bleaching susceptibilities. The present findings are applicable in predicting coral surface warming due to A/V ratios, flow velocity (Re) and irradiance intensity (I) for any coral morphology. Further studies of allometric scaling in Scleractinian corals combining heat and mass transfer under various flow conditions combined with accretionary coral growth will be very valuable.

Chapter 7

Conclusions

Predicting bleaching is confounded by numerous physiological and physical factors that arise at both the individual colony scale (assessing whether a coral is bleached or not) and at the reef and regional scales (how large an area is bleached). Current conventional techniques which primarily require the remote assessments of sea surface temperature (SST) profiles and imageries are then converted into bleaching prediction products, such as the HotSpots, Degree-Heating-Weeks (DHW), and Degree-Heating-Months (DHM). Although these products have proved quite successful in monitoring the previous mass bleaching events, they do not adequately represent key physiological and physical factors that may lead to thermal stress in the coral microenvironment. The coral thermal microenvironment is defined as the temperature of the colony surface and of the boundary layer directly above it, which can deviate substantially from the SST. This temperature deviation can be a function of several factors, but predominantly heat flux radiation and water flow on over the coral surface morphology. The concept of coral thermal microenvironments has profound implications not only in the context of thermal stress but also in relation to many temperature-controlled processes, such as rates of metabolism and growth. For example, skeletons of massive *Porites sp.* are widely used as proxies of past and present SST. Their rates of linear extension increase by 27% of the mean values with each 1°C warming. However, the relationship between SST along spatial and temporal gradients and coral growth may over-estimate the effects of temperature in coral skeletons with which vary depending on pigmentation or area of percolation openings and increased porosity due to grazers or predators. Thus, a better understanding of how irradiance, flow, and colony morphology affect the coral thermal microenvironments may assist in interpreting some of the spatial and temporal variability observed in coral bleaching and in better predicting the bleaching resistance and may help refine predictions of the effects of climate change on corals.

Some experimental studies have qualitatively identified that thermal stress in

the coral microenvironment can play an important role in the microscale physical processes involved in coral bleaching. However, these studies provided little quantitative data pertaining to the key roles of hydro- and thermal-dynamics in various coral morphologies. Whilst the numerous laboratory and field studies and prediction approaches employed to date have been essential in identifying potential stressors and in understanding the mechanisms of bleaching, such studies have often impeded by the difficulty of precisely imitating field conditions and obtaining accurate monitoring data when dealing with more than one environmental stressor. Furthermore, conventional laboratory methods often have limited utility for determining values of many parameters of interest within the interior of corals. These parameters (i.e., flow, pressure, temperature, etc) related to coral morphology, are likely to be important determinants of mass and heat transfer in corals, and ultimately their sensitivity to bleaching. In contrast to experimental techniques, numerical modelling methods allow for detailed interrogation of these parameters, thanks to the availability of commodity computing resources. Although full scale modelling of coral reef systems is unlikely to be able to replicate the complexity in nature, it is often possible to construct progressive models of physical systems which closely reproduce reality.

This thesis had three main objectives. The research started by constructing the numerical techniques for modelling thermal stress in the coral microenvironment at the individual-, colony-, and reef-scales. The models were then validated against controlled laboratory experiments that explore the effects of water flow, irradiance and pigmentation, and colony morphology on the thermal dynamics of coral microenvironment. This thesis then explored the effect of smooth and polyped (dimpled) coral surface topographies on their overall surface warmings. The validation cases of measuring the daylight illuminances at the meso-scale under multiple sky conditions and modulating the irradiance levels at the microscale of branching and massive coral surfaces were also examined. This thesis then implemented a coupled CFD and hydrodynamics model (coupled ROMS-SWAN) as well as the ray-tracing model (Radiance) to investigate the differential bleaching pattern case study observed in a shallow, reef-flat environment. Finally, this thesis assessed whether corals of the same- and cross-species, but of varying size and shape, may respond differently to thermal stress due to different heat transfer rates and thermal capacities due to the influence of surface area-to-volume (A/V) ratios on thermal scaling in coral microenvironments.

This thesis presented some useful insights into the implications for mass coral bleaching due to thermal stress in coral microenvironments. It has been widely accepted that both high SST and irradiance enhanced the production of oxygen radicals, which in turn cause oxidative stress and damage the photosynthetic mechanisms of the zooxanthellae. The latter was evident from field observations demonstrating that the onset of bleaching was often visible on the upper sides

of colonies while their sides were still normally pigmented. The bleaching severity was often greater in shallow water and decreased with depth, and that the presence of high cloud cover have prevented mass bleaching mortality during SST anomaly that would incurred bleaching. This thesis showed that the extent of surface warming may vary largely to the ambient seawater temperatures which is physiologically significant for organisms such as corals that grow near their upper thermal tolerance limit.

My results and those of the validated results indicate an additional effect of light, in that solar radiation can contribute to increases in the heat load of exposed coral tissue. Both PAR (400-700 nm) and UVR (280-400 nm) have been implicated to cause bleaching. The contribution of waveband to a coral's heat flux is likely to depend on the spectral distribution of light reaching corals and the coral absorptivity. Furthermore, solar radiation could also have a signification implications for bleaching. In summer, corals live close to their upper thermal limit, and increases in temperature as small as 1-2°C above the mean monthly SST anomaly may trigger bleaching. Both the absolute temperature rise above the threshold and the duration of exposure determine the severity of bleaching. Therefore, the severity of bleaching events is predicted based on cumulative stress index (DHW). One DHW represents either a +1°C anomaly lasting 1 week or a +2°C anomaly lasting half a week. A value of 8 DHW is known to trigger mass coral bleaching. Such indices may need to be evaluated in light of the present results showing that although corals may be exposed to a uniform water temperature, differential effects of solar heating may cause some corals to exceed the maximum expected summertime temperature for a longer period of time, and by a larger amount than others. This thesis also tested the hypothesis that corals of the same species, but of varying size and shape, may respond differently to thermal stress because of different heat and mass transfer capacities. These differences could explain some of the observed differences in bleaching susceptibility among taxa. Furthermore, this thesis along with other growing body of study indicated that enhanced water flow can reduce thermal stress and subsequently modulate coral bleaching within and among colonies, sites, and regions.

7.1 Original contributions

The contribution of the preceding four chapters can be summarised as:

- The development of a novel, open source, coupled CFD with ray-tracing and hydrodynamics models to explore the physiological and and environmental stressors – irradiance, water flow, and coral morphological features (colony shape, size, tissue thickness, and pigmentation) – that could ultimately be

used to assess the variability of thermal stress in the coral microenvironments.

- A comprehensive set of CFD validation simulations against the existing experimental data from the literature. The initial simulation predicted the coral surface warming in the steady state and transient irradiance scenarios under a steady laminar and turbulent flow under a controlled laboratory experiments. It also explored the effects of coral surface architectures between smooth and polyped on the overall thermal dynamics in the coral microenvironments.

- This thesis utilised the ray-tracing technique to estimate the quantity (irradiance intensity) and quality (wavelength spectrum) of variation in the light field above and below the water surface before subsequently reaching the coral surface. It also analysed the contributions of water turbidity or clarity, cloud cover, tides, and sea-state to variations in irradiance. Furthermore, this thesis analysed the frequency distribution of microscale irradiance across the massive and branching coral species.

- The development of "ecosystem models" was divided into three stages: firstly, a coupled model of ROMS-SWAN was used to investigate the 2D hydrodynamic nearshore currents based on the available oceanographic data; secondly, the solar irradiance load model was used to quantify the amount of semi-diurnal surface irradiance and the variation of irradiance levels due to turbidity, cloud cover, water depth (tides), and sea-state; finally, CFD simulation was implemented to solve for the coral tissue/surface warming based on coupled dynamics of water flow, heat transfer and irradiance levels in and around corals. This modelling development study can be used as an initial motivation to explore the full range of parameters that could trigger asymmetric bleaching scenario observed by Brown *et al.* (2000).

- Dimensionless analysis of heat and mass transfer to corals provide a powerful alternative to traditional allometric methods in investigations of the effect of size on thermal and metabolic scaling rates. This thesis demonstrated the allometric scaling in thermal dynamics of various coral colonies and underscored two drivers that may determine bleaching susceptibility within or/and among coral species – prediction of heat exponents from the Nusselt-Reynolds ($Nu - Re$) data and the consequent predicted coral tissue warmings from the derived analytical relationship.

The results of this modelling have highlighted the profound importance of CFD modelling for understanding the thermal responses of corals, and therefore,

has the potential to be applied more widely to the current coral bleaching prediction tools. The techniques and methods implemented throughout this thesis will hopefully continue to be developed and more widely used. In combination with more detailed studies of added temporal and spatial gradients, this approach may even allow the construction of physical systems models which closely reproduce reality.

7.2 Recommendations

Although, this thesis is believed to be the most comprehensive set of CFD simulations of corals and coral communities to date (∼170 simulation runs, ∼1000 CPU hours, and ∼200 hours of both pre-and post-processing data to obtain model results), it was not possible to simulate all possible scenarios and scales. Furthermore, with the available computational power is continually increasing, it may provide greater scope for model complexity and shorter time-extensive during the verification and validation stages.

Our understanding of the relationship between temperature microenvironments and the key physiological and environmental stressors is still in its infancy, however the preliminary observations presented here leave no doubt that these relationship are complex and diverse. Future research should extend the current models in a number of ways. It may be possible to incorporate the advection and tidal mixing currents by using a baroclinic hydrodynamic model in order to achieve a more in-depth analysis in a shallow to inshore reef environments. More research is also needed to model the turbulence length scale encountered near corals on the reef, rather than in flow chambers with flow straighteners. Furthermore, flow in the chambers previously used was unidirectional, where flow on shallow reefs is frequently bidirectional from influence of currents due to winds and waves. For the full potential of the model to be realised and employed in management, additional future work that focuses on deeper reef depths (e.g. >10 m) where the spatial effects of vertical and dynamical mixing processes ideally may also be included.

Future research should extend these findings in a number of way. First it may be possible to model the coral growth and morphogenesis using HIRAG (Hydrodynamically Influenced Radiate Accretive Growth) and PORAG (Polyp Oriented Radiate Accretive Growth), which have been gaining grounds in recent years due to their structured implementation details and may be integrated with CFD in parallel schemes. These coral growth programs use a Laplacian growth process by implementing real time-scales of growth and transport. In this approach the geometric description of morphology is absent, instead the growth form is represented by a cluster of solidified lattice sites. However, the results still need

to be validated by comparing against the estimated transport time for diffusion over the yearly skeletal extension rates. Furthermore, profound changes in size require design modifications, including elaborate structural changes and the development of complex internal systems, which likely to evolve over relatively long time scales. This modelling of biological growth and morphogenesis can be used in parallel with CFD solvers, which may better predict the differences influencing bleaching susceptibility in various coral morphologies.

The quantitative and qualitative modelling in this thesis might also be incorporated into the application of Bayesian Belief Networks (BBN) to identify the dependencies of a range of potential causative factors associated with the presence-absence of variables that are related to coral bleaching. Such an approach could attempt to integrate thermal stress in coral microenvironment under various meteorological and oceanographic conditions. Thus, combining the CFD modelling results with BBN may aid to the development of decision support tools that have the potential to assist decision making for the management of complex systems.

7.3 Final comment

Apart from experimental and theoretical approaches, computational methods are important tools for understanding the physical mechanisms of thermal stress in coral microenvironments. The model development and validation results from this thesis are significant to assist in interpreting some of the spatial and temporal variability observed in coral bleaching and in turn may be used to predict bleaching resistance of locations in which flows can be driven by various combination of tides, buoyancy, and internal and surface waves. Furthermore, the temperature microenvironments around corals may further help in better understanding of climate data derived from skeleton of massive *Porites* sp. along spatial or temporal gradients. Finally, it is hoped that the work presented here will facilitate the construction of more realistic and detailed physical systems that closely mimic key hydro- and thermo-dynamic processes happening at colony and/or reef scale environments and subsequently improve coral bleaching predictions.

References

1. Alados-Arboledas, L., F. Olmo, I. Alados, and M. Perez (2000). Parametric models to estimate photosynthetically active radiation in spain. *Agricultural and forest meteorology 101*(2), 187–201. 102

2. Andrews, J. C. and G. L. Pickard (1990). The physical oceanography of coral-reef systems. *Ecosystems of the World 25*, 11–48. 45

3. Anthony, K., S. R. Connolly, and B. L. Willis (2002). Comparative analysis of energy allocation to tissue and skeletal growth in corals. *Limnology and oceanography 47*, 1417–1429. 35

4. Anthony, K. and K. E. Fabricius (2000). Shifting roles of heterotrophy and autotrophy in coral energetics under varying turbidity. *Journal of experimental marine biology and ecology 252*(2), 221–253. 19

5. Anthony, K. and O. Hoegh-Guldberg (2003). Variation in coral photosynthesis, respiration and growth characteristics in contrasting light microhabitats: an analogue to plants in forest gaps and understoreys? *Functional Ecology 17*(2), 246–259. 19

6. Anthony, K., M. Hoogenboom, and S. Connolly (2005). Adaptive variation in coral geometry and the optimization of internal colony light climates. *Functional Ecology 19*(1), 17–26. 118

7. Anthony, K., P. Ridd, A. Orpin, P. Larcombe, and J. Lough (2004). Temporal variation of light availability in coastal benthic habitats: Effects of clouds, turbidity, and tides. *Limnology and Oceanography*, 2201–2211. 18, 19, 96, 117, 161

8. Aro, E.-M., I. Virgin, and B. Andersson (1993). Photoinhibition of photosystem ii. inactivation, protein damage and turnover. *Biochimica et Biophysica Acta (BBA)-Bioenergetics 1143*(2), 113–134. 11

9. Aronson, R. B., J. F. Bruno, W. F. Precht, P. W. Glynn, C. D. Harvell, L. Kaufman, C. S. Rogers, E. A. Shinn, and J. F. Valentine (2003). Causes of coral reef degradation. *Science 302*(5650), 1502–1504. 28

10. Aronson, R. B. and W. F. Precht (2006). Conservation, precaution, and caribbean reefs. *Coral Reefs 25*(3), 441–450. 28

11. Atkinson, M. and R. Bilger (1992). Effects of water velocity on phosphate uptake in coral reef-flat communities. *Limnology and Oceanography 37*(2), 273–279. 16, 193

12. Atkinson, M., E. Kotler, and P. Newton (1994). Effects of water velocity on respiration, calcification, and ammonium uptake of a porites compressa community. 16

13. Atkinson, M., S. Smith, and E. Stroup (1981). Circulation in enewetak atoll lagoon. *Limnol Oceanogr 26*(6), 1074–1083. 26

14. Baird, A. and P. Marshall (2002). Mortality, growth and reproduction in scleractinian corals following bleaching on the great barrier reef. *Marine Ecology Progress Series 237*, 133–141. 2, 19, 161, 162, 189

15. Baird, A. H., R. Bhagooli, P. J. Ralph, and S. Takahashi (2009). Coral bleaching: the role of the host. *Trends in Ecology & Evolution 24*(1), 16–20. 188

16. Baird, M. and M. Atkinson (1997). Measurement and prediction of mass transfer to experimental coral reef communities. *Limnology and oceanography 42*(8), 1685–1693. 16, 34

17. Bak, R. P. and E. H. Meesters (1999). Population structure as a response of coral communities to global change. *American Zoologist 39*(1), 56–65. 20, 162, 190

18. Baker, A. C. (2003). Flexibility and specificity in coral-algal symbiosis: diversity, ecology, and biogeography of symbiodinium. *Annual Review of Ecology, Evolution, and Systematics*, 661–689. 188

19. Baker, A. C., P. W. Glynn, and B. Riegl (2008). Climate change and coral reef bleaching: An ecological assessment of long-term impacts, recovery trends and future outlook. *Estuarine, Coastal and Shelf Science 80*(4), 435–471. 2, 8, 9, 10, 11, 13, 21, 22, 23, 24, 26, 28, 29, 189, 190, 191

20. Barnes, D. and J. Lough (1992). Systematic variations in the depth of skeleton occupied by coral tissue in massive colonies of *Porites* from the great barrier reef. *Journal of Experimental Marine Biology and Ecology 159*(1), 113–128. 35

21. Barnes, D. J. and J. M. Lough (1993). On the nature and causes of density banding in massive coral skeletons. *Journal of Experimental Marine Biology and Ecology 167*(1), 91–108. 96

22. Barnes, D. J. and J. M. Lough (1999). Porites growth characteristics in a changed environment: Misima island, papua new guinea. *Coral Reefs 18*(3), 213–218. 96

23. Barnes, D. J., J. M. Lough, and B. J. Tobin (1989). Density measurements and the interpretation of x-radiographic images of slices of skeleton from the colonial hard coral porites. *Journal of Experimental Marine Biology and Ecology 131*(1), 45–60. 96

24. Barnes, R. (1980). *Invertebrate zoology*. Saunders College Publ. xi, 5, 6

25. Bayraktarov, E., V. Pizarro, C. Eidens, T. Wilke, and C. Wild (2013). Bleaching susceptibility and recovery of colombian caribbean corals in response to water current exposure and seasonal upwelling. *PloS one 8*(11), e80536. 3, 4, 53, 117

26. Bejan, A. and A. D. Kraus (2003). *Heat transfer handbook*, Volume 1. John Wiley & Sons. 192

27. Berkelmans, R. (2002). Time-integrated thermal bleaching thresholds of reefs and their variation on the great barrier reef. *Marine Ecology-Progress Series 229*, 73–82. xi, 13, 14, 21

28. Berkelmans, R., G. Death, S. Kininmonth, and W. J. Skirving (2004). A comparison of the 1998 and 2002 coral bleaching events on the great barrier reef: spatial correlation, patterns, and predictions. *Coral Reefs 23*(1), 74–83. 14, 19, 22, 96, 161

29. Berkelmans, R. and J. Oliver (1999). Large-scale bleaching of corals on the great barrier reef. *Coral reefs 18*(1), 55–60. 22

30. Berkelmans, R. and M. J. Van Oppen (2006). The role of zooxanthellae in the thermal tolerance of corals: a nugget of hopefor coral reefs in an era of climate change. *Proceedings of the Royal Society B: Biological Sciences 273*(1599), 2305–2312. 162

31. Biewener, A. A. (1990). Biomechanics of mammalian terrestrial locomotion. *Science 250*(4984), 1097–1103. 163

32. Bird, J. C. (2005). *Modelling sub-reef thermodynamics to predict coral bleaching: a case study at Scott Reef, WA*. Ph. D. thesis, James Cook University. 22, 24, 27

33. Birkeland, C., P. Craig, D. Fenner, L. Smith, W. E. Kiene, and B. M. Riegl (2008). Geologic setting and ecological functioning of coral reefs in american samoa. In *Coral Reefs of the USA*, pp. 741–765. Springer. 10

34. Booij, N., I. Haagsma, L. Holthuijsen, A. Kieftenburg, R. Ris, A. Van Der Westhuysen, and M. Zijlema (2004). Swan cycle iii version 40.41 user manual. *Delft University of Technology 115*. 49

35. Booij, N., R. Ris, and L. H. Holthuijsen (1999). A third-generation wave model for coastal regions: 1. model description and validation. *Journal of Geophysical Research: Oceans (1978–2012) 104*(C4), 7649–7666. 49, 135

36. Brakel, W. H. (1979). Small-scale spatial variation in light available to coral reef benthos: quantum irradiance measurements from a jamaican reef. *Bulletin of Marine Science 29*(3), 406–413. 194

37. Brandt, M. (2009). The effect of species and colony size on the bleaching response of reef-building corals in the florida keys during the 2005 mass bleaching event. *Coral Reefs 28*(4), 911–924. 20, 162, 163, 190, 191

38. Brown, B. (1997). Coral bleaching: causes and consequences. *Coral reefs 16*(1), S129–S138. 1, 3, 8, 9, 10, 17, 191

39. Brown, B., I. Ambarsari, M. Warner, W. Fitt, R. Dunne, S. Gibb, and D. Cummings (1999). Diurnal changes in photochemical efficiency and xanthophyll concentrations in shallow water reef corals: evidence for photoinhibition and photoprotection. *Coral Reefs 18*(2), 99–105. 11

40. Brown, B. and R. Dunne (2008). Solar radiation modulates bleaching and damage protection in a shallow water coral. *Marine Ecology Progress Series 362*, 99–107. 194

41. Brown, B., R. Dunne, and H. Chansang (1996). Coral bleaching relative to elevated seawater temperature in the andaman sea (indian ocean) over the last 50 years. *Coral Reefs 15*(3), 151–152. 13

42. Brown, B., R. Dunne, M. Goodson, and A. Douglas (2002). Experience shapes the susceptibility of a reef coral to bleaching. *Coral Reefs 21*(2), 119–126. 9, 10, 21, 125, 126, 128, 153

43. Brown, B., R. Dunne, T. Scoffin, and M. Le Tissier (1994). Solar damage in intertidal corals. *Marine ecology progress series. Oldendorf 105*(3), 219–230. 17, 102, 103, 109, 113, 126, 129, 138, 172

44. Brown, B. and Suharsono (1990). Damage and recovery of coral reefs affected by el niño related seawater warming in the thousand islands, indonesia. *Coral reefs 8*(4), 163–170. 19, 189

45. Brown, B. E. (1987). Worldwide death of coralsnatural cyclical events or man-made pollution? *Marine Pollution Bulletin 18*(1), 9–13. 3, 13

46. Brown, B. E., R. P. Dunne, M. Goodson, and A. Douglas (2000). Marine ecology: bleaching patterns in reef corals. *Nature 404*, 142–143. 11, 125, 126

47. Bruno, J., C. Siddon, J. Witman, P. Colin, and M. Toscano (2001). El nino related coral bleaching in palau, western caroline islands. *Coral Reefs 20*(2), 127–136. 15

48. Bruno, J. F. and P. J. Edmunds (1998). Metabolic consequences of phenotypic plasticity in the coral *Madracis mirabilis*: the effect of morphology and water flow on aggregate respiration. *Journal of experimental marine biology and ecology 229*(2), 187–195. 16

49. Bruno, J. F. and E. R. Selig (2007). Regional decline of coral cover in the indo-pacific: timing, extent, and subregional comparisons. *PLoS one 2*(8), e711. 24

50. Burchard, H. (2002). *Applied turbulence modelling in marine waters*, Volume 100. Springer. 27

51. Bythell, J., P. Pan, and J. Lee (2001). Three-dimensional morphometric measurements of reef corals using underwater photogrammetry techniques. *Coral Reefs 20*(3), 193–199. 21

52. Calder, W. A. (1996). *Size, function, and life history*. Courier Dover Publications. 163

53. Calkins, J. and T. Thordardottir (1980). The ecological significance of solar uv radiation on aquatic organisms. 17

54. Carpenter, L. W. and M. R. Patterson (2007). Water flow influences the distribution of photosynthetic efficiency within colonies of the scleractinian coral¡ i¿ montastrea annularis¡/i¿(ellis and solander, 1786); implications for coral bleaching. *Journal of Experimental Marine Biology and Ecology 351*(1), 10–26. 159

55. Chancerelle, Y. (2000). Méthodes destimation des surfaces développées de coraux scléractiniaires à léchelle dune colonie ou dun peuplement. *Oceanologica acta 23*(2), 211–219. 21

56. Chang, S., C. Elkins, M. Alley, J. Eaton, and S. Monismith (2009). Flow inside a coral colony measured using magnetic resonance velocimetry. *Limnology and Oceanography 54*(5), 1819. 34

57. Chen, H., V. Patel, and S. Ju (1990). Solutions of reynolds-averaged navier-stokes equations for three-dimensional incompressible flows. *Journal of Computational Physics 88*(2), 305–336. 252

58. Chollett, I., P. J. Mumby, and J. Cortes (2010). Upwelling areas do not guarantee refuge for coral reefs in a warming ocean. *Marine Ecology Progress Series 416*, 47–56. 3

59. CIE (1996). 003/e-1996: Spatial distribution of daylight. *CIE Standard: overcast sky and clear sky*. 267

60. Cocito, S., S. Sgorbini, A. Peirano, and M. Valle (2003). 3-d reconstruction of biological objects using underwater video technique and image processing. *Journal of experimental marine biology and ecology 297*(1), 57–70. 21

61. Coles, S. (1997). Reef corals occurring in a highly fluctuating temperature environment at fahal island, gulf of oman (indian ocean). *Coral Reefs 16*(4), 269–272. 126

62. Coles, S. and B. E. Brown (2003). Coral bleachingcapacity for acclimatization and adaptation. *Advances in marine biology 46*, 183–223. 3, 9, 10, 11, 21, 22

63. Coles, S. and P. Jokiel (1977). Effects of temperature on photosynthesis and respiration in hermatypic corals. *Marine Biology 43*(3), 209–216. 13

64. Coles, S. L. and Y. H. Fadlallah (1991). Reef coral survival and mortality at low temperatures in the arabian gulf: new species-specific lower temperature limits. *Coral Reefs 9*(4), 231–237. 13

65. Cooper, T., R. OLeary, and J. Lough (2012). Growth of western australian corals in the anthropocene. *Science 335*(6068), 593–596. 159, 161

66. Cooper, T. F. (2008). *Coral bioindicators of environmental conditions on coastal coral reefs*. Ph. D. thesis, James Cook University. 36, 84

67. Côté, I., J. Gill, T. Gardner, and A. Watkinson (2005). Measuring coral reef decline through meta-analyses. *Philosophical Transactions of the Royal Society B: Biological Sciences 360*(1454), 385–395. 24

68. Cowen, R. K. and S. Sponaugle (2009). Larval dispersal and marine population connectivity. *Annual Review of Marine Science 1*, 443–466. 34

69. Craig, P., G. DiDonato, D. Fenner, and C. Hawkins (2005). The state of coral reef ecosystems of american samoa. *The state of coral reef ecosystems of the United States and pacific freely associated states*, 312–337. 10

70. Dahl, A. L. (1973). Surface area in ecological analysis: quantification of benthic coral-reef algae. *Marine Biology 23*(4), 239–249. 21

71. Dahlgren, C. and J. Marr (2004). Back reef systems: important but overlooked components of tropical marine ecosystems. *Bulletin of Marine Science 75*(2), 145–152. 17

72. Darula, S. and R. Kittler (2002). Cie general sky standard defining luminance distributions. *Proceedings eSim*, 11–13. 267

73. Day, T., L. Nagel, M. J. Van Oppen, and M. J. Caley (2008). Factors affecting the evolution of bleaching resistance in corals. *The American Naturalist 171*(2), E72–E88. 21, 23

74. Dennison, W. C. and D. J. Barnes (1988). Effect of water motion on coral photosynthesis and calcification. *Journal of Experimental Marine Biology and Ecology 115*(1), 67–77. 16, 126

75. Denny, M. W. (1985). Wave forces on intertidal organisms: A case study. *Limnology and Oceanography 30*(6), 1171–1187. 16

76. Denny, M. W. (1988). *Biology and the mechanics of the wave-swept environment*. Princeton University Press Princeton. 16

77. Death, G., K. E. Fabricius, H. Sweatman, and M. Puotinen (2012). The 27-year decline of coral cover on the great barrier reef and its causes. *Proceedings of the National Academy of Sciences 109*(44), 17995–17999. 2, 10

78. Dimond, J. L., B. J. Holzman, and B. L. Bingham (2012). Thicker host tissues moderate light stress in a cnidarian endosymbiont. *The Journal of experimental biology 215*(13), 2247–2254. 122

79. Ditlev, H. (1978). Zonation of corals (scleractinia: Coelenterata) on intertidal reef flats at ko phuket, eastern indian ocean. *Marine Biology 47*(1), 29–39. 128, 129

80. Done, T. J. (1999). Coral community adaptability to environmental change at the scales of regions, reefs and reef zones. *American Zoologist 39*(1), 66–79. 20, 162, 190

81. Done, T. T. et al. (1982). Photogrammetry in coral ecology: a technique for the study of change in coral communities. In *Proceedings of the 4th International Coral Reef Symposium, Manila, 1981-pages: 2: 315-320*. Marine Sciences Center, University of the Philippines. 21

82. Donner, S. D., W. J. Skirving, C. M. Little, M. Oppenheimer, and O. Hoegh-Guldberg (2005). Global assessment of coral bleaching and required rates of adaptation under climate change. *Global Change Biology 11*(12), 2251–2265. 26

83. Douglas, A. (2003). Coral bleaching - how and why? *Marine Pollution Bulletin 46*(4), 385–392. 3

84. Downs, C., J. E. Fauth, J. C. Halas, P. Dustan, J. Bemiss, and C. M. Woodley (2002). Oxidative stress and seasonal coral bleaching. *Free Radical Biology and Medicine 33*(4), 533–543. 11

85. Dubinsky, Z. and P. L. Jokiel (1994). Ratio of energy and nutrient fluxes regulates symbiosis between zooxanthellae and corals. 5

86. Dunne, R. and B. Brown (1996). Penetration of solar uvb radiation in shallow tropical waters and its potential biological effects on coral reefs; results from the central indian ocean and andaman sea. *Marine Ecology Progress Series 144*(1), 109–118. 102, 112, 113, 126, 128

87. Dunne, R. and B. Brown (2001). The influence of solar radiation on bleaching of shallow water reef corals in the andaman sea, 1993–1998. *Coral Reefs 20*(3), 201–210. 102, 113, 126, 128, 138

88. Dustan, P. (1975). Growth and form in the reef-building coral montastrea annularis. *Marine Biology 33*(2), 101–107. 194

89. Edmunds, P. and R. Gates (2002). Normalizing physiological data for scleractinian corals. *Coral Reefs 21*(2), 193–197. 20, 86, 162, 163, 172

90. Edmunds, P. J. (2005). The effect of sub-lethal increases in temperature on the growth and population trajectories of three scleractinian corals on the southern great barrier reef. *Oecologia 146*(3), 350–364. 190

91. Edson, J., T. Paluszkiewicz, S. Sandgathe, L. Vincent, L. Goodman, T. Curtin, J. Hollister, M. Colton, S. Anderson, E. Andreas, et al. (1999). Coupled marine boundary layers and air-sea interaction initiative: Combining process studies, simulations, and numerical models. *Office of Naval Research, Arlington*. 46

92. Egbert, G. D. and S. Y. Erofeeva (2002). Efficient inverse modeling of barotropic ocean tides. *Journal of Atmospheric & Oceanic Technology 19*(2). 137

93. Fabricius, K. (2006). Effects of irradiance, flow, and colony pigmentation on the temperature microenvironment around corals: Implications for coral bleaching? *Limnology and Oceanography 51*(1), 30–37. 2, 19, 29, 30, 34, 75, 83, 161, 189, 192

94. Fabricius, K. E. (2005). Effects of terrestrial runoff on the ecology of corals and coral reefs: review and synthesis. *Marine pollution bulletin 50*(2), 125–146. 53

95. Falkowski, P. G., P. L. Jokiel, and R. Kinzie (1990). Irradiance and corals. *Ecosystems of the world 25*, 89–107. 19

96. Falter, J. L., M. J. Atkinson, and M. A. Merrifield (2004). Mass-transfer limitation of nutrient uptake by a wave-dominated reef flat community. *Limnology and Oceanography 49*(5), 1820–1831. 34

97. Ferreira, T. and W. Rasband (2012, October). *ImageJ User Guide* (Version 1.46r ed.). http://rsbweb.nih.gov/ij/docs/guide/user-guide.pdf. 167

98. Ferziger, J. H. and M. Perić (1999). *Computational methods for fluid dynamics*. Springer Berlin. 44, 87, 139, 252

99. Fine, M., E. Meroz-Fine, and O. Hoegh-Guldberg (2005). Tolerance of endolithic algae to elevated temperature and light in the coral montipora monasteriata from the southern great barrier reef. *Journal of experimental biology 208*(1), 75–81. 19

100. Finelli, C. M., B. S. Helmuth, N. D. Pentcheff, and D. S. Wethey (2006). Water flow influences oxygen transport and photosynthetic efficiency in corals. *Coral Reefs 25*(1), 47–57. 16, 18, 193, 194

101. Fisk, D. D., T. T. Done, et al. (1985). Taxonomic and bathymetric patterns of bleaching in corals, myrmidon reef. In *Proceedings of the 5th International Coral Reef Congress, Tahiti, 27 May-1 June 1985-pages: 6: 149-154*. 189

102. Fitt, W. and M. Warner (1995). Bleaching patterns of four species of caribbean reef corals. *The Biological Bulletin 189*(3), 298–307. 11, 138

103. Fitt, W. K., B. E. Brown, M. E. Warner, and R. P. Dunne (2001). Coral bleaching: interpretation of thermal tolerance limits and thermal thresholds in tropical corals. *Coral Reefs 20*(1), 51–65. 3, 11, 13

104. Fricke, H., E. Vareschi, and D. Schlichter (1987). Photoecology of the coral leptoseris fragilis in the red sea twilight zone (an experimental study by submersible). *Oecologia 73*(3), 371–381. 19

105. Fujioka, Y. (1999). Mass destruction of the hermatypic corals during a bleaching event in ishigaki island, southwestern japan. *Galaxea*, 41–50. 19, 189

106. Gardner, T. A., I. M. Côté, J. A. Gill, A. Grant, and A. R. Watkinson (2003). Long-term region-wide declines in caribbean corals. *Science 301*(5635), 958–960. 24

107. Gates, R. (1990). Seawater temperature and sublethal coral bleaching in jamaica. *Coral reefs 8*(4), 193–197. 191

108. Gates, R. D. and P. J. Edmunds (1999). The physiological mechanisms of acclimatization in tropical reef corals. *American Zoologist 39*(1), 30–43. 22

109. Gibson, R., R. Atkinson, and J. Gordon (2007). Coral reefs of the andaman seaan integrated perspective. *Oceanography and marine biology: an annual review 45*, 173–194. 128, 129, 130, 131

110. Gill, J. A., A. R. Watkinson, J. P. McWilliams, and I. M. Côté (2006). Opposing forces of aerosol cooling and el niño drive coral bleaching on caribbean reefs. *Proceedings of the National Academy of Sciences 103*(49), 18870–18873. 15

111. Gille, S. T., E. J. Metzger, and R. Tokmakian (2004). Seafloor topography and ocean circulation. Technical report, DTIC Document. 27

112. Glazier, D. S. (2005). Beyond the 3/4-power law: variation in the intra-and interspecific scaling of metabolic rate in animals. *Biological Reviews 80*(4), 611–662. 190

113. Gleason, D. F. and G. M. Wellington (1993). Ultraviolet radiation and coral bleaching. *Nature Publishing Group*. 17

114. Gleeson, M. and A. Strong (1995). Applying mcsst to coral reef bleaching. *Advances in Space Research 16*(10), 151–154. 13

115. Glynn, P. (1993). Coral reef bleaching: ecological perspectives. *Coral reefs 12*(1), 1–17. 1, 3, 9, 10, 13, 15, 22, 161, 189

116. Glynn, P. and L. D'croz (1990). Experimental evidence for high temperature stress as the cause of el nino-coincident coral mortality. *Coral reefs 8*(4), 181–191. 3, 13

117. Glynn, P. W. (1983). Extensive bleachingand death of reef corals on the pacific coast of panama. *Environmental Conservation 10*(02), 149–154. 19, 189

118. Glynn, P. W. (1984). Widespread coral mortality and the 1982-83 el nino warming event. *Environmental Conservation 11*(2), 133–146. 15

119. Glynn, P. W. (1988). El niño-southern oscillation 1982-1983: nearshore population, community, and ecosystem responses. *Annual Review of Ecology and Systematics 19*(1), 309–346. 189

120. Glynn, P. W. (1990a). Coral mortality and disturbances to coral reefs in the tropical eastern pacific. *Elsevier oceanography series 52*, 55–126. 15, 19, 189

121. Glynn, P. W. (1990b). *Global ecological consequences of the 1982-83 El Niño-southern oscillation*. Access Online via Elsevier. 13, 15

122. Glynn, P. W. (1991). Coral reef bleaching in the 1980s and possible connections with global warming. *Trends in Ecology & Evolution 6*(6), 175–179. 3, 13

123. Glynn, P. W. (1996). Coral reef bleaching: facts, hypotheses and implications. *Global Change Biology 2*(6), 495–509. 3, 9, 13

124. Goreau, T., R. Hayes, and A. Strong (1997). Tracking south pacific coral reef bleaching by satellite and field observations. In *Proceedings of the 8th International Coral Reef Symposium*, Volume 2, pp. 1491–1494. 13

125. Goreau, T., T. McClanahan, R. Hayes, and A. Strong (2000). Conservation of coral reefs after the 1998 global bleaching event. *Conservation Biology 14*(1), 5–15. 117

126. Goreau, T. F. (1959). The ecology of jamaican coral reefs i. species composition and zonation. *Ecology*, 67–90. 191

127. Goreau, T. F. (1963). Calcium carbonate deposition by coralline algae and corals in relation to their roles as reef-builders. *Annals of the New York Academy of Sciences 109*(1), 127–167. 194

128. Goreau, T. J. (1991). *Elevated sea surface temperatures correlate with Caribbean coral reef bleaching*. US Department of Commerce, National Oceanic and Atmospheric Administration. 13

129. Goreau, T. J. (1992). Bleaching and reef community change in jamaica: 1951–1991. *American Zoologist 32*(6), 683–695. 3, 13

130. Goreau, T. J. and R. L. Hayes (1994). Coral bleaching and ocean" hot spots". *Ambio-Journal of Human Environment Research and Management 23*(3), 176–180. 13, 23

131. Gould, S. J. (1966). Allometry and size in ontogeny and phylogeny. *Biological Reviews 41*(4), 587–638. 86, 162, 195

132. Gould, S. J. (1977). *Ontogeny and phylogeny*. Harvard University Press. 163, 195

133. Gourlay, M. R. and G. Colleter (2005). Wave-generated flow on coral reefs-an analysis for two-dimensional horizontal reef-tops with steep faces. *Coastal engineering 52*(4), 353–387. 34

134. Graus, R. R. and I. G. MacIntyre (1976). Light control of growth form in colonial reef corals: computer simulation. *Science 193*(4256), 895–897. 28

135. Graus, R. R. and I. G. Macintyre (1982). Variation in growth forms of the reef coral montastrea annularis (ellis and solander): a quantitative evaluation of growth response to light distribution using computer simulation. *Smithson Contrib Mar Sci 12*, 441–464. 28, 194

136. Gregg, W. W. and K. Carder (1990). A simple spectral solar irradiance model for cloudless maritime atmospheres. *Limnology and Oceanography 35*. 17

137. Guest, J. R., A. H. Baird, J. A. Maynard, E. Muttaqin, A. J. Edwards, S. J. Campbell, K. Yewdall, Y. A. Affendi, and L. M. Chou (2012). Contrasting patterns of coral bleaching susceptibility in 2010 suggest an adaptive response to thermal stress. *PLoS ONE 7*(3), e33353. 19, 83, 162

138. Haidvogel, D. B., H. Arango, W. Budgell, B. Cornuelle, E. Curchitser, E. Di Lorenzo, K. Fennel, W. Geyer, A. Hermann, L. Lanerolle, et al. (2008). Ocean forecasting in terrain-following coordinates: Formulation and skill assessment of the regional ocean modeling system. *Journal of Computational Physics 227*(7), 3595–3624. 49

139. Harriott, V. J. (1985). Mortality rates of scleractinian corals before and during a mass bleaching event. *Marine ecology progress series. Oldendorf 21*(1), 81–88. 189

140. Hearn, C. J. (2011). Perspectives in coral reef hydrodynamics. *Coral Reefs 30*(1), 1–9. 34, 45

141. Hedges, L. V., I. Olkin, M. Statistiker, I. Olkin, and I. Olkin (1985). Statistical methods for meta-analysis. 24

142. Helmuth, B. and K. Sebens (1993). The influence of colony morphology and orientation to flow on particle capture by the scleractinian coral *Agaricia agaricites*. *Journal of Experimental Marine Biology and Ecology 165*(2), 251–278. 28

143. Helmuth, B. S., K. P. Sebens, and T. L. Daniel (1997). Morphological variation in coral aggregations: branch spacing and mass flux to coral tissues. *Journal of Experimental Marine Biology and Ecology 209*(1), 233–259. 96

144. Hench, J. L., J. J. Leichter, and S. G. Monismith (2008). Episodic circulation and exchange in a wave-driven coral reef and lagoon system. *Limnology and Oceanography 53*(6), 2681. 34

145. Hench, J. L. and J. H. Rosman (2013). Observations of spatial flow patterns at the coral colony scale on a shallow reef flat. *Journal of Geophysical Research: Oceans 118*(3), 1142–1156. 47

146. Heron, M., S. Heron, and W. Skirving (2008). Mitigation of coral bleaching on the reef front by wave mixing. 22

147. Heron, S., G. Liu, L. Arzayus, W. Skirving, and A. Strong (2004). A benefit from hurricanes. *Pervasive Computing and Communication Security (PERSEC)*. 15

148. Heron, S. F. and W. J. Skirving (2004). Satellite bathymetry use in numerical models of ocean thermal stress. *Gayana (Concepción) 68*(2), 284–288. 27

149. Hoegh-Guldberg, O. (1988). A method for determining the surface area of corals. *Coral Reefs 7*(3), 113–116. 20, 21

150. Hoegh-Guldberg, O. (1999a). Climate change, coral bleaching and the future of the world's coral reefs. *Marine and freshwater research 50*(8), 839–866. xi, 1, 2, 8, 9, 10, 11, 12, 13, 16, 22, 23, 26

151. Hoegh-Guldberg, O. (1999b). Climate change, coral bleaching and the future of the world's coral reefs. *Marine and freshwater research 50*(8), 839–866. 122, 138

152. Hoegh-Guldberg, O., M. Fine, W. Skirving, R. Johnstone, S. Dove, and A. Strong (2005). Coral bleaching following wintry weather. *Limnology and Oceanography 50*(1), 265–271. 13

153. Hoegh-Guldberg, O. and R. J. Jones (1999). Photoinhibition and photoprotection in symbiotic dinoflagellates from reef-building corals. *Marine Ecology Progress Series 183*, 73–86. 19

154. Hoegh-Guldberg, O., P. Mumby, A. Hooten, R. Steneck, P. Greenfield, E. Gomez, C. Harvell, P. Sale, A. Edwards, K. Caldeira, et al. (2007). Coral reefs under rapid climate change and ocean acidification. *science 318*(5857), 1737–1742. 1, 2, 9, 22, 28

155. Hoegh-Guldberg, O. and B. Salvat (1995). Periodic mass-bleaching and elevated sea temperatures: bleaching of outer reef slope communities in moorea, french polynesia. *Marine ecology progress series. Oldendorf 121*(1), 181–190. 2, 19, 161, 189

156. Holmes, G. (2008). Estimating three-dimensional surface areas on coral reefs. *Journal of Experimental Marine Biology and Ecology 365*(1), 67–73. 20, 21, 86, 163, 172

157. Holmes, G., J. Ortiz, P. Kaniewska, and R. Johnstone (2008). Using three-dimensional surface area to compare the growth of two pocilloporid coral species. *Marine biology 155*(4), 421–427. 21

158. Hoogenboom, M. O., K. Anthony, and S. R. Connolly (2006). Energetic cost of photoinhibition in corals. *Marine Ecology Progress Series 313*, 1–12. 83

159. Hopley, D. and R. Barnes (1985). Structure and development of a windward fringing reef, orpheus island, palm group, great barrier reef. In *Proc. Fifth Int. Coral Reef Congr*, Volume 3, pp. 141–146. 45

160. Houghton, J. T. (1996). *Climate change 1995: The science of climate change: contribution of working group I to the second assessment report of the Intergovernmental Panel on Climate Change*, Volume 2. Cambridge University Press. 26

161. Hueerkamp, C., P. W. Glynn, L. D'Croz, J. L. Mate, and S. B. Colley (2001). Bleaching and recovery of five eastern pacific corals in an el niño-related temperature experiment. *Bulletin of Marine Science 69*(1), 215–236. 15

162. Hughes, T. P., A. H. Baird, D. R. Bellwood, M. Card, S. R. Connolly, C. Folke, R. Grosberg, O. Hoegh-Guldberg, J. Jackson, J. Kleypas, et al. (2003). Climate change, human impacts, and the resilience of coral reefs. *Science 301*(5635), 929–933. 1, 2, 9, 10, 28

163. Iglesias-Prieto, R., J. L. Matta, W. A. Robins, and R. K. Trench (1992). Photosynthetic response to elevated temperature in the symbiotic dinoflagellate symbiodinium microadriaticum in culture. *Proceedings of the national Academy of Sciences 89*(21), 10302–10305. 11, 191

164. Iglesias-Prieto, R. and R. K. Trench (1994). Acclimation and adaptation to irradiance in symbiotic dinoflagellates: Responses of the photosynthetic unit to changes in photon flux density. *Marine ecology progress series. Oldendorf 113*(1), 163–175. 191

165. Incropera, F. P. (2011). *Fundamentals of heat and mass transfer*. John Wiley & Sons. 192, 193

166. IOC, I. (2003). Bodc (intergovernmental oceanographic commission, international hydrographic organization, and british oceanographic data centre), 2003, centenary edition of the gebco digital atlas: Liverpool, united kingdom, published on behalf of the ioc and the iho as part of the general bathymetric chart of the oceans, bodc, cd-rom. *Centenary edition of the GEBCO digital atlas. Liverpool, UK: IOC, IHO, and BODC*. 135

167. Jackson, J. (1979). Morphological strategies of sessile animals. *Biology and systematics of colonial organisms. Academic Press, London*, 499–555. 194

168. Jackson, J. B., M. X. Kirby, W. H. Berger, K. A. Bjorndal, L. W. Botsford, B. J. Bourque, R. H. Bradbury, R. Cooke, J. Erlandson, J. A. Estes, et al. (2001). Historical overfishing and the recent collapse of coastal ecosystems. *science 293*(5530), 629–637. 24

169. Jaubert, J. (1977). Light, metabolism and growth forms of the hermatypic scleractinian coral synaraea convexa verrill in the lagoon of moorea (french polynesia). In *Proc 3rd Int Coral Reef Symp*, Volume 1, pp. 483–488. 194

170. Jerlov, N. (1950). Ultra-violet radiation in the sea. 17

171. Jerlov, N. (1976). *Marine optics*, Volume 14. Elsevier Science Ltd. xii, xix, 53, 54, 55, 100, 113, 129

172. Jerlov, N. G. (1968). *Optical oceanography*, Volume 5. Elsevier. 55

173. Jimenez, I., M. Kuhl, A. Larkum, and P. Ralph (2008). Heat budget and thermal microenvironment of shallow-water corals: Do massive corals get warmer than branching corals? *Limnology and Oceanography 53*(4), 1548–1561. 30, 34, 60, 61, 74, 83, 138, 161, 189, 192

174. Jimenez, I., A. Larkum, P. Ralph, and M. Kühl (2012). In situ thermal dynamics of shallow water corals is affected by tidal patterns and irradiance. *Marine Biology*, 1–10. 189

175. Jimenez, I. M., M. Kühl, A. W. Larkum, and P. J. Ralph (2011). Effects of flow and colony morphology on the thermal boundary layer of corals. *Journal of The Royal Society Interface 8*(65), 1785–1795. xiii, 34, 37, 84, 93, 189

176. Johnsen, S. and E. A. Widder (1999). The physical basis of transparency in biological tissue: ultrastructure and the minimization of light scattering. *Journal of theoretical biology 199*(2), 181–198. 5

177. Johnson, K. G., A. F. Budd, and T. A. Stemann (1995). Extinction selectivity and ecology of neogene caribbean reef corals. *Paleobiology*, 52–73. 194

178. Jokiel, P. and S. Coles (1990). Response of hawaiian and other indo-pacific reef corals to elevated temperature. *Coral reefs 8*(4), 155–162. 3, 13, 19, 189, 194

179. Jokiel, P. L. (1978). Effects of water motion on reef corals. *Journal of Experimental Marine Biology and Ecology 35*(1), 87–97. 16, 126

180. Jokiel, P. L. (1980). Solar ultraviolet radiation and coral reef epifauna. *Science 207*(4435), 1069–1071. 17

181. Jokiel, P. L. and E. K. Brown (2004). Global warming, regional trends and inshore environmental conditions influence coral bleaching in hawaii. *Global Change Biology 10*(10), 1627–1641. 15

182. Jokiel, P. L., J. York, and H. Richard (1982). Solar ultraviolet photobiology of the reef coral pocillopora damicornis and symbiotic zooxanthellae. *Bulletin of Marine Science 32*(1), 301–315. 17

183. Jones, A. M., N. Cantin, R. Berkelmans, B. Sinclair, and A. Negri (2008). A 3d modeling method to calculate the surface areas of coral branches. *Coral Reefs 27*(3), 521–526. 20, 21, 86, 163, 172

184. Jones, R. and O. Hoegh-Guldberg (2001). Diurnal changes in the photochemical efficiency of the symbiotic dinoflagellates (dinophyceae) of corals: photoprotection, photoinactivation and the relationship to coral bleaching. *Plant, Cell & Environment 24*(1), 89–99. 11, 16, 19

185. Jones, R., O. Hoegh-Guldberg, A. Larkum, and U. Schreiber (1998). Temperature-induced bleaching of corals begins with impairment of the CO2 fixation mechanism in zooxanthellae. *Plant, Cell & Environment 21*(12), 1219–1230. xi, 11, 12

186. Jones, R. J. and D. Yellowlees (1997). Regulation and control of intracellular algae (zooxanthellae) in hard corals. *Philosophical Transactions of the Royal Society of London. Series B: Biological Sciences 352*(1352), 457–468. 5

187. Joshi, K. B. (2013). *Modeling of Bio-inspired Jellyfish Vehicle for Energy Efficient Propulsion*. Ph. D. thesis, Virginia Tech. 60, 86

188. Kaandorp, J. (1999). Morphological analysis of growth forms of branching marine sessile organisms along environmental gradients. *Marine Biology 134*(2), 295–306. 28, 194

189. Kaandorp, J. A., E. A. Koopman, P. M. Sloot, R. P. Bak, M. J. Vermeij, and L. E. Lampmann (2003). Simulation and analysis of flow patterns around the scleractinian coral *Madracis mirabilis*. *Philosophical Transactions of the Royal Society of London. Series B: Biological Sciences 358*(1437), 1551–1557. 28, 34

190. Kaandorp, J. A. and J. E. Kübler (2001). *The algorithmic beauty of seaweeds, sponges and corals*. Springer. 21, 28

191. Kaandorp, J. A., C. P. Lowe, D. Frenkel, and P. M. Sloot (1996). Effect of nutrient diffusion and flow on coral morphology. *Physical Review Letters 77*(11), 2328. 28

192. Kaandorp, J. A. and P. Sloot (2001). Morphological models of radiate accretive growth and the influence of hydrodynamics. *Journal of Theoretical Biology 209*(3), 257–274. 28, 194

193. Kaandorp, J. A., P. M. Sloot, R. M. Merks, R. P. Bak, M. J. Vermeij, and C. Maier (2005). Morphogenesis of the branching reef coral madracis mirabilis. *Proceedings of the Royal Society B: Biological Sciences 272*(1559), 127–133. 28, 194

194. Kaiser, P., D. Schlichter, and H. Fricke (1993). Influence of light on algal symbionts of the deep water coral leptoseris fragilis. *Marine Biology 117*(1), 45–52. 19

195. Kaniewska, P., K. R. Anthony, and O. Hoegh-Guldberg (2008). Variation in colony geometry modulates internal light levels in branching corals, acropora humilis and stylophora pistillata. *Marine biology 155*(6), 649–660. 19, 118

196. Kaniewska, P., S. H. Magnusson, K. Anthony, R. Reef, M. Kühl, and O. Hoegh-Guldberg (2011). Importance of macro- versus microstructure in modulating light levels inside coral colonies. *Journal of Phycology 47*(4), 846–860. 118, 122

197. Kanwisher, J. W. and S. A. Wainwright (1967). Oxygen balance in some reef corals. *The Biological Bulletin 133*(2), 378–390. 20, 21

198. Klaus, J. S. and A. F. Budd (2003). Comparison of caribbean coral reef communities before and after plio-pleistocene faunal turnover: analyses of two dominican republic reef sequences. *Palaios 18*(1), 3–21. 194

199. Kleypas, J. (1996). Coral reef development under naturally turbid conditions: fringing reefs near broad sound, australia. *Coral Reefs 15*(3), 153–167. 18

200. Kleypas, J. A., G. Danabasoglu, and J. M. Lough (2008). Potential role of the ocean thermostat in determining regional differences in coral reef bleaching events. *Geophysical Research Letters 35*(3), L03613. 10

201. Kraines, S., T. Yanagi, M. Isobe, and H. Komiyama (1998). Wind-wave driven circulation on the coral reef at bora bay, miyako island. *Coral Reefs 17*(2), 133–143. 16, 128

202. Kuffner, I. (2001). Effects of ultraviolet radiation and water motion on the reef coral porites compressa dana: a flume experiment. *Marine Biology 138*(3), 467–476. 16

203. Kühl, M. (2005). Optical microsensors for analysis of microbial communities. *Methods in enzymology 397*, 166–199. 19

204. Kühlmann, D. H. (1988). The sensitivity of coral reefs to environmental pollution [incl. ishigaki island]. *Ambio 17*. xi, 6

205. Laforsch, C., E. Christoph, C. Glaser, M. Naumann, C. Wild, and W. Niggl (2008). A precise and non-destructive method to calculate the surface area in living scleractinian corals using x-ray computed tomography and 3d modeling. *Coral Reefs 27*(4), 811–820. 21

206. LaJeunesse, T., H. Reyes-Bonilla, and M. Warner (2007). Spring bleaching among pocillopora in the sea of cortez, eastern pacific. *Coral Reefs 26*(2), 265–270. 13

207. Lambo, A. and R. Ormond (2006). Continued post-bleaching decline and changed benthic community of a kenyan coral reef. *Marine pollution bulletin 52*(12), 1617–1624. 10

208. Larson, J., R. Jacob, and E. Ong (2005). The model coupling toolkit: A new fortran90 toolkit for building multiphysics parallel coupled models. *International Journal of High Performance Computing Applications 19*(3), 277–292. 49

209. Lasker, H. R. (1981). Phenotypic variation in the coral montastrea cavernosa and its effects on colony energetics. *The Biological Bulletin 160*(2), 292–302. 194

210. Ledlie, M., N. Graham, J. Bythell, S. Wilson, S. Jennings, N. Polunin, and J. Hardcastle (2007). Phase shifts and the role of herbivory in the resilience of coral reefs. *Coral Reefs 26*(3), 641–653. 10

211. Leigh, E. and T. Rowell (1995). The evolution of mutualism and other forms of harmony at various levels of biological organization. *Ecologie 26*(3), 131–158. 191

212. Lesser, M. (1997). Oxidative stress causes coral bleaching during exposure to elevated temperatures. *Coral Reefs 16*(3), 187–192. xi, 11, 12

213. Lesser, M. and J. Shick (1989). Effects of irradiance and ultraviolet radiation on photoadaptation in the zooxanthellae of aiptasia pallida: primary production, photoinhibition, and enzymic defenses against oxygen toxicity. *Marine Biology 102*(2), 243–255. 17

214. Lesser, M., W. Stochaj, D. Tapley, and J. Shick (1990). Bleaching in coral reef anthozoans: effects of irradiance, ultraviolet radiation, and temperature on the activities of protective enzymes against active oxygen. *Coral Reefs 8*(4), 225–232. 11, 191

215. Lesser, M. P. (1996). Elevated temperatures and ultraviolet radiation cause oxidative stress and inhibit photosynthesis in symbiotic dinoflagellates. *Limnology and oceanography 41*(2), 271–283. 11

216. Lesser, M. P. (2004). Experimental biology of coral reef ecosystems. *Journal of Experimental Marine Biology and Ecology 300*(1), 217–252. 3

217. Lesser, M. P. (2006). Oxidative stress in marine environments: biochemistry and physiological ecology. *Annu. Rev. Physiol. 68*, 253–278. 8

218. Lesser, M. P. and J. H. Farrell (2004). Exposure to solar radiation increases damage to both host tissues and algal symbionts of corals during thermal stress. *Coral reefs 23*(3), 367–377. 17

219. Lesser, M. P., V. M. Weis, M. R. Patterson, and P. L. Jokiel (1994). Effects of morphology and water motion on carbon delivery and productivity in the reef coral, *Pocillopora damicornis*: Diffusion barriers, inorganic carbon limitation, and biochemical plasticity. *Journal of Experimental Marine Biology and Ecology 178*(2), 153–179. 16, 126, 193, 194

220. Lienhard, J. H. (2011). *A heat transfer textbook*. Courier Dover Publications. 192

221. Liu, G., A. E. Strong, and W. Skirving (2003). Remote sensing of sea surface temperatures during 2002 barrier reef coral bleaching. *Eos, Transactions American Geophysical Union 84*(15), 137. 4, 13, 15, 24

222. Lobban, C. S., P. J. Harrison, and M. J. Duncan (1985). *The physiological ecology of seaweeds*. Cambridge University Press Cambridge. 16

223. Loch, K., W. Loch, H. Schuhmacher, and W. R. See (2002). Coral recruitment and regeneration on a maldivian reef 21 months after the coral bleaching event of 1998. *Marine Ecology 23*(3), 219–236. 189

224. Loch, K., W. Loch, H. Schuhmacher, and W. R. See (2004). Coral recruitment and regeneration on a maldivian reef four years after the coral bleaching event of 1998. part 2: 2001–2002. *Marine Ecology 25*(2), 145–154. 19

225. Lough, J. and D. Barnes (2000). Environmental controls on growth of the massive coral porites. *Journal of Experimental Marine Biology and Ecology 245*(2), 225–243. 96

226. Lowe, R. J., J. L. Falter, J. R. Koseff, S. G. Monismith, and M. J. Atkinson (2007). Spectral wave flow attenuation within submerged canopies: Implications for wave energy dissipation. *Journal of geophysical research 112*(C5), C05018. 34

227. Lowe, R. J., J. L. Falter, S. G. Monismith, and M. J. Atkinson (2009a). A numerical study of circulation in a coastal reef-lagoon system. *Journal of Geophysical Research 114*(C6), C06022. 34, 45

228. Lowe, R. J., J. L. Falter, S. G. Monismith, and M. J. Atkinson (2009b). Wave-driven circulation of a coastal reef-lagoon system. *Journal of Physical Oceanography 39*(4), 873–893. 34

229. Lowe, R. J., J. R. Koseff, and S. G. Monismith (2005). Oscillatory flow through submerged canopies: 1. velocity structure. *Journal of Geophysical Research: Oceans (1978–2012) 110*(C10). 34

230. Loya, Y., K. Sakai, K. Yamazato, Y. Nakano, Y. Sambali, and R. van Woesik (2001). Coral bleaching: the winners and the losers. *Ecology Letters 4*(2), 122–131. 19, 86, 122, 161, 162, 189, 190

231. Lyzenga, D. R. (1978). Passive remote sensing techniques for mapping water depth and bottom features. *Applied optics 17*(3), 379–383. 27

232. Magnusson, S. H., M. Fine, and M. Kühl (2007). Light microclimate of endolithic phototrophs in the scleractinian corals montipora monasteriata and porites cylindrica. *Marine Ecology Progress Series 332*, 119–128. 19

233. Manzello, D. P., R. Berkelmans, and J. C. Hendee (2007). Coral bleaching indices and thresholds for the florida reef tract, bahamas, and st. croix, us virgin islands. *Marine Pollution Bulletin 54*(12), 1923–1931. xi, 13, 14

234. Manzello, D. P., M. Brandt, T. B. Smith, D. Lirman, J. C. Hendee, and R. S. Nemeth (2007). Hurricanes benefit bleached corals. *Proceedings of the National Academy of Sciences 104*(29), 12035–12039. 15

235. Mardaljevic, J. (1995). Validation of a lighting simulation program under real sky conditions. *Lighting research and Technology 27*(4), 181–188. 102

236. Mardaljevic, J. (1999). *Daylight simulation: validation, sky models and daylight coefficients*. Ph. D. thesis, De Montfort University. xvii, 266, 267, 268, 270, 271

237. Mardaljevic, J. (2000). Simulation of annual daylighting profiles for internal illuminance. *Lighting Research and Technology 32*(3), 111–118. 102

238. Marsh, J. A. (1970). Primary productivity of reef-building calcareous red algae. *Ecology*, 255–263. 20, 21

239. Marshall, P. and A. Baird (2000). Bleaching of corals on the great barrier reef: differential susceptibilities among taxa. *Coral reefs 19*(2), 155–163. 19, 22, 161, 162, 189

240. Marshall, P. and H. Schuttenberg (2006). *A reef manager's guide to coral bleaching*. Great Barrier Reef Marine Park Authority. 8

241. Mass, T., S. Einbinder, E. Brokovich, N. Shashar, R. Vago, J. Erez, and Z. Dubinsky (2007). Photoacclimation of stylophora pistillata to light extremes: metabolism and calcification. *Marine Ecology Progress Series 334*, 93–102. 19

242. Mass, T., A. Genin, U. Shavit, M. Grinstein, and D. Tchernov (2010). Flow enhances photosynthesis in marine benthic autotrophs by increasing the efflux of oxygen from the organism to the water. *Proceedings of the National Academy of Sciences 107*(6), 2527. 34, 159

243. Mayor, A. G. (1914). *The effects of temperature upon tropical marine animals*. Carnegie Institution of Washington. 10

244. McClanahan, T. (2000). Bleaching damage and recovery potential of maldivian coral reefs. *Marine Pollution Bulletin 40*(7), 587–597. 19

245. McClanahan, T., M. Ateweberhan, N. Graham, S. Wilson, C. Sebastian, M. M. Guillaume, and J. Bruggemann (2007). Western indian ocean coral communities: bleaching responses and susceptibility to extinction. 15

246. McClanahan, T. and J. Maina (2003). Response of coral assemblages to the interaction between natural temperature variation and rare warm-water events. *Ecosystems 6*(6), 551–563. 19, 189

247. McClanahan, T., J. Maina, R. Moothien-Pillay, and A. Baker (2005). Effects of geography, taxa, water flow, and temperature variation on coral bleaching intensity in mauritius. *Marine ecology. Progress series 298*, 131–142. 194

248. McClanahan, T., J. Maina, C. Starger, P. Herron-Perez, and E. Dusek (2005). Detriments to post-bleaching recovery of corals. *Coral Reefs 24*(2), 230–246. 10

249. McClanahan, T. R., M. Ateweberhan, C. A. Muhando, J. Maina, and M. S. Mohammed (2007). Effects of climate and seawater temperature variation on coral bleaching and mortality. *Ecological Monographs 77*(4), 503–525. 10, 13, 15

250. McWilliams, J. P., I. M. Côté, J. A. Gill, W. J. Sutherland, and A. R. Watkinson (2005). Accelerating impacts of temperature-induced coral bleaching in the caribbean. *Ecology 86*(8), 2055–2060. 2

251. Meesters, E., G. Nieuwland, G. Duineveld, A. Kok, and R. Bak (2002). Rna/dna ratios of scleractinian corals suggest acclimatisation/adaptation in relation to light gradients and turbidity regimes. *Marine ecology. Progress series 227*, 233–239. 117

252. Menter, F., M. Kuntz, and R. Langtry (2003). Ten years of industrial experience with the sst turbulence model. *Turbulence, heat and mass transfer 4*, 625–632. 140, 261

253. Menter, F. R. (1994). Two-equation eddy-viscosity turbulence models for engineering applications. *AIAA journal 32*(8), 1598–1605. 140

254. Merks, R., A. Hoekstra, J. Kaandorp, and P. Sloot (2003a). Models of coral growth: spontaneous branching, compactification and the laplacian growth assumption. *Journal of theoretical biology 224*(2), 153–166. 28, 194

255. Merks, R., A. Hoekstra, J. Kaandorp, and P. Sloot (2003b). A problem solving environment for modelling stony coral morphogenesis. In *Computational ScienceICCS 2003*, pp. 639–648. Springer. 194

256. Meyer, J. L. and E. T. Schultz (1985). Tissue condition and growth rate of corals associated with schooling fish. *Limnology and oceanography 30*(1), 157–166. 21

257. Monismith, S. G. (2007). Hydrodynamics of coral reefs. *Annu. Rev. Fluid Mech. 39*, 37–55. 28, 34, 45, 192

258. Moore, J. A., L. M. Bellchambers, M. R. Depczynski, R. D. Evans, S. N. Evans, S. N. Field, K. J. Friedman, J. P. Gilmour, T. H. Holmes, R. Middlebrook, et al. (2012). Unprecedented mass bleaching and loss of coral across 12 of latitude in western australia in 2010–11. *PloS one 7*(12), e51807. 28

259. Motoda, S. (1940). The environment and the life of massive reef coral, goniastrea aspera verrill, inhabiting the reef flat in palao. *Palao Trop Biol Stn Stud 2*, 61–104. 20

260. Muko, S., K. Kawasaki, K. Sakai, F. Takasu, and N. Shigesada (2000). Morphological plasticity in the coral porites sillimaniani and its adaptive significance. *Bulletin of Marine Science 66*(1), 225–239. 118, 194

261. Muller-Parker, G. and C. F. D'Elia (1997). Interactions between corals and their symbiotic algae. *Life and death of coral reefs*, 96–113. xi, 5, 6, 7

262. Mumby, P., W. Skirving, A. Strong, J. Hardy, E. LeDrew, E. Hochberg, R. Stumpf, and L. David (2004). Remote sensing of coral reefs and their physical environment. *Marine Pollution Bulletin 48*(3-4), 219–228. xix, 24, 25

263. Mumby, P. J. (1999). Bleaching and hurricane disturbances to populations of coral recruits in belize. *Marine Ecology Progress Series 190*, 27–35. 19, 162, 190

264. Mumby, P. J., J. R. Chisholm, A. J. Edwards, S. Andrefouet, and J. Jaubert (2001). Cloudy weather may have saved society island reef corals during the 1998 enso event. *Marine Ecology-Progress Series 222*, 209. 2, 15, 17, 18, 22, 55, 117, 161

265. Munk, W. H. and M. C. Sargent (1948). Adjustment of bikini atoll to ocean waves. *Transactions, American Geophysical Union 29*, 855–860. 26

266. Muscatine, L. and J. W. Porter (1977). Reef corals: mutualistic symbioses adapted to nutrient-poor environments. *Bioscience*, 454–460. 1, 8

267. Nakamura, T., R. Van Woesik, et al. (2001). Water-flow rates and passive diffusion partially explain differential survival of corals during the 1998 bleaching event. *Marine Ecology Progress Series 212*, 301–304. 16, 189, 192, 194

268. Nakamura, T., R. Van Woesik, and H. Yamasaki (2005). Photoinhibition of photosynthesis is reduced by water flow in the reef-building coral acropora digitifera. *Marine Ecology Progress Series 301*, 109–118. 16, 126, 159, 194

269. Naumann, M. S., W. Niggl, C. Laforsch, C. Glaser, and C. Wild (2009). Coral surface area quantification–evaluation of established techniques by comparison with computer tomography. *Coral Reefs 28*(1), 109–117. 21

270. Nield, D. A. and A. Bejan (2006). *Convection in porous media*. springer. xii, 39

271. Odum, H. T. and E. P. Odum (1955). Trophic structure and productivity of a windward coral reef community on eniwetok atoll. *Ecological Monographs*, 291–320. 21

272. Oliver, J. (1985). Recurrent seasonal bleaching and mortality of corals on the great barrier reef. In *Proceedings of the Fifth International Coral Reef Congress*, Volume 4, pp. 206. 189

273. Ong, R., A. King, B. Mullins, M. Caley, and T. Cooper (2012). CFD simulation of low reynolds-number turbulence models in coral thermal microenvironment. In *Australian Fluid Mechanics Society*. 189

274. Ong, R., A. King, B. Mullins, T. Cooper, and M. Caley (2011). Computational fluid dynamics model of thermal microenvironments of corals. Modelling and Simulation (MODSIM). 189

275. Ong, R., A. King, B. Mullins, T. Cooper, and M. Caley (2012). Development and validation of computational fluid dynamics models for prediction of heat transfer and thermal microenvironments of corals. *PLoS One 7*(6), e37842. 83, 86, 87, 96, 161, 169, 189, 192

276. OpenCFD Ltd. (2010, August). *OpenFOAM - User Guide*. OpenCFD Ltd. Version 1.7, http://www.openfoam.com/. 44, 138, 139, 253, 254

277. Osborne, K., A. M. Dolman, S. C. Burgess, and K. A. Johns (2011). Disturbance and the dynamics of coral cover on the great barrier reef (1995–2009). *PLoS One 6*(3), e17516. 2, 10

278. Packard, G. C. and T. J. Boardman (1988). The misuse of ratios, indices, and percentages in ecophysiological research. *Physiological Zoology*, 1–9. 162

279. Pandolfi, J. M., R. H. Bradbury, E. Sala, T. P. Hughes, K. A. Bjorndal, R. G. Cooke, D. McArdle, L. McClenachan, M. J. Newman, and G. Paredes (2003). Global trajectories of the long-term decline of coral reef ecosystems. *Science 301*(5635), 955–958. 24

280. Pandolfi, J. M., J. B. Jackson, N. Baron, R. H. Bradbury, H. M. Guzman, T. P. Hughes, C. Kappel, F. Micheli, J. C. Ogden, and H. Possingham (2005). Are U.S. coral reefs on the slippery slope to slime? *Science 307*(5716), 1725–1726. 24

281. Parmesan, C. and G. Yohe (2003). A globally coherent fingerprint of climate change impacts across natural systems. *Nature 421*(6918), 37–42. 24

282. Parnell, K. (1988). The hydrodynamics of fringing reef bays in the great barrier reef marine park. In *Proc 6th Int Coral Reef Symp*, Volume 2, pp. 503–508. 45

283. Patankar, S. V. (1980). *Numerical heat transfer and fluid flow: Computational Methods in Mechanics and Thermal Science*. Hemisphere Publishing Corp. xvii, 239, 248

284. Patankar, S. V. and D. B. Spalding (1972). A calculation procedure for heat, mass and momentum transfer in three-dimensional parabolic flows. *International Journal of Heat and Mass Transfer 15*(10), 1787–1806. 252

285. Patterson, M. R. (1992a). A chemical engineering view of cnidarian symbioses. *American Zoologist 32*(4), 566–582. 20, 38, 86, 192, 193, 194

286. Patterson, M. R. (1992b). A mass transfer explanation of metabolic scaling relations in some aquatic invertebrates and algae. *Science 255*(5050), 1421–1423. 38, 166, 167, 190, 192

287. Patterson, M. R. and K. P. Sebens (1989). Forced convection modulates gas exchange in cnidarians. *Proceedings of the National Academy of Sciences 86*(22), 8833–8836. 16, 192

288. Patterson, M. R., K. P. Sebens, and R. R. Olson (1991). In situ measurements of flow effects on primary production and dark respiration in reef corals. *Limnology and Oceanography 36*(3), 936–948. 16, 34, 166, 192, 193, 194

289. Paulson, C. A. and J. J. Simpson (1977). Irradiance measurements in the upper ocean. *Journal of Physical Oceanography 7*(6), 952–956. 55, 115, 116

290. Pawlowicz, R., B. Beardsley, and S. Lentz (2002). Classical tidal harmonic analysis including error estimates in matlab using t_tide. *Computers & Geosciences 28*(8), 929–937. 141

291. Peters, R. H. (1986). *The ecological implications of body size*, Volume 2. Cambridge University Press. 163

292. Phongsuwan, N. (1998). Extensive coral mortality as a result of bleaching in the andaman sea in 1995. *Coral Reefs 17*(1), 70–70. 17

293. Phongsuwan, N. (2002). Coral reefs in thailand. *Unpublished paper. Phuket Marine Biological Center, Phuket, Thailand*. 130

294. Pickard, G. (1986). Effects of wind and tide on upper-layer currents at davies reef, great barrier reef, during mecor (july-august 1984). *Marine and Freshwater Research 37*(5), 545–565. 45

295. Pittock, A. B. (1999). Coral reefs and environmental change: adaptation to what? *American Zoologist 39*(1), 10–29. 3, 13

296. Podestá, G. P. and P. W. Glynn (1997). Sea surface temperature variability in panama and galapagos: extreme temperatures causing coral bleaching. *Journal of Geophysical Research: Oceans (1978–2012) 102*(C7), 15749–15759. 13, 14, 15

297. Pond, S. and G. L. Pickard (1983). *Introductory dynamical oceanography*. Gulf Professional Publishing. 18

298. Porter, J. W. (1976). Autotrophy, heterotrophy, and resource partitioning in caribbean reef-building corals. *American Naturalist*, 731–742. 83, 85, 194

299. Potemra, J. T., M. E. Luther, and J. J. O'Brien (1991). The seasonal circulation of the upper ocean in the bay of bengal. *Journal of Geophysical Research: Oceans (1978–2012) 96*(C7), 12667–12683. 131

300. Prahl, H. v. (1983). Blanqueo masivo y muerte de corales en la isla de gorgona, pacífico colombiano. *Cespedesia 12*, 125–29. 15

301. Prahl, H. v. (1985). Blanqueo masivo y muerte de corales hermatípicos en el pacífico colombiano atribuidos al fenómeno de el niño 1982-83. *Boletín Erfen 12*, 22–24. 15

302. Preisendorfer, R. W. (1986). Secchi disk science: Visual optics of natural waters. *Limnol. Oceanogr 31*(5), 909–926. 52

303. Prosser, C. L. (1991). *Comparative animal physiology*. John Wiley & Sons. 22

304. Rao, S. A., S. K. Behera, Y. Masumoto, and T. Yamagata (2002). Interannual subsurface variability in the tropical indian ocean with a special emphasis on the indian ocean dipole. *Deep Sea Research Part II: Topical Studies in Oceanography 49*(7), 1549–1572. 131

305. Raz-Bahat, M., H. Faibish, T. Mass, and B. Rinkevich (2009). Three-dimensional laser scanning as an efficient tool for coral surface area measurements. *Limnol. Oceanogr.: Methods 7*, 657–663. 21

306. Reinhart, C. F. and O. Walkenhorst (2001). Validation of dynamic radiance-based daylight simulations for a test office with external blinds. *Energy and Buildings 33*(7), 683–697. 102

307. Riegl, B. (1999). Corals in a non-reef setting in the southern arabian gulf (dubai, uae): fauna and community structure in response to recurring mass mortality. *Coral Reefs 18*(1), 63–73. 10

308. Riegl, B. (2002). Effects of the 1996 and 1998 positive sea-surface temperature anomalies on corals, coral diseases and fish in the arabian gulf (dubai, uae). *Marine biology 140*(1), 29–40. 19, 162, 190

309. Riegl, B. and W. E. Piller (2003). Possible refugia for reefs in times of environmental stress. *International Journal of Earth Sciences 92*(4), 520–531. 3

310. Roache, P. J. (1998). *Verification and validation in computational science and engineering*. Hermosa. 265

311. Roberts, H. H., S. P. Murray, and J. N. Suhayda (1975). Physical processes in fringing reef system. *Journal of Marine Research 33*(2), 233–260. 45

312. Roberts, H. H., P. A. Wilson, and A. Lugo-Fernández (1992). Biologic and geologic responses to physical processes: examples from modern reef systems of the caribbean-atlantic region. *Continental Shelf Research 12*(7), 809–834. 45

313. Roche, R., R. Abel, K. Johnson, and C. Perry (2010). Quantification of porosity in acropora pulchra (brook 1891) using x-ray micro-computed tomography techniques. *Journal of Experimental Marine Biology and Ecology*. 74

314. Rogers, C. S., J. Miller, E. M. Muller, P. Edmunds, R. S. Nemeth, J. P. Beets, A. M. Friedlander, T. B. Smith, R. Boulon, C. F. Jeffrey, et al. (2008). Ecology of coral reefs in the us virgin islands. In *Coral Reefs of the USA*, pp. 303–373. Springer. 10

315. Rowan, R. (2004). Coral bleaching: thermal adaptation in reef coral symbionts. *Nature 430*(7001), 742–742. 22, 191

316. Rowan, R., N. Knowlton, A. Baker, and J. Jara (1997). Landscape ecology of algal symbionts creates variation in episodes of coral bleaching. *Nature 388*(6639), 265–269. 161, 191

317. Roy, C. and F. Blottner (2001). Assessment of one-and two-equation turbulence models for hypersonic transitional flows. *Journal of Spacecraft and Rockets 38*(5), 699–710. 78

318. Saha, S., S. Moorthi, H.-L. Pan, X. Wu, J. Wang, S. Nadiga, P. Tripp, R. Kistler, J. Woollen, D. Behringer, et al. (2010). The ncep climate forecast system reanalysis. *Bulletin of the American Meteorological Society 91*(8). 136

319. Saji, N., B. N. Goswami, P. Vinayachandran, and T. Yamagata (1999). A dipole mode in the tropical indian ocean. *Nature 401*(6751), 360–363. 131

320. Saxby, T., W. C. Dennison, and O. Hoegh-Guldberg (2003). Photosynthetic responses of the coral montipora digitata to cold temperature stress. *Marine Ecology Progress Series 248*, 85–97. 13

321. Schmidt-Nielsen, K. (1984). *Scaling: why is animal size so important?* Cambridge University Press. 162, 163, 195

322. Sebens, K., S. Grace, B. Helmuth, E. Maney Jr, and J. Miles (1998). Water flow and prey capture by three scleractinian corals, madracis mirabilis, montastrea cavernosa and porites porites, in a field enclosure. *Marine Biology 131*(2), 347–360. 34

323. Sebens, K., B. Helmuth, E. Carrington, and B. Agius (2003). Effects of water flow on growth and energetics of the scleractinian coral agaricia tenuifolia in belize. *Coral Reefs 22*(1), 35–47. 16, 34

324. Shashar, N., S. Kinane, P. Jokiel, and M. Patterson (1996). Hydromechanical boundary layers over a coral reef. *Journal of Experimental Marine Biology and Ecology 199*(1), 17–28. 192

325. Shchepetkin, A. F. and J. C. McWilliams (2005). The regional oceanic modeling system (roms): a split-explicit, free-surface, topography-following-coordinate oceanic model. *Ocean Modelling 9*(4), 347–404. 49, 135

326. Shen, C. and T. Evans (2001). Surface-to-subsurface velocity projection for shallow water currents. *Journal of geophysical research 106*, 6973–6984. xvi, 49, 140, 151

327. Shenkar, N., M. Fine, and Y. Loya (2005). Size matters: bleaching dynamics of the coral oculina patagonica. *Marine Ecology Progress Series 294*, 181–188. 19, 83, 162

328. Shibata, K. and F. T. Haxo (1969). Light transmission and spectral distribution through epi-and endozoic algal layers in the brain coral, favia. *The Biological Bulletin 136*(3), 461–468. 19

329. Simpson, J. and J. Hunter (1974). Fronts in the irish sea. *Nature 250*, 404–406. 27

330. Skirving, W., M. Heron, and S. Heron (2006). The hydrodynamics of a bleaching event: Implications for management and monitoring. *Coral Reefs and Climate Change: Science and Management*, 145–161. 15, 22, 24

331. Smith, J. M. (1999). *The major transitions in evolution*. Perseus Books. 191

332. Smith, L., J. Gilmour, A. Heyward, and M. Rees (2006). Mass-bleaching, mortality and slow recovery of three common groups of scleractinian corals at an isolated reef. In *Proceedings of the 10th International Coral Reef Symposium*, Volume 1, pp. 651–656. 10

333. Smith, L. W. and C. Birkeland (2007). Effects of intermittent flow and irradiance level on back reef *Porites* corals at elevated seawater temperatures. *Journal of Experimental Marine Biology and Ecology 341*(2), 282–294. 159, 193

334. Smith, R. C. and K. S. Baker (1979). Penetration of uv-b and biologically effective dose-rates in natural waters. *Photochemistry and Photobiology 29*(2), 311–323. 17

335. Smith, S. V. and R. Buddemeier (1992). Global change and coral reef ecosystems. *Annual Review of Ecology and Systematics 23*, 89–118. 22, 23

336. Spillman, C., O. Alves, and D. Hudson (2011). Seasonal prediction of thermal stress accumulation for coral bleaching in the tropical oceans. *Monthly Weather Review 139*(2), 317–331. 28

337. Stimson, J. and R. A. Kinzie (1991). The temporal pattern and rate of release of zooxanthellae from the reef coral *Pocillopora damicornis* under nitrogen-enrichment and control conditions. *Journal of Experimental Marine Biology and Ecology 153*(1), 63–74. 21

338. Storlazzi, C. D., A. S. Ogston, M. H. Bothner, M. E. Field, and M. Presto (2004). Wave-and tidally-driven flow and sediment flux across a fringing coral reef: Southern molokai, hawaii. *Continental Shelf Research 24*(12), 1397–1419. 128

339. Stumpf, R. P., K. Holderied, and M. Sinclair (2003). Determination of water depth with high-resolution satellite imagery over variable bottom types. *Limnology and Oceanography 48*(1-2), 547–556. 27

340. Sweatman, H., S. Delean, and C. Syms (2011). Assessing loss of coral cover on australias great barrier reef over two decades, with implications for longer-term trends. *Coral Reefs 30*(2), 521–531. 2, 10

341. Symonds, G., K. P. Black, and I. R. Young (1995). Wave-driven flow over shallow reefs. *Journal of Geophysical Research: Oceans 100*(C2), 2639–2648. 26

342. Szmant, A., L. Ferrer, and L. FitzGerald (1990). Nitrogen excretion and o: N ratios in reef corals: evidence for conservation of nitrogen. *Marine Biology 104*(1), 119–127. 5

343. Taebi, S., R. J. Lowe, C. B. Pattiaratchi, G. N. Ivey, and G. Symonds (2012). A numerical study of the dynamics of the wave-driven circulation within a fringing reef system. *Ocean Dynamics 62*(4), 585–602. 26

344. Tennekes, H. and J. L. Lumley (1972). *A first course in turbulence*. The MIT press. 254

345. Thomas, F. I. M. and M. J. Atkinson (1997). Ammonium uptake by coral reefs: Effects of water velocity and surface roughness on mass transfer. *Limnology and Oceanography 42*(1), 81–88. 34

346. Thompson, D. W. (1966). *On growth and form*. Cambridge University Press. 164

347. Thornhill, D. J., R. D. Rotjan, B. D. Todd, G. C. Chilcoat, R. Iglesias-Prieto, D. W. Kemp, T. C. LaJeunesse, J. M. Reynolds, G. W. Schmidt, and T. Shannon (2011). A connection between colony biomass and death in caribbean reef-building corals. *PloS One 6*(12), e29535. 161

348. Tolman, H. L. (2002). User manual and system documentation of *wavewatch – iii* version 2.22. Technical report. 137

349. Tomczak, M. and J. S. Godfrey (2003). *Regional oceanography: an introduction*. Daya Books. 129

350. Tregenza, P. (1983). The monte carlo method in lighting calculations. *Lighting Research and Technology 15*(4), 163–170. 50

351. Trench, R. K. (1993). Microalgal-invertebrate symbioses: a review. *Endocytobiosis Cell Res 9*(13), 175. 191

352. Uchiyama, Y., J. C. McWilliams, and A. F. Shchepetkin (2010). Wave–current interaction in an oceanic circulation model with a vortex-force formalism: Application to the surf zone. *Ocean Modelling 34*(1), 16–35. 152

353. Ulstrup, K. E., R. Hill, and P. J. Ralph (2005). Photosynthetic impact of hypoxia on in hospite zooxanthellae in the scleractinian coral pocillopora damicornis. *Mar Ecol Prog Ser 286*, 125–132. 193

354. Vago, R., E. Vago, Y. Achituv, M. Ben-Zion, and Z. Dubinsky (1994). A non-destructive method for monitoring coral growth affected by anthropogenic and natural long term changes. *Bulletin of marine science 55*(1), 126–132. 86

355. Van Duin, E. H., G. Blom, F. J. Los, R. Maffione, R. Zimmerman, C. F. Cerco, M. Dortch, and E. P. Best (2001). Modeling underwater light climate in relation to sedimentation, resuspension, water quality and autotrophic growth. *Hydrobiologia 444*(1-3), 25–42. 18

356. Van Oppen, M. J. and J. M. Lough (2008). *Coral Bleaching*. Springer. 4

357. van Woesik, R., A. Irikawa, R. Anzai, and T. Nakamura (2012). Effects of coral colony morphologies on mass transfer and susceptibility to thermal stress. *Coral Reefs*, 1–7. 193

358. Van Woesik, R., A. Irikawa, and Y. Loya (2004). Coral bleaching: signs of change in southern japan. In *Coral Health and Disease*, pp. 119–141. Springer. 19, 162, 190

359. Varkey, M., V. Murty, and A. Suryanarayana (1996). Physical oceanography of the bay of bengal and andaman sea. *Oceanography and marine biology: an annual review 34*, 1–70p. 131

360. Vaughan, T. (1914). Reef corals of the bahamas and of southern florida. *Carnegie Institution of Washington 11*. 10

361. Veal, C., K. Michael, and M. Nunez (2010). Partitioning of underwater direct and diffuse ultraviolet irradiance in a shallow water coral reef. *Marine and Freshwater Research 60*(12), 1244–1253. 138

362. Veal, J., G. Holmes, M. Nunez, O. Hoegh-Guldberg, and J. Osborn (2010). A comparative study of methods for surface area and three-dimensional shape measurement of coral skeletons. *Limnology and Oceanography: Methods 8*(May), 241–253. 20, 21, 86

363. Veron, J. (1995). *Corals in space and time: the biogeography and evolution of the Scleractinia*. Cornell University Press. 19, 83, 162

364. Veron, J. (2000). *Corals of the world*, Volume 1-3. Australian Institute of Marine Science. 19, 83, 162

365. Veron, J. and M. Pichon (1976). *Scleractinia of eastern Australia, Part 1*, Volume 1. Canberra: Australian Government Printing Office. 194

366. Versteeg, H. and W. Malalasekera (1995). *An Introduction to Computational Fluid Dynamics: The Finite Volume Approach*. Longman Scientific, Technical. xvii, 44, 139, 242, 243, 244, 245, 254

367. Vinayachandran, P., N. Saji, and T. Yamagata (1999). Response of the equatorial indian ocean to an unusual wind event during 1994. *Geophysical Research Letters 26*(11), 1613–1616. 131

368. Vogel, S. (1981). Life in moving fluids. *The physical biology of tlow. Princeton, N.. I.: Princeton University Press, Princeton. New Jersey*. 16

369. Vollmer, S. V. and P. J. Edmunds (2000). Allometric scaling in small colonies of the scleractinian coral siderastrea siderea (ellis and solander). *The Biological Bulletin 199*(1), 21–28. 162

370. Wakeford, M., T. Done, and C. Johnson (2008). Decadal trends in a coral community and evidence of changed disturbance regime. *Coral Reefs 27*(1), 1–13. 10

371. Ward, G. (1990). Visualization. *Lighting Design and Application 20*(6), 4–20. 50, 102

372. Ward, G. J. (1992). Measuring and modeling anisotropic reflection. *ACM SIGGRAPH Computer Graphics 26*(2), 265–272. 50, 102

373. Ward, G. J. (1994a). Adaptive shadow testing for ray tracing. In *Photorealistic Rendering in Computer Graphics*, pp. 11–20. Springer. 50, 102

374. Ward, G. J. (1994b). The radiance lighting simulation and rendering system. In *Proceedings of the 21st annual conference on Computer graphics and interactive techniques*, pp. 459–472. ACM. 50, 102, 269, 271

375. Ward, G. J. (1994c, August). *The RADIANCE Synthetic Imaging System* (Version 4 ed.). Version 4, http://radsite.lbl.gov/radiance/. 49, 50, 51, 88, 102, 126, 271

376. Ward, G. J. and P. Heckbert (1992). Irradiance gradients. In *Third Eurographics Workshop on Rendering*, Volume 8598. 50, 102

377. Ward, G. J. and F. M. Rubinstein (1988). A new technique for computer simulation of illuminated spaces. *Journal of the Illuminating Engineering Society 17*(1), 80–91. 51, 102

378. Ward, G. J., F. M. Rubinstein, and R. D. Clear (1988). A ray tracing solution for diffuse interreflection. *ACM SIGGRAPH Computer Graphics 22*(4), 85–92. 51, 102

379. Ward, G. L. and R. Shakespeare (1998). *Rendering with Radiance*. Morgan Kaufmann Publishers. 51, 102, 266, 271

380. Warner, J. C., B. Armstrong, R. He, and J. B. Zambon (2010). Development of a coupled ocean–atmosphere–wave–sediment transport (coawst) modeling system. *Ocean modelling 35*(3), 230–244. 135

381. Warner, J. C., N. Perlin, and E. D. Skyllingstad (2008). Using the model coupling toolkit to couple earth system models. *Environmental Modelling & Software 23*(10), 1240–1249. 135

382. Warner, J. C., C. R. Sherwood, R. P. Signell, C. K. Harris, and H. G. Arango (2008). Development of a three-dimensional, regional, coupled wave, current, and sediment-transport model. *Computers & Geosciences 34*(10), 1284–1306. 49

383. Warner, M., W. Fitt, and G. Schmidt (1996). The effects of elevated temperature on the photosynthetic efficiency of zooxanthellae in hospite from four different species of reef coral: a novel approach. *Plant, Cell & Environment 19*(3), 291–299. 11, 17, 191

384. Warner, M. E., W. K. Fitt, and G. W. Schmidt (1999). Damage to photosystem ii in symbiotic dinoflagellates: a determinant of coral bleaching. *Proceedings of the National Academy of Sciences 96*(14), 8007–8012. 11, 17

385. Webster, P. J., A. M. Moore, J. P. Loschnigg, and R. R. Leben (1999). Coupled ocean–atmosphere dynamics in the indian ocean during 1997–98. *Nature 401*(6751), 356–360. 128, 131

386. Weinberg, S. (1976). Submarine daylight and ecology. *Marine Biology 37*(4), 291–304. 18, 56, 116

387. Weller, R. and S. Anderson (1996). Surface meteorology and air-sea fluxes in the western equatorial pacific warm pool during the toga coupled ocean-atmosphere response experiment. *Journal of Climate 9*(8), 1959–1990. 46

388. Wheeler, W. N. (1988). Algal productivity and hydrodynamics-a synthesis. *Progress in phycological research 6*, 23–58. 16

389. White, F. (1988). *Heat and Mass Transfer*. Addison-Wesley Publishing Co. 166, 190, 192

390. Wilcox, D. C. (1998). *Turbulence modeling for CFD*, Volume 2. DCW industries La Canada, CA. 140

391. Wilkinson, C. (2000). Status of coral reefs of the world: 2004. *Global Coral Reef Monitoring Network, Australia 18*, 473–491. 3, 9, 13, 19, 189

392. Wilkinson, C. (2004). Status of coral reefs of the world. *Global Coral Reef Monitoring Network, Australia 2*. 10

393. Wilkinson, C. R. (1999). Global and local threats to coral reef functioning and existence: review and predictions. *Marine and Freshwater Research 50*(8), 867–878. 15

394. Wilkinson, C. R., D. Souter, and G. C. R. M. Network (2008). *Status of Caribbean coral reefs after bleaching and hurricanes in 2005*. Global Coral Reef Monitoring Network. 9, 10

395. Williams, E. H. and L. B. Willaims (1990). The world-wide coral reef bleaching cycle and related sources of coral mortality. *Atoll Research Bulletin 335*, 1–71. 3, 9, 13

396. Woesik, V. et al. (2001). Coral bleaching: the winners and the losers. *Ecology Letters 4*(2), 122–131. 19, 162

397. Wooldridge, S. A. (2009). Water quality and coral bleaching thresholds: Formalising the linkage for the inshore reefs of the great barrier reef, australia. *Marine Pollution Bulletin 58*(5), 745–751. 22

398. Wright, L. D. (1995). Morphodynamics of inner continental shelves. 18

399. Wyatt, A. S., R. J. Lowe, S. Humphries, and A. M. Waite (2010). Particulate nutrient fluxes over a fringing coral reef: relevant scales of phytoplankton production and mechanisms of supply. *Mar. Ecol. Prog. Ser 405*, 113–130. 34

400. Yamazato, K. (1981). A note on the expulsion of zooxanthellae during summer, 1980, by the okinawan reef-building corals. *Sesoko Mar Sci Lab Tech Rep 8*, 9–18. 189

401. Yonge, C. M., A. Nicholls, and M. J. Yonge (1931). *Studies on the physiology of corals*, Volume 1. British Museum. 11

Appendix 1: Numerical Flow Modelling or Basic CFD

This appendix is intended to serve as an abridged introduction to Computational Fluid Dynamics (CFD). However, for those without prior experience in CFD, this section should not in any way affect the main framework of this thesis. On the other hand, for those with prior experience in CFD that are seeking for more background, the resources or reference section includes more sophisticated sources of information.

This appendix introduces and discusses some of the basic principles of CFD starting from a general overview, governing equations of the mathematical models, discretization methods, brief introduction to OpenFOAM, concept of turbulence modelling, and some basic error estimations.

Overview

Prediction of heat transfer and fluid flow processes can be obtained by two main methods: experimental investigation and theoretical calculation (Patankar, 1980). This section briefly discuss each and then compare the two.

The most reliable information about physical processes could only be obtained by actual measurement. However, experimental investigations involving full-scale equipment are, in most cases, prohibitively expensive. Alternatively, one may perform small-scale models and extrapolating the resulting information at the end to full scale. Nevertheless, small-scale models do not always represent all the features of the full-scale models; for instance, important phenomena (i.e. combustion, turbulence, etc) may not be scalable and often omitted from the model tests, which further reduces the usefulness of the test results. Finally, it is important to note that there are serious difficulties of measurement in many situations, and that the measuring instruments are not free from errors.

Such problems may be resolved with the help of numerical prediction that suitably represent the full-scale of physical process. Numerical model used for fluid dynamics problems mainly consists of a set of partial differential equations.

If classical mathematics techniques were to be used for solving such equations, there would be little hope of predicting many cases of practical interest with closed form solution. Fortunately, the development of numerical methods and the availability of large digital computers hold the promise that the implications of a mathematical model can be worked out for almost any practical problems. Furthermore, computer analysis offers several advantages with respect to experimental investigation: low cost, speed, complete and detailed information, capability in simulating both realistic and ideal conditions. At the same time, numerical method is not free from flaws, for examples, problems for which an adequate mathematical description has not yet been worked out, and solving numerical models sometimes can be more expensive and require longer time to run than experimental investigations.

The starting point of a numerical method is the **Mathematical Model**, i.e. the set of partial differential equations and boundary conditions. Fluid dynamic science teaches that exact conservation laws describe the behavior of all flows: no matter the type of flow, it will respect the general governing equations. General purpose methods however are often impractical, if not impossible, to solve so it is more convenient to include simplifications in the mathematical model and develop a solution method designed for that particular set of equations. Then a suitable **Discretization Method**, approximating the set of differential equations by a system of algebraic equations for the variables at a number of discrete points in space and time, is necessary. The most important discretization methods are: Finite Difference Method (FDM), Finite Volume Method (FVM) and Finite Element Method (FEM). The discrete locations where the variables want to be calculated, are defined by the **Numerical Grid**. The numerical grid is a discrete representation of the flow domain (both in space and time) through the use of a finite number of subdomains.

Then a **Finite Approximation** technique has to be selected taking in consideration the choice for the discretization method and the numerical grid. This choice influence a lot the accuracy of the solution as well as the development, coding, debugging and the speed of the solution method. More accurate approximations involve, in fact, more nodes and give usually a fuller coefficient matrix. A compromise between accuracy and efficiency is always necessary. Once this large system of non-linear algebraic equations has been built by discretization techniques, it must be solved using a **Solution Method**. Such methods use successive linearisation of the equations and the resulting linear systems are almost always solved by iterative techniques. Usually there are two levels of iterations: inner iterations, within which the linear equation are solved, and the outer iterations, that deal with the non linearity and coupling of the equations. As last point, it is important to determine suitable **Convergence Criteria**. It is fundamental to well set stopping conditions for both the inner and the outer cycles

in order to obtain accurate solution in an efficient way.

Once defined, numerical methods must be checked in order to establish whether a the result is appropriate or not. The most important parameters are:

- **Consistency:** discretization should become exact as the grid spacing tends to zero. In other words truncation error, i.e. the difference between exact and discretized equation, must go to zero as $\triangle t \to 0$ and $\triangle x \to 0$.
- **Stability:** errors appearing in the course of numerical solution process do not magnify. For iterative methods, stable methods are the ones that do not diverge.
- **Convergence:** the solution of the discretized equation tends towards the exact solution as the grid spacing tends to zero. It is a very difficult property to demonstrate, it is usually accepted to test grid-independence for a solution.
- **Conservation:** solution must respect conservation of physical quantities both on local and global scale. It is a very important property because limits solution error. Even if on fine grids non-conservative schemes can also lead to correct solutions, conservative ones are usually preferred.
- **Boundedness:** solution should lie within proper bounds. Boundedness is difficult to guarantee and often unbounded schemes have stability and convergence problems too.
- **Realizability:** guarantee a model to give physically realistic solutions for the phenomena it is representing. Usually in connection with phenomena too complex to be directly simulated.
- **Accuracy:** is the property of well approximating the exact solution, in other words limiting modeling, discretization and iteration errors.

Physical principles and mathematical model

In this section conservation equations for mass, momentum and energy for non reacting mono-phase compressible flows, will be described. Firstly, equations are derived in the most general form as possible. The same approach has been used to obtain all the basic equation for fluid motion: apply the appropriate fundamental physical principle to a suitable model of the flow and then extract the mathematical equations which embody such physical principles. The fluid flow has been modeled with infinitesimal control volume (CV) fixed in space

with the fluid moving through it. As a consequence equations are proposed in the differential conservation form. Secondly, an appropriate model for the fluid is proposed: simplifications for the cases of interest such as ideal gas and Newtonian fluid are introduced. Thirdly, passage in manipulating the set of governing equations, i.e. steady-state simplification and turbulence modeling.

Continuity equation

The fundamental physical concept standing behind the continuity equation is that mass is conserved. In other words the rate of increase of mass in fluid element must equal the net rate of flow of mass into fluid element or the rate of change of mass in particle is equal to zero (Versteeg and Malalasekera, 1995)

$$\frac{D\,m}{D\,t} = 0. \tag{1}$$

With reference to Figure 1, the rate of increase of mass in the fluid element is

$$\frac{\partial}{\partial t}(\rho\,\sigma x\,\sigma y\,\sigma z) = \frac{\partial \rho}{\partial t}\sigma x\,\sigma y\,\sigma z, \tag{2}$$

thus the net rate of flow of mass into fluid element is:

$$\begin{aligned}
&\left(\rho\,u - \frac{\partial(\rho\,u)}{\partial x}\frac{1}{2}\sigma x\right)\sigma y\,\sigma z - \left(\rho\,u - \frac{\partial(\rho\,u)}{\partial x}\frac{1}{2}\sigma x\right)\sigma y\,\sigma z \\
&+\left(\rho\,v - \frac{\partial(\rho\,v)}{\partial y}\frac{1}{2}\sigma y\right)\sigma x\,\sigma z - \left(\rho\,v - \frac{\partial(\rho\,v)}{\partial y}\frac{1}{2}\sigma y\right)\sigma x\,\sigma z \\
&+\left(\rho\,w - \frac{\partial(\rho\,w)}{\partial z}\frac{1}{2}\sigma z\right)\sigma x\,\sigma y - \left(\rho\,w - \frac{\partial(\rho w)}{\partial z}\frac{1}{2}\sigma z\right)\sigma x\,\sigma y \\
&= -\left(\frac{\partial(\rho\,u)}{\partial x} + \frac{\partial(\rho\,v)}{\partial y} + \frac{\partial(\rho\,w)}{\partial z}\right)\sigma x\,\sigma y\,\sigma z
\end{aligned} \tag{3}$$

Eq. 2 and Eq. 3 together give the well known differential continuity equation in conservation form:

$$\frac{\partial \rho}{\partial t} + \nabla\cdot(\rho\vec{U}) = 0. \tag{4}$$

Momentum equation

From Newton's second law directly follows the momentum equation: the rate of increase of momentum of fluid particle equals the sum of forces on fluid particle:

$$m\frac{D\vec{U}}{Dt} = F_s + Fb. \tag{5}$$

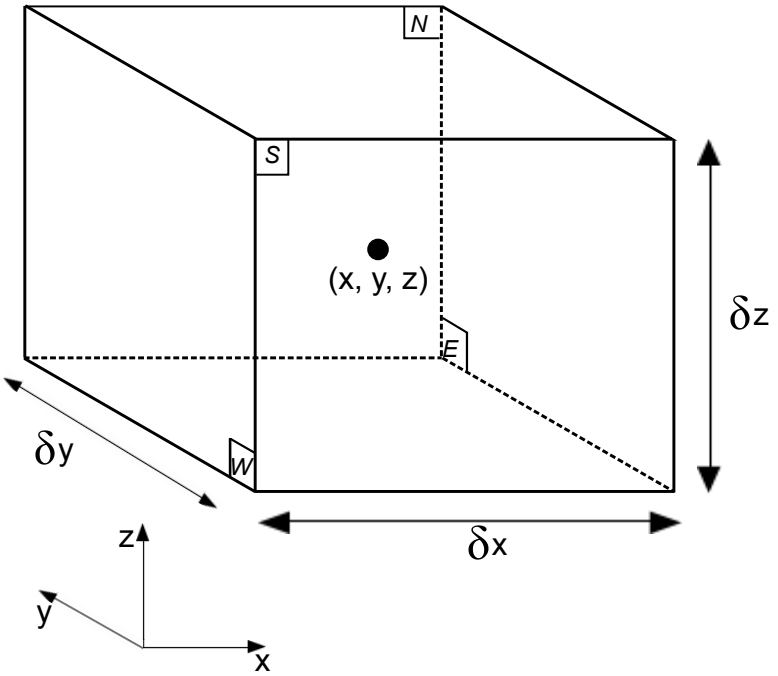

Figure 1. Fluid element for conservation laws. Adapted from (Versteeg and Malalasekera, 1995)

where F_s and F_b are surface forces (defined upon CV boundaries) and body forces (defined upon the volume itself), respectively. It is common to separate surface forces into pressure, the hydrostatic part of the stress tensor, and viscous stress, the deviatoric part.

Surface forces balance in the x-direction (East-West faces) is needed to derive x-momentum equation (Figure 2)

$$\begin{aligned} &\left[\left(p-\frac{\partial p}{\partial x}\frac{1}{2}\sigma x\right)-\left(\tau_{xx}-\frac{\partial \tau_{xx}}{\partial x}\frac{1}{2}\sigma x\right)\right]\sigma y\,\sigma z \\ +&\left[-\left(p+\frac{\partial p}{\partial x}\frac{1}{2}\sigma x\right)+\left(\tau_{xx}+\frac{\partial \tau_{xx}}{\partial x}\frac{1}{2}\sigma x\right)\right]\sigma y\,\sigma z \\ &=\left(-\frac{\partial p}{\partial x}+\frac{\partial \tau_{xx}}{\partial x}\right)\sigma x\,\sigma y\,\sigma z, \end{aligned} \tag{6}$$

then on North-South faces:

$$-\left(\tau_{yx}-\frac{\partial \tau yx}{\partial y}\frac{1}{2}\sigma y\right)\sigma x\,\sigma z+\left(\tau_{yx}+\frac{\partial \tau yx}{\partial y}\frac{1}{2}\sigma y\right)\sigma x\,\sigma z=\frac{\partial \tau_{yx}}{\partial y}\sigma x\,\sigma y\,\sigma z, \tag{7}$$

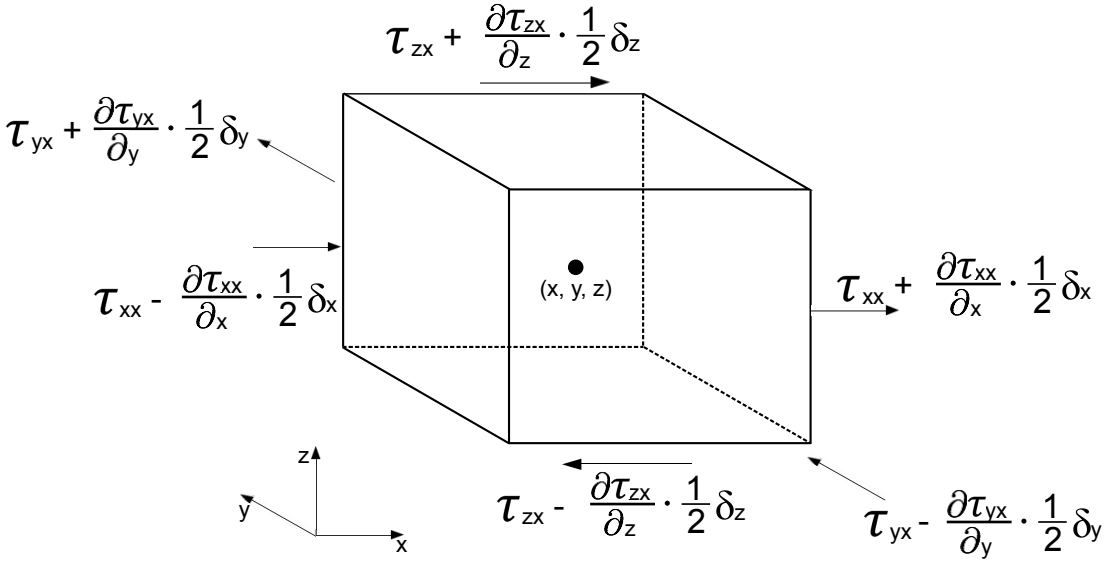

Figure 2. Stress component in the x-direction. Adapted from (Versteeg and Malalasekera, 1995)

and on Top-Bottom faces:

$$-\left(\tau_{zx}-\frac{\partial \tau zx}{\partial z}\frac{1}{2}\sigma z\right)\sigma x\,\sigma y+\left(\tau_{zx}+\frac{\partial \tau zx}{\partial z}\frac{1}{2}\sigma z\right)\sigma x\,\sigma y=\frac{\partial \tau_{zx}}{\partial z}\sigma x\,\sigma y\,\sigma z. \quad (8)$$

Putting Eq. 6, Eq. 7, Eq. 8 together, x-component of the momentum equation is given by:

$$\frac{\partial(\rho\,u)}{\partial t}+\nabla\cdot\left(\rho u\vec{U}\right)=\frac{\partial(-p+\tau_{xx}}{\partial x}+\frac{\partial \tau_{yx}}{\partial y}+\frac{\partial \tau_{zx}}{\partial z}+f_{bx}, \quad (9)$$

similarly can be written for y-direction:

$$\frac{\partial(\rho\,v)}{\partial t}+\nabla\cdot\left(\rho v\vec{U}\right)=\frac{\partial \tau_{xy}}{\partial x}+\frac{\partial(-p+\tau_{yy}}{\partial y}+\frac{\partial \tau_{zy}}{\partial z}+f_{by}, \quad (10)$$

and z-direction:

$$\frac{\partial(\rho\,w)}{\partial t}+\nabla\cdot\left(\rho w\vec{U}\right)=\frac{\partial \tau_{xz}}{\partial x}+\frac{\partial \tau_{yz}}{\partial y}+\frac{\partial(-p+\tau_{zz}}{\partial z}+f_{bz}, \quad (11)$$

Energy equation

The energy equation is derived from the first principle of thermodynamics stating that the rate of change of energy of a fluid particle is equal to the rate of heat

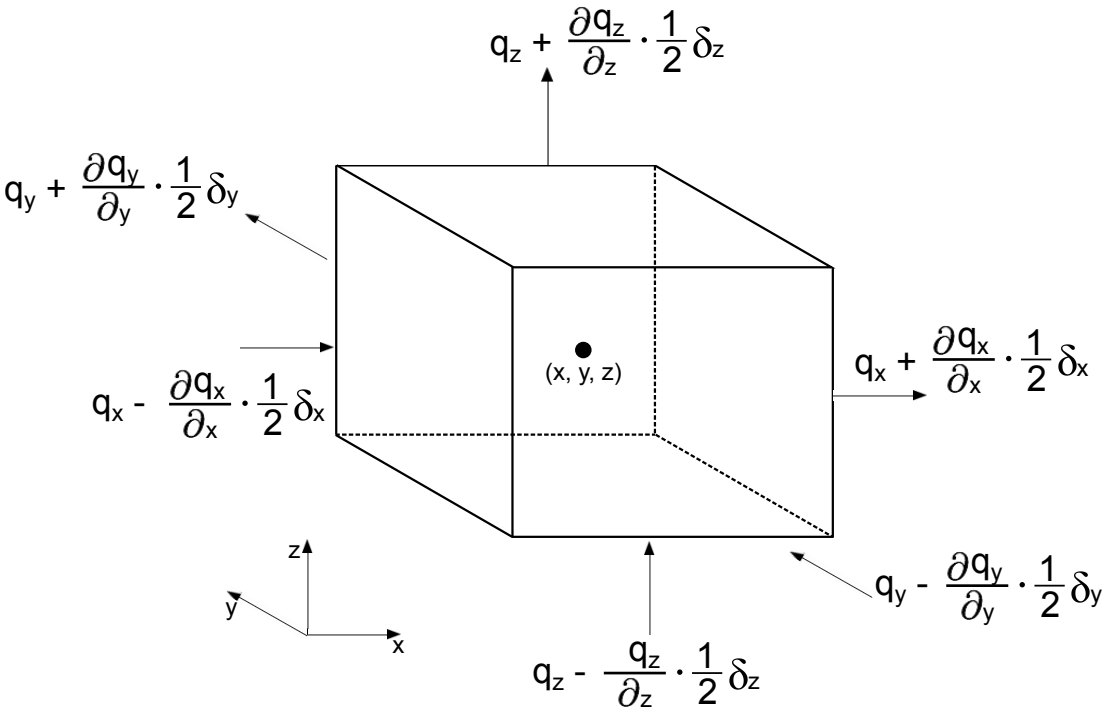

Figure 3. Heat flux vector. Adapted from (Versteeg and Malalasekera, 1995)

addition to the fluid particle plus the rate of work done on the particle

$$m\frac{DE}{Dt} = \dot{Q} + W. \tag{12}$$

Referring to Figure 3, the net rate of heat transfer due to heat flow in the x-direction is:

$$\left[\left(q_x + \frac{\partial q_x}{\partial x}\frac{1}{2}\sigma x\right) - \left(q_x - \frac{\partial q_x}{\partial x}\frac{1}{2}\sigma x\right)\right]\sigma y\sigma z = -\frac{\partial q_x}{\partial x}\sigma x\,\sigma y\,\sigma z, \tag{13}$$

accounting for the y and z-directions, the rate of heat transfer per unit volume is:

$$-\frac{\partial q_x}{\partial x} - \frac{\partial q_y}{\partial y} - \frac{\partial q_z}{\partial z} = \nabla \cdot \vec{q}. \tag{14}$$

Furthermore, from Fourier's law:

$$\vec{q} = -k\,\nabla T, \tag{15}$$

giving finally:

$$\dot{Q} = -\nabla \cdot (k\,\nabla T)\sigma x\,\sigma y\,\sigma z. \tag{16}$$

The net rate of work done on the particle by surface forces acting on x-direction is:

$$\begin{aligned}
&\left[\left(\rho\, u - \frac{\partial \rho\, u}{\partial x}\frac{1}{2}\sigma x\right) - \left(\rho\, u + \frac{\partial \rho\, u}{\partial x}\frac{1}{2}\sigma x\right)\right]\sigma y\,\sigma z \\
&+\left[-\left(\tau_{xx}\, u - \frac{\partial \tau_{xx}}{\partial x}\frac{1}{2}\sigma x\right) + \left(\tau_{xx}\, u + \frac{\partial \tau_{xx}}{\partial x}\frac{1}{2}\sigma x\right)\right]\sigma y\,\sigma z \\
&+\left[-\left(\tau_{yx}\, u - \frac{\partial \tau_{yx}\, u}{\partial y}\frac{1}{2}\sigma y\right) + \left(\tau_{yx}\, u + \frac{\partial \tau_{yx}\, u}{\partial y}\frac{1}{2}\sigma y\right)\right]\sigma x\,\sigma z \\
&+\left[-\left(\tau_{zx}\, u - \frac{\partial \tau_{zx}\, u}{\partial z}\frac{1}{2}\sigma z\right) + \left(\tau_{zx}\, u + \frac{\partial \tau_{zx}\, u}{\partial z}\frac{1}{2}\sigma z\right)\right]\sigma x\,\sigma y \\
&= \left[\frac{\partial(u(-p+\tau_{xx}))}{\partial x} + \frac{\partial(u\,\tau_{yx})}{\partial y} + \frac{\partial(u\,\tau_{zx})}{\partial z}\right]\sigma x\,\sigma y\,\sigma z.
\end{aligned} \tag{17}$$

Following the same approach for the y and z-directions as in Eq. 17 and summing all up, the total rate of work done on the fluid particle by surface stress is:

$$W = \left(-\nabla\cdot(\rho\, U) + \frac{\partial \tau_{ij}\, U_i}{\partial x_j}\right)\sigma x\,\sigma y\,\sigma z. \tag{18}$$

Working around Eq. 18, Eq. 16, and Eq. 12, the energy equation is given by adding the rate of work done by body forces as a source term S_h:

$$\frac{\partial \rho\, E}{\partial t} + \nabla\cdot\left(\rho\, E\,\vec{U}\right) = -\nabla\cdot\left(\rho\,\vec{U}\right) + \frac{\partial \tau_{ij}\, U_i}{\partial x_j} + \nabla\cdot(k\,\nabla T) + S_h. \tag{19}$$

sometimes the term $\frac{\partial \tau_{ij}\, U_i}{\partial x_j}$ is referred to as the viscous dissipation term Φ.

Discretization approach

After the physical mathematical model has been derived, the goal is to manipulate it in a form suitable for computer calculations. First step on this path regards the discretization of the equations. The main task of a discretization approach is to convert a partial differential equation, valid on the entire domain, into a set of discrete algebraic equation, one for every node considered. The value at the node is, of course, put in relation with "neighbor" nodes, the simultaneous satisfaction of all the equation in the set then give the numerical solution. The most popular discretization techniques are presented and discussed:

- **Finite Difference Method** (FDM) approximates conservation equations in differential form substituting partial derivatives via truncated Taylor

series expansions or polynomial fitting. Even if, in principle, it can be applied to all kind of grids, actual applications are limited to structured grids where grid lines are used as local coordinate lines. In such a way in fact, it is easy to obtain higher-order schemes. The biggest drawback of FDM is that it does not enforce conservation, consequently it is very hard to get reliable simulations of complex geometries and use is restricted to the simple ones.

- **Finite Volume Method** (FVM) works with the integral form of the conservation equations. The domain is divided into finite volumes whose centroid represent the calculation node. Grid just define boundaries in between different volumes and need not to be related to any metrics. Interpolation is used to express variable values at the surface in terms of nodal values. This method is conservative by construction as long as surface integrals for volumes sharing the same face are equal for both of them. The disadvantage of FVM in comparison with FDM is that building higher than second order schemes for 3D simulation is much more difficult due to the three levels of approximation introduced: interpolation, differentiation and integration. Because of its very physical approach, ease to be understood and implemented, FVM is the most widely used approach.

- **Finite Element Method** (FEM) may appear similar to FVM, the distinguish feature is the weight function: conservation equations are multiplied by a weight function before being integrated. Solution is supposed to adhere within each volume to a shape function constructed from values at the corners of the elements. Such an hypothesis is substituted into the conservation equations whose derivative with respect to nodal value is put to zero, selecting so the residual minimizing allowed function. The main advantage in using FEM is the ability in dealing with arbitrary geometries, while the main drawback, common to all integral methods, is that the resulting matrix may result not well structured meaning that efficient solving method are difficult to implement.

Finite Volume Method

FVM is based on conservation equations in the integral form. To obtain the governing equations, integration over a finite volume must be performed. To better fix ideas and not to avoid irrelevant calculation, detailed presentation of this method will be done considering the generic conservation equation for a

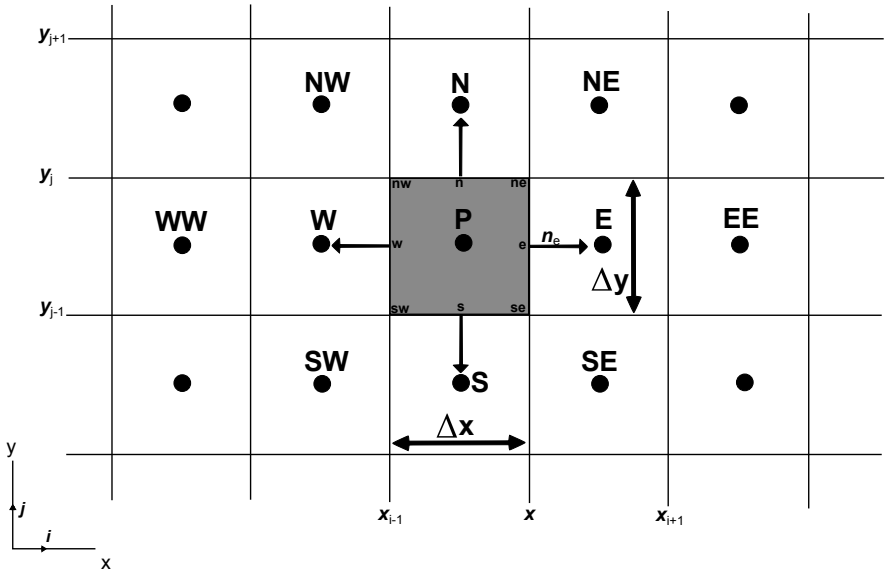

Figure 4. Typical bi-dimensional quadrilateral control volume. Adapted from (Patankar, 1980)

transported scalar Φ:

$$\int_S \vec{J}_\Phi \cdot \vec{n}\, dS = \underbrace{\int_S \rho\, \Phi \left(\vec{U} \cdot \vec{n}\right) dS}_{\text{Convection}} - \underbrace{\int_S \Gamma_\Phi \left(\nabla \Phi \cdot \vec{n}\right) dS}_{\text{Diffusion}} = \underbrace{\int_\Omega q\, \Phi\, d\,\Omega}_{\text{Source}}. \tag{20}$$

Such an equation applies over each CV and the entire domain as well, underlying once again the main feature of FVM: global conservation. To obtain an algebraic equation the three integral must be approximated by quadrature formula. In the following discussion about approximation techniques the bi-dimensional quadrilateral CV in Figure 4 has been considered.

Approximation of volume integrals: Source terms

Source terms require integration over the entire CV. Approximations of such integrals basically reduce in calculating an averaged value $\bar{q}$ for the source terms to be multiplied by the volume

$$Q_P = \int_\Omega q\, d\Omega = \bar{q}\, \Omega. \tag{21}$$

The first and easiest approximation just replaces the mean value with the value at the CV center node

$$Q_P = q_P\, \Omega. \tag{22}$$

Such approximation is obviously exact if q is constant or varies linearly, in any other case is second order accurate. Higher order of accuracy schemes can be obtained via shape function or interpolation.

Approximation of surface integrals

The net flux through the CV boundaries is obtained summing over the six faces, the surface integral of the total flux normal vector j composed by convective and diffusive contributions:

$$\int_S \vec{J} \cdot \vec{n}\, dS = \int_S J_n\, dS = \sum_k \int_{S_k} j\, dS = \sum_k \chi_k. \tag{23}$$

To exactly calculate surface integrals, the value of j is needed everywhere on the face S_k. This is of course impossible as long as only nodal values of Φ are computed, it is so necessary to introduce some approximations. Usually two level of approximation are introduced:

- the integral is approximated in terms of the variable values at one or more locations on the cell face (*face approximation*).
- the cell-face values are approximated in terms of nodal values (*nodal approximation*).

For each type several approximation modes have been proposed. For the face approximation:

- midpoint rule - the value over the face is equal to the value at cell-face center $\chi_e = j_e S_e$. This approximation is of second-order accuracy.
- trapezoid rule - the value on the face is the mean between face extremes (cell vertex) shared with 'neighbor' cells $\chi_e = S_e \frac{1}{2}(j_{ne} + j_{se})$. This approximation is second order too.
- Simpson's rule - the value on the face is a combination of the value at the center of the face and the values at the vertices $\chi_e = S_e \frac{1}{6}(j_{ne} + 4j_e + j_{se})$. This approximation is forth order.

$\vec{J}$ is composed by two different contributions: convection and diffusion. These two terms indeed behave in a quite different manner as will be shown in the following.

Diffusive flux

Discretization of the diffusive fluxes gives, using midpoint rule and assuming linear variation:

$$\int_S \Gamma_\Phi \left(\nabla\Phi \cdot \vec{n}\right) dS = \sum_k S_k \left(\rho\,\Gamma_\Phi\,\nabla\Phi\right)_k = \sum_k S_k \left(\rho\,\Gamma_\Phi\right)_k \left(\nabla\Phi\right)_k . \tag{24}$$

To compute gradients on the boundary face e:

$$\left(\nabla\Phi\right)_e = \frac{\Phi_E - \Phi_P}{\chi_E - \chi_P}. \tag{25}$$

To compute the gradient in other way that is:

$$\left(\nabla\Phi\right)_P = \frac{1}{\Omega}\sum_k S_k\,\Phi_k, \tag{26}$$

and find the corresponding value on the face e interpolating $(\nabla\Phi)_P$ and $(\nabla\Phi)_E$ with finite approximation schemes.

Convective flux

The discretization of the convective fluxes gives using the midpoint rule:

$$\int_S \rho\,\Phi \left(\vec{U}\cdot\vec{n}\right) dS = \sum_k S_k \left(\rho\,\Phi\,U_n\right)_k = \sum_k S_k \left(\rho\,U_n\right)_k \Phi_k = \sum_k F_k\,\Phi_k. \tag{27}$$

Transport of Φ across the boundary faces has been computed in quite a direct way, the problem has now shifted in finding an expression for Φ_k involving only nodal values.

Interpolation techniques

Interpolation is needed to obtain the function values at quadrature points. This section presents some of the most common interpolation schemes to get values at locations other than computational nodes.

Upwind difference scheme (UDS)

This approximation is equivalent to using a backward forward difference approximation for first derivative. Such interpolation scheme result in being stable,

boundedness criterion always satisfied, but numerically diffusive. Consider in fact Taylor series expansion:

$$\Phi_e = \Phi_p + (x_e - x_p)\left(\frac{\partial \Phi}{\partial x}\right)_P + \frac{(x_e - x_p)^2}{2}\left(\frac{\partial^2 \Phi}{\partial x^2}\right)_P + H. \tag{28}$$

UDS neglect all terms but the first so it is a first order scheme. The first neglected term behave like a diffusive flux:

$${j_e}^d = \Gamma_e \left(\frac{\partial \Phi}{\partial x}\right)_e, \tag{29}$$

meaning that scalars are diffused normally and parallel to the flow. The coefficient of numerical diffusion is proportional to grid dimension and to mass flux, moreover is magnified for multidimensional oblique to the grid flows. To avoid such inaccuracy, fundamental in case of shocks or rapid changes, mesh must be refine a lot because the scheme is only first order accurate.

Central difference scheme (CDS)

In analogy with finite difference differential approximation, linear interpolation can be implemented for FVM: the value at CV-face center is a linear interpolation, with distance as weighting factor, of the values at the centers;

$$\Phi_e = \Phi_E \lambda_e + \Phi_P (1 - \lambda_e), \tag{30}$$

with $\lambda_e = (x_e - x_P) = (x_E x_P)$. Taylor series expansion for Φ_E at point x_P shows that Eq. 30 is second order accurate vanishing all first order terms in the truncation error.

$$\Phi_e = \Phi_E \lambda_e + \Phi_P (1 - \lambda_e) - \frac{(x_e - x_p)(x_E - x_p)}{2}\left(\frac{\partial^2 \Phi}{\partial x^2}\right)_P + H. \tag{31}$$

Having eliminated the numerical diffusion, the leading term of the truncation error is quadratic and may produce oscillatory solutions. In spite of such oscillatory behavior CDS, being the simplest second order, is one the most widely used differencing scheme.

Solution method

Previous sections were dealing with building up the algebraic equations to be solved for a generic scalar Φ transported by a known flow field. It is important to underline that the flow field cannot be known a priori and scalar quantities

for which conservation equations were derived $(\rho, \rho U_i, p)$ are responsible for the development of the flow field. Hence, the equations are not independent one from the other but on the contrary different scalar conservation laws result to be tightly coupled. In other words the Navier-Stokes Equations cannot be solved separately but must be treated like a real system meaning that in the conservation equation for scalar Φ_1, all other Φ_S cannot be considered known but should be treated as variables too. This results in a strong non-linearity of the system, for example convective or viscous dissipation terms.

Many different algorithms can be used to improve convergence properties for this cycle usually called **outer cycle**, most of which separate the system in equations to be solved sequentially and not contemporary. Once the Navier-Stokes equations are linearized, they appear in the final form:

$$A \cdot \Phi = Q \tag{32}$$

where A is the sparse coefficient matrix for all the conservation laws and the equation of state, Φ is the solution vector for all variables and Q is the source vector. Linear systems are solvable using, for example, Gauss elimination techniques or Cramer rule.

Methods for solving linear systems are commonly classified into two main groups: direct methods and iterative methods. Direct methods handle the matrix with linear algebra rules to reduce it in a form from which extraction of final solution can be done quite easily. Every well posed linear system can be solved directly but the sparse matrix A (every node depends on the value of not so many other nodes) gives decomposition matrices that are not sparse increasing the computational cost considerably. Iterative methods instead starts from a guessed solution and use the system to successively refine it. If each iteration is affordable and the number of iteration is small enough, this is usually the case in CFD, iterative methods result in being much faster than direct ones. This iterative cycle is called **inner cycle**. The algorithms used in this thesis are the Incomplete Cholesky preconditioned Conjugate Gradient (ICCG), Incomplete Cholesky preconditioned Biconjugate Gradient (BICCG) and the Algebraic Multi Grid (AMG). For details on such methods, refer to (Chen et al., 1990; Ferziger and Perić, 1999; Patankar and Spalding, 1972)

OpenFOAM

The OpenFOAM stands for Open Field Operation and Manipulation; it is the software being evaluated in the course of this thesis. This chapter is intended to give the reader who is unfamiliar with it an idea of OpenFOAM; it is by no means an attempt at a complete documentation.

It is an object-oriented numerical simulation toolkit for continuum mechanics, written in C++ programming. The code is released as free and open source software under the GNU General Public License, it is maintained by OpenFOAM Foundation Ltd (http://www.openfoam.com) (OpenCFD Ltd., 2010). The core technology of OpenFOAM is a flexible set of modules, which can be used to build a wealth of: solvers, to simulate specific problems in engineering mechanics: utilities, to perform pre- and post- processing: libraries, to create toolboxes that are accessible to the solvers/utilities, such as libraries of physical models.

OpenFOAM covers an impressive range of applications with solvers ranging from a simple potential flow solver (potentialFoam) over incompressible steady-state (simpleFoam), transient laminar (icoFoam) turbulent (turbFoam) or dynamic mesh (icoDyMFoam) solvers, compressible steady-state (rhoSimpleFoam) or transient and supersonic turbulent (sonic-TurbFoam) solvers to multiphase flow solvers (e. g., interFoam), LES solvers (oodles), combustion codes (dieselEngineFoam), electromagnetics (mhdFoam), solid stress analysis (solidDisplacementFoam) and even finance (financialFoam) solvers.

This section discusses briefly the specific details of OpenFOAM in helping CFD programmers. First and most important thing is that the toolkit implements operator-based implicit and explicit second and fourth-order Finite Volume (FV) discretization in three dimensional space and on curved surface. Differential operators can be treated like finite volume calculus (fvc) or finite volume method (fvm) operators. The former performs explicit derivatives returning a field, whereas the latter is an implicit derivation converting the expression into matrix coefficients. Explicit equivalent for the common operators such as curl, gradient, etc, are defined and implemented.

To give an example of the capability of CFD code, let's consider standard equation like momentum conservation:

$$\frac{\partial \rho \vec{U}}{\partial t} + \nabla \cdot \left(\rho \vec{U} \vec{U} \right) - \nabla \cdot \left(\mu \nabla \vec{U} \right) = -\nabla p. \tag{33}$$

It can be written in OpenFOAM as:

```
1  solve
2  (
3      fvm::ddt(rho, U)
4    + fvm::div(phi, U)
5    - fvm::laplacian(mu, U)
6      ==
7    - fvc::grad(p)
8  );
```

Important feature allowed by object programming is the dimensional check, physical quantities objects are in fact constructed with a reference to their dimensions and so only valid dimensional operations can be performed. Avoiding errors and permitting an easier understanding, come directly as a consequence of an easier debug.

OpenFOAM is flexible in defining new models and solvers in the simplest way. Its strength in fact stands in being open not only in terms of source code but, what's more, in its inner structure and hierarchical design, giving the user the opportunity to fully extend its capability. Moreover, the possibility of using top-level libraries containing a set of models for the same purpose which refer to the same interface, guarantees programmers for smooth and efficient integration with the built-in functionality. New models can be added to the appropriate model table at link-time and become available in the same manner as the supplied models.

Most of the selections necessary to set up calculations are done at runtime, meaning that options can change while the code is running. For further information about how to use and how to program OpenFOAM see (OpenCFD Ltd., 2010).

Turbulence modelling

It is known that, for low velocities, wall-bounded flows are smooth and adjacent layers of fluid slide past each other in an orderly fashion. When velocity is high instead the flow become intrinsically unsteady and chaotic even with constant boundary conditions: the flow is said to be turbulent.

In turbulent flow we usually divide the variables in one time-averaged part U, which is independent of time (when the mean flow is steady), and one fluctuating part u so that $U = U + u$.

There is no definition on turbulent flow, but it has a number of characteristic features (see (Tennekes and Lumley, 1972; Versteeg and Malalasekera, 1995)) such as:

- **Irregularity**: Turbulent flow is irregular, random and chaotic. The flow consists of a spectrum of different scales (eddy sizes) where largest eddies are of the order of the flow geometry. At the other end of the spectra we have the smallest eddies which are by viscous forces (stresses) dissipated into internal energy. Even though turbulence is chaotic it is deterministic and is described by the Navier-Stokes equations.

- **Time fluctuations**: Superimposed upon a mean value for each quantities: $\Phi(t) = \overline{\Phi} + \Phi'(t)$. Connected with this is the extension to three dimensions

also for bi-dimensional flows: velocity fluctuates always in 3D.

- **Diffusivity**: In turbulent flow the diffusivity increases. This means that the spreading rate of boundary layers increases as the flow becomes turbulent. The turbulence increases the exchange of momentum in e.g. boundary layers and reduces or delays thereby separation at bluff bodies such as cylinders, airfoils and cars. The increased diffusivity also increases the resistance (wall friction) in internal flows such as in channels and pipes.

- **Eddies**: fluid packets intermingle and fill the shear layer with a wide range of length scales, coexist at the same time and at the same place.

- **Large Reynolds Numbers**: Turbulent flow occurs at high Reynolds number. For example, the transition to turbulent flow in pipes occurs that $\mathrm{Re}_D \simeq$2,300, and in boundary layers at $\mathrm{Re}_x \simeq$100,000.

- **Dissipation**: Turbulent flow is dissipative, which means that kinetic energy in the small (dissipative) eddies are transformed into internal energy. The small eddies receive the kinetic energy from slightly larger eddies. The slightly larger eddies receive their energy from even larger eddies and so on. The largest eddies extract their energy from the mean flow. This process of transferred energy from the largest turbulent scales (eddies) to the smallest is called *cascade process*.

- **Mixing**: is much stronger than in laminar flows. Turbulent eddies actively increase diffusion by moving in the three dimensions. Heat transfer and friction are strongly enhanced.

Transition from laminar and turbulent regime always occurs when a certain, called critical, Reynolds number is reached. Starting from such a description, turbulence is likely to be anisotropic: only the smallest eddies in fact are non-directional, with bigger ones strongly dependent on mean flow direction.

Boussinesq assumption

In eddy viscosity turbulence models the Reynolds stresses are linked to the velocity gradients via the turbulent viscosity: this relation is called the Boussinesq assumption, where the Reynolds stress tensor in time averaged Navier-Stokes equation is replaced by the turbulent viscosity multiplied by the velocity gradients.

Models for turbulence

Turbulence models are generally classified according to which governing equations they apply to. Within these broader categories, they are further broken down by the number of additional transport equations which one must solve in order to compute the model contributions.

- **Direct Numerical Simulation** (DNS): it is not a model, Navier-Stokes Equations are computed in their most general form meaning that the complete spectrum of involved frequencies and length scales are solved. This approach is only feasible at current time for Low Reynolds number flows, due to limitation on computer resources, and used mainly as validation test for other approaches or as an help in understanding turbulence physics.

- **Large Eddy Simulation** (LES): remembering that energy is contained mainly in the largest scales, this model reduces the range of interest only to the biggest vortices. It employs, in fact, a time dependent three dimensional computation of the large-eddy structure and a model for the small scales. It basically consists in altering in space the Navier-Stokes Equations with a high-pass filter, resolving for scales that actually are the energy-containing scales and modelling dissipation subrange behavior.

- **Reynolds Averaged Navier Stokes** (RANS): Navier-Stokes Equations are averaged in time on a period big enough to contain also lowest frequency oscillation. The unsteady behavior of the turbulent flows is completely neglected, turbulence become a steady phenomenon simply considering the effects of fluctuations onto the mean flow. At the state of art RANS simulations are the standard for flows involving heat transfer of industrial interest. In fact unsteady phenomena result in being determinant for such simulations.

- **Hybrid**: this class is aiming in taking advantage of low computational cost of the RANS approach and the good confidence of LES simulation. The idea is to use the two approaches in different areas where flow conditions are diverse. In particular LES is used only in the zone were RANS simulations are likely to fail, namely separating zone.

RANS approach

This methodology is based on the decomposition of the flow variables into a mean and a fluctuating part. The Navier-Stokes equation for momentum is then solved for the mean values. Considering incompressible flows, the velocity and pressure

components are substituted by

$$U_i = \langle U_i \rangle + U_i^{'} \tag{34}$$

$$p = \langle p \rangle + p^{'} \tag{35}$$

If the terms in Navier-Stokes equations are averaged the following relations for the mass and momentum conservation are obtained:

$$\frac{\partial \langle U_i \rangle}{\partial x_i} = 0 \tag{36}$$

$$\rho \frac{\partial \langle U_i \rangle}{\partial t} + \rho \langle U_j \rangle \frac{\partial \langle U_i \rangle}{\partial x_j} = -\frac{\partial \langle p \rangle}{\partial x_j} + \frac{\partial}{\partial x_j}\Big(\langle \tau_{ij} - \rho \langle U_i^{'} U_j^{'} \rangle \Big) \tag{37}$$

These are known as the Reynolds-Averaged Navier-Stokes equations (RANS). This is the same as Navier-Stokes equations except for the term

$$\tau_{ij}{}^{R} = -\rho \langle U_i^{'} U_j^{'} \rangle = -\rho \Big(\langle U_i U_j \rangle - \langle U_i \rangle \langle U_j \rangle \Big) \tag{38}$$

which constitutes the so-called Reynolds-stress tensor. It represents the transfer of momentum due to turbulent fluctuations. The laminar viscous stresses are calculated using Reynolds-averaged velocity components,

$$\langle \tau_{ij} \rangle = \mu \left(\frac{\partial U_i}{\partial x_j} + \frac{\partial U_j}{\partial x_i} \right) \tag{39}$$

In the 3D case the Reynolds-stress tensor consists of nine components

$$\rho \langle U_i^{'} U_j^{'} \rangle = \begin{pmatrix} \rho \Big\langle \Big(U_1^{'} \Big)^2 \Big\rangle & \rho \Big\langle U_1^{'} U_2^{'} \Big\rangle & \rho \Big\langle U_1^{'} U_3^{'} \Big\rangle \\ \rho \Big\langle U_2^{'} U_1^{'} \Big\rangle & \rho \Big\langle \Big(U_2^{'} \Big)^2 \Big\rangle & \rho \Big\langle U_2^{'} U_3^{'} \Big\rangle \\ \rho \Big\langle U_3^{'} U_1^{'} \Big\rangle & \rho \Big\langle U_3^{'} U_2^{'} \Big\rangle & \rho \Big\langle \Big(U_3^{'} \Big)^2 \Big\rangle \end{pmatrix} \tag{40}$$

The task of Reynolds averaged turbulence modelling is to express the Reynolds stress tensor in terms of the known quantities. The most popular approach is to use the Boussinesq approximation, which prescribes a linear relation of the form:

$$\overline{U'U'} = \nu_t (\nabla U + (\nabla U)^T) + \frac{2}{3} k I \tag{41}$$

where

$$k = \frac{1}{2} \overline{U' \cdot U'} = \frac{1}{2} \langle U_i^{'} U_i^{'} \rangle = \frac{1}{2} \left[\Big\langle \Big(U_1^{'} \Big)^2 \Big\rangle + \Big\langle \Big(U_2^{'} \Big)^2 \Big\rangle + \Big\langle \Big(U_3^{'} \Big)^2 \Big\rangle \right] \tag{42}$$

The kinematic eddy viscosity nu_t can be evaluated in many different ways:

- Zero-equation models - V_s and L_s are calculated directly from the local mean flow quantities (e.g. Prandtl's mixing-length model)
- One-equation models - V_s is calculated from a suitable transport equation, usually the turbulent kinetic energy, and the length scale, L_s, is prescribed empirically (e.g. Prandtl's k-L model)
- Two-equation models - V_s and L_s are both calculated from transport equations, usually kinetic energy and its dissipation rate

The fundamental limitation of zero equation models is the assumption that Reynolds Stress can be modelled on mean flow: turbulence does not in fact respond instantly to changes in mean flow but rather adjusts over a time scale typical of the turbulent structure. One equation models, even if feels the influence of fluctuating properties via turbulent kinetic energy equation, do still depend on geometry via the definition of a characteristic length. First, in order of complexity, class of model to be independent on the definition of an appropriate length scale is the two equations class. This property is fundamental in predicting many type of flows, for example recirculating flows: mixing length in fact cannot be used for flows in which diffusion and convection are not negligible.

Wall functions

For both velocity and turbulent kinetic energy no-slip condition stands at the wall. To force the correct near-wall behavior however it is important to have a good guess for the mean value of turbulent viscosity for U and of production and dissipation term for k .

The natural way to treat wall boundaries is to make the grid sufficiently fine so that the sharp gradients prevailing there are resolved. Often, when computing complex three-dimensional flow, that requires too much computer resources. An alternative is to assume that the flow near the wall behaves like a fully developed turbulent boundary layer and prescribe boundary conditions employing wall functions. The assumption that the flow near the wall has the characteristics of a that in a boundary layer if often not true at all. However, given a maximum number of nodes that we can afford to use in a computation, it is often preferable to use wall functions which allows us to use fine grid in other regions where the gradients of the flow variables are large.

In a fully turbulent boundary layer the production term and the dissipation term in the log-law region ($30 < y^+ < 100$) are much larger than the other terms. The log-log law can be written as

$$\frac{U}{u_*} = \frac{1}{\kappa} \log\left(\frac{E u_* y}{\nu}\right). \tag{43}$$

where E is a constant value of 9.0. Comparing this with the standard form of the log-law

$$\frac{U}{u_*} = A \log\left(\frac{u_* y}{\nu}\right) + B \tag{44}$$

where

$$A = \frac{1}{\kappa} \qquad B = \frac{1}{\kappa} \log E \tag{45}$$

Setting grid

The low Re turbulence model is employed in the region of viscous sublayer, which approximately lies in y^+ around 1. The dimensionless quantity of normalised distance from the wall, y^+, is defined as

$$y^+ = \frac{y \cdot u_\star}{\nu} \qquad u_\star = \sqrt{\frac{\tau_w}{\rho}} \tag{46}$$

$$\tau_w = \frac{C_f \rho {U_0}^2}{2} \qquad C_f = \frac{0.0791}{Re^{-0.3}} \tag{47}$$

where y is the actual distance from the wall, $u_\star$ is the friction velocity, and τ_w is the wall shear stress.

A rule of thumb for setting the first gridline for a low-Re turbulence model is to choose a value y^+ around 1 and using mesh grading in order to avoid building a mesh with unnecessary many cells. The grading, G, is defined as the length of the last cell width, t_2, divided by the first cell width, t_1. The number of cell layers, c_l, has been chosen as the same number as the grading for easier calculation of the required y value.

Low-Re number turbulence models

In the previous section we discussed wall functions which are used in order to reduce the number of cells. However, we must be aware that this is an approximation which, if the flow near the boundary is important, can be rather crude. In many internal flows where all boundaries are either walls, symmetry planes, inlet or outlets the boundary layer may not be that important, as the flow field is often pressure-determined. For external flows, however, the flow conditions in the boundaries are almost invariably important. When we are predicting heat transfer it is in general no good idea to use wall functions, because the heat transfer at the walls are very important for the temperature field in the whole domain. The disadvantage of low-Re models is that a very fine grid is required in each near-wall zone. Consequently, the computer-storage and runtime requirements are much greater than those of the wall-function approach.

$k-\epsilon$ Launder-Sharma model

$$\frac{\partial \rho \bar{U} k}{\partial x} + \frac{\partial \rho \bar{V} k}{\partial y} = \frac{\partial}{\partial y}\left[\left(\mu + \frac{\mu_t}{\sigma_k}\right)\frac{\partial k}{\partial y}\right] + \mu_t\left(\frac{\partial \bar{U}}{\partial y}\right)^2 - \rho\epsilon \tag{48}$$

$$\begin{aligned}\frac{\partial \rho \bar{U} \tilde{\epsilon}}{\partial x} + \frac{\partial \rho \bar{V} \tilde{\epsilon}}{\partial y} &= \frac{\partial}{\partial y}\left[\left(\mu + \frac{\mu_t}{\sigma_\epsilon}\right)\frac{\partial \tilde{\epsilon}}{\partial y}\right] \\ &+ c_{1_\epsilon} f_1 \frac{\tilde{\epsilon}}{k}\mu_t\left(\frac{\partial \bar{U}}{\partial y}\right)^2 - c_{\epsilon_2} f_2 \rho \frac{\tilde{\epsilon}^2}{k} + E\end{aligned} \tag{49}$$

$$\mu_t = c_\mu f_\mu \rho \frac{k^2}{\epsilon} \tag{50}$$

$$\epsilon = \tilde{\epsilon} + D \tag{51}$$

where

$$f_\mu = \exp\left(\frac{-3.4}{(1 + R_T/50)^2}\right) \tag{52}$$

$$f_1 = 1 \tag{53}$$

$$f_2 = 1 - 0.3\exp(-{R_T}^2) \tag{54}$$

$$D = 2\mu\left(\frac{\partial \sqrt{k}}{\partial y}\right)^2 \tag{55}$$

$$E = 2_\mu \frac{\mu_t}{\rho}\left(\frac{\partial^2 \bar{U}}{\partial y^2}\right)^2 \tag{56}$$

$$R_T = \frac{k^2}{\nu\tilde{\epsilon}} \tag{57}$$

$k-\omega$ Wilcox model

$$\nu_t = \frac{k}{\omega} \tag{58}$$

$$\frac{\partial(\rho k)}{\partial t} + U_j \frac{\partial(\rho k)}{\partial x_j} = \tau_{ij}\frac{\partial U_i}{\partial x_j} - \beta^* k\omega + \frac{\partial}{\partial x_j}\left[(\nu + \sigma^*\nu_T)\frac{\partial k}{\partial x_j}\right] \tag{59}$$

$$\frac{\partial(\rho \omega)}{\partial t} + U_j \frac{\partial(\rho \omega)}{\partial x_j} = \alpha\frac{\omega}{k}\tau_{ij}\frac{\partial U_i}{\partial x_j} - \beta\omega^2 + \frac{\partial}{\partial x_j}\left[(\nu + \sigma\nu_T)\frac{\partial \omega}{\partial x_j}\right] \tag{60}$$

where

$$\alpha = \frac{5}{9} \tag{61}$$

$$\beta = \frac{3}{40} \tag{62}$$

$$\beta^* = \frac{9}{100} \tag{63}$$

$$\sigma = \frac{1}{2} \tag{64}$$

$$\sigma^* = \frac{1}{2} \tag{65}$$

$$\tag{66}$$

$k-\omega$ Shear Stress Transport model

The modelled equations for the turbulent kinetic energy k and the specific dissipation rate ω are given in details by Menter *et al.* (2003) (Menter et al., 2003).

$$\nu_t = \frac{a_1 k}{\max(a_1\omega, SF_2)} \tag{67}$$

$$\frac{\partial(\rho k)}{\partial t} + U_j\frac{\partial(\rho k)}{\partial x_i} = \tilde{P}_k - \beta^*\rho k\omega + \frac{\partial}{\partial x_j}\left[(\mu + \sigma_k\nu_t)\frac{\partial k}{\partial x_i}\right] \tag{68}$$

$$\begin{aligned}\frac{\partial(\rho\omega)}{\partial t} + U_j\frac{\partial(\rho\omega)}{\partial x_j} = \alpha\rho S^2 - \beta\rho\omega^2 + \frac{\partial}{\partial x_j}\left[(\nu + \sigma_\omega\nu_t)\frac{\partial\omega}{\partial x_j}\right] \\ +2(1-F_1)\rho\sigma_{\omega 2}\frac{1}{\omega}\frac{\partial k}{\partial x_i}\frac{\partial\omega}{\partial x_i}\end{aligned} \tag{69}$$

where

$$F_2 = \tanh\left[\left[\max\left(\frac{2\sqrt{k}}{\beta^* \omega y}, \frac{500\nu}{y^2\omega}\right)\right]^2\right] \tag{70}$$

$$P_k = \min\left(\tau_{ij}\frac{\partial U_i}{\partial x_j}, 10\beta^* k\omega\right) \tag{71}$$

$$F_1 = \tanh\left[\left[\min\left[\max\left(\frac{\sqrt{k}}{\beta^*\omega y}, \frac{500\nu}{y^2\omega}\right), \frac{4\sigma_{\omega 2}k}{CD_{k\omega}y^2}\right]\right]^4\right] \tag{72}$$

$$CD_{k\omega} = \max\left(2\rho\sigma_{\omega 2}\frac{1}{\omega}\frac{\partial k}{\partial x_i}\frac{\partial \omega}{\partial x_i}, 10^{-10}\right) \tag{73}$$

$$\phi = \phi_1 F_1 + \phi_2(1 - F_1) \tag{74}$$

$$\alpha_1 = \frac{5}{9}, \alpha_2 = 0.44 \tag{75}$$

$$\beta_1 = \frac{3}{40}, \beta_2 = 0.0828 \tag{76}$$

$$\beta^* = \frac{9}{100} \tag{77}$$

$$\sigma_{k1} = 0.85, \sigma_{k2} = 1 \tag{78}$$

$$\sigma_{\omega 1} = 0.5, \sigma_{\omega 2} = 0.856 \tag{79}$$

Spalart-Allmaras model

Spalart-Allmaras model is a one equation model which solves a transport equation for a viscosity-like variable $\tilde{\nu}$. This may be referred to as the Spalart-Allmaras variable.

The turbulent eddy viscosity is given by

$$\nu_t = \tilde{\nu} f_{v1} \tag{80}$$

$$f_{v1} = \frac{x^3}{x^3 + C_{v1}^3} \tag{81}$$

$$x = \frac{\tilde{\nu}}{\nu} \tag{82}$$

$$\frac{\partial \tilde{\nu}}{\partial t} + u_j\frac{\partial \tilde{\nu}}{\partial x_j} = C_{b1}[1 - f_2]\tilde{S}\tilde{\nu} + \frac{1}{\sigma}\Big(\nabla\cdot[(\nu + \tilde{\nu})\nabla\tilde{\nu}] + C_{b2}\nabla\nu|^2\Big) - \left[C_{\omega 1}f_\omega - \frac{C_{b1}}{\kappa^2}f_{t2}\right]\left(\frac{\tilde{\nu}}{d}^2\right) + f_{t1}\triangle U^2 \tag{83}$$

$$\tilde{S} = S + \frac{\tilde{\nu}}{\kappa^2 d^2} f_{v2}, \tag{84}$$

$$f_{v2} = 1 - \frac{x}{1 + x f_{v1}} \tag{85}$$

where

$$S = \sqrt{2\Omega_{ij}\Omega i f} \tag{86}$$

$$\Omega_{ij} = \frac{1}{2}\left(\frac{\partial u_i}{\partial x_j} - \frac{\partial u_j}{\partial x_i}\right) \tag{87}$$

$$f_\omega = g\left[\frac{1 + {C_{\omega 3}}^6}{g^6 + {C_{\omega 3}}^6}\right]^{1/6} \tag{88}$$

$$g = r + C_{\omega 2}(r^6 - r) \tag{89}$$

$$r = \frac{\tilde{\nu}}{\tilde{S}\kappa^2 d^2} \tag{90}$$

$$f_{t1} = C_{t1} g_t \exp\left(- C_{t2} \frac{{\omega_t}^2}{\triangle U^2}\left[d^2 + {g_t}^2 {d_t}^2\right]\right) \tag{91}$$

$$f_{t2} = C_{t3} \exp(-C_{t4} x^2) \tag{92}$$

where d is the distance to the closest surface. The constants are given below

$$\sigma = 2/3 \tag{93}$$

$$C_{b1} = 0.1355 \tag{94}$$

$$C_{b2} = 0.622 \tag{95}$$

$$\kappa = 0.41 \tag{96}$$

$$C_{w1} = \frac{C_{b1}}{\kappa^2} + \frac{1 + C_{b2}}{\sigma} \tag{97}$$

$$C_{w2} = 0.3 \tag{98}$$

$$C_{w3} = 2 \tag{99}$$

$$C_{v1} = 7.1 \tag{100}$$

$$C_{t1} = 1 \tag{101}$$

$$C_{t2} = 2 \tag{102}$$

$$C_{t3} = 1.1 \tag{103}$$

$$C_{t4} = 2 \tag{104}$$

Basic error estimations

Can be subdivided into:

- Examine iterative convergence
- Examine consistency
- Examine spatial (grid) convergence
- Examine temporal convergence
- Compare CFD results to experimental data
- Examine model uncertainties (i.e. turbulence models)

Iterative convergence

Generally, CFD methods involve some iterative scheme to arrive at the simulation results. Here it is assumed that the iteration is with respect to time or a pseudo-temporal quantity and some type of time step is taken at each iteration. A steady-state flow simulation involves starting with a uniform or fabricated flow field and iterating in time until the steady-state flow field is obtained. This is termed iterative convergence, but requires some criteria for determining convergence. Criteria include:

Residuals. The residuals of the equations are the change in the equations over an iteration. These are usually scaled or normalized. One usually looks for the residuals to reach a certain level and then level-off as an indication of iterative convergence. For a time-marching, steady-state strategy, this involves examining whether the residual has been reduced a certain number (usually 3-4) of orders of magnitude.

Results. The CFD simulation has the objective of determining some quantity such as lift, drag, recovery, etc. One can track the values of such engineering quantities with respect to iteration and define iterative convergence when these quantities converge. The convergence criteria is usually defined by acceptable error in these values. It is often the case that certain quantities may reach convergence at a different rate than other quantities. One can check that a monitored flow value (such as thrust, drag, or boundary layer profile) has remained unchanged with respect to the number of iterations.

Solution convergence

One can evaluate convergence by checking for consistency in the flow field. The conservation relations require a balance of fluxes through a control surface. For a closed duct, the flow through the duct should be conserved. Low-speed flow over a closed body should have zero drag. Other such consistency relations can be defined for specific flow fields. These provide verification of the code since the consistency relations are usually a statement of some analytic result.

Temporal convergence

Samples of scalar transport (pressure) are taken then compared to the exact solutions, p_{ex}, and the difference is set relative to reference (pressure) for the problem.

$$(\bar{p_1}, \bar{p_2}, ..., \bar{p_{100}}) = [(p_1 - p_{\text{ex},1})/p_{\text{ref}}, (p_2 - p_{\text{ex},2})/p_{\text{ref}}, ..., (p_{100} - p_{\text{ex},100})/p_{\text{ ref}}] \quad (105)$$

the root mean square (RMS) error ε_{rms} is defined

$$\varepsilon_{\text{rms}} = \sqrt{\frac{1}{100}\sum_{i=1}^{100} \bar{p_i}^2} = \sqrt{\frac{\bar{p_1}^2 + \bar{p_2}^2 + ... + \bar{p_{100}}^2}{100}} \quad (106)$$

Spatial convergence

As the grid is refined (grid cells become smaller and the number of cells in the flow domain increase) and the time step is refined (reduced) the spatial and temporal discretization errors, respectively, should asymptotically approaches zero, excluding computer round-off error.

Methods for examining the spatial and temporal convergence of CFD simulations are presented in the book by Roache (Roache, 1998). They are based on use of Richardson's extrapolation.

Appendix 2: Radiance - scenes, sky models, and daylight sim.

This appendix is served as an introduction to the Radiance study guide. For a detailed explanation, refer to the text *Rendering with Radiance* (Ward and Shakespeare, 1998).

Radiance provides a number of object creation programs which can be used to create simple scenes, however, the complexity of these models is limited. The most efficient way to create a 3-D geometry in Radiance scene is by using a CAD or 3D modelling packages and importing the geometry through commonly used 3D file formats to Radiance. Some examples of converters are such as 3DS, OBJ, and DXF formats.

The Radiance standard release includes the sky model general program called **gensky**. This utility program will produce Radiance format sky luminance distribution for four sky model types, with the option to create a sun description for the non-overcast sky model types, which are:

- the uniform luminance model;
- the CIE overcast sky model;
- the CIE clear sky model;
- the Matsuura intermediate sky model.

The absolute luminance of any of these sky luminance patterns is controlled using either the zenith luminance or the diffuse horizontal illuminance. The sun position can either be defined by altitude and azimuth or calculated by gensky from the time and geographical coordinates (Mardaljevic, 1999). The overcast and clear CIE models are representations of extreme sky types. Intermediate sky is a somewhat hazy variant of the clear sky, where the Sun is not as bright as with the clear sky and the brightness changes are not as drastic (Mardaljevic, 1999).

The CIE overcast sky model: The overcast model takes the standard CIE form for this type of sky. The luminance at an angle ξ by the formula (CIE, 1996; Darula and Kittler, 2002):

$$L_\xi = \frac{L_\xi(1 + 2\cos\xi)}{3} \tag{107}$$

where L_ξ is the luminance at an angle ξ from the zenith and L_ξ is the zenith luminance.

The CIE standard clear sky model: The CIE clear sky model is normalised to zenith luminance and the sky luminance distribution is given by (CIE, 1996; Darula and Kittler, 2002):

$$L = L_\xi \frac{(1 - e^{(-0.32/\sin\gamma_r)})(0.91 + 10e^{-3\theta} + 0.45\cos^2\theta)}{(1 - e^{-0.32})(0.91 + 10e^{-3(\pi/2-\gamma_s)} + 0.45\sin^2\gamma_s)} \tag{108}$$

where γ_r is the sky point altitude, γ_s is the solar altitude, and θ is the angle between the sun and the sky point.

The CIE intermediate sky model: The model is based on the Matsuura formulation which describe sky conditions that have a higher turbidity than the CIE clear sky model (CIE, 1996; Darula and Kittler, 2002):

$$L(\gamma_r, \theta) = \frac{L_z \cdot a \cdot b}{2.326} \tag{109}$$

where

$$a = [1.3\sin(5.6 - 3.6\,\xi) + 3.1]\sin(4.4 - 2.6\,\xi_s) + 6.37 - \xi \tag{110}$$
$$b = \mathrm{EXP}[-0.563\,\theta[(2.629 - \xi)(1.562 - \xi_s) + 0.812]] \tag{111}$$
$$L_z = \text{diffuse horizontal irradiance} \tag{112}$$
$$\xi = \pi/2 - \gamma_r \tag{113}$$
$$\xi_s = \pi/2 - \gamma_s \tag{114}$$
$$\theta = \text{angle from sun to sky point} \tag{115}$$
$$\gamma_r = \text{sky point altitude} \tag{116}$$
$$\gamma_s = \text{sun altitude} \tag{117}$$

The sky distributions along an arc where the sun was assumed to be at an altitude of $\gamma = 0°$ (due North) across the zenith to $\gamma = 0°$ (due South), together with false-colour luminance maps for the clear, intermediate, and overcast models is plotted on Figure 5 (Mardaljevic, 1999).

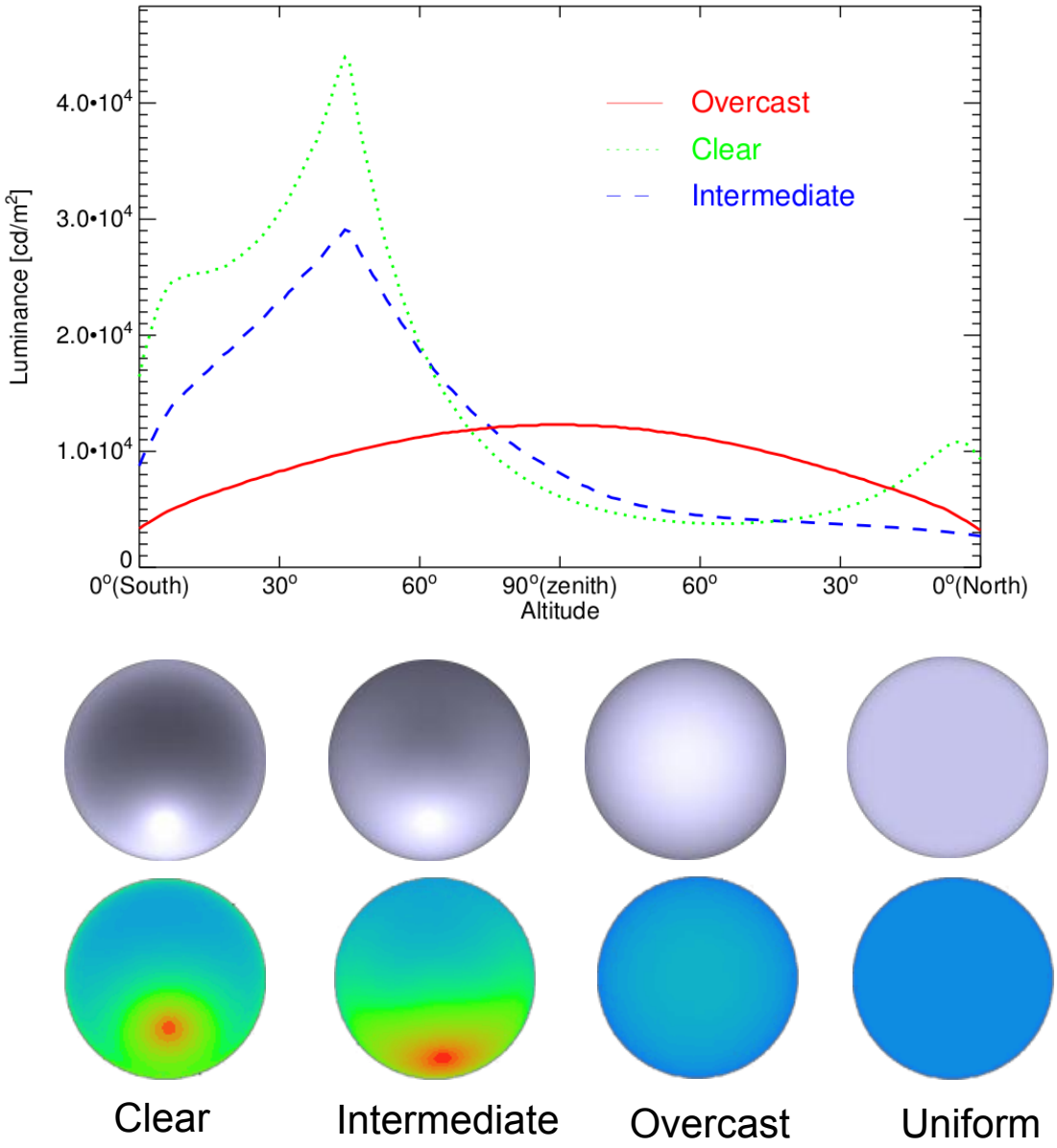

Figure 5. Luminance profile and maps for various sky models. Adapted from Mardaljevic (1999) (Mardaljevic, 1999).

The rtrace program is used to calculate radiance and irradiance. The output is a triad of predicted values for spectral (RGB) horizontal irradiance. To convert the spectral irradiance triad to irradiance:

$$I = 0.265I_R + 0.670I_G + 0.065I_B \tag{118}$$

Because the sum of the multiplying factors is 1, the achromatic irradiance equals 3.141593, which is the value for π. Comparing this with an analytically derived result. For any sky of radiance $B(\theta, \phi)$ the horizonal irradiance is given by:

$$I = \int_0^2 \pi \int_0^\pi 2B(\theta, \phi) \sin\theta \cos\theta \, d\,\theta \, d\,\phi \tag{119}$$

where for a uniform sky, $B(\theta, \phi) = B$, giving:

$$I = B \int_0^2 \pi \int_0^\pi \sin\theta \cos\theta \, d\,\theta \, d\,\phi = \pi B \tag{120}$$

which, for a sky of unit radiance, gives

$$I = \pi \tag{121}$$

This value for irradiance is what the rtrace simulation predicted.

The below diagram (Figure 6) illustrates the Radiance program schematic to calculate daylight irradiance (Ward, 1994b). Dark greys-diamonds represent programs while light-grey rectangles represent states of data. The diagram can be broken into three stages of data, the first stage is the scene input, followed by the compiled model, and the simulation output.

The input parameters for the sky model programs were derived from measurements of the global horizontal illuminance, the direct normal illuminance, and the sun position. The following operations summarise the automation sequence of the solar altitude angle and irradiance at every hour as follows:

1. Generate Radiance format skies using gensky
2. Create Radiance octree for the sun and sky description
3. Execute rtrace to calculate the external illuminances and write to temporary file
4. Add sun and sky description to the octree
5. Execute rtrace to calculate the illuminances and write to temporary file

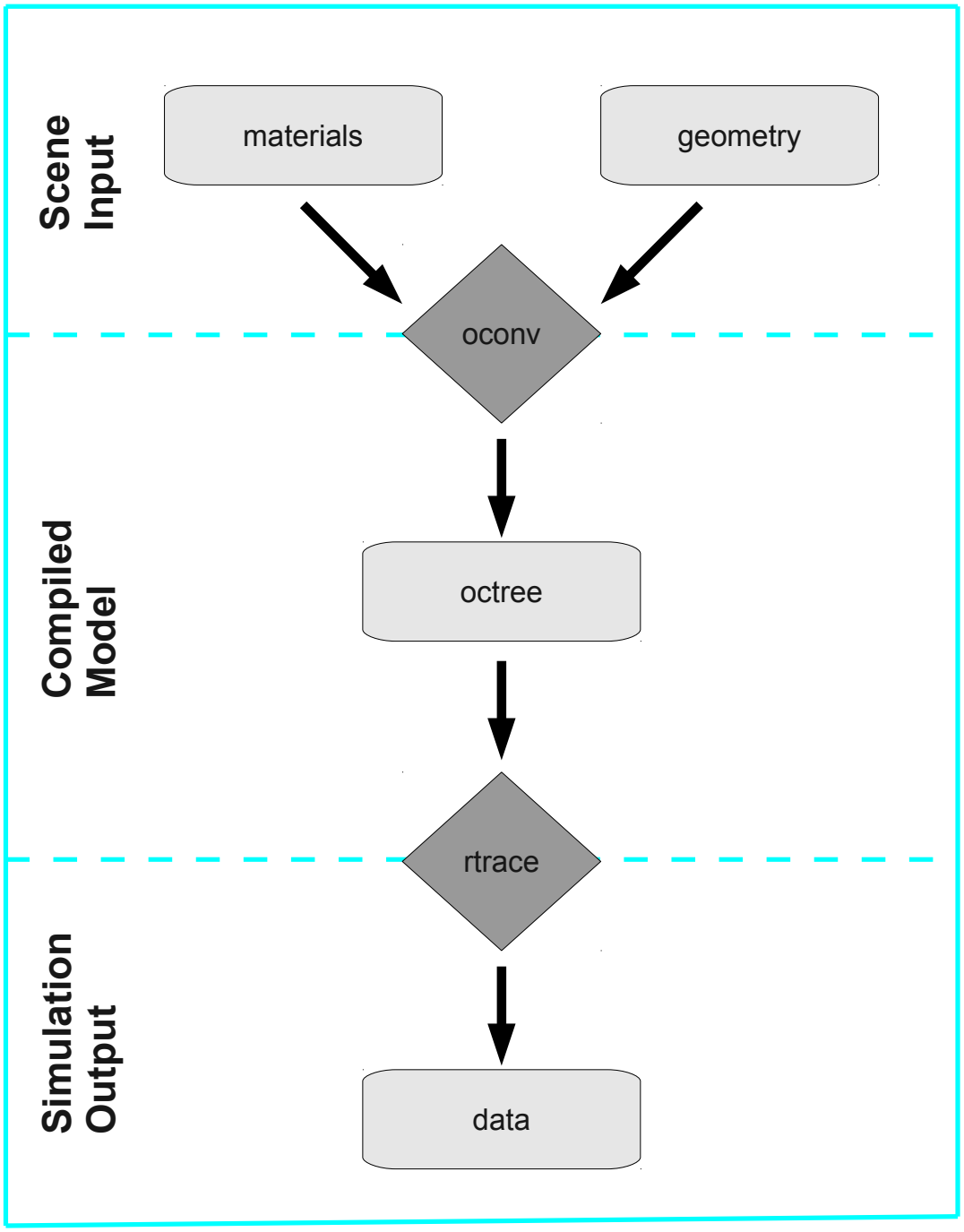

Figure 6. Radiance flowchart to calculate daylight irradiance. Adapted from Mardaljevic (1999) (Mardaljevic, 1999).

Description of sun and sky are generated with the `gensky` command. It produces two objects of type source, one for the sky hemisphere and one for the ground. The arguments to gensky are the month, day, and hour (local standard time). To start with, we created a sunny sky for Phuket on 4 March 1993 with the output file called *sky.rad*.

```
$ gensky 3 4 12:15 +s -a 7.48 -o -98.25 -m -99 > sky.rad
# gensky 3 4 12:15 +s -a 7.48 -o -98.25 -m -99
# Local solar time: 12.00
# Solar altitude and azimuth: 75.4 0.1
# Ground ambient level: 18.2

void light solar
0
0
3 7.18e+06 7.18e+06 7.18e+06

solar source sun
0
0
4 -0.000315 -0.251636 0.967822 0.5

void brightfunc skyfunc
2 skybr skybright.cal
0
7 1 3.15e+01 3.02e+01 1.64e+00 -0.000315 -0.251636 0.967822
```

This gives us a clear sunny sky and put the elements together in one octree file using oconv and then execute the `rtrace` program to determine the horizontal irradiance due to the specified sky.

```
$ oconv sky.rad > sky.oct
$ echo "0 0 0 0 0 1" | rtrace -h -I -ab 1 -ad 256 sky.oct
```

For more detailed backgrounds and examples on the Radiance daylight simulation, refer to the (Mardaljevic, 1999; Ward, 1994b,c; Ward and Shakespeare, 1998).